

Jagiellonian University  
M. Smoluchowski Institute of Physics



Detection of metastable  $\text{He}_2^*$   
molecules in helium plasma

Bartosz Głowacz

PhD Thesis  
Atomic Optics Department

Supervisors: prof. dr hab. Tomasz DOHNALIK  
and D.R. at CNRS Pierre-Jean NACHER

Cracow 2011

# Contents

<b>Contents</b>	<b>2</b>
<b>List of Figures</b>	<b>5</b>
<b>List of Tables</b>	<b>12</b>
<b>1 Introduction</b>	<b>15</b>
<b>2 He<sub>2</sub> molecule</b>	<b>19</b>
2.1 Formation of He <sub>2</sub> molecules . . . . .	19
2.2 Theoretical description of the helium dimer . . . . .	22
2.2.1 Approximations of V(R) potential . . . . .	24
2.2.2 Electronic molecular states . . . . .	27
2.2.3 Symmetries of the rotational levels and transition selection rules . . . . .	33
2.2.4 Intensities of the transition lines and molecular densities . . . . .	38
<b>3 Blue laser setup</b>	<b>43</b>
3.1 Second Harmonic Generation in PP-KTP . . . . .	45
3.1.1 Conversion efficiency . . . . .	47
3.1.2 Matching tolerances . . . . .	50
3.2 465 nm laser setup - description . . . . .	54
3.2.1 Laser setup components . . . . .	54
3.2.1.1 Laser diodes . . . . .	54
3.2.1.2 Nonlinear PP-KTP crystal . . . . .	55
3.2.2 Setup for SFG - construction scheme . . . . .	55
3.2.3 Laser output wavelength tuning . . . . .	56
3.3 Laser performance - experimental results . . . . .	59
3.3.1 Output power and efficiency . . . . .	59
3.3.2 Tuning range and matching conditions . . . . .	59
3.3.2.1 Laser wavelength calibration . . . . .	59
3.3.2.2 Matching conditions . . . . .	61
3.3.3 Matching tolerances in the experiment . . . . .	64
3.4 Conclusions . . . . .	67
<b>4 Absorption measurements on helium molecule - experimental results</b>	<b>69</b>
4.1 Experimental setup . . . . .	69
4.1.1 Laser frequency scan acquisition scheme . . . . .	70

4.1.2	Frequency scans recordings procedure . . . . .	71
4.1.3	Density decay rates experiment description . . . . .	72
4.2	Measurement data processing and reduction . . . . .	72
4.2.1	Processing of the recorded data files in numerical lock-in software . . . . .	73
4.2.2	Absorption line profile position determination . . . . .	74
4.2.3	Absorption line frequency scan signal to molecular absorption scaling . . . . .	75
4.2.3.1	Square 100% modulation in hardware and numerical lock-in detection . . . . .	75
4.2.3.2	Partial sine amplitude modulation . . . . .	76
4.3	Absorption lines shape . . . . .	77
4.4	Position of absorption lines . . . . .	88
4.4.1	Wavelength calibration of the laser setup . . . . .	89
4.4.2	Isotopic mixture cell - recordings of multiple lines . . . . .	89
4.5	Intensities of absorption lines . . . . .	99
4.5.1	Rotational temperature determination from relative absorption rates . . . . .	99
4.5.2	Dynamics of helium molecule . . . . .	103
4.5.2.1	Molecular and atomic density decay curves . . . . .	104
4.5.2.2	Atomic and molecular coupled rate equations . . . . .	106
<b>5</b>	<b>Investigations on Metastability Exchange Optical Pumping dynamics with blue laser</b>	<b>111</b>
5.1	Basics of MEOP . . . . .	111
5.2	Achievements in MEOP in standard and non-standard conditions . . . . .	114
5.3	MEOP angular momentum budget and laser induced relaxation . . . . .	115
5.4	Description of MEOP experiment with blue light transmission measurement . . . . .	117
5.4.1	MEOP experimental setup - design . . . . .	117
5.4.1.1	General constraints . . . . .	117
5.4.1.2	Nuclear polarization measurement method choice - pros and cons . . . . .	118
5.4.1.3	Blue laser in MEOP setup . . . . .	120
5.4.2	MEOP experimental setup - realization . . . . .	120
5.4.3	Acquisition scheme and measurements protocols . . . . .	122
5.4.3.1	Acquisition scheme and recorded signals . . . . .	122
5.4.3.2	Measurements protocol . . . . .	124
5.5	Experimental data reduction and processing . . . . .	126
5.5.1	Polarization build-up and decay curve for $M_{eq}$ and $T_{disch}$ determination . . . . .	127
5.5.2	Metastable atoms number density determination . . . . .	129
5.6	Experimental results of MEOP with molecular density measurements . . . . .	130
5.6.1	Discharge intensity . . . . .	131
5.6.2	Results of MEOP - nuclear polarization values . . . . .	133
5.6.3	Light induced relaxation and molecular absorption rates at $M_{eq}$ . . . . .	134
5.6.4	Atomic and molecular metastable species density change with polarization . . . . .	137
5.7	Absorption measurements in presence of OP pump beam at $M = 0$ . . . . .	138
<b>6</b>	<b>Conclusion and outlook</b>	<b>141</b>

<b>A</b>	<b>Absorption measurements</b>	<b>143</b>
<b>B</b>	<b>Sellmeier equation and coefficients</b>	<b>147</b>
<b>C</b>	<b>Constants</b>	<b>149</b>
	<b>Bibliography</b>	<b>151</b>

# List of Figures

2.1	Potential curve of two interacting helium atoms. Red curve represents Coulomb repulsive interaction, blue - induced dipole ( $\vec{d}_a, \vec{d}_b$ ) attraction - van der Waals force. The addition of these interaction results in the characteristic shape of the potential (black curve) with well of $D_e$ depth at the $R_e$ inter molecular distance. . . . .	20
2.2	Potential curves for He <sub>2</sub> molecule [37]. Red - potential curve for $a^3\Sigma_u^+$ state, blue - potential curve for $e^3\Pi_g$ state. . . . .	21
2.3	Hund's coupling (b). Detailed description in the text. . . . .	29
2.4	Scheme of rotational sublevels of $a^3\Sigma_u^+$ and $e^3\Pi_g$ states of <sup>4</sup> He <sub>2</sub> and <sup>3</sup> He <sub>2</sub> (next page), being a consequence of discussed coupling scheme and wavefunction symmetry properties (paragraph 2.2.2 (c)). The possible transition (according to the rules explained in subsection 2.2.3(e)) from exemplary rotational sublevels and its fine structure are marked - the notation is explained in subsection 2.2.3(f). The absence of even numbered rotational levels for helium-4 isotope is characteristic. . . . .	31
2.4	. . . . .	32
3.1	Simulated curves of Boyd-Kleinman focusing factor (a) and its square root (b) in function of $\sigma$ . . . . .	48
3.2	Change of the optimized $\sigma = \sigma_m$ in function of $\xi$ . . . . .	49
3.3	Variation of the $h(\sigma_m, \xi)$ values with $\xi$ showing the existence of a single maximum $\xi_m$ . . . . .	50
3.4	Variation of the FWHM of $h(\sigma, \xi)$ curve main peak with $\xi$ in $\sigma$ values scale - $\Delta\sigma_{1/2}$ (a) as well as $\frac{\Delta k_{QPMl}}{2}$ units (b). On the graph (b) the value FWHM value for no-focus ( $\xi = 0 \Rightarrow w_0 \rightarrow 0$ ) limit $\Delta(\frac{\Delta k_{QPMl}}{2})_{1/2} = 2.78$ . . . . .	51
3.5	Laser set-up. LD1, 2: LD at 923.58, 937.6 nm; M: mirror; AM: angle mirror; P: prism; L: lens; HM:hot mirror; LPF: low pass filter. HM and LPF both filter out the 465 nm radiation. Detailed description in the text. . . . .	56
3.6	Change of the laser diode wavelength (LD 937 nm) with the voltage controlled diode current. G=10 indicates the voltage controller setting range. . . . .	57
3.7	Infra red laser diodes change witch the feeding current tuning within 140 to 170 mA. . . . .	58

3.8	(a) The relation between the wavelength of absorption line maximum and corresponding laser diodes temperature on which the emitted blue light wavelength calibration relies. Black squares represents the lines recorded for ${}^3\text{He}_2^*$ , blue squares - lines recorded for ${}^4\text{He}_2^*$ . Designation of recognized molecular transitions are given next to the points written with the proper font color. The red line represents the linear fit - the calibration curve. Error bars on the points for temperature values comes from the accuracy of the line maximum position determination (including error caused by hysteresis effect) and the accuracy of the temperature measurement with the thermistor ( $\pm 1^\circ\text{C}$ ). (b) The wavelength-LD current driving voltage control coefficient $\frac{d\lambda}{dV}$ in laser diodes temperature tuning range. The decay with the $T_{LD}$ increase is visible, however the lack of enough number of points beyond 16-21 $^\circ\text{C}$ makes finding meaningful functional expression difficult. Errors are the resultant of the accuracy of absorption lines maxima position determination . . . . .	60
3.9	Wavelengths generated by the infra-red laser diodes in terms of their temperature $T_{LD}$ within 10-40 $^\circ\text{C}$ range. . . . .	61
3.10	Crystal and laser diodes temperature matching points fulfilling quasi-phase matching condition within available tuning range of both temperatures. . . . .	62
3.11	Matching line of the crystal temperature in function of generated blue wavelength - $\lambda_b$ . . . . .	62
3.12	Quasi-phase matching condition fulfilled at the various wavelengths of fundamental infra-red beams $\lambda_{av}$ . Several slopes are present due to discrepancies in the coefficients of the Sellmeier's equation met in the references. The matching wavelength related to the $\lambda_{av}$ used when the tolerance curves were measured (subsection 3.3.3) and the crystal temperature matched to this wavelength. . . . .	63
3.13	The crystal (a) and laser diodes (b) quasi-phases matching curves - the output laser power versus the temperature of crystal and laser diode respectively. The laser diodes temperature for the top peak value corresponds to the temperature setting of ${}^3\text{He}_2^*$ Q(2) line with the crystal temperature fulfilling the quasi-phase matching condition . . . . .	65
3.14	Fit of the dependency of the output blue power $\sqrt{P_b}$ and $P_b$ (b) on the laser diode temperature according to the eq.(3.25) . . . . .	66
3.15	Fit of the dependency of the blue power $\sqrt{P_b}$ (a) and $P_b$ (b) on the crystal temperature according to the eq.(3.25) . . . . .	66
4.1	Optical setup scheme for absorption measurements on molecules (with use of 465 nm laser) and atoms (with use of 1083 nm laser). The measurements on both species has to be performed independently as it is required to put the optical elements suitable for 1083 nm (red dashed line - IR beam path, black dashed lines - MIR metallic mirrors and PDIR - photodiode for infra-red wavelength) on the way of blue beam (solid blue line - beam path, solid black line - MB - mirrors and PDV - photodiode for visible wavelengths). . . . .	69
4.2	Scheme of the acquisition setup for the absorption frequency scans using voltage (triangle course of the V(t) function) control of 937 nm laser diode current supply being a component of the blue laser setup. . . . .	70

4.3	(a) Numerical lock-in output signal of transmitted blue laser beam (black solid curve) with laser diode current control voltage (red) in function of the recording time. The record last 1.5 period of voltage triangular function allowing comparison of the line profiles and positions reproducibility with the negative (black) and positive (red) voltage slope (b). . . . .	74
4.4	Comparison of the molecular absorption lineshapes of Q branche of two isotopologues $^3\text{He}_2^*$ and $^4\text{He}_2^*$ recorded in isotopic pure gases at 66.7 mbar each. Graphs (a)-(d) present pairs of the lines with the same odd-N value. Graph (e) shows the even-N numbered lines of $^3\text{He}_2^*$ . The SNR of the odd-N numbered Q lines of $^3\text{He}_2^*$ is lower than of the $^4\text{He}_2^*$ due to 1:3 statistical ratio of the line intensities. . . . .	78
4.5	Compilations of the molecular lines scans of the Q branch with odd N values for 8 - (a), 128 - (b) and 266.7 - (c) mbar pure $^3\text{He}$ pressure cells. Due to low SNR (graph (a)) or high pressure broadening effect(graphs (b) and (c)) these profiles are not suitable for the analysis of the complex lineshapes of odd-N numbered lines clearly distinguishable at 67.6 mbar. The noise on the curves of the graph (a) was averaged - for visualization of the noise magnitude non-averaged curves are shown in the inset. . . . .	79
4.6	Comparison of the first odd-N numbered line profile Q(1) with the first even-N numbered Q(2) profile. Q(1), the less distorted line from the odd-N numbered group is still broader than even-N numbered lines. . . . .	80
4.7	Lorentzian half width of Voigt profiles for Q(2) transition absorption lines at 8.66.7, 128 and 267 mbar pressure of $^3\text{He}$ . Linear fit to the experimental points has been performed providing the slope value $32.5 \pm 0.5$ MHz and intercept $0.85 \pm 0.07$ GHz . . .	82
4.8	Graphs with even-N numbered Q branch line profiles for 8 mbar pure $^3\text{He}$ cell. The curve described by the Voigt function was fit to each profile showing regular residue maxima at negative frequencies. . . . .	83
4.9	Graphs with even-N numbered Q branch line profiles for 66.7 mbar pure $^3\text{He}$ cell. The curve described by the Voigt function was fit to each profile showing regular residue maxima at negative frequencies. The last two graphs present the profile of P(2) and R(0) lines. For the former line small Voigt fit residue maximum at positive frequency is present, whereas in the latter line profile any explicit maximum can be distinguished. . . . .	84
4.10	Graphs with even-N numbered Q branch line profiles for 128 mbar pure $^3\text{He}$ cell. The curve described by the Voigt function was fit to each profile showing regular residue maxima at negative frequencies. The last graph presents the profile of P(2) line. Small fit residue maximum can be distinguished for positive frequency, as in case of data for 66.7 mbar. . . . .	85
4.11	Graphs with even-N numbered Q branch line profiles for 266 mbar pure $^3\text{He}$ cell. The curve described by the Voigt function was fit to each profile, however, in case of this pressure characteristic maxima of the fit residues seen at lower pressures are not observed. . . . .	86

4.12	Comparison of the only well-resolved absorption lines of ( <sup>3</sup> He- <sup>4</sup> He)* with the profile of Q(2) line of <sup>3</sup> He <sub>2</sub> * . Mixture lines, although one odd-N numbered and the second even-N numbered are of the same shape (compare with the difference of even-N and odd-N numbered lines for <sup>3</sup> He <sub>2</sub> * ), similar to the "not-distorted" even-N numbered line (i.e.Q(2)) of <sup>3</sup> He <sub>2</sub> * isotopologue. Small broadening, in comparison with Q(2) of <sup>3</sup> He <sub>2</sub> * , is present on the negative frequency wings for Q(2) and Q(3) lines of the heteronuclear dimer, what is confirmed in the existence of fit residue maxima relatively (as compared to the line height) higher than for Q(2) lines . . . . .	87
4.13	(a) Compensation of the wavelength change due to 937 nm laser diode current by the laser diodes temperature ( <i>T<sub>LD</sub></i> ) change providing tuning of the blue laser setup to Q(2) transition of <sup>3</sup> He <sub>2</sub> * ; (b) the proportionality curve of laser diode current <i>I</i> <sub>937</sub> and control voltage <i>V</i> . Linear fits to both curves provide the slope values of <i>dI/dV</i> and <i>dI/dT</i> necessary for rescaling the voltage scale of the scans to the temperature. . . . .	90
4.14	Three frequency scans of close lying molecular lines (a) doublet of <sup>3</sup> He <sub>2</sub> * and <sup>4</sup> He <sub>2</sub> * lines Q(2) and Q(5) respectively; (b) triplet consisting of <sup>3</sup> He <sub>2</sub> * , <sup>4</sup> He <sub>2</sub> * and ( <sup>3</sup> He- <sup>4</sup> He)* ; doublet of P(3) and P(2) <sup>4</sup> He <sub>2</sub> * and <sup>3</sup> He <sub>2</sub> * isotopologues. . . . .	91
4.15	Frequency scans of close lying <sup>3</sup> He <sub>2</sub> * and <sup>4</sup> He <sub>2</sub> * molecular lines of which one is overlapped with the absorption line of ( <sup>3</sup> He- <sup>4</sup> He)* . . . . .	92
4.16	Frequency scans of close lying <sup>3</sup> He <sub>2</sub> * and <sup>4</sup> He <sub>2</sub> * molecular lines of which one is overlapped with the absorption line of ( <sup>3</sup> He- <sup>4</sup> He)* . . . . .	94
4.17	Example of the frequency scan containing only two absorption lines of <sup>3</sup> He <sub>2</sub> * and ( <sup>3</sup> He- <sup>4</sup> He)* used to determination of mixture line position assuming the value of $\frac{d\lambda}{dV}$ to be known from the frequency scan of 3 lines - including Q(1) of <sup>3</sup> He <sub>2</sub> * - see Fig.4.16. . . . .	94
4.18	Frequency scans of three absorption lines: two of the ( <sup>3</sup> He- <sup>4</sup> He)* molecule and one of <sup>4</sup> He <sub>2</sub> * overlapped with one of the former ones. . . . .	95
4.19	Frequency scans of partially overlapped absorption lines of <sup>3</sup> He <sub>2</sub> * and ( <sup>3</sup> He- <sup>4</sup> He)* . Graph (c) can be compared with Fig.4.15(b) where the same complex of Q <sup>34</sup> (8) and Q <sup>33</sup> (7) is shown, however, here the range of higher frequency is presented containing the P <sup>34</sup> (2) absorption line. . . . .	95
4.20	Frequency scans of partially overlapped absorption lines of <sup>3</sup> He <sub>2</sub> * and ( <sup>3</sup> He- <sup>4</sup> He)* . . . . .	96
4.21	Positions of all the helium molecule isotopologues <sup>3</sup> He <sub>2</sub> * , <sup>4</sup> He <sub>2</sub> * and ( <sup>3</sup> He- <sup>4</sup> He)* absorption lines of <i>a</i> <sup>3</sup> Σ <sub>u</sub> <sup>+</sup> (0) - <i>e</i> <sup>3</sup> Π <sub>g</sub> (0) transition around 465 nm. Overlapping of the lines are present according to the information in the Table 4.8 . . . . .	98
4.22	Comparison of the linear fits to the ln( <i>T/T<sub>Q(2)</sub></i> ) (under the natural logarithm - the relative blue light transmission ratio for chosen transition from N rotational sub-level); <i>T<sub>Q(2)</sub></i> is a blue laser beam transmission tuned to Q(2) transition) dependency on rotational sublevels energy difference Δ <sub><i>F</i></sub> = <i>F(N)</i> - <i>F(2)</i> in 8, 66.7, 128 and 266 mbar pure <sup>3</sup> He cell. From the slope value the rotational temperature <i>T<sub>rot</sub></i> has been determined (see the text and the Table 4.9) . . . . .	101

4.23	Comparison of the rotational temperatures between two isotopologues $^3\text{He}_2^*$ and $^4\text{He}_2^*$ at the pressure of 66.7 mbar. Investigations were performed in two separate isotopic pure cells for two discharge regimes - weak and strong in each case. Change in the slope value indicates the change in $T_{rot}$ . Higher the absolute value of the negative slope, lower the temperature - for the weak discharges $T_{rot}$ is lower than for strong discharge regime in case of both isotopologues. Temperatures are higher for $^3\text{He}_2^*$ than for $^4\text{He}_2^*$ . . . . .	103
4.24	Time decay curves of atomic (red lines) and molecular (black lines) relative to the static situation (before switching off the plasma discharges -for Time <0 s on the graphs) densities expressed as the ratio of transmission logarithms $\ln(T)/\ln(T_{static})$ in pure $^3\text{He}$ cells at: (a) 8 mbar, (b) 66.7 mbar, (c) 128 mbar, (d) 267 mbar. Ordinate axis on graphs (a)-(d) are in ln scale showing non-exponential character of both atomic and molecular decays. . . . .	104
4.25	Pressure change of the atomic (a) and molecular (b) decay times. The values of half-decay $\tau_{0.5}$ are given on the graphs for every pressure, $y=0.5$ curve is plotted as a guide for the eye. The early time decay part is blown-up on the graph (c) to present the increase of molecular density in respect to the static value before Time=0 s. The percentage values of signal increase are given for each pressure. . .	105
4.26	Difference between the decay curves for three isotopologues of $\text{He}_2^*$ . Relative increase of the molecular density is given on the graph as well as half-decay times and static molecular absorption are compared - both increase with the mass of molecule.	106
4.27	Comparison of the atomic $^3\text{He}$ and $^4\text{He}$ density decay curves in the 1:1 isotopic mixture cell at 66.7 mbar. Absorption values and corresponding $n_m$ densities are given on the figure measured on $C_{6-7}$ and $D_0$ transitions. $C_8$ nor $C_9$ has been used to determinate metastable atoms density for $^3\text{He}$ as they overlap with $D_1$ and $D_2$ transition lines of the second isotope in the gas mixture - see Fig.5.1. . . . .	108
5.1	Calculated absorption spectra of $^3\text{He}^*$ (a) and $^4\text{He}^*$ (b) at 300 K, pressure 32 mbar and null magnetic field B. Doppler and pressure broadening effects has been taken into account. The lines designation is given according to well established nomenclature [53]. Notice the frequency scale and overlapping of $C_8$ and $C_9$ lines with $D_2$ and $D_1$ if absorption spectroscopy in isotopic mixture gas is performed. . . . .	113
5.2	Arrangement of the optical elements for MEOP setup realisation with simultaneous 465 nm laser transmission measurement mounted on a single breadboard 120x30 cm. Pump, infra-red (IR) probe and 465 nm probe beams paths are shown. PBS - polarizing beam splitter, $\lambda/4$ - quarterwave plate, PD - photodiode, M - mirror for the IR or 465 nm wavelength, f - the value of lenses focal lengths. In the small square part of the setup - polarization analyzer - the cutting plane of the PBS before the PD of the second IR probe beam is $45^\circ$ to the drawing plane (breadboard plane).	121
5.3	Block scheme of the measurement and acquisition setup. Detailed description of the optical part inside the magnetic field coils is given in 5.4.2 with Fig.5.2. . . . .	123
5.4	Time chart of the IR and blue probe beams course in the absence of OP light. Absolute values of absorptions can be deduced from the signals value in proper time periods. . . . .	125

5.5	Time chart of the IR and blue probe beams course in the absence of OP light. Absolute values of absorptions can be deduced from the signals value in proper time periods. . . . .	126
5.6	Build up and the decay of polarization as a function of time for the MEOP experiment performed with protocol B. The discontinuities of the presented curve corresponds to the periods when the discharges were off. Apparent value of the polarization $M = M_{app}$ has been marked with the dashed line as well as the decay period (330-420 s) after the OP beam was blocked. Recording performed for the "weak" discharges and 0.17 W of absorbed pump power at $M_{eq}$ ; time constant applied in the numerical lock-in $\tau_{LIA}=0.2$ s. . . . .	127
5.7	Decay part of the MEOP experiment recording curve shown in the linear scale (a) and logarithmic scale of ordinate (b). The red solid lines represent exponential fit - graph (a) and the linear fit - graph (b) to the experimental data. This MEOP recording has been performed at "strong" discharge level where the difference between exponential character of the decay in linear scale of ordinate is clear when compared to the linear character in ln scale. This difference for "weak" discharges (fig.5.6) is not as emphatic due to longer decay time. . . . .	128
5.8	Discharge stability during 4 h series of the MEOP measurements in 32 mbar cell expressed as a stability of $T_{disch}$ value . Regime of strong discharge (40% of IR probe, $C_8$ absorption). Presented data results from the exponential fits to the 15 s decay recordings in the absence of pump beam within protocol C. With the line, the $T_{disch}$ value is presented obtained from B-protocol recording where recording of the decay lasts 90 s. All the values from protocol C recordings agree within the error bars with the B-protocol value. . . . .	132
5.9	Values of $^3\text{He}$ nuclear polarization in condition of the balance between build-up and relaxation - "equilibrium" state, obtained in the MEOP for various absorbed OP light powers for two discharge regimes: "weak" (black squares) and "strong" (red squares). $M_{eq}$ values is presented in terms of the absorbed pump laser power at this $M = M_{eq}$ . . . . .	134
5.10	Laser induced relaxation rates $\Gamma_{laser}$ in function of absorbed OP beam power at $M_{eq}$ - when build-up kinetics are balanced by relaxation processes. Both abscissa and ordinate of the main graph are given in the log scale to exaggerate the dependency in the range of low absorbed power that in the linear scale of both axes (inset) is not clear. Two discharge regimes at 32 mbar, 0.82 mT are presented showing both the same functional dependency character (linear, within one slope) of $\Gamma_{laser}$ in terms of absorbed pump power. Black/red squares - data for "weak"/ "strong" discharge regime, black/red dashed line - $\Gamma_{decay}$ values at this rf excitations. Solid black/red lines are the linear function fits independently to the data of both discharge regimes.	135

5.11	Values of $-\ln(T)$ for 465 nm laser light tuned to Q(2) molecular transition for 32 mbar cell in which MEOP experiment is performed in parallel. Transmittances are measured at $M_{eq}$ and shown as a function of the absorbed IR pump laser power nuclear polarization. Red/black squares - data for "strong"/"weak" discharges. On the graph (a) the $-\ln(T) \propto N_M$ has been shown while on (b) $-\ln(T)/\ln(T(W_{abs} = 0)) \propto N_M/N_M(W_{abs} = 0)$ - relative $-\ln(T)$ in respect to the value in absence of the OP beam are presented. On the graph (b) the linear fits to the two "discharge" regimes are shown. On the graph (a) black/red/blue solid lines are the linear fits for comparable absorption power ranges in case of both discharge regimes: ("weak" full range up to 0.3 W)/("strong" up to 0.4 W)/("strong" up to 0.2 W) of absorbed pump laser power. . . . .	136
5.12	Relative change in respect to the value at $M = 0$ of metastable $^3\text{He}$ atoms density with nuclear polarization $M$ during its decay when no OP is present. The polarization decrease is toward the origin of the horizontal axis what is reflection of the $M$ evolution in the time domain. . . . .	137
5.13	Relative change in respect to the value at $M = 0$ of $^3\text{He}_2^*$ density with nuclear polarization $M$ during its decay . . . . .	138
5.14	Comparison of $-\ln(T) \propto N_M$ values measured at $M = M_{eq}$ (red squares) and $M = 0$ (black squares) in "weak" (a) and "strong" (b) discharge regimes in function of the absorbed pump beam power $W_{abs}$ . . . . .	139

# List of Tables

3.1	Parameters of the simulated curves describing the Boyd-Kleinman versus $\sigma$ dependency for various $\xi$ values. . . . .	49
3.2	Compilation of the references with PP-KTP applications to SHG and SFG providing the view on $d_{eff}$ coefficient values for various wavelengths and crystal grating periods. . . . .	49
3.3	Results of the $\sqrt{P_b}$ fit performed to the experimental data of $T_{LD}$ and $T_{cr}$ matching curves. . . . .	66
4.1	Full width at half maximum of <b>even</b> $N$ -numbered absorption lines profiles of $^3\text{He}_2$ at 8-267 mbar pressure range. For the 66.7 mbar two discharge excitation regimes has been studied - <i>weak</i> ( $w$ ) and <i>strong</i> ( $s$ ) (details further in the text). . . . .	80
4.2	Full width at half maximum of <b>odd</b> $N$ -numbered absorption lines profiles of $^3\text{He}_2$ at 8-267 mbar pressure range. For the 66.7 mbar two discharge excitation regimes has been studied - <i>weak</i> ( $w$ ) and <i>strong</i> ( $s$ ) (details further in the text). The error of the FWHM values for odd- $N$ transitions of 8 mbar $^3\text{He}$ cell are especially higher due to very low SNR of the profiles recordings - Fig. 4.5 (a) . . . . .	81
4.3	Full width at half maximum of $^4\text{He}_2$ absorption lines profiles of at 66.7 mbar pressure. Two discharge excitation regimes has been studied - <i>weak</i> ( $w$ ) and <i>strong</i> ( $s$ ) . . . . .	81
4.4	Absorption values for observed molecular transitions for $^3\text{He}_2^*$ at different pressures between 8 to 266.7 mbar of isotopic pure cells. For 66.7 mbar two discharge regimes are considered of weak and strong rf excitation. The plasma condition inside the cells can be compared via 1083 nm absorption on $C_8$ atomic transition given in the first row of the absorption values. NR - not recorded in the experiment. . . . .	88
4.5	Absorption values for observed molecular transitions for $^4\text{He}_2^*$ at 66.7 mbar of isotopic pure cell. Two discharge regimes are considered of weak and strong rf excitation. The plasma condition inside the cell can be compared via 1083 nm absorption on $D_0$ atomic transition given in the first row of the absorption values. . . . .	88
4.6	Molecular constants for $(^3\text{He}-^4\text{He})^*$ calculated with use of the mass scaling relations applied to known rotational constants for $^3\text{He}_2^*$ and $^4\text{He}_2^*$ isotopologues. $T_e + G(\nu = 0)$ is energy of so-called <i>band origin</i> . All the values are given in $\text{cm}^{-1}$ unit. . . . .	93

4.7	Position in wavelength scale of 11 absorption lines of within expected tuning range of the blue laser. $\lambda_{calc}$ values are calculated using the molecular constants (Table 4.6), $\lambda_{exp}$ are experimentally determined positions of the lines, $\delta\lambda_{exp}$ are the uncertainties of line positions determination in voltage scale and its scaling to the wavelengths. Calculated values of the positions are in very good agreement (within 3rd decimal place) with given in [46]. . . . .	93
4.8	Absorption values for observed molecular transitions for $^3\text{He}_2^*$ , $^4\text{He}_2^*$ and $(^3\text{He}-^4\text{He})^*$ at 66.7 mbar of isotopic 1:1 mixture cell. Two discharge regimes are considered of weak and strong rf excitation. Some molecular absorption lines are totally (o) or partially (po) overlapped with close lying lines of other isotopologue. Some lines are not available for detection (NA) due to limited blue laser tuning range, there are lines absorptions that has not been measures (NR) . . . . .	97
4.9	Pressure compilation of the relative (in respect to the value for Q(2) transition) absorption lines amplitudes of numerical lock-in output data for $^3\text{He}_2^*$ . These data has been used for the $T_{rot}$ determination (see fig.4.22) using the relation (4.6). The results of obtained rotational temperatures are presented as well. Error values $\delta T_{rot}$ results from the error on line intensities determination of which the ratios were used for temperature determination through the linear fit. In the lowest rows of the table the absolute absorption values measured on the Q(2) transition has been given as a reminder (see Table 4.4) of the considered order of magnitude as well as, for the sine modulation, the X factor values that were applied in $OUT_nLIA$ -to-absorption scaling (see subsection 4.2.3.2). Abbreviations: $n_m$ - density of atoms in $2^3S_1$ state, $w$ - weak discharges excitation, $s$ - strong discharge excitation SIN, SQ - partial sinusoidal and 100% square amplitude modulation, NR- not recorded, NC- not considered for 100% square modulation . . . . .	100
4.10	Pressure compilation of the relative (in respect to the value for Q(3) transition) absorption lines amplitudes of numerical lock-in output data for $^4\text{He}_2^*$ . These data has been used for the $T_{rot}$ determination (see fig.4.23) using the relation (4.6). The results of obtained rotational temperatures are presented as well. Error values $\delta T_{rot}$ results from the error on line intensities determination of which the ratios were used for temperature determination through the linear fit. In the lowest rows of the table the absolute absorption values measured on the Q(2) transition has been given as a reminder (see Table 4.5) of the considered order of magnitude as well as, for the sine modulation, the X factor value that were applied in $OUT_nLIA$ -to-absorption scaling (see subsection 4.2.3.2). Abbreviations: SIN, SQ partial sinusoidal and 100% square amplitude modulation, NC not considered for 100% square modulation . . . . .	102
4.11	Atomic and molecular rates terms for creation and destruction processes in condition of no OP performance. . . . .	107
4.12	Compilation of parameters in the rate equations (4.8) and (4.8). (* ) - Obtained using the $D_{mol}$ value for $^4\text{He}_2^*$ [66] through the isotopic mass scaling: $D_i = D * \sqrt{M/M_i}$ . . . . .	109
5.1	Parameters characterizing the discharge plasma in MEOP experiment at 66.7 mbar of $^3\text{He}$ , 0.82 mT magnetic field in <i>weak</i> and <i>strong</i> regimes of excitation. . . . .	133
B.1	Coefficients of the Sellmeier equation for the $n_z$ refractive index component reported in [69, 70, 72] . . . . .	147

B.2	Coefficients of the Sellmeier equation for the $n_z$ refractive index component reported in [71, 73, 74] . . . . .	148
C.1	Molecular constants for $^4\text{He}_2^*$ and $^3\text{He}_2^*$ reported in [28] and [6] respectively. . . . .	150

# Chapter 1

## Introduction

Metastable molecules ( $\text{He}^*_2$ ) are ubiquitous in helium systems. They are produced by any excitation process that feeds in enough energy to create excited, ionic or metastable atomic species (electric discharge, bombardment by charged particles, irradiation with ionizing radiation or intense laser pulses), provided that the density of ground state atoms is high enough to allow conversion by 3-body collisions. Extensive work has dealt with room temperature gas for basic studies of this unique dimer and of the complex processes involved in He plasmas, with a renewed interest driven by a variety of applications both at low and high pressures.

Studies performed on the simplest molecule after the hydrogen dimer are interesting due to possibility of direct testing of atom-atom interactions (in particular in the context of laser-cooled systems) and comparisons with theoretically computed molecular levels and structure (especially accurate for this few-electron system).

Apart from the gaseous phase in the room temperature  $\text{He}^*_2$  is observed also in dense gas as well as in liquid, droplets, and clusters at cryogenic temperatures (references in [1]). In the superfluid He helium molecules recently have been used as probes of the fluid dynamics on microscopic length scales [2] due to the considerable line broadening induced by the surrounding medium.

Recently, the formation of molecules in helium radio frequency discharge plasma at pressure range 1-300 mbar is suspected to play a significant role in the relaxation processes - responsible for the loss in non-thermal equilibrium nuclear polarization (hyperpolarization) of  $^3\text{He}$  achieved in Metastability Exchange Optical Pumping (MEOP) method [53, 62, 63]. Variety of applications of hyperpolarized  $^3\text{He}$  in fundamental research and biomedical applications, including the main ones [63]: spin filters for polarizing neutrons, scattering targets for investigations of the structure of nucleons, investigations of nonlinear nuclear magnetic resonance (NMR) dynamics in hyperpolarized liquid  $^3\text{He}$ , magnetic resonance imaging (MRI) of the lung in humans and in animals with inhaled gas, encourages to the MEOP efficiency increase (producing the largest amount of highest polarized gas in the shortest time) through investigation and overcome its limitations.

Studies on MEOP has been initiated in 1963 with the method discovery. With development of new powerful laser sources at the wavelength of 1083 nm related to the  $2^3\text{S}_1$ -  $2^3\text{P}$  helium atomic transition used for optical pumping, with adequate spectral characteristics, the significant improvement in achievable nuclear polarization values has been made. Since then the maximum experimentally obtainable polarization values are still limited, and differences between theoretically expected and experimentally measured quantities are observed [57, 59, 63]

especially when the further increase of the pump laser power does not translate into higher polarization values. Detailed studies of this phenomena led to single out the relaxation process induced by the laser radiation used to optical pumping process that depends only on the amount of absorbed power by the metastable helium atoms. Currently there are two mechanisms under consideration that are suspected to play a key role in the laser enhanced relaxation: radiation trapping and exchange collisions between polarized ground state helium atom and the helium metastable molecule.

Initial considerations about the first process, in which the circularly polarized radiation emitted from de-exciting  $\text{He}(2^3\text{P})$ , instead leaving the volume of polarized gas, is reabsorbed by the  $\text{He}(2^3\text{S})$  being a competing process of the simultaneously performed optical pumping, have excluded this mechanism as dominant process causing the difference between measured and expected polarization values.

The second process in which the presence of 1083 nm radiation is crucial is formation of the metastable helium molecules through ternary collisions between excited state atom ( $\text{He}(2^3\text{S})$  or  $\text{He}(2^3\text{P})$ ) and two ground state atoms  $\text{He}(1^1\text{S}_0)$ . As presented in [15] the rate constant for the reaction involving the  $\text{He}(2^3\text{P})$  is about 100 times higher than when  $2^3\text{S}_1$  is colliding with two ground state atoms. It has been proposed [62] that during the collision  $\text{He}^*_2$  - polarized  $\text{He}(1^1\text{S}_0)$  the electronic excitation of the latter can be exchanged with the ground state atom within the molecule so that the polarized nuclei is "imprisoned" in the dimer while unpolarized nuclei is carried by outgoing atom. The nuclear angular momentum of the bounded polarized atom is immediately dissipated in numerous rotational molecular states due to spin-orbit coupling, constituting efficient channel of the relaxation

Preliminary investigation on the helium molecule in the plasma conditions used for MEOP has been performed with use of emission spectroscopy method and laser induced fluorescence [62] providing informations about increased molecular density while 1083 nm is absorbed. These spectroscopic emission studies, where the complex discharge kinetics preclude definitive interpretation of the time-resolved spectra did not allow performing simultaneous MEOP and molecular density change measurements.

From the other hand single-photon absorption is a sensitive technique for direct detection of  $\text{He}^*_2$  and absolute density measurements, thus the need of continuous-wave laser source providing the radiation at one of the molecular transitions wavelength became important.

The most explored in the literature helium molecular transitions are  $a^3\Sigma_u^+ - c^3\Sigma_g^+$  and  $a^3\Sigma_u^+ - e^3\Pi_g$ , in order of the band strength in the whole range of the  $\text{He}_2$  spectrum [47]. However, for Author's knowledge, the latter one is the only for which the oscillator strength can be determined directly from known excited state lifetime [35], allowing the calculation of absolute molecular density if the absorption value on known molecular transition is determined. Apart from that, the spectra at 465 nm offers variety (belonging to P,Q,R branches)[6, 28, 47] of absorption lines within narrow wavelength range of about 2 nm, that is the usual range of laser diodes tuning range. This makes the choice of the transition useful not only for the reason of molecular density changes observations and proper easy transition identification but also allows performing detailed spectroscopy measurements. Thus the choice for obtaining the laser source at 465 nm has been made.

Development of the laser diodes at the wavelengths from lower part of visible light range resulted in various applications from home use - high density optical storage technologies (e.g. Blu-ray, AOD - 405 nm) and high resolution laser printers through something more sophisticated as in medicine (laser-induced fluorescence of cancerous and precancerous cells in

presence of blue laser light) or spectrophotometry in paper manufacturing to scientific use for atomic spectroscopy of chemical elements that have resonant lines in the blue/UV region including aluminum (396 nm), gallium (403 & 417 nm) and indium (450 nm). Unfortunately, at the time of experiment planning, the laser diodes at the wavelength of 465 nm were not available. Well known methods of generation of various laser light wavelengths not available as a simple laser diodes or other compact sources, are the non-linear processes of second harmonic generation (SHG) and sum frequency generation (SFG). With the use of periodically poled crystal KTiOPO<sub>4</sub> (PP-KTP) and two laser light sources (laser diodes) working at 923 nm and 937 nm, generation of 465 nm photon was possible in SFG process - single 930 nm laser diode for SHG was not available at that time.

This work concentrates of the laser setup development and preliminary absorption measurements on the helium molecular species with the emphasize on the simultaneous monitoring of molecular density and MEOP dynamics for 1083 nm laser enhanced relaxation rate origin determination. The manuscript is organized in the following way:

- chapter II - the basic introduction to the molecular physics and spectroscopy is presented focusing on the case of helium metastable dimer as well as its  $e^3\Pi_g$  state. Detailed nomenclature is introduced, symmetries, coupling scheme of the angular momenta relevant in this case are discussed leading to determination of possible transitions within the rotational structure of the states expected in further observation.
- chapter III - begins with short introduction to the twin nonlinear processes of SHG and SFG preparing the background for further laser efficiency discussion. Technical details about components and their arrangement in the final setup realization are described followed by studies of its performance - efficiency of 465 nm laser light generation, crystal and laser diodes phase matching tolerances as well as wavelength tuning range calibration.
- chapter IV - is dedicated to the absorption spectroscopy observations based on frequency scans of absorption line profiles. Experimental setup, data acquisition scheme and its reduction and processing are discussed. The experimental results presentation is begun with observed complex line shape description. Relying on the profiles recordings their position and amplitudes are determined from which laser wavelength calibration has been inferred and the molecular absorption rates obtained. The helium mixture ( $^3\text{He}$ - $^4\text{He}$ )\* molecule line positions are calculated relying on known isotopic mass scaling together with reference data of molecular constant for other isotopologues and confirmed experimentally. The preliminary molecular dynamics of He<sub>2</sub> densities investigations are presented and compared with atomic density evolution during the discharge plasma decay after turning off the excitation source.
- chapter V - introduces the Metastable Exchange Optical Pumping method of  $^3\text{He}$  gas polarization, putting emphasis on the angular momentum budget of the atomic system, where the term responsible for laser enhanced polarization loss appears. Later the conditions of polarization in low magnetic field of order 1 mTesla are described as well as absorption technique of nuclear polarization measurements, altogether putting the constraints on presented experimental setup where MEOP process is simultaneously performed with measurements of molecular density changes. After the discussion of data acquisition, processing and analysis methodology the experimental results are presented

beginning with helium plasma conditions characterization and achieved nuclear polarization values. Laser induced relaxation rate increase with absorbed pump laser power is observed and compared with the increase in molecular density. The molecular formation enhancement is studied also in presence of the OP light and null polarization value.

Selected aspects that could not be treated in the main text corpus are presented in more detail in the appendix of this work.

# Chapter 2

## He<sub>2</sub> molecule

Helium molecules, dimers ubiquitous in helium systems, has been object of investigations since early nineties [5]. However, the work has been concentrated mainly on the molecules consist of most common <sup>4</sup>He isotope[4, 28], which natural abundance in Earth's atmosphere is 1 million higher than of <sup>3</sup>He. The main source of available amount of lighter isotope is tritium decay present in dismantled nuclear weapon, so that the investigations performed on molecular <sup>3</sup>He begun after 1950 [6] resulting, however, in poor amount of references and spectroscopic data.

### 2.1 Formation of He<sub>2</sub> molecules

Helium molecule is an example of a dimer consists of atoms that belong to the noble gases group. In this case completely filled electronic shells of identical atoms excludes formation of covalent or ionic bonds but still existence of stable diatomic molecule is possible. The reason for that is presence of weaker than interactions mentioned before, but the only one in their absence, so called van der Waals force (vdW). This weak, long-distance, attractive electrostatic interaction between atoms is a result of their permanent possession or temporary induction of dipole momentum. For neutral helium atoms the latter case is valid as the electronic cloud has a spherical symmetry. However, due to continuous movement of electrons around the nucleus, temporary shift of the negatively charged cloud is possible and thus temporary formation of dipolar momentum  $\vec{d}$  altogether with generated, at the distance  $R$  from the dipole, electric field vector  $\vec{E}$  of the value  $|\vec{E}| = |\vec{d}|/4\pi\epsilon_0 R^3$ . If we consider two helium atoms He<sub>a</sub> and He<sub>b</sub> at the distance  $R$ , the presence of temporary dipolar momentum  $\vec{d}_a$  and associated electric field  $\vec{E}_a$  has its consequences in inducing dipolar momentum  $\vec{d}_b^{ind} = \alpha\vec{E}_a$  in He<sub>b</sub> atom ( $\alpha$  is electric polarizability). Of course to this induced dipolar momentum of atom He<sub>b</sub> the electric field  $|\vec{E}_b| = |\vec{d}_b|/4\pi\epsilon_0 R^3$  is related, which in turn induces in He<sub>a</sub> time averaged dipolar momentum  $\vec{d}_a^{ind} = \alpha\vec{E}_b$ . Potential energy of interaction between those two induced dipolar momenta is equal to  $E_{ab}^{int} = -|\vec{d}_b||\vec{E}_a|$  and is proportional to the inversion of sixth order of inter atomic distance  $R$  ( $R^{-6}$ ). The forces of considered interaction between two induced dipolar momenta are called dispersive London forces. The expression of full van der Waals interaction energy consists also Keesom electrostatic and Debye induction terms corresponding to two permanent and permanent-induced dipolar momenta interactions. When the inter atomic distance becomes smaller, the weak vdW interaction is dominated by electrostatic Coulomb repulsive interaction.

Composition of these two results in characteristic shape of molecular potential curve with the well at the inter atomic distance  $R_e$ .

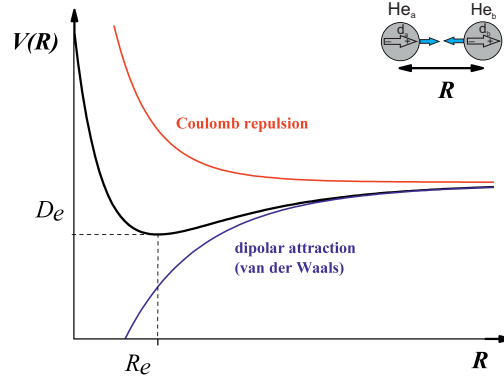
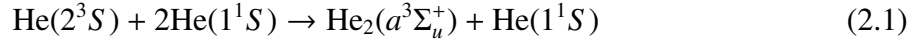


Figure 2.1: Potential curve of two interacting helium atoms. Red curve represents Coulomb repulsive interaction, blue - induced dipole ( $\vec{d}_a, \vec{d}_b$ ) attraction - van der Waals force. The addition of these interaction results in the characteristic shape of the potential (black curve) with well of  $D_e$  depth at the  $R_e$  inter molecular distance.

For the interaction of two ground state helium atoms the interaction potential had been considered as a purely repulsive [7] what translates into the absence of a singlet bound state  $X^1\Sigma_g^+$ . However, later [8] and recent calculations [9] shows the existence of the shallow well at  $5.6 a_0$  (Bohr radius) with depth of about  $7.6 \text{ cm}^{-1}$  while depth less than  $7.4 \text{ cm}^{-1}$  [10] is required for the absence of a bound state. This weakly bound state was observed experimentally [36] after electron impact ionization of a supersonic expansion of helium with translational temperature near 1 mK, as the binding energy had been estimated between 0.8 and 1.6 mK. Such a low energy excludes presence of the ground state molecules in room temperature plasma systems which the Author deals with. As the mentioned  $X^1\Sigma_g^+$  state is the only one below the  $a^3\Sigma_u^+$  which is metastable state due to existing selection rule for dipolar transitions  $\Delta S = 0$ , the later one is mostly considered as the lowest, especially in higher temperature regimes ( $\gg 1\text{mK}$ ). The potential curve of the  $a$  state, with potential well (at  $1\text{\AA}$ ) depth is  $\sim 15700 \text{ cm}^{-1}$  [11], is result of interaction between one ground state He atom ( $1^1S_0$ ) and helium atom in the metastable state ( $2^3S_1$ ). The association of these two atoms however requires presence of one additional ground state atom so that three body collision occurs.



This requirements is the result of presence of the repulsive barrier ( $484 \pm 48 \text{ cm}^{-1}$ ) [11, 12] at intermediate nuclear separations ( $2.75 \pm 0.03 \text{\AA}$ ) [12, 11] before yielding to the attractive well at smaller distance.

Small repulsive barrier is a consequence of competition between the  $\text{He}_2^+(1\sigma_g^2 1\sigma_u)$  core attraction and

$\text{He}(1^1S) + \text{He}(2^3S)$  exchange repulsion. The role of the third body can be explained on the basis of the simple dynamical model in which three-body collision is pictured as two binary collisions in rapid succession. First, the potential repulsive barrier is surmounted in collision between the ground and the metastable state atoms leading to formation of transient  $\text{He}_2(a^3\Sigma_u^+)$  molecule which is stabilized in the second binary collision with  $\text{He}(1^1S)$ . The third body has to

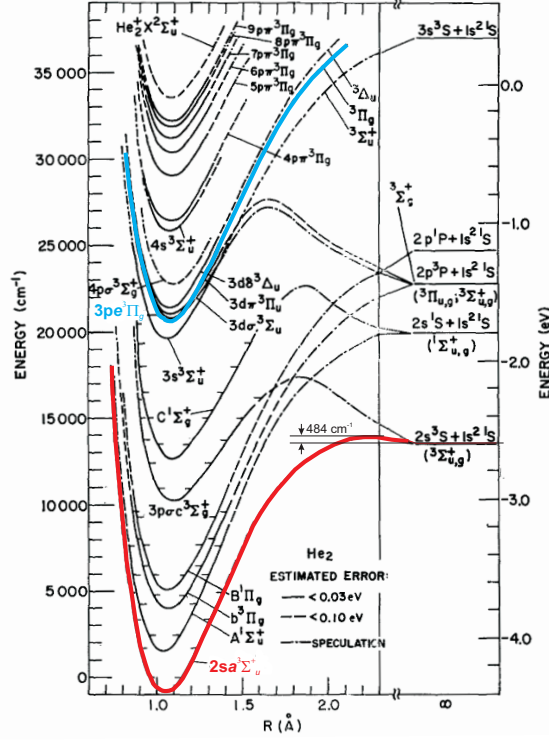


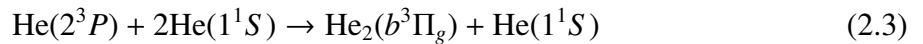
Figure 2.2: Potential curves for He<sub>2</sub> molecule [37]. Red - potential curve for  $a^3\Sigma_u^+$  state, blue - potential curve for  $e^3\Pi_g$  state.

be initially close to the other reactants affecting stabilization before recently formed transient molecule can dissociate. The temperature dependent rate constant<sup>1</sup> is given for metastable state of <sup>4</sup>He by:

$$\delta_m(T) = T[8.7 \exp(-750/T) + 0.41 \exp(-200/T)] \times 10^{-36} \text{ cm}^6 \text{ s}^{-1} \quad (2.2)$$

The value of  $\delta_m(T)$  for <sup>3</sup>He isotope is 33 % higher than given by eq.(2.2) due to increased thermal velocity of the lighter isotope. [12]

Since the exchange repulsion and so the interaction potential depend on the collision geometry, one expects the repulsion to be smaller for the interaction of the He atom in the ground state with the helium in the  $2^3P$  state (populated in resonant absorption of 1083 nm light used in MEOP) than with He( $2^3S_1$ ). The reason for this lies in comparison of  $2s$  and  $2p$  probability density of outer electrons orbitals. When the  $2s$  has spherical symmetry, the  $2p$  has the minimum in its nodal plane. Thus, the exchange repulsion near the  $2p$  nodal plane is insufficient to produce such a barrier at intermediate nuclear separations as in case of potential curve for interaction between He( $2^3S_1$ ) and He( $1^1S$ ) [13], what causes association



<sup>1</sup>The temperature dependent rate constant  $\delta_m(T)$  is a coefficient in differential equation for temporal change of metastable helium atoms density  $n_m$  due to diffusion process ( $D_{at}$  - diffusion coefficient normalized to unit density) and associative ternary collisions with the ground state helium atoms (ground state atoms density  $N \propto P$ ,  $P$ -gas pressure):  $\frac{\partial n_m}{\partial t} = D_{at} \nabla^2 n_m - \delta_m P^2 n_m$ . The product of  $\delta_m P^2$  is the frequency for destruction of  $2^3S$  atoms in three-body collision [12, 13] - see also subsection 4.5.2.2 for reaction eq.(2.1)

easier than in case of (2.1) what has the consequence in rate  $\delta_P(T)$  for molecule formation from  $2^3P$  state [13]<sup>2</sup>:

$$\delta_P(T) = (2.5 + 267T^{-1}) \times 10^{-32} \text{cm}^6 \text{s}^{-1} \quad (2.4)$$

The ratio of rates for formation of molecules given by (2.2) and (2.4) at room temperature (300K) is  $\delta_P(300)/\delta_m(300) \approx 120$  what suggests increased by two orders of magnitude association into molecular species when three body collision (2.3) is considered. In this case the helium molecule in higher excited state  $b^3\Pi_g$  is formed that, however, de-excites to metastable state  $\text{He}_2(a\Sigma_u^+)$ .

Enhanced formation of metastable molecule in presence of 1083 nm laser light (inducing transition  $\text{He}(2^3S) \rightarrow \text{He}(2^3P)$ ) and possibility of nuclear orientation of polarized helium atoms lose in collisions with molecular species gave an indication and motivation for investigations of relation between observed light-induced relaxation of atomic nuclear polarization and molecular formation dynamics.

## 2.2 Theoretical description of the helium dimer

Theoretical models describing pair of atoms associated in diatomic molecules has been already described in many literature sources thus only those issues that are needed for further understanding of the dissertation are presented.

Exact description of diatomic molecule in quantum mechanics comes down to solution of many-body problem including interaction of two nuclei and N electrons. The Schrödinger equation (omitting the spin interactions between nuclei and electrons) has a following form:

$$\left( -\frac{\hbar^2}{2m} \sum_i^N \nabla_i^2 - \frac{\hbar^2}{2M_1} \nabla_1^2 - \frac{\hbar^2}{2M_2} \nabla_2^2 + V(\vec{r}_e, \vec{r}_n) \right) \Psi(\vec{r}_e, \vec{r}_n) = E \Psi(\vec{r}_e, \vec{r}_n), \quad (2.5)$$

$\nabla_i^2$  and  $\nabla_1^2, \nabla_2^2$  are Laplace operators corresponding to kinetic energy of electrons with mass  $m$  and each of nucleus having mass  $M_1$  and  $M_2$  forming the molecule. The total potential energy of a dimer  $V(\vec{r}_e, \vec{r}_n)$  and the total wave function of electrons and nuclei  $\Psi(\vec{r}_e, \vec{r}_n)$  depend on electrons  $\vec{r}_e$  and nuclei  $\vec{r}_n$  spatial coordinates.

Exact solving of the equation (2.5) is not possible as its analytical solution does not exist. However, using certain assumptions, it can be simplified to the form that can be solved. Details of such procedures are well described in the literature, i.e.[16] thus only main steps will be shown leading to the final solutions. Born and Oppenheimer[17] assumed that the variation of internuclear distance (nuclei motion), which due to their mass is relatively slow in comparison with motion of light electrons, has a negligible influence on the latter. This allows separation of  $\Psi(\vec{r}_e, \vec{r}_n)$  into a product of electronic  $\Psi_e(\vec{r}_e; \vec{r}_n)$  and nuclear  $\Psi_n(\vec{r}_n)$  wave functions:

$$\Psi(\vec{r}_e, \vec{r}_n) = \Psi_e(\vec{r}_e; \vec{r}_n) \Psi_n(\vec{r}_n). \quad (2.6)$$

With this assumption the eq. (2.5) splits into two independent equations describing electrons movement in electrostatic field of motionless nuclei (2.7a) and nuclei motion (vibration and

---

<sup>2</sup>The definition of  $\delta_P(T)$  rate coefficient is analogous as for  $\delta_m(T)$  but the differential equation concerns the change of the density of atoms in  $2^3P$  state ( $n_P$ ) and the diffusion process is described by the coefficient  $D_P$

rotation) in effective potential  $V_n(\vec{r}_n) + V_e(\vec{r}_n)$  (2.7b)

$$\left( -\frac{\hbar^2}{2m} \sum_i^N \nabla_i^2 + V_e(\vec{r}_n) \right) \Psi_e(\vec{r}_e; \vec{r}_n) = E_{el} \Psi_e(\vec{r}_e; \vec{r}_n), \quad (2.7a)$$

$$\left( -\frac{\hbar^2}{2M_1} \nabla_1^2 - \frac{\hbar^2}{2M_2} \nabla_2^2 + V_n(\vec{r}_n) + V_e(\vec{r}_n) \right) \Psi_n(\vec{r}_n) = E \Psi_n(\vec{r}_n), \quad (2.7b)$$

$E_{el}$  and  $E$  are the electrons energy in the nuclei field and total energy of molecule respectively, while  $V_e$  and  $V_n$  are electronic and Coulomb internuclear interaction potentials. It has to be pointed out that in  $\Psi_e(\vec{r}_e; \vec{r}_n)$  the nuclear coordinates dependency is parametric ( $\vec{r}_n$  is not a variable here) what is the consequence of  $V_e$  variation with internuclear distance.

Solutions of eq.(2.7b) are of the special meaning in terms of interpretation of complex molecular absorption and emission spectra that exhibit the structure related to the relative movement of nuclei. However, symmetries of electronic wave functions  $\Psi_e$ , solutions of eq.(2.7a), decide about characteristics of the whole molecular state. Transformation of coordinate system in eq.(2.7b) into the center of the mass (CM) allows separation of relative nuclei motion from motion of the molecule as a whole. In the CM system  $R_{CM}$  and  $R$  coordinates appears which are describing position of the mass center and the intermolecular distance, as well as reduced mass  $\mu$  and total mass of nuclei  $M$ , so that (2.7b) takes form:

$$\left( -\frac{\hbar^2}{2M} \nabla_{R_{CM}}^2 - \frac{\hbar^2}{2\mu} \nabla_R^2 + V(\vec{R}) \right) \tilde{\Psi}_n(\vec{R}_{CM}, \vec{R}) = E \tilde{\Psi}_n(\vec{R}_{CM}, \vec{R}) \quad (2.8)$$

The wave function  $\tilde{\Psi}_n$  can be decomposed into the part describing the mass center motion  $\exp(i\vec{k}\vec{R}_{CM})$  and relative nuclear  $\chi(R)$  motion:

$$\tilde{\Psi}_n = \exp(i\vec{k}\vec{R}_{CM}) \chi(R), \quad (2.9)$$

with  $\vec{k}$  - wave vector describing the momentum of the molecule. Eigenvalues of eq.(2.8) are given by the sum of kinetic energy of the molecule and its internal energy  $E_{int}$ :

$$E = \frac{\hbar^2 k^2}{2M} + E_{int} \quad (2.10)$$

Considering only this part of (2.9) which depends on internuclear distance it is worth changing the Cartesian into spherical coordinate system as the potential  $V(\vec{R})$  depends only on relative nuclei positions. In this way wavefunction is factorized:  $\chi(\vec{R}) = f(|\vec{R}|)F(\theta, \varphi)$  and transformation of Laplace operator in (2.8) leads to

$$\left( -\frac{\hbar^2}{2\mu} \frac{d^2}{dR^2} - \frac{\hbar^2}{\mu} \frac{1}{R} \frac{d}{dR} + \frac{\hat{L}^2}{2\mu R^2} + V(R) \right) f(|\vec{R}|)F(\theta, \varphi) = E_{int} f(|\vec{R}|)F(\theta, \varphi), \quad (2.11)$$

where  $\hat{L}^2$  is angular momentum operator. Choosing the form of the angular part of the eigenfunction:  $F(\theta, \varphi) = F_{J,M}$  so that it is the eigenfunction of  $\hat{L}^2$ , fulfilling following eigenequations

$$\hat{L}^2 F_{J,M} = \hbar J(J+1) F_{J,M} \quad (2.12a)$$

and

$$\hat{L}_z F_{J,M} = \hbar M F_{J,M}, \quad (2.12b)$$

quantization rules for quantum number of orbital angular momentum  $J$  and its projection  $M$  on quantization  $z$  axis appears:

$$J = 0, 1, 2, \dots, \quad (2.13a)$$

$$-J \leq M \leq J, M \in \mathbb{Z}. \quad (2.13b)$$

Applying identity (2.12a) to (2.11) and assuming the term  $\frac{\hbar^2}{\mu} \frac{1}{R} \frac{d}{dR}$  is a small perturbation [18], thus it can be neglected, simplifying (2.11) to:

$$\left( -\frac{\hbar^2}{2\mu} \frac{d^2}{dR^2} + \frac{\hbar^2 J(J+1)}{2\mu R^2} + V(R) \right) f(|\vec{R}|) = E_{int} f(|\vec{R}|), \quad (2.14)$$

which does not contain any angular coordinate and describes only the radial part of the wave function  $\chi(\vec{R})$ . Its dependency on the value of quantum number  $J$  and  $M$  that has  $2J+1$  possible values leads to  $(2J+1)$ -fold degeneracy.

At this stage further solution of Schrödinger equation depends on choice of a function describing  $V(R)$  potential.

## 2.2.1 Approximations of $V(R)$ potential

The eigenproblem (2.14) represents the motion in a given potential, consists of terms responsible for centrifugal force and bonding potential between the nuclei, which has to have the minimum if the bond state is considered. Thus approximation of small oscillations about equilibrium internuclear distance (minimum of the potential curve)  $R_e$  can be applied. This leads to approximation of  $V(R)$  by expansion around  $R_e$  up to the second (harmonic oscillator) and the third (anharmonic oscillator) order of magnitude terms. Despite the model of a simple harmonic oscillator has no physical meaning in terms of proper description of diatomic molecule potential, simple results that can be obtained in this way can build up ones intuition for further understanding of more accurate, however more complicated, models.

**(a) Harmonic oscillator and rigid rotator** The expansion of  $V(R)$  up to the second order term is given by:

$$V(R) \approx V(R_e) + \frac{1}{2} k (R - R_e)^2, \quad (2.15)$$

where  $k$  is a second order derivative of the potential at  $R = R_e$  popularly known as a spring constant.

With this potential, assuming also small oscillations, where changes of  $R$  around  $R_e$  are much smaller than the equilibrium value, that  $R \approx R_e$  in the second term of (2.14), we obtain:

$$\left( -\frac{\hbar^2}{2\mu} \frac{d^2}{dR^2} + \frac{\hbar^2 J(J+1)}{2\mu R_e^2} + \frac{1}{2} k (R - R_e)^2 + V(R_e) \right) f(|\vec{R}|) = E_{int} f(|\vec{R}|), \quad (2.16)$$

Solution of (2.16) represents the internal energy of the molecule:

$$E_{int}(J, \nu) = V(R_e) + \hbar\omega_e \left( \nu + \frac{1}{2} \right) + B_e (J(J+1)). \quad (2.17)$$

Introduced rotational constant

$$B_e = \frac{\hbar^2}{2\mu R_e^2} \quad (2.18)$$

is related to the nuclear moment of inertia of the rotating molecule,  $\omega_e = \sqrt{\frac{k}{\mu}}$  is a frequency of harmonic oscillations which energy quantization is provided by a discrete values of vibrational quantum number  $\nu = 0, 1, 2, \dots$ . Components of eq.(2.17) can be interpreted as the electronic energy  $E_e$ , the energy of vibrational motion  $E_\nu$  and the rotational energy  $E_r$ , so that  $E_{int} = E_e + E_\nu + E_J$ .  $E_e$  is the value at the bottom of the potential minimum. In molecular spectroscopy energy is often expressed in the wavenumber unit [ $\text{cm}^{-1}$ ] term values  $T = E/hc$  and the total energy of molecule is given by:

$$T(\nu, J) = T_e + G(\nu) + F_\nu(J), \quad (2.19)$$

being the sum of electronic, vibrational and rotational terms. In the notation of the rotational term, by adding the subscript  $\nu$ , the parametric dependency of molecular rotational motion on vibrations has been emphasized, as it will be shown below, both can't be in fact considered separately.

### (b) Anharmonic oscillator and non-rigid rotator

To obtain more accurate and physical results further approximation of the potential  $V(R)$  has to be made by adding the third order expansion term in (2.15):

$$V(R) \approx V(R_e) + \frac{1}{2}k(R - R_e)^2 + \frac{1}{3}g(R - R_e)^3, \quad (2.20)$$

$g$  is the third order derivative of potential at  $R = R_e$ . Solution of (2.14) with anharmonic potential (2.20) provides equations for vibrational and rotational energy terms:

$$G(\nu) = \omega_e \left( \nu + \frac{1}{2} \right) - \omega_e x_e \left( \nu + \frac{1}{2} \right)^2 + \dots, \quad (2.21a)$$

$$F(J) = B_\nu J(J + 1) + D_\nu (J(J + 1))^2 + \dots. \quad (2.21b)$$

$\omega_e x_e$  is a constant which is a measure of the anharmonicity of the oscillator. Here, the rotational constants  $B_\nu$  and  $D_\nu$  are related to the moment of inertia and centrifugal force respectively. They are given by following expressions parametrically dependent on vibrational quantum number  $\nu$  and constants  $\alpha_e, \beta_e$  describing the coupling strength of vibrational and rotational motion:

$$B_\nu = B_e - \alpha_e \left( \nu + \frac{1}{2} \right) + \dots, \quad (2.22a)$$

$$D_\nu = D_e + \beta_e \left( \nu + \frac{1}{2} \right) + \dots. \quad (2.22b)$$

Rotational constant  $B_e$  was defined by (2.18) assuming the lack of oscillations. Under the same condition  $D_e$  is given by:

$$D_e = \frac{4B_e^3}{\omega_e^2}. \quad (2.23)$$

(c) **Morse potential** Very useful, especially in terms of the analysis of rotational structure of the molecular spectrum, is the Morse potential given by [19]:

$$V(R) = D_e \exp^{-2\beta(R-R_e)} - 2D_e \exp^{-\beta(R-R_e)} \quad (2.24)$$

This representation correctly reproduces only the vicinity of the potential minimum (low  $\nu$  values) and exhibits nonphysical behavior for  $R = 0$  giving the finite value of repulsive potential. This work, however, considers the transition at around 465 nm which occurs between the states of which vibrational number is both equal 0 and Morse potential approximation can be applied by use of relations given below. It has to be remarked that  $D_e$  in (2.24) is **not** the rotational constant (2.23) but is the depth of the potential well at the minimum of internuclear distance  $R = R_e$  (see fig.2.1). The common designation of these quantities is well embedded in molecular terminology thus using proper remarks emphasizing each time the meaning of used  $D_e$  symbol seems to be less problematic than defining other designation to distinguish one from another. Moreover, the use of  $D_e$  as the rotational constant is predominant in this work. Very useful expressions of Pekeris and Dunham related to Morse potential allow calculation of  $\alpha_e, \beta_e$  and therefore rotational constants  $B_v, D_v$  (required in eq.(2.21b)) on the basis of usually known  $B_e, \omega_e$  and  $\omega_e x_e$  for a given molecule. After Pekeris [20]:

$$\alpha_e = \frac{6B_e}{\omega_e} \left( \sqrt{\omega_e x_e B_e} - B_e \right) \quad (2.25)$$

After Dunham [21]

$$\beta_e = D_e \left( \frac{8\omega_e x_e}{\omega_e} - \frac{5\alpha_e}{B_e} - \frac{\alpha_e^2 \omega_e}{24B_e^3} \right) \quad (2.26)$$

These identities are useful when  $\alpha_e$  and  $\beta_e$  values are not reported in any experimental or theoretical reference (as is the case for helium-3 isotope), while the other molecular constants are usually known or can be obtained i.e. applying the isotopic correction.

#### (d) **Molecular constants isotopic corrections**

Working with different isotopes of the same diatomic molecule, as it is the case in this work, results in several consequences for the molecular electronic states, what will be discussed later. However, at this stage it seems to be useful to provide an information about influence of isotopic mass change on the values of molecular constants presented in earlier paragraphs. As the oscillation frequency  $\omega_e$  depends on the reduced mass  $\mu$  it is obvious that the isotopic change of the mass of one or both atoms affects the vibrational energy but the also rotational energy, as the rotational constants are functions of reduced mass. After [16], indicating the quantities for isotopic molecule by superscript  $i$  and defining  $\rho = \sqrt{\frac{\mu}{\mu^i}}$ , the relations between isotopic molecular constants are given below:

for vibrational constants:

$$\omega_e^i = \rho \omega_e, \quad \omega_e^i x_e^i = \rho^2 \omega_e x_e \quad (2.27)$$

for rotational constants:

$$B_e^i = \rho^2 B_e, \quad \alpha_e^i = \rho^3 \alpha_e, \quad D_e^i = \rho^4 D_e, \quad \beta_e^i = \rho^5 \beta_e. \quad (2.28)$$

## 2.2.2 Electronic molecular states

Born-Oppenheimer approximation separates electronic and nuclear motion what results in two Schrödinger equations (2.7a) and (2.7b). Before, several potential approximations and resulting solutions for energy values were described for nuclear part, where the advantage of spherical symmetry of internuclear interaction was taken. In case of the electronic Schrödinger equation not the spherical but the axial symmetry of the field in which the electrons move complicates the problem of finding satisfactory approximation and numerical methods have to be engaged. This, however, won't be discussed here leaving the place for, more useful in terms of further analysis and discussion, description of the electronic states by the quantum numbers related to present angular momenta and their proper coupling. Also the symmetries of these states, deciding about the molecular spectra are discussed.

### (a) Electron angular momenta in the molecules

One of the consequences of reduced symmetry (from spherical to axial) when transfer from separated atoms to diatomic molecule is made. is change of the electrons constant of motion. For atoms the orbital angular momentum  $L$  is the constant. In the axial symmetry of the molecule only the component of  $L$  about the internuclear axis is a constant of the motion that takes values:

$$M_L = L, L - 1, L - 2, \dots, -L \quad (2.29)$$

However, the direction of motion of all electrons which decides about the sign of  $M_L$  has no influence on the energy value, thus a two-fold degeneracy of the states with equal  $|M_L|$  occurs, which is more appropriate value to classify the electronic states than  $L$ . To stay in agreement with nomenclature, the designation is introduced:

$$\Lambda = |M_L|. \quad (2.30)$$

The  $\Lambda$  as the modulus of the component of electronic orbital angular momentum vector  $L$  can take  $L + 1$  different values ranging from 0 to  $L$ . For each of  $\Lambda \neq 0$  ( $\equiv |M_L| \neq 0$ ) two fold-degeneracy is present. Designation of the electronic states by the successive Greek letters:  $\Sigma, \Pi, \Delta, \Phi, \dots$  is related to the value of  $\Lambda = 0, 1, 2, 3, \dots$

In the same manner like in case of atoms, spins of individual electron results in total electronic spin vector  $S$  and associated quantum number  $S$ , being half-integral or integral depending on the odd or even total number of electrons. If the molecular rotation is neglected,  $S$  is fixed in space (it can rotate only in case of external magnetic field presence), unless states other than  $\Sigma$  ( $\Lambda = 0$ ) are considered. In other case the orbital motion of the electrons about the internuclear axis results in internal magnetic field along this axis. Thus, for  $\Pi, \Delta, \Phi, \dots$  states precession of  $S$  occurs around the field direction so that the only constant is the total spin component about the axis of the dimer denoted by  $\Sigma$  (it should be not confused with the same symbol used for  $\Lambda = 0$  state designation). In contrast to  $\Lambda$ , spin component  $\Sigma$  can take both positive and negative values:  $\Sigma = S, S - 1, S - 2, \dots, -S$  (altogether  $(2S+1)$  values) and is not defined when  $\Lambda = 0$ .

The total electronic angular momentum of the molecule about the nuclear axis  $\Omega$  is, contrary to the  $J$  - vector sum of  $L$  and  $S$  for atoms, the algebraic sum of  $\Lambda$  and  $\Sigma$ :

$$\Omega = |\Lambda + \Sigma|. \quad (2.31)$$

When  $\Lambda = 0$ ,  $\Omega$  is not defined, in other case it has  $(2S + 1)$  different values corresponding to different energies of the resulting molecular states.  $(2S + 1)$  value is called multiplicity of the state and is added as a left superscript in the electronic state term symbol, while the value of  $\Omega$  can be optionally added in the right subscript:

$$n^{2S+1}\Lambda_{\Omega,g/u}^{+/-} \quad (2.32)$$

The symbol  $n$  in eq. (2.32) is substituted by the letter  $X$  for the ground state of the molecule and successive capital letters  $A, B, C, \dots$  for the excited states with the same multiplicity as the ground state. For excited states with order multiplicity successive small letters are used  $a, b, c, \dots$ . The meaning of the symbols  $g$  or  $u$  and  $+$  or  $-$  is given in (a) as they reflect the state symmetry properties.

### (b) Rotation and electronic motion coupling

When the total electronic spin  $S$  behavior was discussed, depending on the value of  $\Lambda$ , rotation of molecule was neglected. It was of course temporary approximation and the consequence of this degree of freedom on electronic motion has to be considered, i.e. what quantum numbers describes the rotational levels in the different types of electronic states. As in case of the atomic physics different couplings between existing angular momenta are considered (i.e. spin-orbit coupling.) Electronic angular momenta as well as angular momenta of the rotational motion of a dimer becomes coupled. So called Hund's coupling cases refers to different possibilities of interaction between existing angular momenta, that depends on a given molecular state and set of describing it quantum numbers. There are five different coupling schemes denoted by successive letters (a)-(e). As in this dissertation the transition occurs between  $a^3\Sigma_u^+$  and  $e^3\Pi_g$  states of  $\text{He}_2$  that are, after [22, 23], well described by coupling case (b), only this scheme will be explained in details (for explanation of other cases the Reader is referred to the popular handbooks treating about molecular systems, especially diatomic, i.e. [16, 24]). Belonging to the certain coupling case will determine further description of the rotational levels structure of electronic states and choice of a good quantum number of total angular momentum.

**(c) Hund's coupling case (b) and molecular energy levels scheme** The Hund's coupling case (b) assumes lack or very weak coupling of  $S$  to the internuclear axis. It is the case when we deal with the state described by  $\Lambda = 0 \Rightarrow \Sigma$  state (no magnetic field in molecule axis direction  $\rightarrow$  no  $S$  precession) but also for  $\Lambda \neq 0 \Rightarrow \Pi$  state, when a light molecule is considered ( $\text{He}_2$  is one of the lightest dimers) so as  $S$  may be very weakly coupled to the internuclear axis. Vector coupling diagram is shown on the Fig.2.3

In general case, resulting from  $\mathbf{L}$  precession about the internuclear axis component  $\Lambda$ , as a vector is coupled to the angular momentum of rotating nuclei  $\mathbf{R}$ , forming  $\mathbf{N}$  - the total angular momentum apart from spin. The corresponding to  $\mathbf{N}$  vector quantum number is:

$$N = \Lambda, \Lambda + 1, \Lambda + 2, \dots \quad (2.33)$$

$N$  can take all the integral values from 0 up. For  $\Lambda = 0$   $\mathbf{N}$  is identical with  $\mathbf{R}$  - perpendicular to internuclear axis. Further  $\mathbf{N}$  adds to  $\mathbf{S}$  forming the total angular momentum  $\mathbf{J}$ . The magnetic coupling between  $\mathbf{S}$  and  $\mathbf{N}$  results from a very slight magnetic moment in the direction of  $\mathbf{N}$  being a consequence of molecular rotation. For a given  $N$ , possible  $J$  values are given by:

$$J = (N + S), (N + S - 1), (N + S - 2), \dots, |N - S|, \quad (2.34)$$

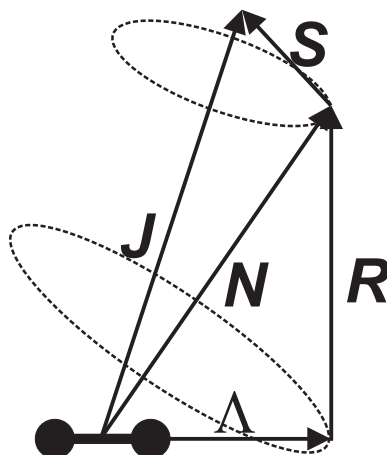


Figure 2.3: Hund's coupling (b). Detailed description in the text.

so  $(2S+1)$  components can be distinguished (except when  $N < S$ , when only one  $J$  value occurs). For completeness the presence of non-zero nuclear spin  $\mathbf{I}$  has to be introduced into considerations as it is the case for  $^3\text{He}_2$  and  $^3\text{He}-^4\text{He}$  molecules. For two identical nuclei each with nuclear spin  $I_1 = I_2 = I$  the quantum number of total nuclear spin is given:

$$T = 2I, 2I - 1, \dots, 0. \quad (2.35)$$

The total angular momentum of molecule including spin of the nuclei  $\mathbf{F}$  is resultant of  $\mathbf{J}$  and  $\mathbf{T}$ . Corresponding quantum number is:

$$F = (J + T), (J + T - 1), \dots, |J - T|, \quad (2.36)$$

so each level described by  $J$  has  $(2T + 1)$  components.

Following abovementioned rules of angular momenta coupling and resulting values of quantum numbers that can be taken, the scheme of the rotational sublevels of the electronic states  $a^3\Sigma_u^+$  and  $e^3\Pi_g$  can be drawn as on Fig.2.4 and Fig.2.4. Not going into the details about meaning of "+" and "u" or "g" designations, that will be discussed later in the part of chapter dedicated to the states symmetry and transition rules, it is shown how abovementioned coupling scheme is reflected in the level structure. In  $^3\Sigma$  state for each value of quantum number  $N$  (except  $N = 0$ )  $J$  takes 3 values  $(N + 1), N, (N - 1)$ , as  $S = 1$  here. It has to be emphasized that the order of level position in terms of energy is not in order with increasing  $J$  value. Rotational level with  $J = N + 1$  (in the literature often labeled as  $F_1$ ; confusion with (2.36) should be avoided) is in between lower lying  $J = N$  ( $F_2$ ) and  $J = N - 1$  ( $F_3$ ). For the details about the splitting of  $N$ -sublevels into terms with different  $J$  values the Reader is sent to [16] p.223 where equations for energy terms depending on spin-spin and spin-orbit splitting constants  $\lambda$  and  $\gamma$  are given.

Looking at the rotational levels scheme of  $e^3\Pi_g$  state, the absence of  $N = 0$  is worth noting, which is a consequence of  $\Lambda = 1$  in (2.33). Non-zero  $\Lambda$  value results also in double splitting for each of  $J$ . In case of  $^3\Pi$  state the energy of rotational sublevels described by  $J$  for certain  $N$  increases with decreasing value of  $J$ . For the same reason as for  $\Sigma$  state the Reader is sent to [16] p.227 & 235 for detailed information about equation for energy terms taking into account splitting of sublevels described by common value of  $N$  as well as  $\Lambda$  doubling of levels described by single  $J$  number.

Distinction between different levels of the fine structure is out of interest of this work as the size of splitting is of the same order [26, 27] as combined Doppler and collisional absorption lines broadening  $\Delta$  in conditions of experiments performed by the Author. (several GHz).

Resolving the absorption lines fine structure is thus not possible, however its existence affects apparently the width and shape (distortion) of the lines. Ignoring the fine structure in further considerations, the Author decided to use simpler, than those to which the reference is given above in [16], formula for the rotational energy (given by (2.21b) in which  $J$  has to be replaced by  $N$  for rotational levels in Hund's case (b) ).

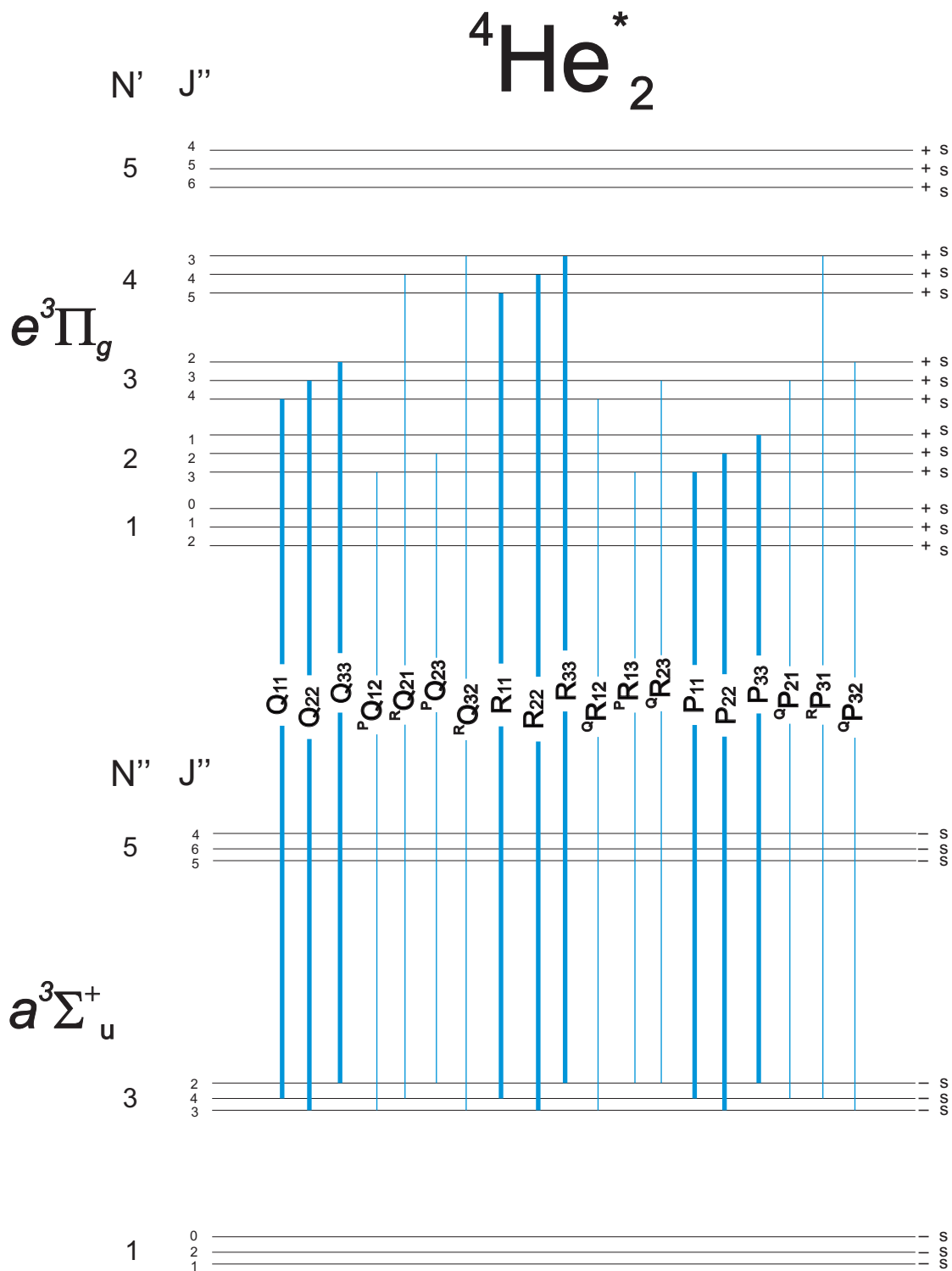


Figure 2.4: Scheme of rotational sublevels of  $a^3\Sigma_u^+$  and  $e^3\Pi_g$  states of  ${}^4\text{He}_2$  and  ${}^3\text{He}_2$  (next page), being a consequence of discussed coupling scheme and wavefunction symmetry properties (paragraph 2.2.2 (c)). The possible transition (according to the rules explained in subsection 2.2.3(e)) from exemplary rotational sublevels and its fine structure are marked - the notation is explained in subsection 2.2.3(f). The absence of even numbered rotational levels for helium-4 isotope is characteristic.

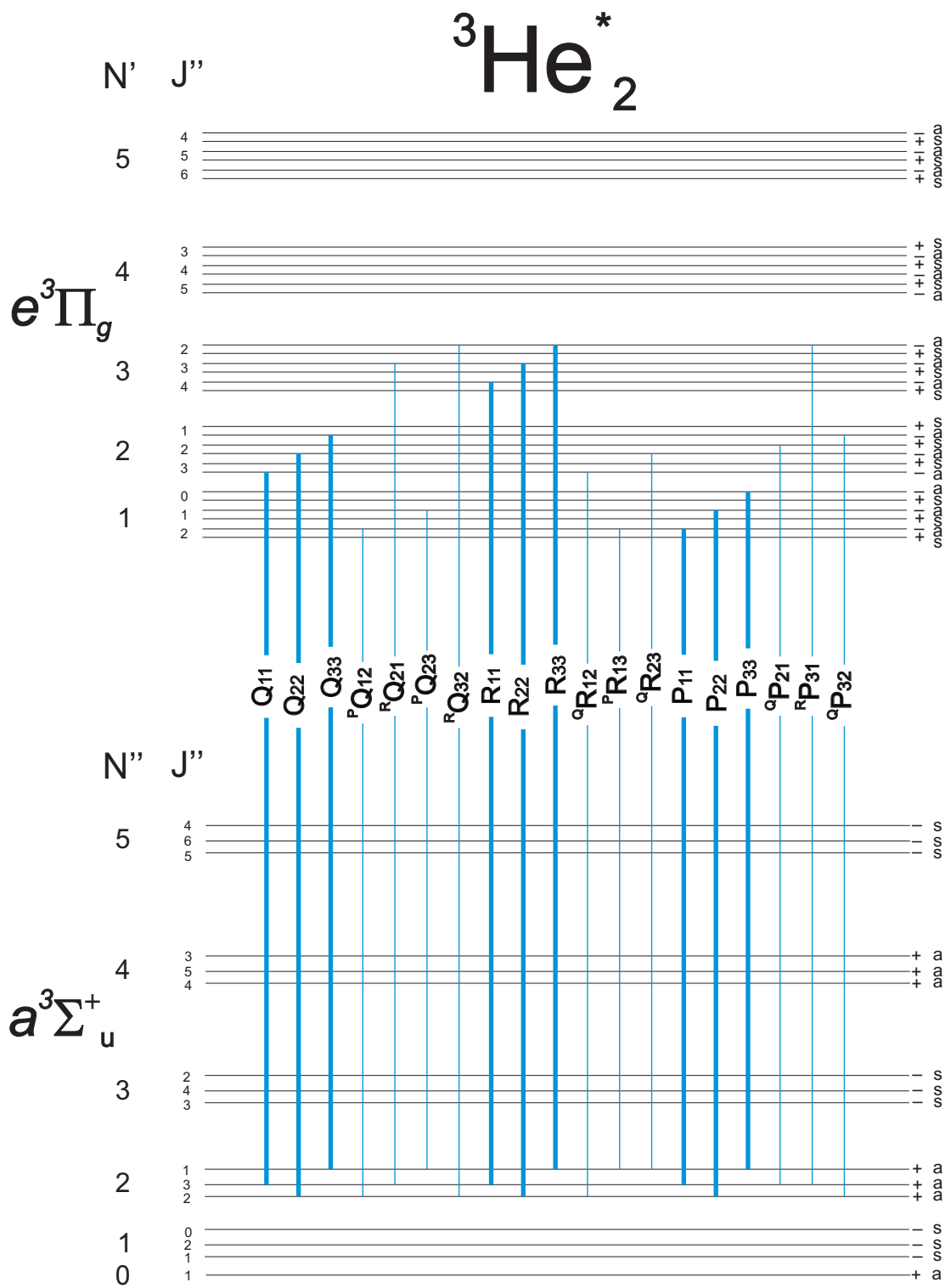


Figure 2.4

### 2.2.3 Symmetries of the rotational levels and transition selection rules

For determination of which sublevels of the rotational structure of the  $a^3\Sigma_u^+$  and  $e^3\Pi_g$  states shown on Fig.2.4 are involved in dipolar transitions induced by the laser light or observed as emission lines, a transition rules has to be known, that are determined by the symmetry properties of molecules. So-called selection rules are the consequence of molecular wave function properties as well as dipolar momentum operator features. Thus, some general rules can be obtained independent of the angular momenta coupling schemes and those that holds only in certain Hund's cases. After describing relevant symmetries of rotational levels, their consequences in general transition rules and those valid only for case (b) are discussed.

**(a) Symmetry in respect to reflection at the origin** Looking at the Schrödinger equation (2.5) since del ( $\nabla$ ) operator (defined as a first order spatial derivative  $\frac{\partial}{\partial r_k}$  or explicitly  $\frac{\partial}{\partial x_k} + \frac{\partial}{\partial y_k} + \frac{\partial}{\partial z_k}$ , where  $k$  denotes particle considered) is raised to the second power, changing the sign of the system coordinates (all particles, i.e. electrons and nuclei) that is  $\vec{r}_e$  and  $\vec{r}_n \rightarrow -\vec{r}_e, -\vec{r}_n$  results in a new total eigenfunction. It has the same properties as  $\Psi$  in (2.5) but can differ in sign:  $\pm\Psi$ . The state described by the total wave function that is the solution of transformed Schrödinger equation and preserves the sign of  $\Psi$  is called *positive*, if it is contrary - *negative* state.

However, this general definition does not provide directly any information about connection between quantum numbers describing the structure of the molecule and states symmetry. To obtain this information it is worth looking at the total wave function distinguishing parts describing the electronic, the vibrational and the rotational contributions. It was partially made in eq. (2.6) at the beginning of the section 2.2, where separation of electronic  $\Psi_e(\vec{r}_e; \vec{r}_n)$  and nuclear  $\Psi_n(\vec{r}_n)$  parts were identified. The second - nuclear part depends only on nuclei coordinates and describes vibrational and rotational motion of the molecule. It is thus natural to look at the nuclear wave function as a resultant of two parts describing these, however mutually dependent, degrees of freedom [16]. That gives:

$$\Psi_n(\vec{r}_n) = \frac{1}{r} \Psi_v \Psi_r, \quad (2.37)$$

Explicit dependency of vibrational and rotational parts on nuclei spatial coordinates is not shown, however it is worth noting that the vibrational part depends only on the magnitude of the distance  $r$  between the nuclei and during inversion of the coordinates procedure it remains unaltered. On the other hand rotational part  $\Psi_r$  is described only by  $\vartheta, \varphi$  angles when spherical coordinate system is considered. In this system reflection of the rotator ( $\Lambda = 0$ ) at the origin is achieved by replacing  $\vartheta$  by  $\pi - \vartheta$  and  $\varphi$  by  $\pi + \varphi$ . It can be shown [16] that during such reflection at the origin  $\Psi_r$  remains unchanged for even values of rotational number  $N$  (those sublevels are *positive*) and change the sign to  $-\Psi_r$  for odd  $N$  values (*negative* sublevels). In the most interesting for the Author Hund's case (b)  $\mathbf{N}$  is coupled with electron spin  $\mathbf{S}$  resulting in  $\mathbf{J}$  so the question can be raised, why the symmetry of rotational eigenfunction depends on  $N$  value and not on the total number  $J$ . The answer lies in the fact that the function representing orientation of the electrons spins  $\beta_e$ , by which the total eigenfunction in eq.(2.6) should be multiplied (by now only electronic coordinate function  $\Psi$  was considered) is independent of an inversion. Thus, for one given value of  $N$  each of sublevels with different  $J$  resulting from (2.34) has the same *positive* or *negative* symmetry. In case of the state for which  $\Lambda \neq 0$  (i.e.  $\Pi$  state), as was mentioned 2.2.2(c)  $\Lambda$ -doubling occurs and for each  $J$  value one component is

*positive* and the other is *negative*. For each of  $J$  values the upper sublevel is positive for even  $N$  value and negative for odd  $N$ , while lower lying sublevel has the opposite sign.

Finally the symmetry properties of reflection at the origin of  $\Psi_e$  eigenfunction has to be considered, for the purpose of which inversion can be equivalently treated as combination of rotation of the molecule through  $180^\circ$  about an axis perpendicular to the internuclear axis and reflection at the plane perpendicular to this rotational axis and passing through the internuclear axis. The first operation does not alter  $\Psi_e$ , because it depends on coordinates of the electrons relative to the nuclei but the second transformation can change the sign of  $\Psi_e$ , so that the electronic state can have positive (designated as  $+$  in the right superscript of molecular electronic state symbol i.e.  $\Sigma^+$ ) or negative ( $-$ ) symmetry.

In case of the  $\Sigma$  states the product of rotational  $\Psi_r$  and electronic  $\Psi_e$  eigenfunctions symmetries to the reflection at the origin gives the total symmetry of rotational level described by the quantum number  $N$ . Thus, for  $\Sigma^+$  even- $N$ -numbered rotational levels are positive and odd- $N$ -numbered are negative while for  $\Sigma^-$  state it is reversed even- $N$ -numbered are negative, odd- $N$ -numbered are positive.

One can also identify  $\Pi^+$  and  $\Pi^-$  states with the mentioned before symmetries for  $\Lambda \neq 0$  case (however it is not common in these states designation) as the upper of doubled  $J$  sublevels change their sign with  $N$  like  $\Sigma^+$  and the lower sublevels like  $\Sigma^-$ .

There is an additional symmetry for  $\Psi_e$  function when the dimers consisted of two nuclei with the same charge (isotopes, i.e.  $^3\text{He}_2$ ,  $^4\text{He}_2$  and  $^3\text{He}-^4\text{He}$ ) are considered. In this case the field in which electrons move has, in addition to the symmetry axis, a center of symmetry and the field remains unaltered when the nuclei are reflected at this center. Then, if reflection of only electrons coordinates at the origin is performed:  $\vec{r}_e \rightarrow -\vec{r}_e$  (before inversion at the origin of all the particles - electrons and nuclei - was considered) the state of which the electronic eigenfunction preserves the sign is called *even* (designated by subscript  $_g$ ), in opposite case is called *odd* state (designated by subscript  $_u$ ).

**(b) Nuclear spin symmetry** During the discussion about the symmetry of the molecular eigenfunction, the nuclear spin influence was omitted. If the two nuclei of the molecule are identical, each possessing the spin  $I_1 = I_2 = I$ , after their permutation the total molecular wavefunction  $\Psi$  can preserve (symmetry) or change its sign (antisymmetry). The former occurs for nuclei with integral and 0  $I$  values (bosons), while the latter case occurs for nuclei with  $I$  half-integral (fermions).

The presence of the nuclear spin requires introduction of the spin function  $\beta_n$  describing spatial state of two nuclei in (2.6). Function  $\beta_n$  can be either symmetric (ortho) or antisymmetric (para) in respect to the exchange of the nuclei. For a given  $I$ :

$$(I + 1)(2I + 1) \text{ is the number of symmetric} \quad (2.38a)$$

and

$$I(2I + 1) \text{ is the number of antisymmetric } \beta_n \text{ functions.} \quad (2.38b)$$

For  $I = 0$  spin there is only one symmetric  $\beta_n$  and for  $I = \frac{1}{2}$  there are 3 possible symmetric functions and only one antisymmetric  $\beta_n$ . This, on the other hand, has the consequence in

the rotational level occurrence to fulfill requirements of parity of total (including  $\beta_n$  and  $\beta_e$ ) molecular wavefunction  $\Psi(\vec{r}_e, \vec{r}_n, \beta_e, \beta_n)$  for bosons and fermions.

For bosons with  $I = 0$  symmetry of total wave function can be provided only if the rest of  $\Psi(\vec{r}_e, \vec{r}_n, \beta_e)$  without  $\beta_n$ , here symmetric, is also symmetric. Thus, antisymmetric rotational levels do not occur at all. For fermions with half-integral  $I$  value both symmetric and antisymmetric rotational levels are allowed, however, due to mentioned multiplicity of symmetric  $\beta_n$ , antisymmetric rotational levels occurs  $\frac{I+1}{I}$  times more frequent as the symmetric (for symmetric  $\beta_n$   $\Psi(\vec{r}_e, \vec{r}_n, \beta_e)$  has to be antisymmetric and reverse).

**(c) Nuclear spin influence on the electronic and the rotational wave functions symmetries** As the nuclei exchange can be alternatively performed as first the reflection of all the particles at the origin and then the reflection of only the electrons at the origin, the properties of homonuclear wave function transfers to the symmetry of electronic state and rotational levels which thus can be for bosons symmetric and for fermions antisymmetric in respect to the exchange of the nuclei. Taking into account the previous discussion about symmetries to the reflection at the origin for dimers with like nuclei it is straightforward that:

$$\text{for } \Sigma_g^+ N\text{-even states are symmetric } \equiv s, N\text{-odd states are antisymmetric } \equiv a \quad (2.39a)$$

$$\text{for } \Sigma_u^+ N\text{-even states are antisymmetric } \equiv a, N\text{-odd states are symmetric } \equiv s \quad (2.39b)$$

$$\text{for } \Sigma_g^- N\text{-even states are antisymmetric } \equiv a, N\text{-odd states are symmetric } \equiv s \quad (2.39c)$$

$$\text{for } \Sigma_u^- N\text{-even states are symmetric } \equiv s, N\text{-odd states are antisymmetric } \equiv a \quad (2.39d)$$

The same rules occurs for  $\Pi$  states where distinction between  $\Pi^+$  and  $\Pi^-$  is useful as then the similarity with  $\Sigma^{+/-}$  is easier to see.

**(d) Symmetries for helium isotope molecules** Knowing the symmetry properties of the total wave function in respect to the reflection at the origin and nuclei exchange as well as possible combinations of electronic states determined by these symmetries, the discussed rules can be applied in case of the  $a^3\Sigma_u^+$  and  $e^3\Pi_g$  states of  $^3\text{He}_2$  and  $^4\text{He}_2$  isotopes.

Since helium-4 atom has zero value of the nuclear spin the symmetry rules for homonuclear bosonic molecule are valid. Only the symmetric rotational levels exist which together with only symmetric  $\beta_n$ , gives the total wave function symmetric to the nuclei exchange. Thus, for the  $a^3\Sigma_u^+$  state only odd- $N$  numbered levels are possible and each even- $N$  numbered levels is missing. This results in absence of even-numbered lines in the rotational spectrum of this molecule.

Atoms of which  $^3\text{He}_2$  consists of have half-integral nuclear spin  $I = \frac{1}{2}$  so both symmetric and antisymmetric rotational levels occur as  $\beta_n$  can also be either symmetric or antisymmetric, however with different statistical weights. According to (2.38a) and (2.38b) there are 3 times more frequent symmetric functions  $\beta_n$  than antisymmetric. Simultaneously the total wave function for fermions has to be antisymmetric to the nuclei permutation, what results in three times more frequent rotational levels with even- $N$  value (antisymmetric) than with odd ones, when  $a^3\Sigma_u^+$  is considered. As it will be shown in [ref.experimental chapter] and was reported by [6] this symmetry properties results in the alternation of rotational spectra lines in ratio 3:1 between even numbered and odd numbered transitions.

For the heteronuclear dimer  $^3\text{He}-^4\text{He}$  the division of the rotational states into symmetric or antisymmetric ones disappears in respect to the nuclei exchange, as this operation leads to the configuration that is different from the initial one. In this case no missing rotational levels or any statistical weights of their occurring is expected.

**(e) Dipolar transition selection rules for helium dimer**

The first and general selection rule, valid for any atomic system, concerns the quantum number  $J$  of the total angular momentum:

$$\Delta J = 0, \pm 1 \text{ with the restriction } J = 0 \not\leftrightarrow J = 0. \quad (2.40)$$

Selection rules of dipolar transition results from the properties of dipole moment operator which is the function of electrons coordinates  $\hat{d} = \sum e_i \hat{r}_i$  and therefore is antisymmetric to the reflection at the origin and at any plane through the internuclear axis. The matrix element of the dipole moment :

$$\int \Psi^{i*} \hat{d} \Psi^f dr_e \quad (2.41)$$

is non-zero only if the value under the integral is independent (i.e. does not change the sign) of any transformation of coordinates. This occurs when one of the total wave functions describing the  $i$  or  $f$  states between which the transition occurs is symmetric and the other is antisymmetric in respect to the reflection at the origin and at any plane through the internuclear axis. From this and previous discussion about the symmetries, transition rules results:

*the positive terms combine only with the negative and vice versa:*

$$+ \leftrightarrow -, \quad + \leftrightarrow +, \quad - \leftrightarrow - \quad (2.42)$$

*the even (g) electronic states combine only with the odd (u)*

$$g \leftrightarrow u, \quad g \leftrightarrow g, \quad u \leftrightarrow u \quad (2.43)$$

$\Sigma^+$  state cannot combine with  $\Sigma^-$ :

$$\Sigma^+ \leftrightarrow \Sigma^+, \quad \Sigma^- \leftrightarrow \Sigma^-, \quad \Sigma^+ \not\leftrightarrow \Sigma^-, \quad (2.44)$$

while both  $\Sigma^+$  and  $\Sigma^-$  combine with  $\Pi$  state.

For the states with defined quantum number  $\Lambda$  (valid for Hund's case (a) & (b) ) there is the selection rule:

$$\Lambda = 0, \pm 1 \quad (2.45)$$

Because the dipolar moment operator does not change its sign when the nuclei of homonuclear molecule possessing the spin are interchanged:

*only symmetric terms can combine with symmetric and antisymmetric only with antisymmetric*

$$s \leftrightarrow s, \quad a \leftrightarrow a, \quad s \not\leftrightarrow a \quad (2.46)$$

As for atoms, for Hund's case (b) where the resultant spin  $\mathbf{S}$  is defined, the transition rule for corresponding quantum number is:

$$\Delta S = 0, \quad (2.47)$$

that connects only the states with equal multiplicities.

When both states between which possibility of transition occurrence is considered are within Hund's case (b), the following rule holds for the quantum number  $N$  of the total angular momentum apart from spin:

$$\Delta N = 0, \pm 1, \quad (2.48)$$

with restriction that:  $\Delta N = 0$  is forbidden for  $\Sigma \leftrightarrow \Sigma$  transitions.

On the value of  $\Delta N$  the designation of the transitions relies, so that: each transition with  $\Delta N = 0$  belongs to so called  $Q$  branch with  $\Delta N = -1$  to  $P$  branch and with  $\Delta N = 1$  to  $R$  branch. Additionally information about the value of  $N''$  (value of rotational quantum number  $N$  in the bottom state of the transition; for the top state it is marked as  $N'$ ) is given next to the designation of the branch:  $Q(N'')$ ,  $P(N'')$ ,  $R(N'')$ . This formalism of bottom '' and top ' levels of the transition designation extends also to the other quantum numbers describing the states as well as molecular rotational and vibrational constants (i.e.,  $B_e''$ ,  $B_e'$ ,  $\omega_e''x_e''$ ,  $\omega_e'x_e'$ ,  $\alpha_e'$  etc.).

**(f)  $a^3\Sigma_u^+ \rightarrow e^3\Pi_g$  transition details for  $\text{He}_2$**

The analysis of the Fig.2.4 and 2.4 together with the transition rules for helium molecule as described in paragraph 2.2.3 (e) leads to conclusion that each transition described by  $\Delta N$  value ( $P(N'')$ ,  $Q(N'')$ ,  $R(N'')$ ) has several components with different  $J''$  and  $J'$  combinations preserving the relation (2.34) and selection rule (2.40).<sup>3</sup> These are the fine structure of the line components and, as mentioned earlier 2.2.2(c), are beyond the resolving power of the experiment due to absorption line Doppler and collisional broadening. It is the same order as the fine structure splittings of the components and additional broadening and distortion of the lines is thus possible. As a consequence, all the transitions occurring from a common  $N''$  rotational level within one value of  $\Delta N$  will be treated as a single line without entering into its fine structure details. This approach will simplify the identification of the absorption lines by comparison with the only reference [6] for  $^3\text{He}_2$  as well as with [28] for  $^4\text{He}_2$  ( $v' (= 0) - v'' (= 0)$ ) vibrational band transition of  $a^3\Sigma_u^+ - e^3\Pi_g$  on which the 465 nm laser wavelength calibration is based on. It will also give a possibility of using well known dependencies for the energies of the rotational levels eq.(2.21b) together with the proper statistics to obtain their population and correlate it with measured laser transmission values. Having that in mind for  $^4\text{He}_2$  only odd- $N''$  numbered transitions  $P$ ,  $Q$ ,  $R$  are expected in the  $a^3\Sigma_u^+ - e^3\Pi_g$  spectrum with the lack of  $P(1)$  due to absence of  $N' = 0$  rotational level in the  $e$  state. In case of  $^3\text{He}_2$  both even and odd  $N''$  numbered transitions are expected as well as  $R(0)$  transition. Due to statistics resulting from non-zero  $I = \frac{1}{2}$  nuclear spin of  $^3\text{He}$  atoms discussed in paragraph 2.2.3(b) there is 3:1 alternation of the spectral lines intensities (even- $N''$  to odd- $N''$  numbered lines). For the

<sup>3</sup>In case of resolved transition occurring from the fine structure  $J''$  sublevels the designation of the transitions is different. Instead of notation i.e.  $Q(N'')$  (meaning  $\Delta N(N'')$ ), the following is used:  $^{\Delta N}\Delta J_{F',F''}(N'')$ .  $\Delta N$  and  $\Delta J$  are substituted by respective  $P, Q, R$  letter and when  $\Delta N = \Delta J$  the letter corresponding to  $\Delta N$  is omitted in the superscript.  $F'$  and  $F''$  can take value of 1,2 or 3 what means that  $J = N + 1$ ,  $J = N$ , or  $J = N - 1$  for the upper ' or the lower '' state respectively.

mixture helium molecule  $^3\text{He}$ - $^4\text{He}$  any absence or intensities alternation of the lines is expected as statistics for homonuclear molecule is not valid here anymore.

## 2.2.4 Intensities of the transition lines and molecular densities

The information about the molecular dynamics (formation, decay) can be obtained by quantitative measurements on the molecular spectrum, however the absolute density of the molecular species can be obtained only in the absorption techniques. Making use of the laser setup described in 3 the measurements of the laser light transmission through the absorber - helium molecules formed in the plasma - is possible. Assuming the linear regime of absorption (no dependency of absorption on electromagnetic wave intensity), according to eq. (A.5) the intensity  $I_{if}(\vec{r})$  change of the laser light propagating on the distance  $dz$  along the  $z$  axis through the absorber -  $n_M^i(\vec{r})$  - (number density) molecules in the initial  $i$  state of the transition to the  $f$  state is given by:

$$\frac{dI(\vec{r})}{dl} = -I_{if}(\vec{r})\sigma_{if}(\omega)n_M^i(\vec{r}), \quad (2.49)$$

where the dependency of the intensity change and number density on the spatial coordinates  $\vec{r}$  in the laser beam frame is given explicitly.  $\sigma_{if}$  is the cross section for the transition from the initial  $i$  to the final  $f$  state and depends on the transition frequency  $\omega_{fi}$ .

### (a) Distribution of molecules among rotational levels

Equation (2.49) gives an information about the population of only the initial state of the transition which, for a given wavelength of exciting light, is the number density of single rotational sublevel described by the  $N''$  number. In fact, the interesting value is the total number density  $N_M$  of molecules that are distributed along the laser beam path. Thus, it can be written that:

$$n_M^i = N_M s^i(n'', v'', N'', p), \quad (2.50)$$

where  $n'', v'', N'', p$  are the principal quantum number, vibrational and rotational quantum numbers as well as the parity of the initial transition sublevel respectively. For the case of  $\Sigma$  state in Hund's coupling (b), after [29], the distribution function  $s^i(n'', v'', N'', p)$  is given by:

$$s^i(n'', v'', N'', p) = \frac{2\phi(2S'' + 1)(2N'' + 1) \exp\left[\frac{-hc}{kT}(T_e + G(v'') + F(N''))\right]}{Q_{el}Q_{vib}Q_{rot}}, \quad (2.51)$$

where  $h, c, k, T$  are Planck constant, speed of light in vacuum, Boltzmann constant and the temperature. The vibrational  $G(v'')$  and rotational  $F(N'')$  energies are given by eq. (2.21a) and (2.21b) respectively.  $Q_{el}$ ,  $Q_{vib}$  and  $Q_{rot}$  are the electronic, vibration and rotation partition functions given by eq.(2.52a) -(2.52c):

$$Q_{el} = \sum_{\text{all states}} (2S'' + 1) \exp\left(\frac{hc}{kT}T_e\right), \quad (2.52a)$$

$$Q_{vib} = \sum_{v=0}^{v_{max}} \exp\left(\frac{hc}{kT}G(v'')\right), \quad (2.52b)$$

$$Q_{rot} = \frac{kT}{hcB_v} \text{ (for temperatures } > 0^\circ\text{C)}. \quad (2.52c)$$

The  $\phi$  parameter of eq.(2.51), that is resultant of a sublevel parity  $p$  is given by:

- for homonuclear molecules
  - with spinless nuclei molecules ( $^4\text{He}_2$ ):  $\phi = 1$
  - with odd-half-integral spin nuclei molecules ( $^3\text{He}_2$ ,  $I = \frac{1}{2}$ ):
 
$$\phi = \frac{I}{2I+1} = \frac{1}{4} \text{ in case of } s \text{ levels}$$

$$\phi = \frac{I+1}{2I+1} = \frac{3}{4} \text{ in case of } a \text{ levels.}$$
- for heteronuclear molecules:  $\phi = \frac{1}{2}$

According to [29] the series given by eq. (2.52b) should be terminated at  $\nu_{max}$  which is the greatest integer value less than or equal to  $\nu = \frac{\omega_e}{2\omega_e x_e} - \frac{1}{2}$ .

**(b) Absorption cross-section for  $a^3\Sigma_u^+ - e^3\Pi_g$  transition for  $^3\text{He}_2$  and  $^4\text{He}_2$  molecules**

Important in terms of absolute the  $N_M$  value determination from absorption measurements is the absorption cross-section  $\sigma_{if}(\omega)$  for the transition between rotational levels ( $i$  - initial, lower " - in case of absorption;  $f$  final, upper ' - in case of absorption) of considered electronic states. The angular transition frequency ( $\omega$ ) dependence of  $\sigma_{if}$  is explicit as well as hidden in the normalized absorption line profile function  $w(\omega - \omega_{fi})$  that contains the Doppler and collisional broadening contributions (discussed in details in Appendix A), where the relation between cross-section and the line strength  $S_{fi}$  is given by eq. (A.6):

$$\sigma_{if}(\omega) = \frac{1}{g_i} \frac{\pi\omega_{if}}{3\epsilon_0\hbar c} S_{fi} w(\omega - \omega_{fi}), \quad (2.53)$$

The degeneracy factor  $g$  that appears is, for the molecular state, given by:

$$g = (2 - \delta_{0,\Lambda})(2S + 1) \quad (2.54)$$

According to the relation (A.7)  $S_{fi} \propto |\int \Psi^{f*} \hat{d} \Psi^i d\tau|^2$ . Taking into account the Born-Oppenheimer approximation which gave the eq. (2.6) and (2.37) the integral can be written as:

$$d_{fi} = \int \Psi_e'^* \frac{1}{r} \Psi_v'^* \Psi_r'^* \hat{d} \Psi_e'' \frac{1}{r} \Psi_v'' \Psi_r'' d\tau \quad (2.55)$$

After [16], division of the electric moment  $\hat{d}$  into the sum of parts depending on the electrons  $\hat{d}_e$  and depending on the nuclei  $\hat{d}_n$  can be performed. Separation of electrons' and nuclei spatial coordinates  $d\tau = d\tau_e r^2 \sin\vartheta dr d\vartheta d\varphi$ , where  $r$  is internuclear distance and  $d\tau_e$  is the volume of the space of the electronic coordinates, together with the orthogonality condition of the wave functions describing different electronic states  $\int \Psi_e' \Psi_e'' d\tau_e = 0$ , results in:

$$d_{fi} = \int \Psi_e'^* \hat{d}_e \Psi_e'' d\tau_e \int \Psi_v'^* \Psi_v'' dr \int \sin\vartheta \Psi_r'^* \Psi_r'' d\vartheta d\varphi \quad (2.56)$$

The first integral is so called electronic transition moment  $R_e$  which square is proportional to the electronic transition probability. The square of the second integral:  $|\int \Psi_v'^* \Psi_v'' dr|^2 \equiv S(v', v'')$  is the Franck-Condon factor, for which the following sum rule is valid:

$$\sum_{v'} S(v', v'') = \sum_{v''} S(v', v'') = 1 \quad (2.57)$$

The summation in the third integral of (2.56) is taken over the  $\vartheta$  and  $\varphi$  angles only, on which the rotational part of the wavefunction depends (sec.2.2.3(a)), that is described by rotational quantum numbers  $J$ . Thus, for a given  $i$  and  $f$  states, the set of  $J'', J'$  quantum numbers are given, and the integral takes the constant value. Its square is denoted as:  $\left| \int \sin \vartheta \Psi_r'^* \Psi_r'' d\vartheta d\varphi \right|^2 \equiv S_{HL}(J', J'')$

After [29], in case of the molecule, the line strength  $S_{fi}$  of a single line is given by:

$$S = \frac{S_{HL}(J', J'') S(v', v'') R_e^2}{(2 - \delta_{0,\Lambda})(2S + 1)(2J + 1)} \quad (2.58)$$

$S_{HL}$  is the Hönl-London coefficient given for each of P,Q,R-form branches of  ${}^3\Pi$ (Hund case b)– $\Sigma$  transition in the *Table 5* of [33]. These coefficients are expressed in terms of the  $J''$  value of the fine structure levels, however, they can be given in terms of  $J'$  number of the excited state, using simple substitution from relations between  $J''$  and  $J'$  occurring for  $P, Q$  and  $R$  branches.

In the denominator of eq. (2.58)  $S$  and  $J$  are substituted by  $S'$  and  $J'$  or  $S''$  and  $J''$  when  $S_{HL}$  is expressed in terms of  $J'$  or  $J''$  respectively

The Hönl-London coefficients has to follow sum rules:

- for transitions having the same upper ( $J'$ ) or lower ( $J''$ ) levels the Hönl-London factors sum up to  $(2J' + 1)$  or  $(2J'' + 1)$  respectively
- sum of Hönl-London factors for all the branches in a band is  $(2 - \delta_{0,\Lambda})(2S + 1)(2J + 1)$  when the factors are expressed in terms of  $J$ , or  $(2 - \delta_{0,\Lambda})(2S + 1)(2N + 1)$  when they are expressed in terms of  $N$ .

Summing up the  $S_{HL}$  factors from [33] for common  $J''$  values ( $J'' = N'' + 1, J'' = N''$  or  $J'' = N'' - 1$ ) results in the value of  $\frac{1}{3}(2J'' + 1)$  that means - each Hönl-London factor given in the reference shall be multiplied by the factor of 3. Then, summing up  $S_{HL}$  of all possible branches P,Q,R of the band, value  $3(2J'' + 1)$  is achieved, what agrees with summing rule ( $S=1$  for the triplet states that are under consideration,  $\delta_{0,0} = 1$ ). Also the summing of coefficients expressed in terms of  $N''$  value leads to expected value of  $3(2N'' + 1)$ . For the case when no fine structure resolving of the spectral lines is considered, the Hönl-London factors can be arranged into the three groups corresponding to  $\Delta N = -1, 0$  or  $1$  values ( $P, Q, R$  branches in terms of  $N$  value change). Expressing the factors in terms of  $N''$  and summing all the factors in each group leads to the three Hönl-London coefficients for the  $P(N'')$ ,  $Q(N'')$  and  $R(N'')$  transitions:

$$\text{for } P \text{ branch: } S_{HL} = \frac{3}{2}(N'' - 1) \quad (2.59a)$$

$$\text{for } Q \text{ branch: } S_{HL} = \frac{3}{2}(2N'' + 1) \quad (2.59b)$$

$$\text{for } R \text{ branch: } S_{HL} = \frac{3}{2}(N'' + 2) \quad (2.59c)$$

The sum of abovegiven coefficients is equal to  $3(2N'' + 1)$  as it is at the same time the sum for all the transitions from common  $N''$  but also the sum of all the branches in the band. Using

the Hönl-London coefficients expressed in terms of  $N''$ , the line strength  $S$  can be calculated for  $P(N'')$ ,  $Q(N'')$  and  $R(N'')$  transitions using formula (2.58) in which  $J$  is substituted by  $N''$ .

However, for completeness of  $S$  calculation, the value of product of  $R_e^2$  and  $S(v', v'')$ , named band strength, is needed. If the lifetime  $\tau_f$  of the excited rotational level  $f$  (described by certain  $N'$  and  $v'$  numbers) is known, its reciprocal can be decomposed into the sum of Einstein coefficients for spontaneous emission ( $A_{fi}$ ) from common  $f$  level to the possible lower state  $i$  (described by  $N''$  and  $v''$ ):

$$\sum_i A_{fi} = \frac{1}{\tau_{f(N', v')}} \quad (2.60)$$

Each of  $A_{fi}$  Einstein coefficients can be expressed in term of  $S_{fi}$  using relation:

$$A_{fi} = \frac{1}{g_f} \frac{2\omega_{fi}^3}{3h\epsilon_0 c^3} S_{fi} \quad (2.61)$$

After [34], approximation for every transition within one  $v' - v''$  band:  $\omega_{fi} \approx \omega_{v', v''}$  can be applied in equations: (A.6) and (2.61). The  $\omega_{v', v''}$  is the mean angular frequency of all the transitions within the band, normally substituted as a band origin (frequency corresponding to fictitious Q(0) transition of the band). With this approximation the (2.60) and (2.61) result in:

$$\frac{1}{\tau_{f(N', v')}} = \frac{1}{g_f} \frac{2}{3h\epsilon_0 c^3} \sum_{i(N'', v'')} \omega_{v', v''}^3 \frac{S_{HL}(N'_f, N''_i) S(v', v'') R_e^2}{(2 - \delta_{0, \Lambda'}) (2S' + 1) (2N' + 1)} \quad (2.62)$$

For all the transitions between rotational levels of upper and lower states within one single vibrational band, the value of  $S(v', v'') R_e^2$  is a constant. The sum of the  $S_{HL}(N'_f, N''_i)$  coefficients over  $i$  levels translates into the sum of Hönl-London coefficients for all possible transitions occurring from common  $N'$  level, which is, as before, the sum of the factors for all the possible branches in the band and equal to:  $(2 - \delta_{0, \Lambda'}) (2S' + 1) (2N' + 1)$ . As the consequence it can be written:

$$\frac{1}{\tau_{f(N', v')}} = \frac{1}{g_f} \frac{2}{3h\epsilon_0 c^3} R_e^2 \sum_{i(v'')} \omega_{v', v''}^3 S(v', v'') \quad (2.63)$$

According to the expression (2.63) all rotational levels within one vibrational level have the same radiative lifetime. This is in agreement with what is reported by [31, 32].

After [35] where the indication of the value of Franck-Condon for 0-0 band is given as  $S(0, 0) = 0.95$ , considering eq. (2.57), the de-excitation from  $e^3\Pi_g (v = 0)$  occurs almost totally to the lowest vibrational level of  $a^3\Sigma_u^+$ . Moreover, the transition energy of any other band  $0 - v'' \neq 0$  is lower than in case of 0-0 band, thus the associated angular frequencies  $\omega_{v', v'' \neq 0}$  are lower, what decreases, anyhow poor, contribution of  $S(v', v'' \neq 0)$  to the overall lifetime of  $e^3\Pi_g (v = 0)$ . This justifies the following approximation:

$$\frac{1}{\tau_{f(N', v'=0)}} \approx \frac{1}{g_f} \frac{2\omega_{0,0}^3}{3h\epsilon_0 c^3} R_e^2 S(0, 0) \quad (2.64)$$

The value of  $e^3\Pi_g (v = 0)$  lifetime is reported in [35] and amounts to:  $\tau_{v=0} = 67s$ . Using this value along with relations: (A.6), (2.58) and (2.64) as well as with appropriate value of Hönl-London coefficients  $S_{HL}$ , allow calculation of the absorption cross-section  $\sigma_{if}$  essential

for absolute molecular density calculation from absorption measurements. The reference [35] from which the radiative lifetime of  $e^3\Pi_g$  has been taken focuses also on the measurement of the lifetimes in the two other excited molecular  $d$  and  $f$  states. Their investigations are performed using both the absorption and emission methods. In the former case the transmission of the pulse dye laser is recorded after single pass through 1 m long cell filled with  $^4\text{He}$  gas at 3 bar excited with electron beam pulses in the room temperature conditions. The combination of the results obtained in absorption measurements as well as saturation (the transmission of the laser was measured in function of the laser intensity providing saturation curve) allowed proper choice of the absorption cross-section value and the density of metastable molecule values giving a best agreement with their experimental data when the differential rate equation for the transmitted laser intensity and molecular density were considered.

# Chapter 3

## Blue laser setup

Absorption studies on the helium metastable state performed on chosen transition  $a^3\Sigma_u^+ (0) - e^3\Pi_g (0)$  requires the source of the laser radiation at the wavelength about 465 nm. The probing character of the measurements, especially when planned in parallel to the Metastability Exchange Optical Pumping process, does not require high laser powers that could perturb the helium plasma conditions. Values of order of tens or hundreds  $\mu\text{W}$  are sufficient for the absorption measurements with good SNR. Important issue of the required laser source is its wavelength tuning range and spectral width so that the part of the spectrum containing several rotational components of  $a-e$  transition can be observed. According to [6, 28] the tuning range of 2 nm is sufficient to observe several Q branch components as well as single R and P branch lines. Expected Doppler broadening for the helium molecule of about 3 GHz at the room temperature requires low spectral width of the laser source (several MHz) to allow good resolution of performed measurements. At the time of planning the investigation on the molecules in helium plasma in MEOP conditions such laser source was not commercially available. Well known nonlinear process of Second Harmonic Generation (SHG) gives the possibilities of obtaining laser beam of various wavelengths not available directly from the semiconductor laser sources, that recently are very popular due to their compactness and various spectral characteristics (e.g. narrowness, monomode emission). Generation of the laser light at 465 nm requires the laser diode working at the wavelength of 930 nm in infra-red (IR) range for SHG process to be performed as well as the nonlinear media. Among the best commercially available efficient nonlinear medium providing wide phase matching bandwidth are periodically poled  $\text{KTiOPO}_4$  (PP-KTP) crystals. They are often chosen for its properties such as high value of the effective nonlinear coefficient  $d_{eff}$ , operating around room temperature conditions at visible wavelengths, high flexibility of choice in the grating period suited to the targeted wavelength as well as good quality and reasonable price. Suggested by commonly met conversion efficiencies normalized to the crystal length  $L_{cryst}$  ( $\eta \equiv \frac{P_{out}}{L_{cryst}P_{in}^2}$ ) of about 2.8 %  $\text{W}^{-1}\text{cm}^{-1}$  at 461 nm reported in [40] for SHG and 2.2 %  $\text{W}^{-1}\text{cm}^{-1}$  at 492 nm given in [41] for Sum Frequency Generation (SFG), one expects second harmonic output power up to 300  $\mu\text{W}$  using 100 mW laser diode output power. According to what has been said before, this amount of power would be sufficient for the probe beam source. When the components of the designed setup were being completed 930 nm emitting diode was not available or later has shown up on the market providing only 40 mW of output power, while, for other laser diodes emitting in the vicinity of 930 nm that are 923 nm and 937 nm 100 mW of maximum power each was specified. Hence, reaching desired 465 nm wavelength with 923 and 937 nm diodes required using other nonlin-

ear process of the same origin as SHG - the Sum Frequency Generation (SFG). The advantage of the both wavelength proximity (14 nm) is that the conditions here are very close to the SHG case and the same optics (suitable for this infra-red wavelength) can be used (crystal, mirrors), however the optical cavity design has to be planned so that these two beams will be overlapped before focusing into the small waist inside the nonlinear crystal. Similarity of SHG and SFG in this case facilitates the theoretical description of the latter process allowing easier comparison with obtained results. This approximation is sufficient in respect to the need of rough characterization of the laser setup performance and efficiency that was not the main goal in this work, however satisfactory agreement between expected and measured efficiency value and matching tolerances has been achieved. In this chapter the basics of up-conversion process theory is introduced constituting the background for further efficiency and working parameters tolerances estimation according to the laser setup performance tests. The construction details are then described emphasizing the original design of 3 prisms used for beams overlapping. Comparison and discussion of experimental results and theoretical predictions of the laser working parameters is given.

### 3.1 Second Harmonic Generation in PP-KTP

The nonlinear processes rely on the presence of higher than linear terms in the response of the media to the applied electric field  $E(z, t)$  associated with propagating electromagnetic wave. Induced electric polarization  $P(z, t)$  resulting from the spatial separation of the centers of positive and negative charges of the atoms is given by:

$$P(z, t) = \epsilon_0 \chi^{(1)} E(z, t) + \epsilon_0 \chi^{(2)} [E(z, t)]^2 + \dots, \quad (3.1)$$

where  $\chi^{(n)}$  is the  $n$ -order expansion of electric susceptibility of the media,  $\epsilon_0$  is the permittivity of free space.

In general the  $E(z, t)$  can be resultant of more than one electric field components related to a different, propagating together in the same  $z$  direction, electromagnetic waves (called fundamentals) of frequency  $\omega_i$  and wave vector  $k_i$ , where  $i = 1, 2, \dots$ , according to the number of monochromatic waves. For the case of two electromagnetic waves interacting with the nonlinear media, oscillation of  $P(z, t)$  with resultant of several frequency components occurs, being the second harmonics ( $2\omega_1$  and  $2\omega_2$ ), frequency sum ( $\omega_1 + \omega_2$ ) and frequency difference ( $\omega_1 - \omega_2$ ). Fulfilling the relation between the fundamental wave vectors  $k_1, k_2$  and wave vector of generated harmonic  $k_b$ , called phase-matching condition for SFG (3.2), maximizes the generation of sum-frequency component, while other frequencies are well suppressed. Analogous relation eq.(3.3) can be obtained when the SFG is being approximated by the SHG process, so that  $k_{av} = \frac{k_1+k_2}{2}$ , where  $k_{av} = \frac{2\pi n_{av}}{\lambda_{av}}$ , having  $\lambda_{av} = \frac{\lambda_1+\lambda_2}{2}$  thanks to  $\lambda_1 \approx \lambda_2$ .

$$\Delta k^{SFG} = k_b - (k_1 + k_2) \Rightarrow \frac{\Delta k^{SFG}}{2\pi} = \frac{n_b}{\lambda_b} - \frac{n_1}{\lambda_1} - \frac{n_2}{\lambda_2} = 0 \quad (3.2)$$

$$\Delta k^{SHG} = k_b - 2k_{av} = 0 \Rightarrow \frac{\Delta k^{SHG}}{2\pi} = \frac{n_b}{\lambda_b} - \frac{n_{av}}{\lambda_{av}} \quad (3.3)$$

Both relations (3.2) and (3.3) are valid for *plane wave* approximation for the incident beams. In other case (for example focused beams)  $\Delta k^{SFG} \neq 0$  and  $\Delta k^{SHG} \neq 0$

The phase matching condition can be also understood in the way that the wave at the frequency of interest generated locally in one section of the crystal has to add up in phase with all the waves of the same frequency generated in the other crystal sections.

Practically the phase-matching condition reduces to:  $2n_b - n_1$  for the case of SHG or  $2n_b - n_1 - n_2$  for SFG. Fulfilling this is problematic, as common nonlinear materials exhibit the normal dispersion ( $n_b > n_1, n_2$ ). Some crystals, however, shows the birefringence among its crystallographic axes, that is, if the wave is polarized along one axis (i.e.  $b$ -axis) it travels slower than the wave which is polarized along other axis (i.e.  $c$ -axis). Thus, when the polarization of the fundamental wave is constrained to the "slow" axis  $b$ , and the polarization of second harmonic along the "fast" axis  $c$ , the phase velocity due to dispersion can be compensated for by the phase velocity difference due to birefringence. This is so called birefringence phase-matching and is sensitive not only to the fundamental wavelength but also on the crystal temperature and orientation in respect to the direction of waves propagation and polarization. This method has several limitations among which there is insufficient birefringence of the crystal material to provide phase-matching at the wavelength of interest or the nonlinearity associated with this type of phase-matching is too low to be useful. This is the case for the wavelength desired in this work - 465 nm. Thus, the Author in his laser setup for sum-frequency generation,

uses periodically poled KTP crystal, achieving so-called quasi-phase-matching. It relies on the artificial structuring of the nonlinear material, so that the crystal is divided to  $N = \frac{l}{\Lambda}$  segments, called domains, in which the effective nonlinear coefficient  $d_{eff}$  (that is related to second order electric susceptibility[38] - commonly used instead of  $\chi^{(2)}$ ) alternately changes the sign. The  $\Lambda$  is called grating period (twice the length of the domain),  $l$  is the crystal length. Periodically change of  $d_{eff}$  every distance of  $\Lambda$ , adapted to desired nonlinear process and wavelength of interest, prevents acquiring, by already generated and propagating in the material harmonic wave, more than  $\pi$  factor of the phase difference with locally generated harmonic. In this way amplitude of generated wave is accumulated along the whole crystal length. In this method the phase-matching conditions eq. (3.2) and (3.3) have to be redefined and are called quasi-phase-matching (QPM) conditions (not equalized to 0 to maintain the generality):

$$\frac{\Delta k_{QPM}^{SFG}}{2\pi} = \frac{n_b}{\lambda_b} - \frac{n_1}{\lambda_q} - \frac{n_2}{\lambda_2} - \frac{1}{\Lambda} \quad (3.4)$$

$$\frac{\Delta k_{QPM}^{SHG}}{2\pi} = \frac{n_b}{\lambda_b} - \frac{2n_{av}}{\lambda_{av}} - \frac{1}{\Lambda} \quad (3.5)$$

As stated before, the further consideration will base on the SHG theory and so the eq.(3.5) can be rewritten in more convenient way in terms of  $\lambda_{av} = 2\lambda_b$  only:

$$\frac{\Delta k_{QPM}^{SHG}}{2\pi} = \frac{2(n_b - n_{av})}{\lambda_{av}} - \frac{1}{\Lambda} \quad (3.6)$$

In further consideration, for simplicity of notation  $\Delta k_{QPM}^{SHG} \equiv \Delta k_{QPM}$ .

In order to obtain maximal nonlinear response on the second harmonic, the highest nonlinear coefficient of PP-KTP crystal has to be exploited that in this case is  $d_{33}$ [38]. That determines the incident beam (in the experiment - the two beams) polarization direction that has to be parallel to the Z-axis of the crystal. The fixed value of crystal's  $\Lambda$  determines the way in which the output second harmonic wavelength can be varied - it can be made by change of the incident wavelength. However, crystal's temperature needs to be regulated to maintain the condition of quasi-phase matching eq.(3.6). The relevant temperature dependency lies in the refractive indexes of the fundamental and second harmonic, namely its Z-axis component  $n^z$  as all the beams are polarized in one Z axis (see also eq.(3.5), where z axis of the drawing has been chosen to be parallel with Z axis of the crystal). The values of  $n^z$  can be obtained for a given material and known wavelength as well as the material temperature (here the crystal temperature  $T_{cr}$ ) using Sellmeier's equation with coefficients proper for the certain material. Detailed equation as well as the parameters from [73] to [71] are given in the (B). Using the averaged value of those obtained with equation parameters from references given, at  $20^\circ C n_b^z(465 \text{ nm}) = 1.9172$  and  $n_{av}^z(930 \text{ nm}) = 1.8362$ . With  $\lambda_b = \frac{\lambda_{av}}{2} = 465 \text{ nm}$  and these refractive indexes, eq.(3.6) in the plane wave approximation provides rough grating period value in the way that:

$$\Lambda_{QPM} = \frac{\lambda_{av}}{2(n_b^z - n_{av}^z)} = 5.74 \mu m \quad (3.7)$$

This value is close to the specified for the crystal mounted in our experimental setup given in subsection 3.2.1.2. For the simplicity of notation, in further considerations it will be used as follows:  $n_b^z(T_{cr}) = n_b(T_{cr})$  for generated harmonic and  $n_{av}(T_{cr}) = n_{av}(T_{cr})$  for the fundamental wavelength.

### 3.1.1 Conversion efficiency

The estimation of the second harmonic generation process efficiency in which Gaussian laser beam with the wavelength of  $\lambda_{av}$  and power  $P_{av}$  is focused into the nonlinear crystal of length  $l$  can be performed using the formula given in [38, 39, 44]. Assuming that the fundamental and second harmonic generation propagating along the crystallographic axis (no walk-off<sup>1</sup> angle between the beams) are focused in the middle of the crystal ( $l/2$ ) and are not absorbed inside the crystal:

$$\eta_{SHG} = \frac{P_b}{P_{av}^2} = \frac{16\pi^2 d_{eff}^2}{\epsilon_0 c n_{av} n_b \lambda_{av}^3} l h(\sigma, \xi) \quad (3.8a)$$

$$h(\sigma, \xi) = \frac{1}{4\xi} \left| \int_{-\xi}^{\xi} \frac{\exp(i\sigma(\tau))}{(1+i\tau)} d\tau \right|^2 \quad (3.8b)$$

$$d_{eff} = \frac{2d_{33}}{\pi} \quad (3.8c)$$

The  $h(\sigma, \xi)$  is called the *Boyd-Kleinman focusing factor*[39].

- $\sigma = -\frac{b\Delta k_{QPM}}{2}$
- $\xi = l/b = l\lambda_{av}/(2\pi n_{av} w_0^2)$ , where  $w_0$  is the waist of the focused beam - the minimum radius (for which the power reaches  $1/e^2$  of the peak value) of the beam;

It is also assumed that two incident Gaussian beams have the same value of confocal parameter ( $b = 2\pi n_{av} w_0^2 / \lambda_{av}$ ) and propagate along the same axis being spatially overlapped.

The parameters met in the equation (3.8b) appears in the considerations of the geometrical aspects of the nonlinear conversion process of SHG and SFG. The equation for the SHG efficiency (3.8a) shows the dependency on the fundamental and generated harmonic beam intensities, that is the power per unit area, what suggests the possibility of  $\eta$  increase more tightly confined the beam is made. This can be reached by focusing the beam inside the nonlinear crystal. However, stronger the beam confinement is, bigger the diffraction effect occurs, reducing the length on which the beam confinement is maintained. In eq. (3.8a) the appearing of the  $l$  crystal length shows that the interaction length plays a crucial role in the nonlinear process. Thus, for the crystal of a given length the compromise between the strength of focusing and interaction length has to be set.

According to [39] the maximum value that can be reached by Boyd-Kleinman focusing factor is  $h(\sigma_m, \xi_m) = 1.068$  for  $\xi_m = 2.84$ . The subscript  $m$  denotes optimized value providing maximum of the  $h(\sigma, \xi)$  function.

It can be shown, that the function of Boyd-Kleinman focusing factor shown in the eq.(3.8b) is in fact the integration over the real values, so that:

$$h(\sigma, \xi) = \frac{1}{\xi} \left| \int_0^{\xi} \frac{\cos(\sigma\tau) + \tau \sin(\sigma\tau)}{1 + \tau^2} d\tau \right|^2 \quad (3.9)$$

<sup>1</sup>If the fundamental beams are not propagating in the crystallographic axis direction, the generated nonlinear harmonic from the latter part of the crystal is spatially shifted in respect to the harmonic generated in the former part - this wave propagates at the angle  $\rho$  relative to the fundamentals - parameter  $\beta \propto \rho$  appears then in  $h(\sigma, \xi, \beta)$ . At the output, the generated beam has no longer Gaussian distribution. At this work, this is not the case, as fundamental beams propagate along one of the crystal axis - the walk-off angle is  $\rho = 0 = \beta$ .

Further step can be performed to remove the parametric bound of the integral thus obtaining the finite integral as follows:

$$h(\sigma, \xi) = \xi \left| \int_0^1 \frac{\cos(\sigma \xi u) + \xi u \sin(\sigma \xi u)}{1 + (\xi u)^2} du \right|^2 \quad (3.10)$$

Using the OriginLab Corporation Origin 8.0 SR6 version software and "Fitting Integral Function with parametric limit using NAG Library"<sup>2</sup> the simulation of integral  $h(\sigma, \xi)$  function is possible looking at the Boyd-Kleinman focusing factor value change in function of the  $\sigma$  as a variable fixing the value of  $\xi$ . In present work it was found useful to present simulation results of  $\sqrt{h(\sigma, \xi)}$  so that the side lobes are easier to observe and in the same way the function fit to the experimental data performed later in subsection 3.3.3 The simulation for the  $\xi$  values from 1 to 5 has been shown on graph 3.1

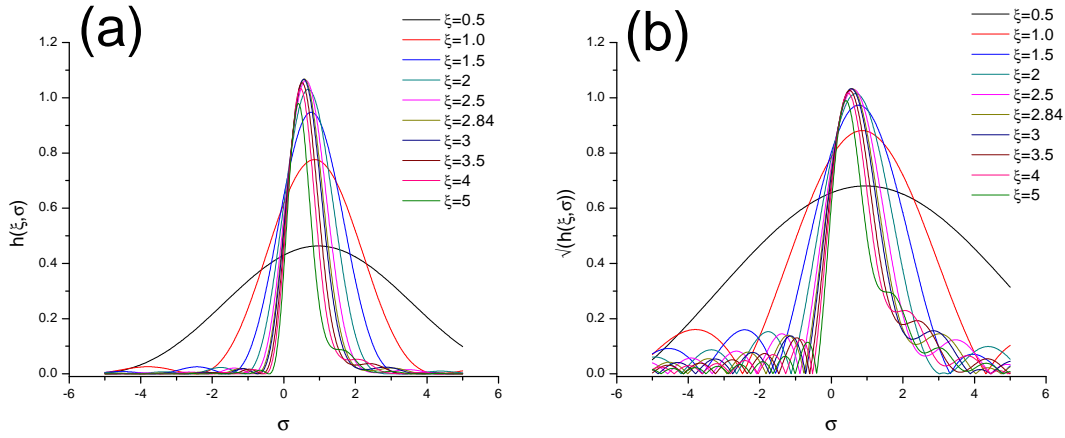


Figure 3.1: Simulated curves of Boyd-Kleinman focusing factor (a) and its square root (b) in function of  $\sigma$

As it can be seen on the fig.3.1 changing the  $\xi$  the amplitude of the main peak is changing (see Fig. 3.3) but also its halfwidth (Fig.3.4) and position in  $\sigma$  as well (Fig.3.2) - these values are also explicitly given in the Table 3.1.

The values of  $\sigma = \sigma_m$  that provides the maximum of the  $h(\sigma, \xi)$  function for a given  $\xi$  within the investigated range are given on the Fig.3.2.

The values of maxima of the  $h(\sigma, \xi) = h(\sigma_m, \xi)$  curves presented on the graph 3.1 are plotted in function of the corresponding  $\xi$  values on the Fig.3.3 showing the maximum value of  $h(\sigma_m, \xi = \xi_m) = 1.068$  is reached for  $\xi = \xi_m = 2.84$  and  $\sigma_m = 0.576$ .

Having the values of  $\sigma_m = 0.576$  and  $\xi_m = 2.84$ , using the definitions of  $\xi$  and  $\sigma$  we obtain:

$$\frac{\Delta k_{QPM}}{2\pi} = -\frac{\sigma_m \xi}{\pi l} = 5.2 \times 10^{-5} \mu m^{-1} \ll \frac{1}{\Lambda}, \quad (3.11)$$

but for  $\Lambda = 5.74 \mu m$  determined before as well as the value specified by the crystal manufacturer  $\Lambda = 5.725 \mu m$  (see subsection 3.2.1.2). It means that the quasi-phase-matching condition  $\Delta k_{QPM}$  can be legitimately reduced to the one for plane wave condition, namely  $\Delta k_{QPM} = 0$

The values of FWHM of the main peak have been plotted, directly in  $\sigma$  units ( $\Delta\sigma_{1/2}$ ) as well as  $\sigma \xi = \frac{\Delta k_{QPM} l}{2}$  on the figures 3.4 (a) and (b).

<sup>2</sup>More info at the website <http://qhwiki.originlab.com>

$\xi$	$\sigma_m$	$h(\sigma_m, \xi)$	$\Delta\sigma_{1/2}$	FWHM [ $\Delta kl/2$ ]	$\eta[W^{-1}]$
1	0.856	0.7761	2.93	2.93	0.01472
1.5	0.766	0.9475	2.04	3.05	0.01796
2	0.686	1.0303	1.59	3.17	0.01954
2.5	0.616	1.0628	1.31	3.29	0.02015
2.84	0.576	1.0677	1.18	3.36	0.02024
3	0.556	1.0668	1.13	3.39	0.02023
3.5	0.506	1.0546	1.00	3.49	0.02
4	0.465	1.0334	0.89	3.58	0.0196
5	0.405	0.9790	0.75	3.74	0.01856

Table 3.1: Parameters of the simulated curves describing the Boyd-Kleinman versus  $\sigma$  dependency for various  $\xi$  values.

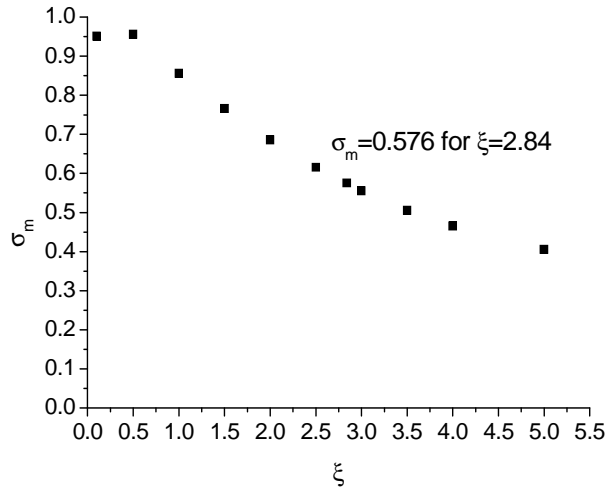


Figure 3.2: Change of the optimized  $\sigma = \sigma_m$  in function of  $\xi$ .

Reference	Process	$\Lambda[\mu m]$	$d_{eff}[pm/V]$	$\lambda_{generated}[nm]$
[41]	SFG	6.99	10	492
[40]	SHG	5.5	9.5	461
[78]	SHG	-	10.8	>1500
[79]	SHG	9	9.5	532
[44]	SHG	9.5	7.8	541

Table 3.2: Compilation of the references with PP-KTP applications to SHG and SFG providing the view on  $d_{eff}$  coefficient values for various wavelengths and crystal grating periods.

Presented figures of the change in full width at half maximum FWHM shows the decrease with  $\xi$  until the limit of not focused beam is reached.

At this moment, every parameter of the equation(3.8a) is available to perform calculation of the expected efficiency, except of  $d_{eff}$ .

For expected  $\eta$  calculation the value  $d_{eff} = 9.5 pm/V$  has been taken as both the wavelength and grating period  $\Lambda$  are the closest one to the case met in this work. Speed of light as well

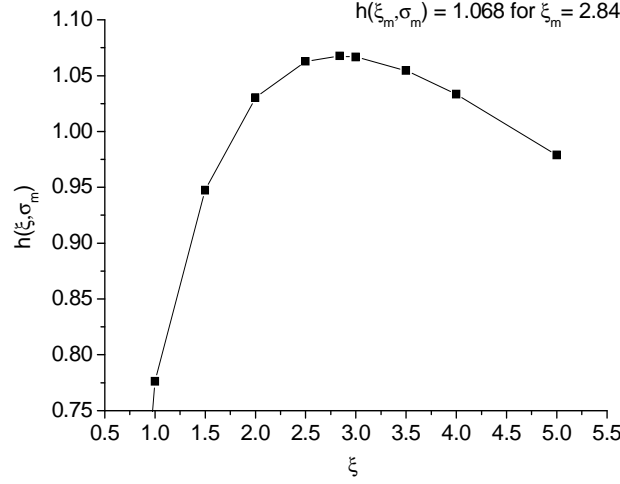


Figure 3.3: Variation of the  $h(\sigma_m, \xi)$  values with  $\xi$  showing the existence of a single maximum  $\xi_m$ .

as the vacuum permittivity are given in the table of constant at the end of the dissertation,  $n_b$  and  $n_{av}$  has been given earlier, and  $\lambda_{av} = 930nm$  is taken. Obtained values of the efficiency  $\eta$  are presented in the table 3.1. The maximum value, for  $h(\sigma_m, \xi_m) = 1.068$  is about  $\eta_{calc} = 2.02\%W^{-1}$ . However, one has to remember that the approximation of SHG has been taken for the SFG process. In [38] the ready equation for SFG efficiency has been presented showing that:

$$\eta_{SFG}^{ref} = \frac{32 * \pi^2 d_{eff}^2}{\epsilon_0 c n_b \lambda_1 \lambda_2 \lambda_b} P_1 P_2 l h(\xi, \sigma) \quad (3.12)$$

The Boyd-Kleinman focusing factor is common for both SFG and SHG. The difference between this equation and (3.8a) is of order of 2 - apart from the difference between 32 and 16 factor there is a difference in the denominator. In (3.12) we have product of three wavelengths of which, in our case, is approximately half of each of the incident wavelengths. This factor of 2 however is approximately canceled out by the presence of third (in (3.8a) there are only two refractive indices) refractive index that is of order of  $\approx 2$ . Thus, our value of estimated efficiency on the basis of SHG for SFG process is underestimated for about factor of 2, and  $\eta_{calc} \approx 4\%W^{-1}$ . Apart from this factor of 2 that appears only here, all the previous consideration are valid and further SHG approximation of SFG will be maintained.

### 3.1.2 Matching tolerances

If one wants to change the generated SHG wavelength by tuning the  $\lambda_{av}$  care should be taken for remaining at the quasi-phase-matching condition:  $\Delta k = \Delta k_{QPM}$  which has to remain constant not to have loses on generated power or totally loose the generation of the second harmonic. It has been already said that the refractive indexes of the crystal depend on its temperature, so it will be considered now how the quasi-phase-matching depends on the crystal temperature and how it is related to the change in  $\lambda_{ave}$  which affecting the QPM process. Let's consider

$$\frac{\Delta k}{2\pi} = \frac{\Delta k_0}{2\pi} - \frac{1}{\Lambda}, \quad (3.13)$$

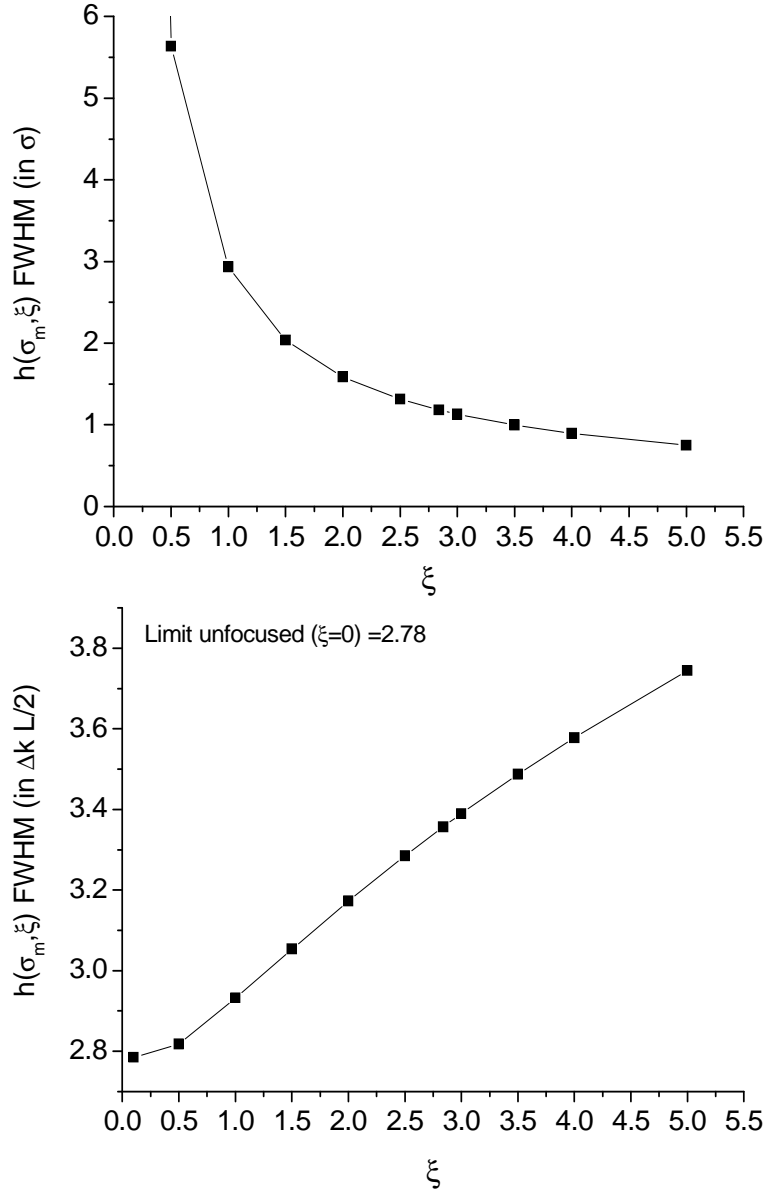


Figure 3.4: Variation of the FWHM of  $h(\sigma, \xi)$  curve main peak with  $\xi$  in  $\sigma$  values scale -  $\Delta\sigma_{1/2}$  (a) as well as  $\frac{\Delta k_{QPM} l}{2}$  units (b). On the graph (b) the value FWHM value for no-focus ( $\xi = 0 \Rightarrow w_0 \rightarrow 0$ ) limit  $\Delta(\frac{\Delta k_{QPM} l}{2})_{1/2} = 2.78$

where

$$\frac{\Delta k_0}{2\pi} = 2 \frac{1}{\lambda_{av}} (n_b(T_{cr}, \lambda_{av}/2) - n_{av}(T_{cr}, \lambda_{av})) \quad (3.14)$$

this means having:

$$\frac{\partial}{\partial T_{cr}} \left[ \left( l \frac{\Delta k_0}{2\pi} - \frac{1}{\Lambda} \right) \right] dT_{cr} = - \frac{\partial}{\partial \lambda_{av}} \left[ \left( l \frac{\Delta k_0}{2\pi} - \frac{1}{\Lambda} \right) \right] d\lambda_{av} \quad (3.15)$$

Very straightforwardly, one has:

$$\frac{\partial}{\partial T_{cr}} \left( \frac{\Delta kl}{2\pi} \right) = \frac{\partial}{\partial T_{cr}} \left( \frac{\Delta k_0}{2\pi} - \frac{1}{\Lambda} \right) + l \frac{\partial}{\partial T_{cr}} \left( \frac{\Delta k_0}{2\pi} \right) - l \frac{\partial}{\partial T_{cr}} \left( \frac{1}{\Lambda} \right) = l \frac{\partial}{\partial T_{cr}} \left( \frac{\Delta k_0}{2\pi} \right) + \alpha l \frac{\Delta k_0}{2\pi} \quad (3.16)$$

where  $\alpha = l^{-1} \frac{\partial l}{\partial T_{cr}}$  is the coefficient of linear expansion. Since  $\frac{\partial l}{\partial T_{cr}} = \alpha l$  and  $\frac{\partial}{\partial T_{cr}} \left[ \frac{1}{\Lambda} \right] = -\frac{\alpha}{\Lambda}$  we write:

$$\frac{\partial}{\partial T_{cr}} \left( \frac{\Delta kl}{2\pi} \right) = 2 \frac{l}{\lambda_{av}} \left[ \left. \frac{\partial n}{\partial T_{cr}} \right|_{T_{cr}, \lambda_{av}/2} - \left. \frac{\partial n}{\partial T_{cr}} \right|_{T_{cr}, \lambda_{av}} \right] + 2\alpha \frac{l}{\lambda_{av}} \left( n_b(T_{cr}, \lambda_{av}/2) - n_{av}(T_{cr}, \lambda_{av}) \right) \quad (3.17)$$

From the other side, for the wavelength variation

$$\begin{aligned} \frac{\partial}{\partial \lambda_{av}} \left( \frac{\Delta kl}{2\pi} \right) &= \frac{\partial}{\partial \lambda_{av}} \left( l \left( \frac{\Delta k_0}{2\pi} - \frac{1}{\Lambda} \right) \right) = \\ &= \frac{l}{\lambda_{av}} \left( \left. \frac{\partial n}{\partial \lambda_{av}} \right|_{T_{cr}, \lambda_{av}/2} - 2 \left. \frac{\partial n}{\partial \lambda_{av}} \right|_{T_{cr}, \lambda_{av}} \right) - \frac{2l}{\lambda_{av}^2} \left( n_b(T_{cr}, \lambda_{av}/2) - n_{av}(T_{cr}, \lambda_{av}) \right) \\ &= 2 \frac{l}{\lambda_{av}} \left[ \frac{1}{2} \left. \frac{\partial n}{\partial \lambda_{av}} \right|_{T_{cr}, \lambda_{av}/2} - \left. \frac{\partial n}{\partial \lambda_{av}} \right|_{T_{cr}, \lambda_{av}} - \frac{1}{\lambda_{av}} \left( n_b(T_{cr}, \lambda_{av}/2) - n_{av}(T_{cr}, \lambda_{av}) \right) \right] \end{aligned} \quad (3.18)$$

### (c) Matching line

If the eq.(3.15) is combined with (3.17) and (3.18),  $T_{cr}^{QPM(\lambda_{av})}$  satisfies:

$$\frac{dT_{cr}^{QPM(\lambda_{av})}}{d\lambda_{av}} = \frac{\frac{1}{2} \left. \frac{\partial n}{\partial \lambda_{av}} \right|_{T_{cr}, \lambda_{av}/2} - \left. \frac{\partial n}{\partial \lambda_{av}} \right|_{T_{cr}, \lambda_{av}} - \frac{1}{\lambda_{av}} \left( n_b(T_{cr}, \lambda_{av}/2) - n_{av}(T_{cr}, \lambda_{av}) \right)}{\left. \frac{\partial n}{\partial T_{cr}} \right|_{T_{cr}, \lambda_{av}/2} - \left. \frac{\partial n}{\partial T_{cr}} \right|_{T_{cr}, \lambda_{av}} + 2\alpha \frac{l}{\lambda_{av}} \left( n_b(T_{cr}, \lambda_{av}/2) - n_{av}(T_{cr}, \lambda_{av}) \right)} \quad (3.19)$$

This is a slope of the line of matching the crystal temperature  $T_{cr}$  to a given  $\lambda_{av}$  at the input of the crystal.

### (d) Matching tolerances

Matching tolerances characterize the sensitivity of conversion efficiency to any of the matching parameters X, i.e., the way efficiency decreases when X departs from its optimal value  $x_0$  while all other operating conditions remain fixed. They are commonly characterized by the corresponding acceptance bandwidth that corresponds to the FWHM of the response curve

$\eta(X)$ , i.e., the range  $\Delta X_{1/2}$  of parameter values  $X$  for which the conversion efficiency satisfies  $\eta(X) \geq \eta_0/2 = \eta(X_0)/2$ .

In the present work the conversion efficiency can be characterized by a temperature bandwidth associated to the control of crystal temperature  $T_{cr}$  and the spectral bandwidth associated to the average input wavelength  $\lambda_{av}$ , that can be varied either by the joint variation of  $\lambda_1$  and  $\lambda_2$  (controlled by the common temperature of the laser diodes (see subsection 3.2.1.1)) or their individual variations (controlled by the LD feeding currents).

Given the limited operating ranges of the LD and crystal, one can write to first order write

$$\sigma(X) = \sigma(X_0) + \left[ \frac{\partial \sigma}{\partial X} \right]_{X_0} (X - X_0), \quad (3.20)$$

for any small variation of phase matching parameter  $X$  around its value at optimal matching  $X_0$ , with  $\sigma(X_0) = \sigma_m(\xi)$ . The acceptance FWHM is then given by

$$\Delta X_{1/2} = \frac{\Delta \sigma_{1/2}(\xi)}{\left[ \frac{\partial \sigma}{\partial X} \right]_{X_0}} \quad (3.21)$$

where  $\Delta \sigma_{1/2}$  is the FWHM of the Boyd-Kleinman focusing factor  $h(\sigma, \xi)$ . The dependence of variation of  $\Delta \sigma_{1/2}$  with focusing parameter  $\xi$  is plotted in fig.3.4 (a).

Using  $\left[ \frac{\partial \sigma}{\partial X} \right]_{X_0} = -\left( \frac{l}{2\xi} \right) \left[ \frac{\partial \Delta k}{\partial X} \right]_{X_0}$ , the expression of the acceptance bandwidths for  $X = T_{cr}$  (crystal matching) and  $X = T_{ld}$  or  $I_{ld}$  - laser diodes current (LD matching) are readily obtained from equations (3.17) and (3.18) and computed (provided, for LD matching, that the change of  $\lambda_{av}$  with either LDs temperature or LD current(s) are known).

## 3.2 465 nm laser setup - description

The small difference of about 14 nm between the fundamental beams requires more demanding solution of beams' spatial overlapping before focusing in the center of the crystal, comparing with other SFG setups, where wavelength difference between initial beams is around 200 nm [41, 42] and simple dichroic mirrors solve the problem. Instead, set of 3 equilateral prisms of which dispersion is sufficient to superimpose angularly separated beams were used increasing the complexity of the system, what is the main drawback of the solution. On the other hand it was balanced by only a single pass of the infra red beams through the crystal - not as in [42] where the resonant cavity was arranged. This of course limited the total conversion efficiency that can be achieved and thus the blue light output power but allowed build compact and robust construction, which is desired to be easily and safely transported between cooperating laboratories, having sufficient output power and tunability to perform absorption measurements on  $\text{He}_2^*$ . In further subsections the components used to the realization of SFG setup are described in details with an emphasis on the main elements - the laser diodes and the nonlinear crystal. Detailed properties of other components such as mirrors (AM,M1-3,KM on the fig. (3.5)), lenses (F1-2), and filter (LPF) are described together with the scheme of assembled blue laser device, so that the relation between their properties and function in the setup is easier to notice.

### 3.2.1 Laser setup components

#### 3.2.1.1 Laser diodes

The sources of the 923 nm (LD1) and 937 nm (LD2) beams are the Toptica DFB (Distributed Feedback [43]) 100 mW, monomode laser diodes. Both laser diodes spectral linewidth is several MHz and nominal wavelengths at 25°C are 923.58 nm and 937.6 nm respectively. The wavelength tuning can be realized with the feeding current (from the lasing threshold values of 53 and 28 up to 180 and 150 mA respectively) or LD temperature change between 5 and 45 °C providing the access to specified wavelength tuning ranges: 922-925 nm and 936.3-938.7 nm respectively. Nominal variation of the wavelength with the temperature ( $d\lambda/dT$  [nm/K]) is 0.08 nm/K for LD1 and 0.06 nm/K for LD2. However, linear fit to the wavelength vs. laser diodes temperature dependency on (Fig.3.9), measured using Coherent WaveMate Wavelength Meter, gave the values of  $0.0578 \pm 0.0006$  nm/K and  $0.0552 \pm 0.0006$  nm/K respectively. The linear fit to the wavelength versus laser diodes feeding current  $I$  gave the values of  $d\lambda_1/dI_1 = 0.00448 \pm 0.00002$  nm/mA and  $d\lambda_2/dI_2 = 0.00607 \pm 0.00004$  nm/mA, as shown on the graph 3.7.

The diodes are placed in separate 9 mm diameter collimation tubes with optics ( $f = 4.5$  mm lens with AR coating). Collimated beams are of elliptical shape with shorter axis in the horizontal plane that is the direction of the emitted light linear polarization. The recorded beam spatial profiles in the plane perpendicular to the propagation direction gave the full width at half maximum (FWHM) values in both horizontal ( $\text{FWHM}_h(923) = 1.2 \pm 0.1$  mm and  $\text{FWHM}_h(937) = 1.2 \pm 0.1$  mm) and vertical ( $\text{FWHM}_v(923) = 1.5 \pm 0.1$  and  $\text{FWHM}_v(937) = 1.8 \pm 0.2$  mm) planes. It shows that the beams has moderate ellipticity of about 25% for both of the diodes.

Two collimating tubes were mounted in a common copper holder allowing simultaneous change of the laser diodes temperature using the thermoelectric cooler (TEC3-2.5 from Thorlabs) attached to the holder. The cooler allows continuous cooling down as well as heating up

the copper holder. In this way the emitted infra-red laser beam wavelengths can be changed. The copper holder due to a good material temperature conductivity, transfers the heat to the collimating tubes and thus to the laser diodes. The temperature of the copper holder is monitored using 10k $\Omega$  thermistor (TH10K from Thorlabs, material MS97). The value of its resistance changing with the temperature is used as a feedback signal for the thermocontroller device that feeds the thermoelectric cooler with the current. The direction of the current flow and its value decides about the temperature of the cooler.

### 3.2.1.2 Nonlinear PP-KTP crystal

A flux grown PP-KTP (periodically poled KTiOPO<sub>4</sub>) crystal (Raicol Crystals Ltd.) has been chosen as the nonlinear media for SFG of 465 nm. The crystal used in the experiment is of 10 mm length (X-axis) and 1x2 mm (ZxY axes) on the cross-section. The nonlinear coefficient  $d_{33}$  for the Z-axis of the crystal (direction of the 1 mm long edge, optical axis of the crystal) has been specified between 11-15 pm/V ( $d_{QPM} = 7 - 9.5\text{pm/V}$ ). The crystal has no anti-reflection coating at any of input or output surfaces.

The crystal, mounted in copper holder has the temperature regulation (between 25 and 50 °C) using the elements as in case of the laser diodes (thermoelectric cooler TEC3-2.5, thermistor TH10K serving the feedback for separate thermocontroller device). Thermal control allows fulfilling the quasi-phase matching condition (eq.(3.6)) when the IR laser diodes wavelength is changed and thus generated sum frequency wavelength is tuned. The phasematching curve for a given wavelength is shown later on fig. (3.13a). The grating value at the room temperature (25°C) has been specified by the manufacturer to be  $\Lambda = 5.725\mu\text{m}$ .

### 3.2.2 Setup for SFG - construction scheme

According to the demands of SFG technique discussed in (3.1) the fundamental infra-red beams need to be spatially overlapped providing simultaneous interaction of two electric fields on the same volume of nonlinear crystal. It was also explained, that the fundamentals focusing in the center of the crystal increases the nonlinear conversion efficiency. Relying on these two conditions, the laser diodes and the crystal together with various optical elements as prisms, mirrors and filters (detailed description further in the text) are arranged as shown on the fig.(3.5).

The infra-red laser diodes LD1 and LD2 mounted in the copper holder, thermally controlled, emit collimated, elliptical shape (short axis in the horizontal plane - beam polarization direction), parallel beams at about 923 nm and 937 nm. The silver coated right angle prism mirror (AM, Thorlabs MRA10-P01, ~99% of reflectivity) together with the broadband dielectric mirror (M1, Thorlabs BB05-E03, >99% reflectivity) are used to decrease the distance between the two parallel beams to approximately 0.5 cm and tilt 937 nm beam by the angle of  $\sim 0.2^\circ$ . Thus, after 75 cm propagation, being reflected by the broadband dielectric mirrors (M1) and (M2) (of the same type as M1), two beams are entering the first of the three dispersive prisms at the angle of minimum deviation, maintaining  $0.2^\circ$  angular difference. The prisms (P1-3, Thorlabs PS851, apex angle  $60^\circ$ ) are made of SF11 glass for which the difference in refractive indexes for 923 and 937 nm light results in the different values of minimum angle of deviation for those wavelengths. Angular difference between the beams changes by  $0.064^\circ$  after passing single prism, so passing through the combination of three prisms allows removing the angular

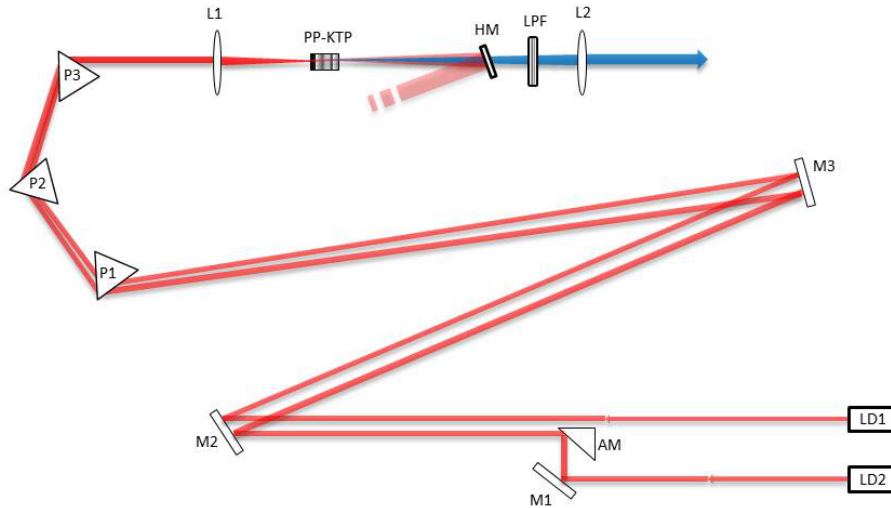


Figure 3.5: Laser set-up. LD1, 2: LD at 923.58, 937.6 nm; M: mirror; AM: angle mirror; P: prism; L: lens; HM: hot mirror; LPF: low pass filter. HM and LPF both filter out the 465 nm radiation. Detailed description in the text.

difference of  $0.2^\circ$  existing at the input of the set. As the consequence overlapped infra-red laser beams enter the PP-KTP crystal being focused by the lens with anti-reflection coating (F1) into the middle of the crystal. The crystal, mounted in the copper holder, is oriented in the way that the short (Z-axis) 1 mm edge is in the horizontal plane and the crystal input facet is perpendicular to the oncoming overlapped beams. In this way the polarization of the infra-red beams (also in horizontal plane) is in the direction of crystal Z-axis, what allows using the nonlinear coefficient  $d_{33}$ .

The fine position of the crystal around the lens focal point can be regulated with the use of XYZ-axis-translation stage to which the copper holder with the crystal is attached. At the output of the crystal, the two IR beams and generated sum-frequency are present and, as the 465 nm beam is relevant, the fundamentals are cut out: first more than 90% is reflected from the hot mirror (HM, Thorlabs FM01) and the remaining IR is stopped at the low pass-filter (LPF, Thorlabs FGB37). Both hot mirror and low pass filter weaken the blue beam by less than 10% and less than 15% respectively, according to the specification graphs published by the manufacturer. Outgoing, diverging beam is collimated by the anti-reflection coated lens (F2). All the setup elements placed on the aluminum raster breadboard  $30 \times 45 \text{ cm}^2$  are protected with the aluminum cover with the hole for the outgoing blue beam and the movable beam stopper. There are 6 BNC connectors: for laser diodes power supply as well as lasers and crystal temperature control and monitoring.

### 3.2.3 Laser output wavelength tuning

The change of laser diodes temperature results in the change of emitted infra-red laser beams wavelengths and thus the wavelength of generated harmonic according to eq.(3.6), the definition of eq.(3.20) and its role in the Boyd-Kleinman focusing parameter. To maintain the quasi-phase-matching condition, the crystal temperature has to be changed when the generated blue wavelength is changed if the maximum available power is needed. Given in subsection 3.2.1.1

$d\lambda/dI$  coefficient informs, that, independently of the laser diodes temperature, the blue wavelength can be tuned by changing the feeding current of one or both the laser diodes. The loose of power due to the quasi-phaseshatching condition can be also compensated by regulation of the crystal temperature, in contrast to the power drop caused by the current decrease. For the need of the experiment the voltage control of the feeding current was applied providing continuity and monotony (with possibility of rate control) of the current/wavelength change as well as reproducibility of the wavelength sweep on condition that the driving voltage amplitude and speed change remains constant from one measurement to another.

For the purpose of absorption line positions determination and thus the laser setup wavelength calibration, as well as for accurate recording of the line profiles (with the emphasis on the line height, width and general shape - fine structure of the line - see section 4.3) both laser wavelength tuning methods were used. First, rough position of the absorption line center was found with the laser diodes temperature tuning and crystal matching. For the fixed temperature settings, the recording of the absorption line profile was made using the 937 nm laser diode current sweep with external voltage (see 3.6) where measured infra-red emitted wavelength change in terms of the voltage driving the current change has been shown together with the fitted slope of the linear dependency.

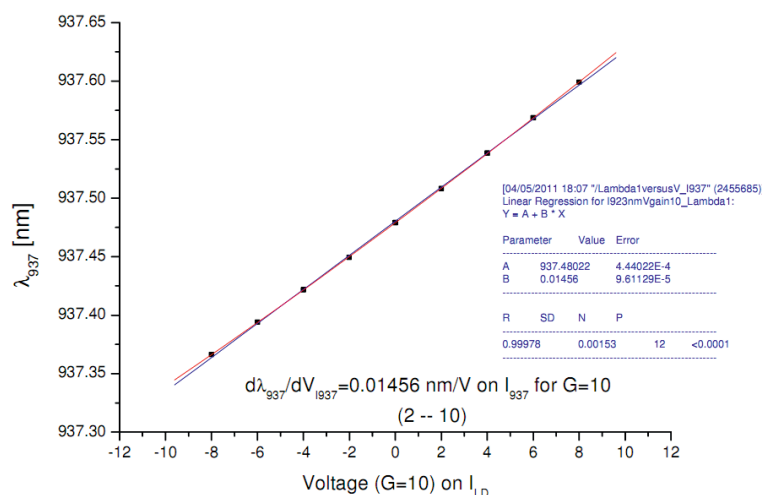


Figure 3.6: Change of the laser diode wavelength (LD 937 nm) with the voltage controlled diode current. G=10 indicates the voltage controller setting range.

Overall dependency of the laser diodes wavelength tuning by the feeding current within 140 to 170 mA has been measured and is presented on the Fig.3.7

Frequency scans were performed using the laser diodes temperature fine regulation also with the driving voltage control resulted in higher hysteresis (when the temperature driving voltage was on positive and negative slope) both in the recorded line position and the shape than it was observed for current tuning. The problems may be caused by too high thermal inertia of the holding copper construction of the laser diodes that was thermally stabilized by thermoelectric element as well as the response time of the thermistor and the feedback loop of

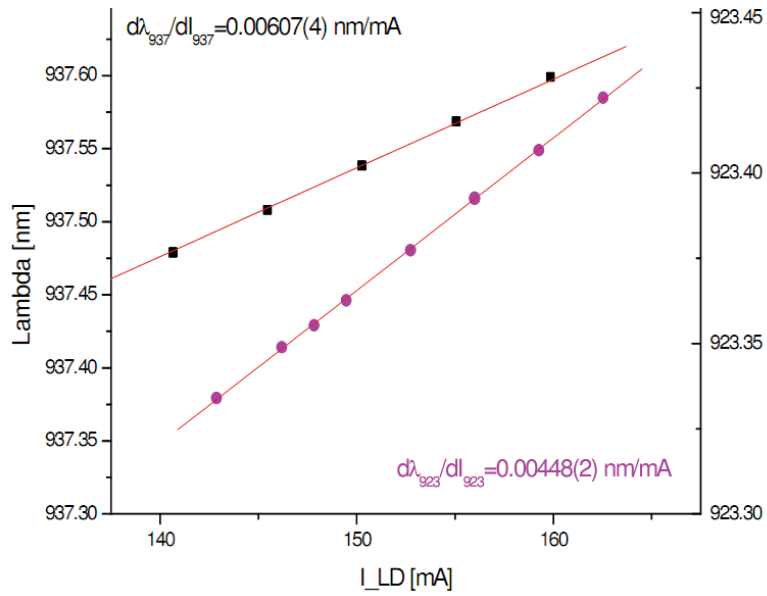


Figure 3.7: Infra red laser diodes change wavelength with the feeding current tuning within 140 to 170 mA.

the thermocontroller. For more details about the methodology of the profiles measurement the Reader is sent to 4.1.2.

## 3.3 Laser performance - experimental results

### 3.3.1 Output power and efficiency

The laser setup described in subsection (3.2.1) and (3.2.2) is generating up to  $P_b = 229 \pm 10 \mu\text{W}$  of blue light power at the output of the crystal, which is weakened by the both hot mirror (HM) and the low pass filter (LPF) to about  $175 \pm 1 \mu\text{W}$ , while the input power of the IR light from the laser diodes are  $P_{923} = 75.4 \pm 0.1 \text{ mW}$  and  $P_{937} = 80.4 \pm 0.1 \text{ mW}$  for 923 nm and 937 nm respectively. The value of efficiency has to be however calculated with the use of  $P_b$  as this comes out from the crystal, thus giving the efficiency value of  $\eta = (3.8 \pm 0.2)\% \text{W}^{-1}$ . The errors of both values are the resultant of the power measurement accuracy. Experimental value is close to the predicted one in terms of SHG approximation of SFG theory given in subsection 3.1.1 ( $\eta_{calc}$ ) and is higher than the values of SHG efficiency of  $2.8 \% \text{W}^{-1} \text{cm}^{-1}$  at 461 nm reported in [40] and SFG efficiency of  $2.2 \% \text{W}^{-1} \text{cm}^{-1}$  at 492 nm given in [41]. Elliptical shape of fundamental beams is in contrast with circular profiles met in the references, what can affect the final value of our conversion efficiency in comparison to the situation with the Gaussian beams, however it was not the purpose of this work to study in detail the SFG process and influence of spatial beam profile on efficiency. For detailed informations the Reader is sent to [75] - [77].

Actually, using the IR waist value  $w_0$  inferred from the focusing parameter  $\xi$  obtained from the fit of measured matching tolerances (see section 3.3.3) is:

$$w_0 = \sqrt{\frac{2\pi\xi n_{av}}{l\lambda_{av}}} = 16.4 \pm \check{E} \mu\text{m}$$

The efficiency value allows calculation of  $d_{eff}$  and  $d_{33}$  (related with (3.8c)) for our pp-KTP crystal.  $d_{eff} = \sqrt{\frac{\eta_{SHG} \epsilon_0 c n_{av} n_b \lambda_{av}^3}{16\pi^2 d_{eff}^2 l h(\sigma, \xi)}} = 11.0 \pm 0.5 \text{ pm/V} \rightarrow d_{33} = 17.2 \text{ pm/V}$ .

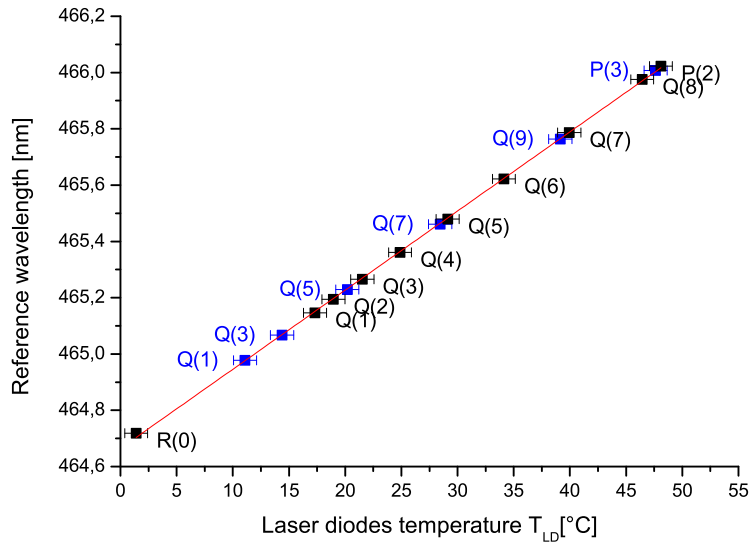
### 3.3.2 Tuning range and matching conditions

#### 3.3.2.1 Laser wavelength calibration

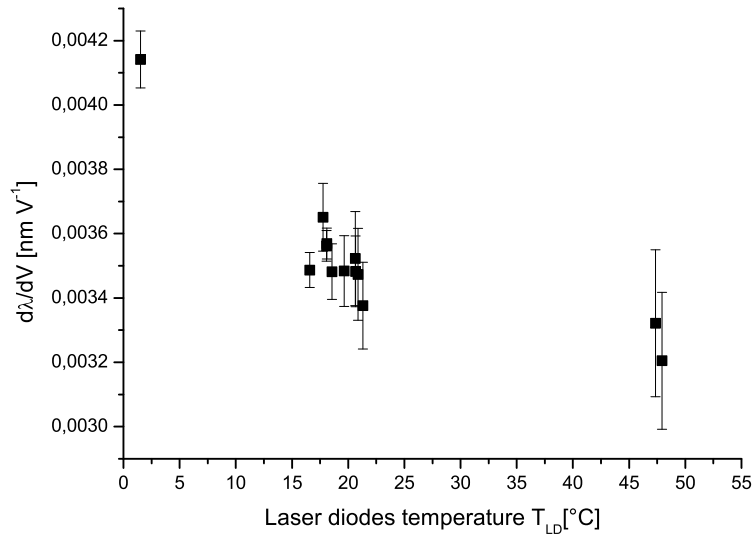
The precise absolute wavelength calibration of the temperature settings of the laser diodes and the crystal relies on the recorded positions of the molecular absorption lines. The positions in wavelength scale are well known for both isotopic molecules  $^3\text{He}_2^*$  [6] and  $^4\text{He}_2^*$  [28]. Within the operating temperature range of the laser diodes and the crystal 10 absorption lines of  $^3\text{He}_2^*$  (Q(1)-Q(8), P(2) and R(0)) and 6 of  $^4\text{He}_2^*$  (Q(1)-Q(9), P(3)) are present. Comparison of the relative lines separations in reference data and recorded positions, together with characteristic line intensities alternation for  $^3\text{He}_2^*$ , allows identification of the experimental transitions in registered spectrum (see fig. (4.21)). The relation between laser diodes temperature settings, corrected for the value of accurate line top peak position from laser diodes current sweep and the absorption lines wavelength positions, on which basis the laser calibration relies, is shown on the graph 3.8a.

The linear fit ( $\lambda = a * T_{LD} + b$ ) to the points presented on the fig. (3.8a) (red curve) provides the parameters of LD temperature - wavelength absolute calibration:  $a = 0.0281 \pm 0.0005 \text{ nm}/^\circ\text{C}$ ,  $b = 464.66 \pm 0.02 \text{ nm}$ .

For the wavelength change through the voltage  $V$  controlled 937 nm laser diode feeding current regulation,  $\frac{d\lambda}{dV}$  coefficient was determined. For this purpose the presence of well sep-



(a)



(b)

Figure 3.8: (a) The relation between the wavelength of absorption line maximum and corresponding laser diodes temperature on which the emitted blue light wavelength calibration relies. Black squares represents the lines recorded for  ${}^3\text{He}_2^*$ , blue squares - lines recorded for  ${}^4\text{He}_2^*$ . Designation of recognized molecular transitions are given next to the points written with the proper font color. The red line represents the linear fit - the calibration curve. Error bars on the points for temperature values comes from the accuracy of the line maximum position determination (including error caused by hysteresis effect) and the accuracy of the temperature measurement with the thermistor ( $\pm 1^\circ\text{C}$ ). (b) The wavelength-LD current driving voltage control coefficient  $\frac{d\lambda}{dV}$  in laser diodes temperature tuning range. The decay with the  $T_{LD}$  increase is visible, however the lack of enough number of points beyond  $16\text{-}21^\circ\text{C}$  makes finding meaningful functional expression difficult. Errors are the resultant of the accuracy of absorption lines maxima position determination

arated multiple (2 or 3) absorption lines within peak to peak voltage amplitude value of 20 V ( $\pm 10$  V) was used for several different laser diodes temperatures. In range of  $T_{LD} = 16-21$  °C several sets of peaks are present, especially those of isotopic pure isotopologues of the molecule (Q(1)-Q(5)), providing approximately constant within the error bars (see fig. (3.8b)) value of  $\frac{d\lambda}{dV} = (3.52 \pm 0.01) \cdot 10^{-3} \text{ nmV}^{-1}$ .

Any departure from the QPM condition results in decrease of the conversion efficiency and lowers the emitted blue beam power while fundamental beams power is maintained constant. This effect can be observed on the graph (3.13a) showing the matching curve for the crystal - the change of measured output power in terms of the regulated crystal temperature. It is a peak curve with the maximum for the temperature providing  $\Lambda$  required in  $\Delta k = 0$  condition.

### 3.3.2.2 Matching conditions

The infra-red laser diodes wavelength is controlled mainly by its temperature (fine control is made with the change of the LD current, however only in the local range of about 0.07 nm). The main constraint on the available range of the infra red beams is the specified working-temperature - that in the room conditions does not allow to go lower than 0°C when the water vapor condensates on the lens (air blowing system could be used to prevent this) as well as overheating the diodes from the other side of temperature scale is not advisable due to the shortening the life of the diodes.

The wavelengths generated by each of the diodes in the 10-40°C temperature range has been measured and presented on the graph 3.9

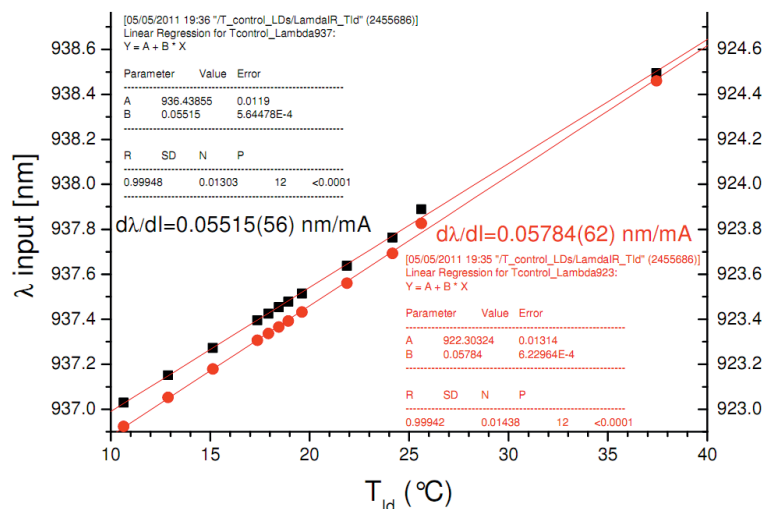


Figure 3.9: Wavelengths generated by the infra-red laser diodes in terms of their temperature  $T_{LD}$  within 10-40°C range.

Analogous constraint on the crystal matching temperature is given, however mainly refers to the upper temperature bound - crystal should not be overheated so that its structure could be damaged irreversibly. Within the both laser diodes and crystal temperature range the points that provides quasi-phase-matching condition according to equation (3.15) has been shown on the Fig.3.10.

According to the curve and the parameters of the fitted linear function on the calibration graph Fig.3.8a  $T_{cr}$  in function of the emitted blue wavelength  $\lambda_b$  can be given as well - Fig.3.11.

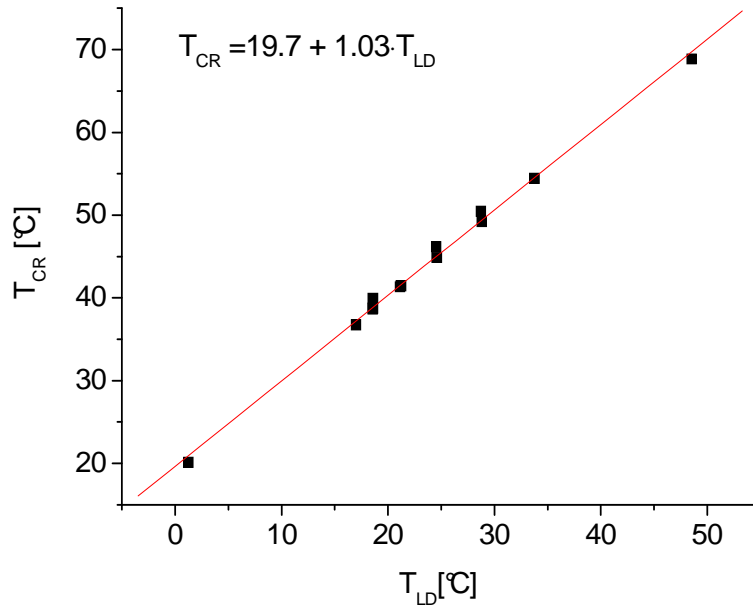


Figure 3.10: Crystal and laser diodes temperature matching points fulfilling quasi-phase matching condition within available tuning range of both temperatures.

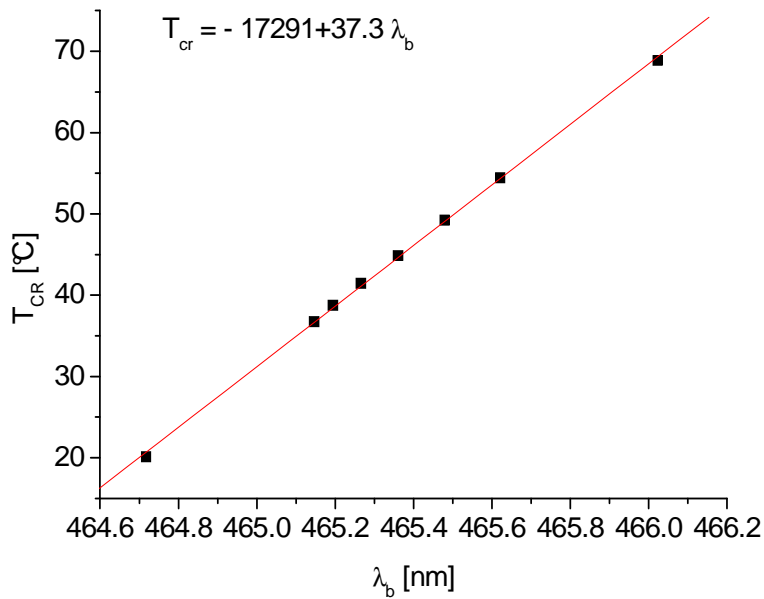


Figure 3.11: Matching line of the crystal temperature in function of generated blue wavelength -  $\lambda_b$

Using the definition of (3.6) one see, that for SHG process the phase matching depends only on the  $\lambda_{av}$  and the difference in the refractive indexes for the fundamental and generated wavelength. Knowing, from the linear function fits (Fig.3.9), the relations between  $T_{LD}$  and each of infra-red wavelengths  $\lambda_1$  and  $\lambda_2$  are set, so that the  $\lambda_{av}$  is known. From the other hand, the relation between the crystal and the laser diodes temperatures that provide the matching conditions also has been set (Fig.3.10) so that  $\lambda_{av}$  in function of  $T_{cr}$  is known as well together with  $\lambda_b$  relation to  $T_{cr}$  (3.11). The refractive indexes, according to the appendix B, can be

calculated for  $\lambda_{av}$  and  $\lambda_b$  in known crystal temperature conditions. Thus, the plot of the values of  $\frac{\Delta k_{QPM}^{SHG}}{2\pi}$  in function of  $\lambda_{av}$  has been made 3.12.

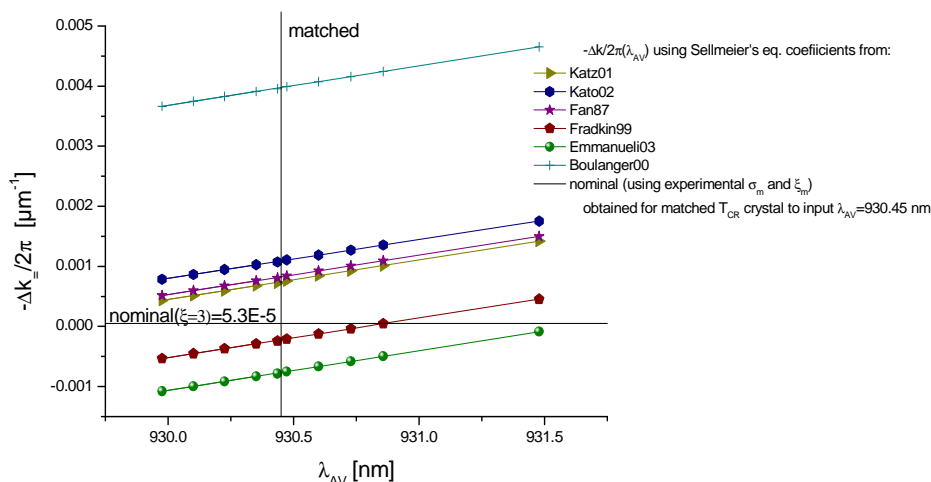


Figure 3.12: Quasi-phase matching condition fulfilled at the various wavelengths of fundamental infra-red beams  $\lambda_{av}$ . Several slopes are present due to discrepancies in the coefficients of the Sellmeier's equation met in the references. The matching wavelength related to the  $\lambda_{av}$  used when the tolerance curves were measured (subsection 3.3.3) and the crystal temperature matched to this wavelength.

Figure 3.12 shows that estimated value of  $\frac{\Delta k_{QPM}^{SHG}}{2\pi}$  using the  $\xi$  parameter from the subsection 3.3.3 is in line with expectations from the calculations performed basing on the crystal and laser diodes temperatures hence the wavelengths, especially that there is scatter  $\pm 0.001$  in  $\frac{\Delta k_{QPM}^{SHG}}{2\pi}$  value due to the discrepancies in Sellmeier's coefficients met in the references [73] - [71]. Author, however, does not conclude about the reliability of these references in terms of the closest agreement with his results, as it was not the purpose of this measurements. The main goal was to check the consistency of the results shown in subsection 3.3.3 and given in this subsection the matching relations of the crystal temperature and infra-red wavelength (for the ranges explored during later experiments on the molecule).

### (a) Matching line slope experimental determination

Recalling the first and the second terms of the right side of the equation eq.(3.17)

$$2 \frac{l}{\lambda_{av}} \left[ \left. \frac{\partial n}{\partial T_{cr}} \right|_{T_{cr}, \lambda_{av}/2} - \left. \frac{\partial n}{\partial T_{cr}} \right|_{T_{cr}, \lambda_{av}} \right] + 2\alpha \frac{l}{\lambda_{av}} \left( n_b(T_{cr}, \lambda_{av}/2) - n_{av}(T_{cr}, \lambda_{av}) \right)$$

The equation for the matching line (3.19) puts a strict constraint on the values of the experimental parameters  $T_{cr}$  and  $T_{ld}$  for which matching is actually achieved. They must satisfy:

$$\left. \frac{dT_{cr}}{dT_{ld}} \right|_{QPM} = \left. \frac{dT_{cr}}{d\lambda_{av}} \right|_{QPM} \frac{d\lambda_{av}}{dT_{ld}} \quad (3.22)$$

$\left. \frac{dT_{cr}}{d\lambda_{av}} \right|_{QPM}$  is given by (3.19).

The experimental value of the derivative  $\frac{d\lambda_{av}}{dT_{ld}}$  is obtained from the measurements of the infrared wavelengths  $\lambda_1$  and  $\lambda_2$  with the high resolution spectrometer (Fig.3.9):  $\frac{d\lambda_{av}}{dT_{ld}} = 0.056510^{-3}$  nm/°C.

The expected value of the coefficient  $\left. \frac{dT_{cr}}{d\lambda_{av}} \right|_{QPM}$  is obtained from the known values of the KTP bulk properties using equation (3.15), as follows:

$$\left. \frac{dT_{cr}}{d\lambda_{av}} \right|_{QPM} = \frac{-\frac{\partial}{\partial \lambda_{av}} \left[ \frac{\Delta kl}{2\pi} \right]}{\frac{\partial}{\partial T_{cr}} \frac{\Delta kl}{2\pi}}$$

The temperature derivative  $\frac{\partial}{\partial T_{cr}} \frac{\Delta kl}{2\pi}$  is given by eq.(3.17). Its first term on the right side of equation equal:

$$2 \frac{l}{\lambda_{av}} \left[ \left. \frac{\partial n}{\partial T_{cr}} \right|_{T_{cr}, \lambda_{av}/2} - \left. \frac{\partial n}{\partial T_{cr}} \right|_{T_{cr}, \lambda_{av}} \right] = 2.15 \cdot 10^4 \left( \left. \frac{\partial n}{\partial T_{cr}} \right|_{T_{cr}, \lambda_{av}/2} - \left. \frac{\partial n}{\partial T_{cr}} \right|_{T_{cr}, \lambda_{av}} \right) \approx$$

$$\approx 2.15 \cdot 10^4 \cdot 1.6 \cdot 10^{-5} = 0.344^\circ\text{C}^{-1}$$

The last term is negligible given  $\alpha = 0.6 - 1110^{-6} \text{ }^\circ\text{C}^{-1}$  [80],  $n(465\text{nm}) - n(930\text{nm}T) = 0.08$  and  $\frac{2L}{\lambda_{av}=2.1510^4}$ , which gives a value in the  $(0.6 - 11) * 1.72 \cdot 10^{-3} \text{ }^\circ\text{C}^{-1}$  range.

Therefore, the value of the derivative is:

$$\frac{\partial}{\partial T_{cr}} \frac{\Delta kl}{2\pi} = 0.344 \text{ }^\circ\text{C}^{-1}.$$

The wavelength derivative  $\frac{\partial}{\partial \lambda_{av}} \left( \frac{\Delta kl}{2\pi} \right) = \frac{\partial}{\partial \lambda_{av}} \left( l \left( \frac{\Delta k_0}{2\pi} - \frac{1}{\Lambda} \right) \right)$  is given by eq.(3.18)

$$\text{With: } \frac{\partial n}{\partial \lambda_{b=465\text{nm}}} = -0.548 \mu\text{m}^{-1}, \frac{\partial n}{\partial \lambda_{av=930\text{nm}}} = -0.055 \mu\text{m}^{-1}$$

$$\text{and } \frac{1}{\lambda_{av}} (n_b(T_{cr}, \lambda_{av}/2) - n_{av}(T_{cr}, \lambda_{av})) = \frac{1}{2} \frac{\Delta k_0}{2\pi} \approx \frac{1}{2\Lambda} = 9.96 \cdot 10^{-2} \mu\text{m}^{-1}.$$

The derivative is thus equal to:

$$\frac{\partial}{\partial \lambda_{av}} \left( \frac{\Delta kl}{2\pi} \right) = 2 \cdot 1.075 \cdot 10^4 \cdot (-0.319 \mu\text{m} - 1) = -6.85 \cdot 10^3 \mu\text{m}^{-1}$$

Finally, over the small tuning range of the laser, the matching line is a straight line with slope:  $\frac{dT_{cr}}{dT_{ld}} = -\left( \frac{-6.8510^3 \mu\text{m}^{-1}}{0.344^\circ\text{C}^{-1}} \right) * 0.0565 \cdot 10^{-3} \text{ nm}/^\circ\text{C} = 1.12$

Calculated value is in agreement within 6% with experimental 1.03 value given on the fig.3.10.

### 3.3.3 Matching tolerances in the experiment

Important in terms of using the blue laser beam for the absorption measurements, especially for obtaining the full absorption line profiles, is the dependency of the output power on the laser diodes temperature tuning, what translates into the wavelength tuning of fundamental beams and therefore the emitted harmonic. The dependency of emitted blue power versus the laser diodes temperature, presented on the fig.(3.13b), is similar to the fig.3.13a - case of the crystal

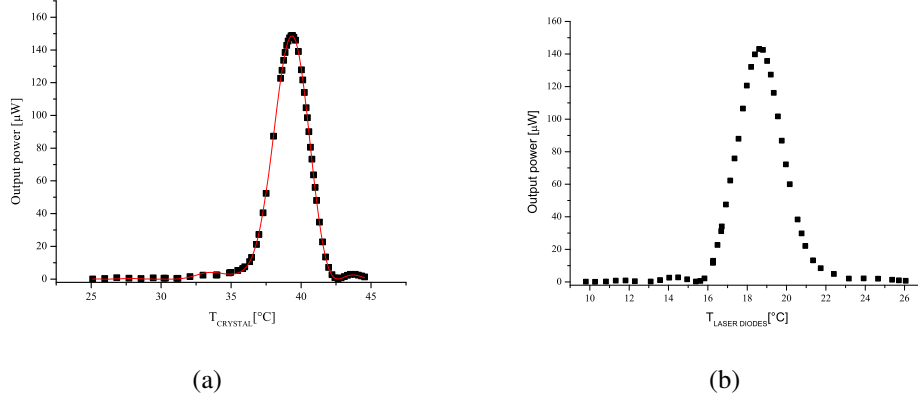


Figure 3.13: The crystal (a) and laser diodes (b) quasi-phasematching curves - the output laser power versus the temperature of crystal and laser diode respectively. The laser diodes temperature for the top peak value corresponds to the temperature setting of  ${}^3\text{He}_2^*$  Q(2) line with the crystal temperature fulfilling the quasi-phase matching condition

matching. The acceptance bandwidth of  $\Delta T_{ld} = 2.7 \pm \dots$  °C for laser diode tuning and  $\Delta T_{cr} = 2.94 \pm \dots$  °C.

These curves (3.13b and 3.13a) are the experimental curves of those shown on the fig.3.1 in which the value of  $\sigma$  has been changed by  $\lambda_{av}$  or  $T_{cr}$  regulation, according to the relation (3.20) with  $X = \lambda_{av}$  or  $X = T_{cr}$  respectively. It is thus possible to perform the function fit of the output power given by the equation (3.8a). Writing it as  $P_b = Ah(\sigma, \xi)$ , where

$A = \frac{P_b}{P_{av}^2} = \frac{16\pi^2 d_{eff}^2}{\epsilon_0 c n_{av} n_b \lambda_{av}^3} P_{av}^2$  as well as having the relation (3.10) one obtains:

$$P_b = A\xi I(\sigma, \xi)^2 \quad (3.23)$$

where

$$I(\sigma, \xi) = \int_0^1 \frac{\cos(\sigma\xi u) + \xi u \sin(\sigma\xi u)}{1 + (\xi u)^2} du \quad (3.24)$$

As it was shown in the 3.1.1, it is worth considering the square root of the harmonic power, as the function is then sensitive to the side lobes, so that the function as:

$$\sqrt{P} = \sqrt{A} \sqrt{\xi} \cdot |I(\sigma, \xi)|, \quad (3.25)$$

with  $\sigma$  taken as:  $\sigma(X) = \sigma(X_0) + \left[ \frac{\partial \sigma}{\partial X} \right]_{X_0} (X - X_0)$  with  $X_0 = T_{LD}$   $X_0 = T_{cr}$  depending on the fitted curve.

The results of the fit are presented on the graphs 3.14 for laser diodes matching and 3.15 for crystal temperature matching. The fits both in  $\sqrt{P_b}$  as well as, for clarity in  $P_b$  has been presented.

The fitted value  $\xi = 3.0$  is close to the optimal value  $\xi_m = 2.84$ . This yields a phase-matched value of the Boyd function (obtained for  $\sigma_m = 0.556$ ) equal to  $h(\sigma_m, \xi_m) = 1.0677$  versus 1.06767 theoretical optimum - only 0.1 % lower than predicted for the most optimal case.

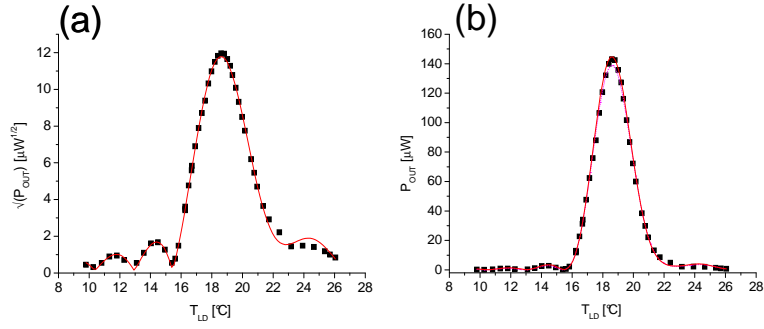


Figure 3.14: Fit of the dependency of the output blue power  $\sqrt{P_b}$  and  $P_b$  (b) on the laser diode temperature according to the eq.(3.25)

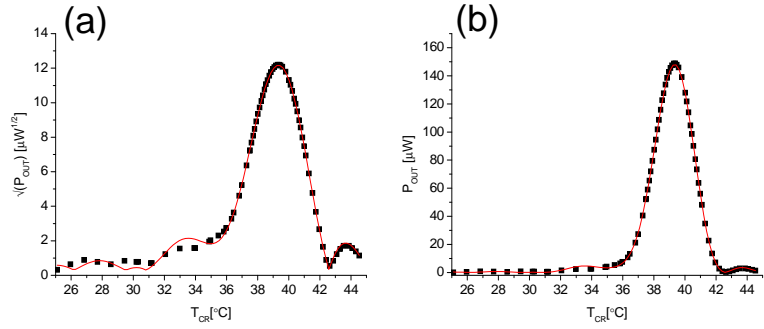


Figure 3.15: Fit of the dependency of the blue power  $\sqrt{P_b}$  (a) and  $P_b$  (b) on the crystal temperature according to the eq.(3.25)

Parameter	$T_{LD}$ matching	$T_{cr}$ matching
A	$126 \pm 3$	$132 \pm 1$
$\xi$	$2.93 \pm 0.09$	$3.06 \pm 0.05$
$\sigma_0$	$0.59 \pm 0.03$	$0.528 \pm 0.005$
$\frac{\partial \sigma}{\partial X} _{X_0}$	$0.42 \pm 0.01$	$-0.385 \pm 0.005$

Table 3.3: Results of the  $\sqrt{P_b}$  fit performed to the experimental data of  $T_{LD}$  and  $T_{cr}$  matching curves.

The focusing parameter  $\xi$  provides a measure of the ir waist inside the crystal,  $w_0 = \sqrt{\left(\frac{l\lambda_{av}}{2\pi n_{av}\xi}\right)} = 16.4\mu m$ .

This, with the focal length of  $f=75$  mm of the lens used to focus infra red beams into the crystal gives the input waist of the beam in FWHM:  $w_{in} = \frac{f\lambda_{av}}{2w_0} = \cdot \pm \cdot \mu m$ , hence a FWHM of the input of incident beam is  $a = \cdot$  with  $\cdot\%$  ellipticity.

$\xi = 3.0$  also yields  $\sigma_m = 0.5556$ , what agrees with averaged fit parameter  $\sigma_0 \geq 0.568 \pm 0.04$  as well as  $\Delta\sigma_{1/2} = 1.1299$  used below for tolerance checks based on known PP-KTP dispersion and laser diodes features.

### (b) Further results - consistency check of the $\sqrt{P_b}$ fits

The fit of experimental data for tolerance curves provides adjusted values of parameter

$f_\sigma = [\frac{\partial \sigma}{\partial X}]|_{X_0}$  that must agree with measured acceptance FWHMs. Equation (3.21) reads:

$$\Delta X_{1/2} = \frac{\Delta \sigma_{1/2}(\xi = 3)}{[\frac{\partial \sigma}{\partial X}]|_{X_0}} = \Delta \sigma_{1/2}(\xi = 3) f_\sigma, \quad (3.26)$$

so that the FWHM should be equal in our experimental conditions to:

$\Delta X_{1/2} = \frac{1.1299}{f_\sigma}$ . In simulations presented in the subsection 3.1.1  $f_\sigma$  has been assumed to equal 1, and the exact value of  $\Delta \sigma_{1/2} = 1.12987$  has been obtained (given in the 3.1 as 1.13). This well agreement encourages to extract both  $\Delta T_{cr}$  and  $\Delta T_{LD}$  values and compare with those measured from the figures 3.13b and 3.13a. So that:

- For  $X = T_{cr}$   
Experimental  $\Delta T_{cr} = 2.94^\circ\text{C}$  FWHM.  
According to the table 3.3  $|f_\sigma| = 0.385 \pm 0.005$  so that  $\Delta T_{cr} = 1.1299/0.385 = 2.935^\circ\text{C}$
- For  $X = T_{LD}$   
Experimental  $\Delta T_{LD} = 2.70^\circ\text{C}$  FWHM.  
According to the table 3.3  $|f_\sigma| = 0.42 \pm 0.01$  and so  $\Delta T_{cr} = 1.1299/0.42 = 2.69^\circ\text{C}$

Perfect agreement between the experiment and calculation has been obtained.

## 3.4 Conclusions

The laser setup based on the Sum Frequency Generation Process has been built and characterized in terms of its efficiency and working parameters. It provides the desired wavelength of about 465 nm in the range of 464.7 to 466.1 nm, that is the band-head of  $a^3\Sigma_u^+(0) - e^3\Pi_g(0)$  transition for helium molecular species  $\text{He}_2^*$  for its three isotopologues  $^4\text{He}_2^*$ ,  $^3\text{He}_2^*$  and  $(^3\text{He}-^4\text{He})^*$ . The tuning range is sufficient for observation of main rotational transitions of the dimer (see observed spectrum Fig.4.21). Emitted power above  $200 \mu\text{W}$  is more than sufficient to perform absorption measurement on molecular helium species with good SNR. Achieved conversion efficiency  $\eta = 3.8\% \text{W}^{-1}$  of the SFG process reaches almost optimum value determined from the theory of nonlinear conversion approximating SFG with the SHG process - legitimate at close enough (14 nm difference) fundamental wavelengths. In these considerations similar derivations of tolerances and matching has been made as for example in [81] and [82] carried out in the loose focusing limit where response to variations of matching parameters scales as  $\text{sinc}^2(\Delta kl/2)$ , hence  $\text{FWHM}(\Delta kL/2)_{1/2} = 2 \cdot 0.4429 \cdot \pi = 2.783$  - here  $\text{FWHM}(\Delta kL/2)_{1/2} = 3.390 \Rightarrow$  fit or a priori knowledge of focusing parameter  $\xi$  needed to quantitatively account for the experimentally tolerances. Overall the performed calculations and expectations stay in agreement with experimental measurements results and fitting procedure. Behavior is in line with expectations for single-pass SHG in PP-KTP, for quasi-optimal optical configuration. The output power, however, sufficient for the measurements in this work, can be increased by introducing several cavity modifications, e.g. multiple pass of the fundamental beams through the crystal achieved inside the resonator cavity. Additionally laser control, currently 100% manual, can be automatized, especially if it comes to the matching of the crystal temperature to the change of fundamental wavelength (change of the laser diodes temperature). One could also think about extending the wavelength tuning range, for example by cooling down the laser diodes less than  $0^\circ\text{C}$ , providing the air blowing onto the lenses not to allow the water vapor

condensation. Going into higher temperature regimes one has to remember about the diodes life shortening then.

## Chapter 4

# Absorption measurements on helium molecule - experimental results

In this chapter the results of absorption measurements performed on helium molecules in metastable  $a^3\Sigma_u^+$  state of  $^3\text{He}_2^*$ ,  $^4\text{He}_2^*$  as well as  $(^3\text{He}-^4\text{He})^*$  are presented with use of the 465 nm laser described in 3. The measurements were performed in sealed pyrex cells usually used for MEOP tests, filled with the gas (isotopic pure or mixture) at different pressures ranging from 8 to 267 mbar. The series of experiments was begun with absorption lines profiles recording from which their position in terms of laser diodes temperature settings was inferred, thus allowing the blue laser wavelength calibration. Using the mass scaling laws for vibrational and rotational constants between molecular isotopologues, heteronuclear dimer wavelength positions were calculated and confirmed by the experiment as well as by [46]. The intensities of the absorption lines were used to rotational temperature determination according to eq. (2.51).

### 4.1 Experimental setup

The experimental setup is a basic configuration of the probe laser beam coming out from the blue laser setup (chapter 3) transmission through the absorber - plasma inside the OP cell (fig.4.1).

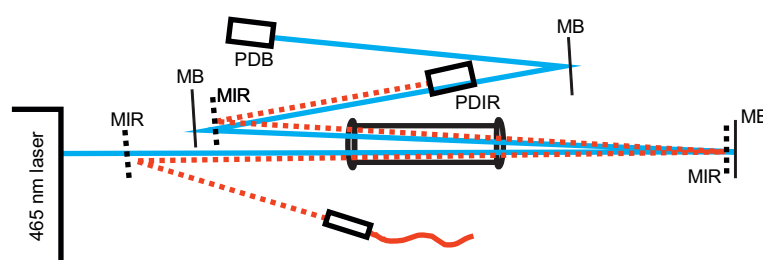


Figure 4.1: Optical setup scheme for absorption measurements on molecules (with use of 465 nm laser) and atoms (with use of 1083 nm laser). The measurements on both species has to be performed independently as it is required to put the optical elements suitable for 1083 nm (red dashed line - IR beam path, black dashed lines - MIR metallic mirrors and PDIR - photodiode for infra-red wavelength) on the way of blue beam (solid blue line - beam path, solid black line - MB - mirrors and PDV - photodiode for visible wavelengths).

The blue beam passes the cell volume twice along its length at small angle in respect to the cylindrical symmetry axis of the cell. The beam is reflected by the MB mirrors - suitable for the visible wavelengths and its power is being measured by the photodiode (PDB) chosen for its sensitivity in the blue region. Double pass of the beam through the rf plasma filling the cell volume provides increased absorption signal in comparison to single pass, while elongating the beam path after the second pass in the cell by reflection on two MB mirrors reduces the amount of a stray light - fluorescent light from the discharge plasma entering PDB. As a complementary measurements the transmission of the IR probe beam through the same OP cell and plasma conditions can be investigated by simply putting the MIR - metallic mirrors of good reflectivity at 1083 nm in front of MB mirrors. The IR probe beam, delivered to the optical table by the fiber is send to the OP cell on similar path as in case of the blue light, and its power is measured by the photodiode PDIR suitable for this wavelength. The presence of the IR beam was mainly used for comparison between the absorption rates between atoms and molecules in the same pressure and plasma conditions, as well as to compare the dynamics of the density decay of both species when the rf excitation is turned off.

Depending on the purpose of the experiment - molecular absorption measurements with blue laser frequency scans or investigations on the density decay rates two different experiment schemes can be distinguished and will be described in following subsections.

#### 4.1.1 Laser frequency scan acquisition scheme

The acquisition and setup control scheme for the realization of frequency scan absorption measurements with use of the 465 nm laser setup is presented on the fig.4.2.

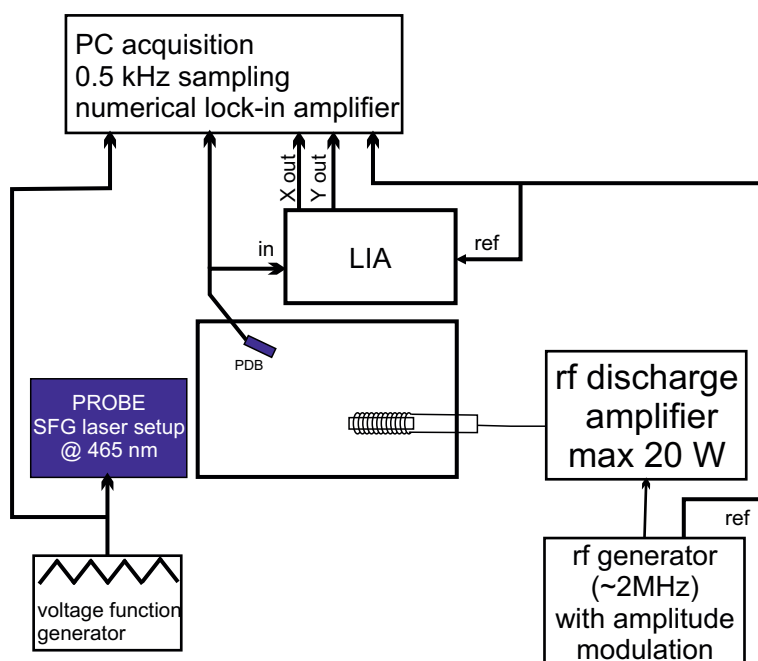


Figure 4.2: Scheme of the acquisition setup for the absorption frequency scans using voltage (triangle course of the  $V(t)$  function) control of 937 nm laser diode current supply being a component of the blue laser setup.

The transmitted power of blue laser beam through the OP cell is measured by the photodiode PDB and the output signal is sent to the input of the lock-in amplifier (LIA) as well as the PC acquisition card. Lock-in detection has been applied together with the rf voltage discharge excitation amplitude modulation, so that the distinction between plasma response to the laser absorption and power fluctuations of the light source can be performed increasing the SNR. 100% of square or partial (up to about 20%) sine amplitude modulation at frequency of a few tens Hz was provided by the voltage generator of which TTL modulation reference signal was sent to the lock-in amplifier and to the PC acquisition card. The rf voltage was then amplified by 20 W power amplifier and sent to the transformer circuit and then to the wire electrodes wound on the OP cell with alternating polarity. The output signals from X and Y (in-phase and quadrature components) channels are sent to the PC acquisition card. The wavelength emitted by the blue laser setup was controlled by the voltage function generator delivering periodical triangle signal to the 937 nm laser diode power supply causing the linear response in the feeding current of the diode, thus allowing emitted infra red wavelength change what results in change of blue laser wavelength as well. The triangle signal has been recorded during the frequency scan measurements.

#### 4.1.2 Frequency scans recordings procedure

The blue laser frequency scans were performed to obtain full absorption line profiles for available by the laser tuning range part of the molecular spectrum for three isotopologues of  $\text{He}_2^*$ . In case of the homonuclear molecules single line profiles scans were performed, while for the heteronuclear isotopologue triplets and even quartets of the absorption lines were present on the single scan. The main restriction in the frequency range value that could be reached in a single scan lies in the departure from the phase matching condition as well as in the drop of the 937 nm lasing power when the feeding current value is being lowered - increase of the current above the maximum specified by the manufacturer also had to be avoided. In fact, the scans within the wavelength range of about 0.07 nm can be performed corresponding to  $\pm 10$  V peak-to-peak amplitude of triangle voltage signal. Usually, however, the voltage amplitude  $\pm 5$  and  $\pm 10$  V were used, depending on the presence of multiple neighboring lines within about 0.07 nm range (helium isotopic mixture cell) or intention of recording full single line profile with long recording of the baseline level for accurate peak height and shape determination. The period of the triangle voltage was set to 0.001 Hz and 0.0005 Hz for short ( $\pm 5$  V) and long ( $\pm 10$  V) scans of which the duration was set to 12.5 and 25 minutes providing equal speed of the voltage driven current change of the laser diode. The acquisition was performed with the 500 Hz frequency.

Before each frequency scan of the single line profile the blue laser was roughly tuned (by the change of the laser diodes and crystal temperature) to the maximum of the chosen absorption line with help of the lock-in amplifier present in the acquisition scheme. In case of the scans of the multiple neighboring lines the blue laser wavelength was roughly set in between the two extreme lines positions. During the frequency scan the laser diodes temperatures as well as crystal's were not changed. As it has been shown on the fig. 3.8b (subsection 3.3.2.1) the linear wavelength change in function of the voltage changes the slope with the laser diodes temperature, what has been taken into account when the transformation between internal voltage scan scale to more appropriate in further considerations GHz or nm units has been performed.

### 4.1.3 Density decay rates experiment description

To compare the atomic and molecular dynamics the laser transmission change recordings after the source of the rf excitation is turned off has been performed. In this experiments the laser had to be constantly tuned to the maximum of chosen absorption line - for the helium atoms the infra-red laser was tuned to the  $C_8$  transition for  $^3\text{He}^*$  and  $D_0$  for  $^4\text{He}^*$ . In the mixture cell measurements on the atoms, the  $C_{6-7}$  line had to be chosen because both  $C_8$  and  $C_9$  overlaps with  $D_{1-2}$  lines (see Fig.5.1). For the molecules, depending on the isotopologue:  $^3\text{He}_2^* - Q(2)$ ,  $^4\text{He}_2^* - Q(3)$ ,  $(^3\text{He}-^4\text{He})^* - Q(3)$  - as those lines provide the highest SNR of all in the available spectra parts for each isotopologue. The tuning of the blue laser wavelength to the line maximum was performed relying on the lock-in displayed demodulated signal of absorption. Basically the setup configuration shown on the fig.4.1 has been used and the output voltages of the photodiodes were sent directly to the oscilloscope device providing on-line observation of the transmission signal. The discharge plasma was 100% amplitude modulated at frequency between 10-50 Hz (depending on the pressure and species under investigation 10-20 Hz for molecules and more for atoms). The TTL signal of the modulation has been used as a trigger signal for the oscilloscope. The frequency of modulation has been chosen to provide switching off the discharge for the time sufficient for recovery of full laser transmission value when there is no absorption due to lack of absorbing molecular or atomic species. The oscilloscope device allowed using up to 512 recorded signals (each resulting from single modulation period) averaging what was necessary due to observed microphonic noise on the laser intensity occurring from time to time. The recordings provided direct values of the laser transmitted power through the helium cell in both situations of discharges *on* (beginning of the decay recording) and for discharges *off* (asymptotic value at the end of the decay curve). This, according to eq.(4.1) allows absorption rates calculation during all the decay and thus the transmission value  $T$  that is convenient value in further considerations as the  $-\ln(T)$  is directly proportional to the absorber density.

## 4.2 Measurement data processing and reduction

Basic spectroscopy measurements performed on the helium molecule between its metastable  $a^3\Sigma_u^+$  and  $e^3\Pi_g$  states including three isotopologues  $^3\text{He}_2^*$ ,  $^4\text{He}_2^*$  and  $(^3\text{He}-^4\text{He})^*$  relies mostly on the transition lines absorption profiles available in the wavelength tuning range of the blue laser setup (chapter 3). The rough determination of the line positions, their amount in considered range as well as relative amplitudes was based on the reading of the absorption signal on the hardware lock-in amplifier display. For isotopic pure ( $^3\text{He}$  and  $^4\text{He}$ ) helium cells it allowed to assign the molecular transitions within the rotational structures of both states to the observed lines, by comparison of the splittings between them and the relative heights (characteristic intensity alternation with 1:3 ratio for  $^3\text{He}_2^*$ , absence of even-N numbered lines for  $^4\text{He}_2^*$ ) with reference data of [6, 37]. The  $(^3\text{He}-^4\text{He})^*$  line positions, both in the wavelength scale and then the laser parameters settings, were first determined in the calculations using the mass scaling rules for the molecular constants and then experimentally confirmed in the frequency scans in 1:1  $^3\text{He}:^4\text{He}$  helium mixture cell.

Accurate determination of the line positions in terms of the laser work-settings (also used to the blue laser setup absolute wavelength calibration), line shapes and the absorption rates has been made by performing and analyzing the frequency scans of the full absorption line

profiles. They were performed by the blue laser light transmission measurement for continuously changed wavelength in the vicinity of earlier determined rough line position. This section describes the way that the recorded data from frequency scans has been processed and parameters as line position and absorption were extracted. Apart from the molecular absorption lines profiles the decay rates of the molecular and atomic species has been investigated, however the data processing here was reduced to only averaging of the discharge *off* signal period at the end of the decay curve when no absorption was expected and asymptotic value was reached, so that the time-change in the transmission T values could be determined. Then the values of  $-\ln(T)$  has been calculated and plotted as a function of time, reflecting directly time evolution of the atomic and molecular densities.

#### 4.2.1 Processing of the recorded data files in numerical lock-in software

Recorded during the 465 nm laser frequency scans data files were processed in the numerical lock-in software written by P.-J. Nacher to demodulate the transmission signal directly from the PDB photodiode. The program was also used in case of signals demodulation of MEOP measurements recordings and its detailed description is given in the subsection 5.4.3.1 as well as in [63]. The recorded by the data acquisition program contain also the X and Y (in-phase and quadrature) outputs of the hardware lock-in amplifier. However, it was found to be more convenient to use the numerical demodulation due to possible repeated choice of lock-in settings as time constant and phase. The only difference lock-in output files in comparison with the MEOP recordings is the generic content of the program, that here are:

- time scale of the experiment
- 937 nm laser diode current driving voltage triangle function
- magnitude (R) of the demodulated signal divided by the averaged transmitted signal of the blue beam
- in-phase (X) component of the demodulated signal divided by the averaged transmitted signal of the blue beam
- quadrature (Y) component of the demodulated signal divided by the averaged transmitted signal of the blue beam

Demodulated signal magnitude R and its in-phase X component are equivalent provided that the phase value is correctly chosen - the quadrature (Y) component is 0 during all the frequency scan.

The example of the demodulated signal, proportional to the absorption, in function of the recording time is shown on the fig.4.3 together with the course of the voltage function applied to the laser diode current supply.

Comparing the position of the lines during one recording that included 1.5 of voltage course period it is shown that the hysteresis of the line maximum position is present. Value of the difference between positions for the negative and positive slope is approximately constant - independent of the considered transition line or the isotopologue and varies between 0.15-0.17 V. The examples of the line position determination are shown and discussed in the next subsection 4.2.2. There is also a small difference of about 0.04 V in position of the lines

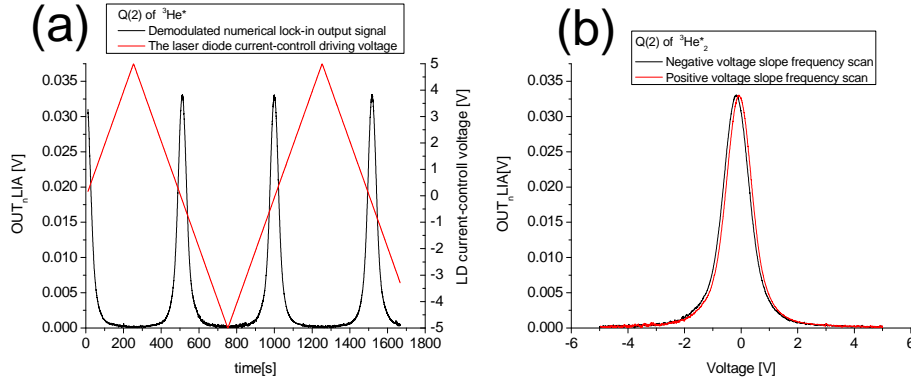


Figure 4.3: (a) Numerical lock-in output signal of transmitted blue laser beam (black solid curve) with laser diode current control voltage (red) in function of the recording time. The record last 1.5 period of voltage triangular function allowing comparison of the line profiles and positions reproducibility with the negative (black) and positive (red) voltage slope (b).

recorded with the same slope. These values were taken into account when the errors of the positions of the line were being determined. To increase the reproducibility and to standardize the analysis procedure, only the line profiles recorded within negative slope of the voltage change were taken into account in further considerations, except for the determination of the line position to the blue laser calibration purposes, where the average of the values on negative and positive slopes were taken as the final value. Simultaneous recording of the transmission signal and the current-control voltage allowed simple scaling of the line profiles in terms of the voltage value on abscissa.

#### 4.2.2 Absorption line profile position determination

Accurate determination of the position of recorded absorption lines in voltage scale and then expressing in the temperature was needed to calibrate the laser setup settings of laser diodes temperature in respect to the line positions in the wavelength scale reported in [6, 28]. For the purposes of the laser calibration the data from scans of 66.7 mbar isotopic pure  $^3\text{He}$  and  $^4\text{He}$  cells were chosen providing high SNR of the observed lines as well as moderate line pressure broadening - the choice is a compromise between the signal magnitude and accuracy of position determination due to the broadening effect.

In these pressure conditions, due to comparable effects of Doppler and collisional broadening effects, separately being described by the Gaussian and Lorentzian line shape functions, the line profile has to be considered as their convolution - Voigt profile. If the observed line profiles would correspond to the single transitions between  $a^3\Sigma_u^+$  and  $e^3\Pi_g$ , then the line position and amplitude would be reduced to Voigt function fit to the experimental data. However, as it is presented in the section 4.3, the line profiles uncover the underlying structure being more (odd-N numbered transitions) or less (even-N numbered transitions) distorted from the expected Voigt shape. Thus, in these conditions the fit of such function is assumed to be loaded with the systematic error, especially for odd-N numbered lines. From the other hand it is known, that the top part of the Voigt profile is mostly influenced by the Gaussian component while the bottom of the line by the Lorentzian. Relying on this property, the Gaussian function fit was performed to the top peak part from about 2/3 of amplitude maximum. In this way - from the

difference between position from Voigt and Gaussian function fits, the additional error value was determined for the recorded line position that, in fact, was taken from the Voigt fit.

Summarizing, in the value of the total error for the position value, the hysteresis value takes into account, the small discrepancy between profiles within chosen voltage change slope as well as the difference in positions resulting from the Voigt and Gaussian fits. While the first two mentioned are approximately independent of the recorded line transition and isotopologue, the last varies due to mentioned line underlying structure and distortion - for even-N numbered and N=1 line amounts to about 0.01 V and 0.14 V for odd-N numbered lines.

Apart from the position of the absorption line determination, the Gauss function fits to the values above 2/3 of the amplitude were performed to obtain accurate value of the amplitude assuming that the baseline level is 0, what leads to an relative error less than 5% in each case, mostly less than 1% of the amplitude value. The relative amplitudes are used later for rotational temperature determination, where the underlying line structure has been neglected and it is assumed the lines correspond to the single transitions between the rotational sublevels described by the rotational numbers N of the states involved in the transition.

### 4.2.3 Absorption line frequency scan signal to molecular absorption scaling

Until this moment any care about the scale in which the ordinate axis of the line profile was expressed has not been taken. It has been written, that the value of numerical lock-in magnitude R divided by the average input signal corrected for the offset value is the amplitude modulation depth. Depending on the function shape of the amplitude modulation used in the frequency scan experiment - 100% square or partial sine, the way to obtaining the real absorption rate is different. The absorption of the laser light of which the power is measured, i.e. by the photodiode, can be expressed in terms of the measured signals  $I_{inc}$  and  $I_{abs}$  that corresponds to the maximum of transmitted power (no absorption - incident laser power before interaction with plasma) and incident beam power weakened through the absorption process in plasma respectively. So that:

$$Abs = (I_{inc} - I_{abs})/I_{inc}, \quad (4.1)$$

assuming both signals are corrected for the common offset value  $\emptyset$ . In both modulation schemes the information about the demodulated signal from the lock-in amplifier is proportional to the  $(I_{inc} - I_{abs})$  difference. In next two paragraphs the extracting of this information for absolute absorption value determination is described for 100% and partial sine modulations.

#### 4.2.3.1 Square 100% modulation in hardware and numerical lock-in detection

**(a) Absorption determination from hardware lock-in output signal** In the square function 100% amplitude modulation scheme, the discharge is periodically switched *off* and *on* - the maximum (no absorption) and the minimum (maximal absorption for certain discharge conditions and laser wavelength tuning). The time-course of the measured transmitted signal for this modulation has a form of the square wave with peak-to-peak amplitude equal to  $(I_{inc} - I_{abs})$ . In such case, according to well established and meet in several device's manuals, the usual hardware lock-in amplifiers provide then the signal  $R^{RMS}$  - RMS (Root Mean Square) value of the peak-to-peak amplitude  $a_1$  of the first term in the square wave expansion in sine

waves ( $R^{RMS} = a_1 \sqrt{2}$ ). The amplitude is thus  $\equiv \sqrt{2} \cdot R^{RMS}$ . To recover the  $(I_{inc} - I_{abs})$  peak-to-peak amplitude of corresponding square wave, the sine amplitude has to be multiplied by the factor of  $\pi/2$  - inversion of the first factor in the sine expansion of a square function. That gives  $(I_{inc} - I_{abs}) = \frac{\pi}{2} \sqrt{2} R^{RMS}$ . According to the absorption definition this difference has to be divided by the offset corrected  $I_{inc}$  signal, that, in fact, is known during the recording as the data acquisition includes the direct photodiode signal during the whole recording. However, extraction of the value of  $I_{inc}$  from the varying with laser power and modulated by the discharge photodiode signal would require extreme effort, the fact of rather low absorption values  $<10\%$  can be utilized as it means that the photodiode signals  $I_{inc}$  and  $I_{abs}$  are very nearly equal in comparison to their absolute values -  $I_{inc}$  can be substituted as an time averaged photodiode signal corrected by the offset:  $(\langle PD \rangle - \emptyset)$  This allows to give the expression for the absorption value determination from the lock-in output signal in RMS:

$$Abs = \frac{\pi/2 \sqrt{2} \cdot R^{RMS}}{\langle PD \rangle - \emptyset} \quad (4.2)$$

**(b) Absorption determination from the numerical lock-in output** For the numerical lock-in demodulation output  $OUT_nLIA$  (eq.(5.9)), that is already expressed in terms of the  $a_1 = \sqrt{2} R^{RMS}$ , the absorption value is simply obtained by the output value multiplication by  $\pi/2$  factor so that:

$$Abs = \frac{\pi}{2} \cdot OUT_nLIA, \quad (4.3)$$

what is equivalent to the eq.(4.2). All the considerations about the denominator value remains valid.

#### 4.2.3.2 Partial sine amplitude modulation

With the partial (small  $< 10\%$ ) amplitude sine modulation the relation between the lock-in output  $R^{RMS}$  (or  $a_i = \sqrt{2} \cdot R^{RMS}$ ) value and  $(I_{inc} - I_{abs})$  is not usually explicitly known. This is in spite of the fact that even the rf voltage amplitude modulation can be quantitatively defined, the plasma response and thus variation of the absorbing species - metastable atom or molecules, not necessarily reflects the same level of modulation as driving voltage. This was not the problem for 100% square modulation where the absence of the discharge definitely sets the null density of absorbers and during the presence of the discharges the density remain constant. Instead of the  $\frac{\pi}{2}$  factor as for 100% square modulation in comparison with equations (4.2) -(4.3), there is unknown value ( $\equiv X$ ) that the  $R^{RMS}$  in the numerator has to be multiplied by:

$$Abs = \frac{X \sqrt{2} \cdot R^{RMS}}{\langle PD \rangle - \emptyset} \quad (4.4)$$

Attempts of the  $X$  coefficient calculation does not provide enough precise values allowing obtain reliable absorption rates - too many unknown parameters such as the plasma response for the applied discharge voltage amplitude modulation is included. The way of determination of the  $X$  factor for one discharge modulation setting and rf excitation conditions (frequency, amplitude) is to determine the absorption for the square 100% modulation case being tuned with the laser to the transition frequency - top of the line profile and then, for the sine modulation, staying tuned with the laser at the same frequency, read the  $R^{RMS}$  signal from the hardware lock-in amplifier,  $\langle PD \rangle$  and the  $\emptyset$ . As for the small amplitude modulation of the discharge average

metastable atoms number density is approximately unchanged, both determined absorption values should be equal, what, for known  $R^{RMS}$  and offset corrected  $\langle PD \rangle$  for sine modulated amplitude, determines the prefactor  $X$ . For each pressure cell, the discharge intensity and sine modulation amplitude the determination of the  $X$  factor has been performed in each series of the frequency scans. The same  $X$  factor, once determined for certain discharge conditions, can be used to determine the peak amplitude absorption for the laser tuned to other transitions, as well as scaling the ordinate axis in the line profile scans where sine amplitude modulation has been used. In the last case, the numerical lock-in output -  $OUT_nLIA$  has to be multiplied by the factor  $X$  only.

### 4.3 Absorption lines shape

Absorption line profiles obtained in the recordings with voltage controlled laser diode 937 nm feeding current change can be distinguished in terms of the value of  $N$  rotational number. The distortion of the lineshape (which for the single transition is expected to be described by Voigt function) corresponding to odd- $N$  numbered transitions is visually greater than in case of even- $N$  numbered transitions, as it is compared on the Fig. 4.4.

The motivation of choice of the 66.7 mbar pressure for lineshapes investigations discussion is a compromise between increase of the molecular absorption with the pressure and collisional broadening that tends to shade the details of the line structure. Recordings of the line profiles performed for the pure  $^3\text{He}$  gas at 8 mbar (Fig.4.5(a)) with low SNR bring no additional information except that the odd- $N$  numbered lines are distorted in the same way - here any difference in the top peak part can't be distinguish due to the noise, as well as determination of any difference in peaks FWHM is not possible - they seems to be equal within the data points scatter. Here, even the Q(1) tends to be distorted as higher odd- $N$  numbered Q-lines. From the other hand, line profile scans in the high pressure pure  $^3\text{He}$  cells as 128 (Fig.4.5(b)) and 266 mbar (Fig.4.5(c)) do not allow to observe characteristic distortion due to the pressure broadening effect. However, here still the Q(1) is outstanding from other odd- $N$  numbered lines as it was the case for 66.7 mbar cell both in pure  $^3\text{He}$  and  $^4\text{He}$  cells.

On the frequency scan of line Q(5) of  $^4\text{He}_2^*$  (Fig.4.4) there is additional line present at longer wavelength from the Q(5) position. This line was identified as R(5) of the (1-1) vibrational band. Another example of such close-lying lines is the P(2) of  $^3\text{He}_2^*$  (considered (0-0) band) with R(2) of (1-1) band, however, here the lines are on the same wavelength positions (see reference data [6]) thus no resolving is possible.

The only difference between odd- $N$  numbered lines for  $N>1$  of both  $^3\text{He}_2^*$  and  $^4\text{He}_2^*$  is broader top part (above about 0.7 of the relative amplitude) of the lines for the former molecule. The only exception in the line profile shapes for odd- $N$  numbered transitions is the line for  $N=1$ . For both  $^4\text{He}_2^*$  and  $^3\text{He}_2^*$  it is the line that exhibits distortion in a lesser degree and is rather similar to the even- $N$  numbered  $^3\text{He}_2^*$  lines, however still, the Q(1) line is broader than the Q(2). what is shown on the fig.4.6.

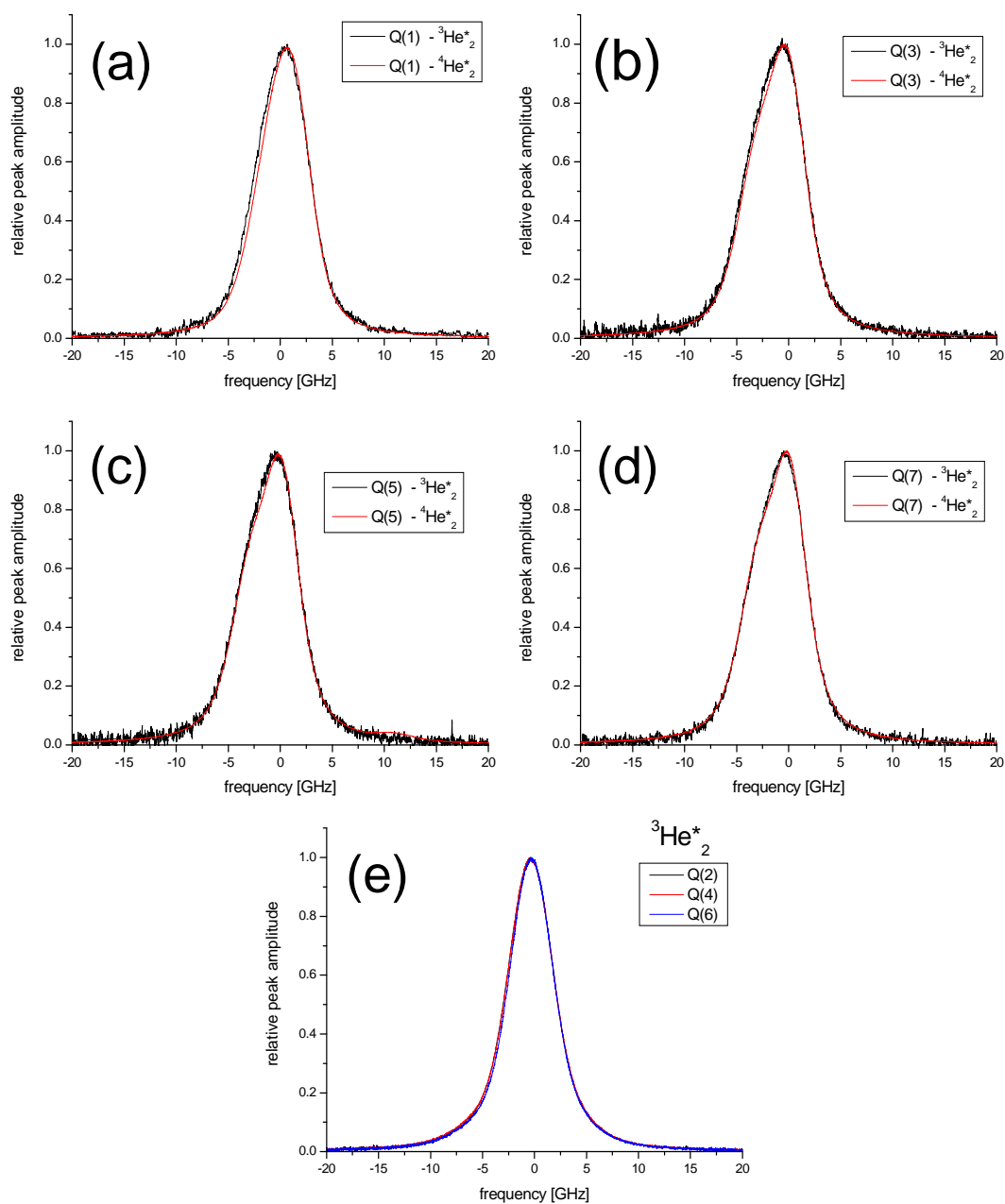


Figure 4.4: Comparison of the molecular absorption lineshapes of Q branch of two isotopologues  $^3\text{He}_2^*$  and  $^4\text{He}_2^*$  recorded in isotopic pure gases at 66.7 mbar each. Graphs (a)-(d) present pairs of the lines with the same odd-N value. Graph (e) shows the even-N numbered lines of  $^3\text{He}_2^*$ . The SNR of the odd-N numbered Q lines of  $^3\text{He}_2^*$  is lower than of the  $^4\text{He}_2^*$  due to 1:3 statistical ratio of the line intensities.

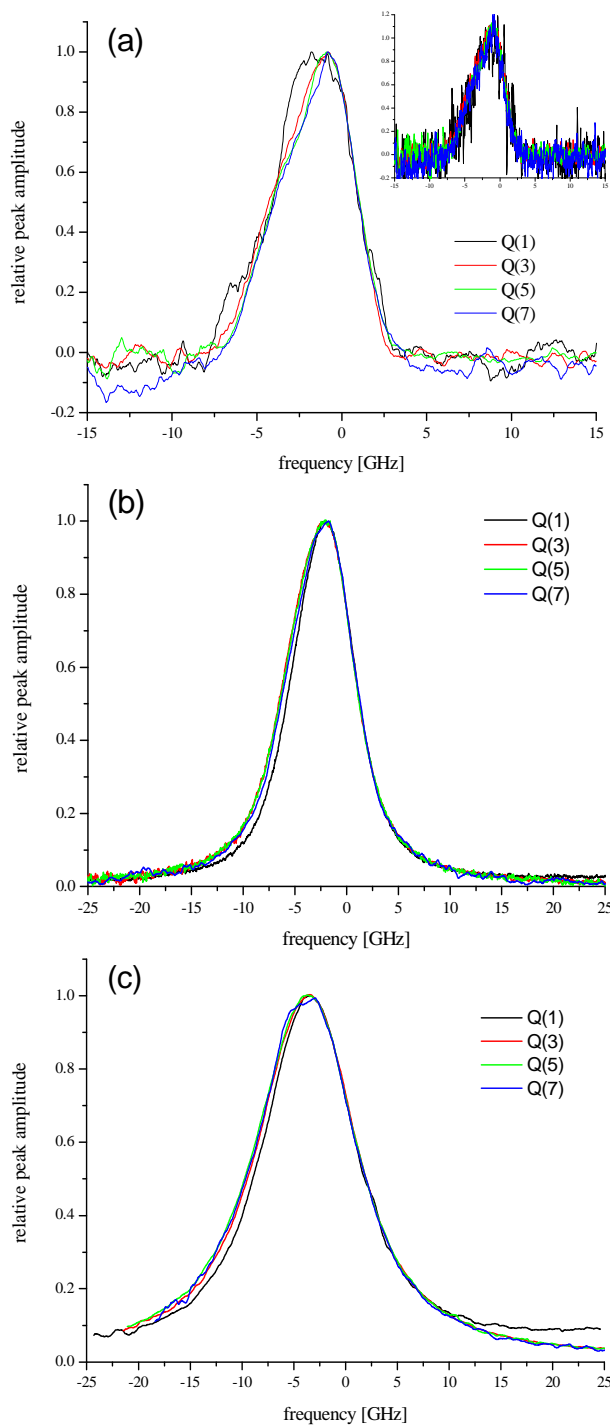


Figure 4.5: Compilations of the molecular lines scans of the Q branch with odd N values for 8 - (a), 128 - (b) and 266.7 - (c) mbar pure  $^3\text{He}$  pressure cells. Due to low SNR (graph (a)) or high pressure broadening effect (graphs (b) and (c)) these profiles are not suitable for the analysis of the complex lineshapes of odd-N numbered lines clearly distinguishable at 67.6 mbar. The noise on the curves of the graph (a) was averaged - for visualization of the noise magnitude non-averaged curves are shown in the inset.

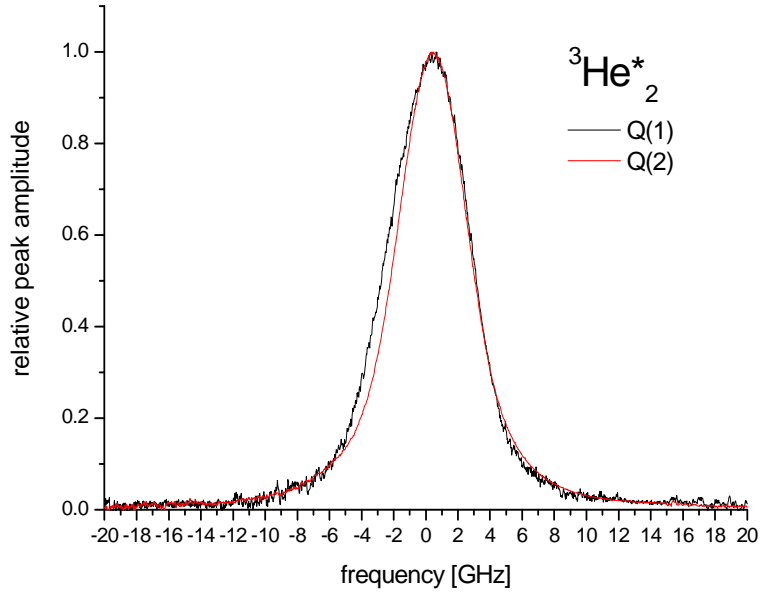


Figure 4.6: Comparison of the first odd- $N$  numbered line profile  $Q(1)$  with the first even- $N$  numbered  $Q(2)$  profile.  $Q(1)$ , the less distorted line from the odd- $N$  numbered group is still broader than even- $N$  numbered lines.

For more quantitative comparison it is useful to look at the full width at half maximum (FWHM) values of absorption profiles presented in the tables 4.1, 4.2 and 4.3.

Line designation	FWHM [GHz]				
	8 mbar	66.7 mbar		128 mbar	267 mbar
		$w$	$s$		
Q(2)	$3.95 \pm 0.04$	$5.26 \pm 0.05$	$5.11 \pm 0.05$	$6.67 \pm 0.05$	$10.59 \pm 0.05$
Q(4)	$4.14 \pm 0.05$	$5.24 \pm 0.03$	$5.13 \pm 0.05$	$6.97 \pm 0.04$	$11.27 \pm 0.05$
Q(6)	$3.95 \pm 0.05$	$5.11 \pm 0.04$	$5.04 \pm 0.06$	$6.74 \pm 0.07$	$11.23 \pm 0.05$
Q(8)	$4.00 \pm 0.47$	$4.96 \pm 0.17$	$5.06 \pm 0.04$	$6.60 \pm 0.11$	$10.94 \pm 0.29$
P(2)		$4.86 \pm 0.05$		$6.54 \pm 0.15$	$10.17 \pm 0.11$
R(0)		$5.62 \pm 0.06$	$5.58 \pm 0.05$		

Table 4.1: Full width at half maximum of **even**  $N$ -numbered absorption lines profiles of  ${}^3\text{He}_2$  at 8-267 mbar pressure range. For the 66.7 mbar two discharge excitation regimes has been studied - *weak* ( $w$ ) and *strong* ( $s$ ) (details further in the text).

In both cases of even and odd- $N$  numbered transitions of  ${}^3\text{He}$  at various pressures the FWHM values clearly changing within one pressure value - the differences are significantly (even 10 times higher than the error bars). Values for odd- $N$  numbered transitions are systematically higher about 0.5-1.5 GHz than those for even- $N$  transitions within one pressure. The fact of varying FWHM values within one pressure (with constant temperature  $\approx 300\text{K}$  value) even for the less distorted from expected Voigt shape line profiles allows to suspect, that here also the complex line structure is present - for single transition lines one would expect the constant value of FWHM within one pressure conditions. Comparison of the results obtained for

Line designation	FWHM [GHz]				
	8 mbar	66.7 mbar		128 mbar	267 mbar
		<i>w</i>	<i>s</i>		
Q(1)	4.56 ±5.58	5.90 ±0.05	5.81 ±0.28	7.16 ±0.05	10.71 ±0.35
Q(3)	5.24 ±0.56	6.40 ±0.03	6.32 ±0.09	7.85 ±0.05	11.41 ±0.10
Q(5)	5.19 ±0.44	6.30 ±0.07	6.24 ±0.09	7.73 ±0.04	11.79 ±0.07
Q(7)	4.46 ±2.05	6.20 ±0.07	6.22 ±0.04	7.55 ±0.04	11.51 ±0.27

Table 4.2: Full width at half maximum of **odd**  $N$ -numbered absorption lines profiles of  $^3\text{He}_2$  at 8-267 mbar pressure range. For the 66.7 mbar two discharge excitation regimes has been studied - *weak* ( $w$ ) and *strong* ( $s$ ) (details further in the text). The error of the FWHM values for odd- $N$  transitions of 8 mbar  $^3\text{He}$  cell are especially higher due to very low SNR of the profiles recordings - Fig. 4.5 (a)

Line designation	66.7 mbar of $^3\text{He}$	
	<i>w</i>	<i>s</i>
	FWHM [GHz]	
Q(1)	5.60 ±0.05	5.64 ±0.05
Q(3)	6.28 ±0.05	6.30 ±0.05
Q(5)	6.27 ±0.05	6.22 ±0.05
Q(7)	6.19 ±0.05	6.21 ±0.04
Q(9)	6.06 ±0.16	6.15 ±0.04

Table 4.3: Full width at half maximum of  $^4\text{He}_2$  absorption lines profiles of at 66.7 mbar pressure. Two discharge excitation regimes has been studied - *weak* ( $w$ ) and *strong* ( $s$ )

different strengths of discharge excitation within single pressure of 66.7 mbar both for  $^3\text{He}$  and  $^4\text{He}$  cells shows the reproducibility of the measurements.

Using the formula of [68] relating Voigt profile half width with the Lorentzian and Gaussian convoluted profiles half widths  $w_L$  and  $w_G$ :

$$w_V = 0.5346 * w_L + \sqrt{0.2166 * w_L^2 + w_G^2} \quad (4.5)$$

inverting the dependency to have  $w_L(w_V)$ , assuming the room temperature plasma conditions ( $w_G=3.26$  GHz, at 300 K for  $^3\text{He}_2^*$  according to the eq.(A.15b) in Appendix A) in the experiments,  $w_L$  pressure dependency can be obtained as shown on the Fig.4.7.

The intercept value at null pressure (no pressure broadening) on the Fig.4.7 indicates 0.85 GHz of natural line width for the helium dimer. According to [35] the lifetime of the molecular excited  $e^3\Pi_g$  that is populated due to 465 nm radiation absorption is about 67 ns that results in the natural broadening of the line of order 15 MHz - more than order of magnitude less than the value obtained here. This proves that none of observed absorption lines corresponds to single transition

It was obvious from the beginning that the odd- $N$  numbered lines profiles posses the underlying structure, indicating that the observed profile does not correspond to a single transition but is the resultant of several absorption lines associated with respective transitions within fine

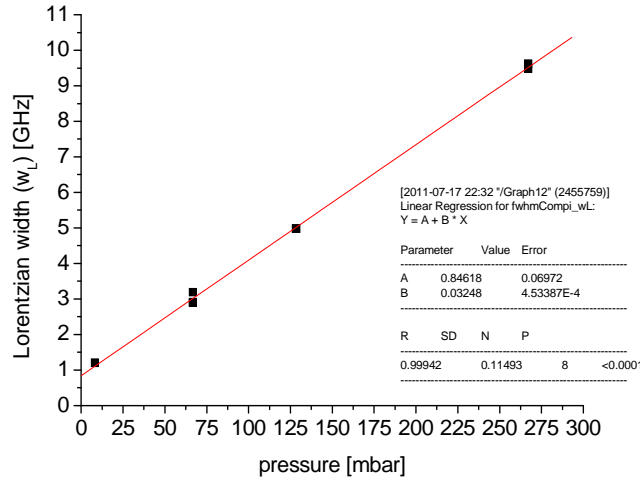


Figure 4.7: Lorentzian half width of Voigt profiles for Q(2) transition absorption lines at 8.66, 7, 128 and 267 mbar pressure of  $^3\text{He}$ . Linear fit to the experimental points has been performed providing the slope value  $32.5 \pm 0.5$  MHz and intercept  $0.85 \pm 0.07$  GHz

or hyperfine structure of rotational sublevels, as it can be concluded from the similarity of the line profiles with those reported in [48].

According to [26, 49, 50] the two farthest fine structure sublevels within one rotational level of  $a^3\Sigma_u^+$  state are separated by 2.2 to 1.2 GHz - decreasing with increasing N value from N=1 to N=9. This is of order of magnitude of the observed line half-widths and their variation (several GHz) so could explain their not symmetrical shape due to overlapping of fine structure components - each of them separately broadened by pressure and collisional effects. Splittings of the fine structure sublevels of  $e^3\Pi_g$  are, for the Author's knowledge, not presented in any reference as well as parameters necessary for their calculation.

The presence of the underlying line structure can be also found with the line profile fitting procedure with the Voigt function in Origin 7.5 data analysis software. Obtained residual data between the experimental points and fitted curve, exhibits regular, across the investigated pressure range, maxima of residual data on the left line slope - Fig.4.8 to Fig.4.11.

This residual data behavior is an indication of the discrepancy between expected Voigt profile and the recorded one which is the resultant of several close lying absorption lines.

The reason of the fact why the even-N numbered of  $^3\text{He}_2^*$  lines look differently from the odd-N numbered in terms of the fine structure is hard to explain, as, for the Author's knowledge, the values of spin-spin  $\lambda$  and spin-rotation  $\gamma$  fine structure coefficients are not known for this isotope. Furthermore, these coefficients for the  $^4\text{He}_2^*$  are given only for the  $a^3\Sigma_u^+$  [48]. The lack of the coefficients in the excited  $e^3\Pi_g$  state doesn't allow to conclude about the reason for the difference in the lineshapes of odd-N and even-N numbered lines. One should exclude the hyperfine structure influence on the basis of similarity of the odd-N numbered lines of both isotopologues. Using the coefficients  $\lambda$  and  $\gamma$  of the  $^4\text{He}_2^*$  in calculations of the  $^3\text{He}_2^*$  fine structure sublevels' separation doesn't bring the answer about the shape difference. The changes of the sublevels' separations are monotonous through N=1,2,3...9 without any significant variation for even-N values, that could result in decrease of line distortion seen for odd-N numbers. Thus, the reason lies in the fine structure of the levels of the excited state or other effect corresponding to the isotopic difference. Unfortunately only the two lines of heteronuclear dimer

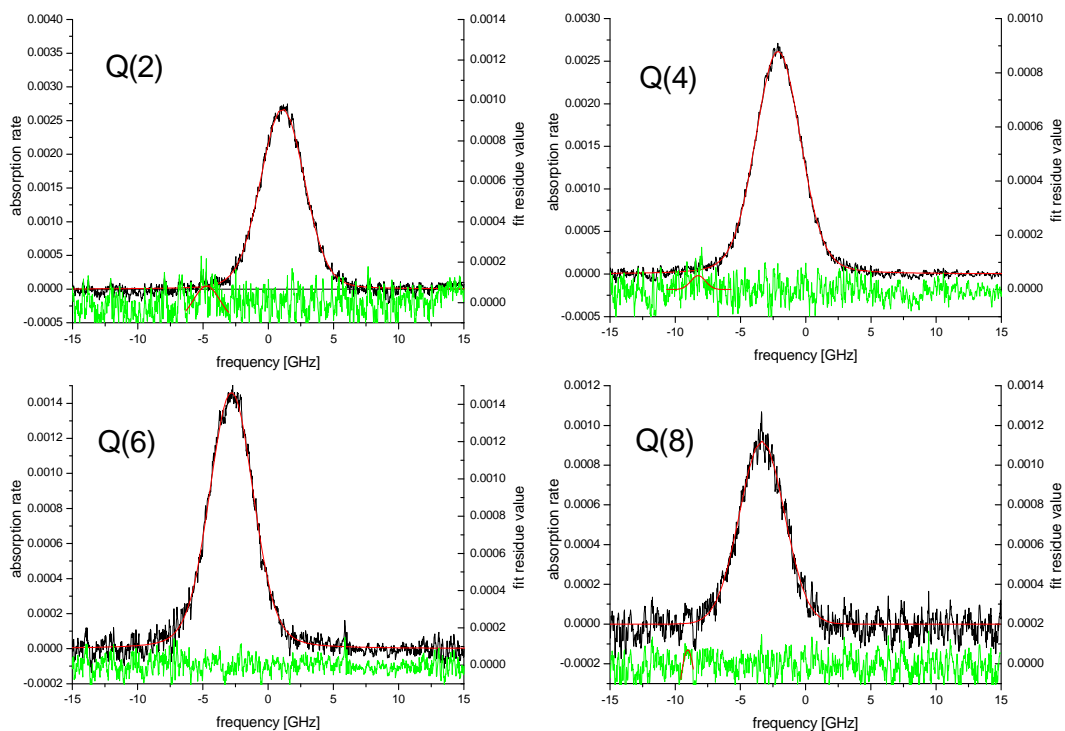


Figure 4.8: Graphs with even-N numbered Q branch line profiles for 8 mbar pure  $^3\text{He}$  cell. The curve described by the Voigt function was fit to each profile showing regular residue maxima at negative frequencies.

( $^3\text{He}$ - $^4\text{He}$ ) $^*$  of Q branch with N=2 and N=3 are well resolved from the spectra of other isotopologues thus their shape can be compared with isotopic pure molecules. The P(2) and Q(4) lines, however separated from their neighbors, experience the influence of their wings, what makes the conclusions about such detailed discrepancy of the profiles doubtful.

The line profile of odd-N numbered line of heteronuclear dimer (Fig.4.12) does not exhibit such strong distortion as in case of two other isotopologues, however, the analysis of residual data of the Voigt fit still shows the maximum on the left side of the peak slope. Presented line distortion due to its internal structure raise the question of possibility of using top peak value of absorption over the cell length for helium molecule in metastable state number density determination. The reference given in the paragraph (b) of subsection 2.2.4 providing the value of the rotational levels lifetime does not mention any internal structure of the line. Thus, no cross-section values can be calculated for the transition occurring within the structures of rotational levels of  $a$  and  $e$  states involved in the N numbered transition. Moreover, the individual lines amplitudes are not resolved within this structure. From the other hand, the discrepancy (residue) of presented even-N numbered line profiles with the fitted Voigt profiles is about 1% of the top peak value and possibly the strongest line components are lying close enough for the assumption of single transition between rotational levels occurring is valid, as it is in the references reporting about the lines positions [6, 28] and excited electronic states' rotational levels lifetimes [35]. Under this assumption the recorded line profiles and their amplitudes allow obtaining the absolute values of metastable molecule densities. Decision of the Author is to use only even-N numbered lines for such calculations, because of, as it was discussed, negligible distortion due to internal line structure. Presence of the line structure pose the difficulties

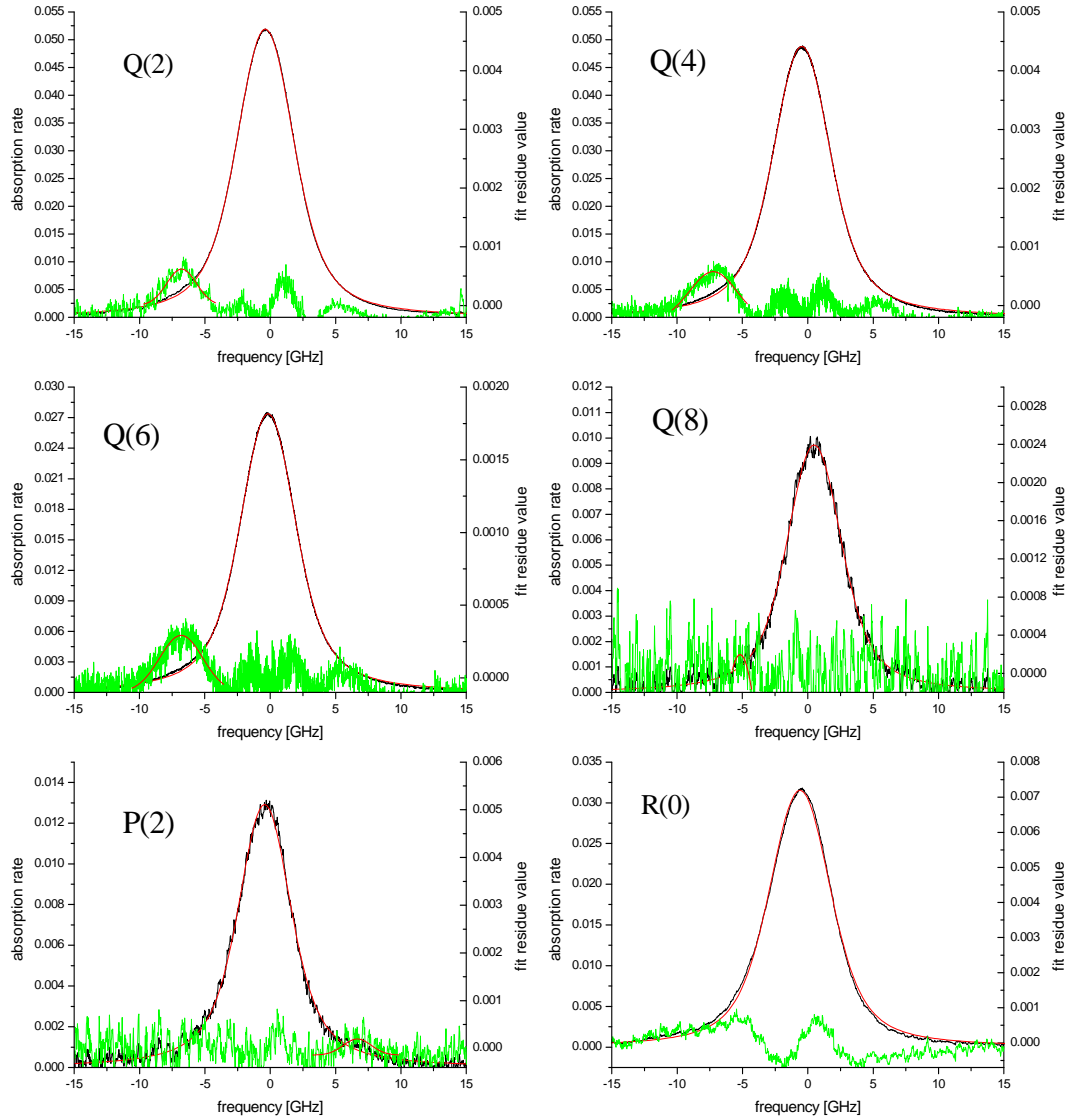


Figure 4.9: Graphs with even-N numbered Q branch line profiles for 66.7 mbar pure  $^3\text{He}$  cell. The curve described by the Voigt function was fit to each profile showing regular residue maxima at negative frequencies. The last two graphs present the profile of P(2) and R(0) lines. For the former line small Voigt fit residue maximum at positive frequency is present, whereas in the latter line profile any explicit maximum can be distinguished.

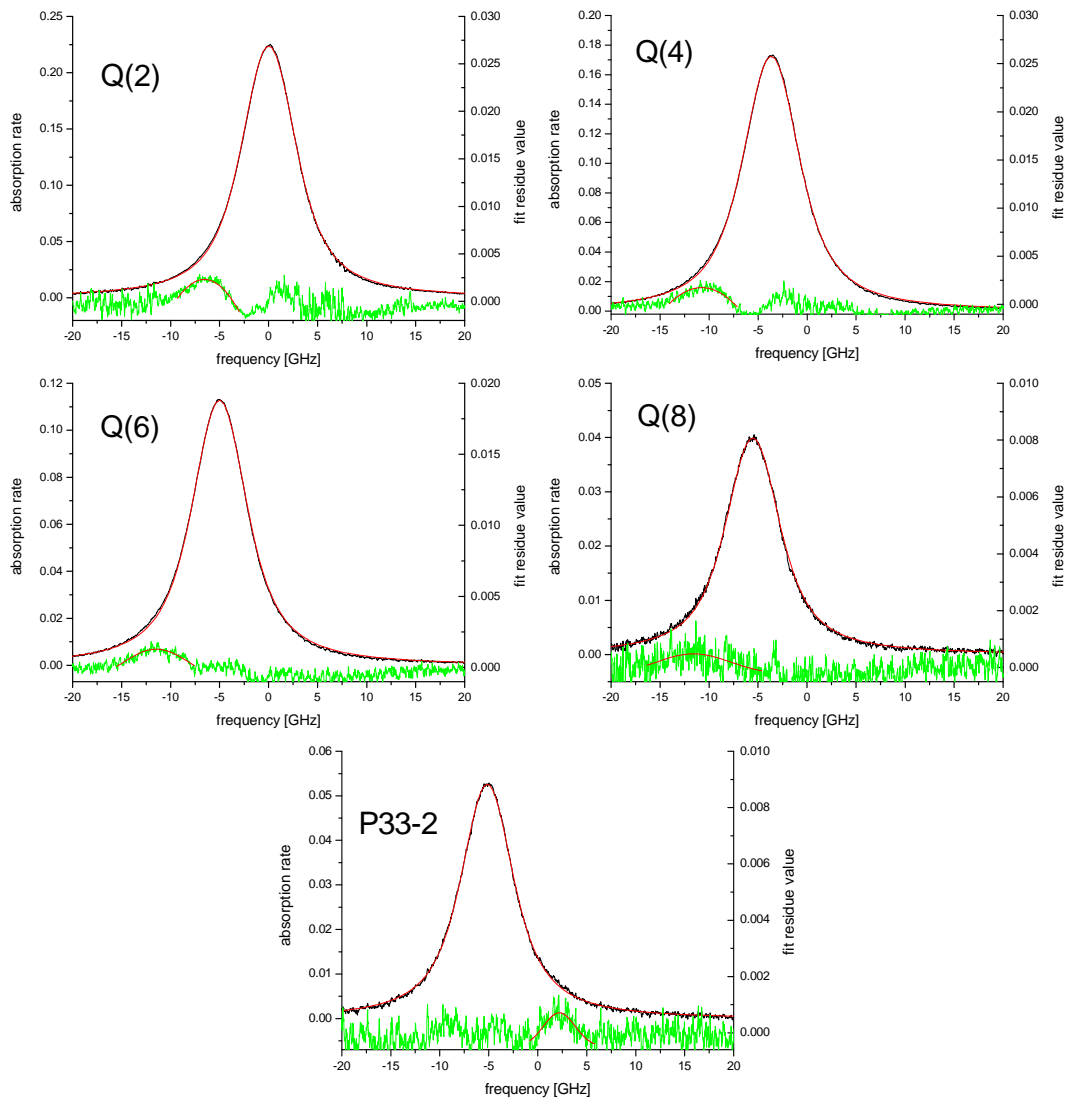


Figure 4.10: Graphs with even-N numbered Q branch line profiles for 128 mbar pure  $^3\text{He}$  cell. The curve described by the Voigt function was fit to each profile showing regular residue maxima at negative frequencies. The last graph presents the profile of P(2) line. Small fit residue maximum can be distinguished for positive frequency, as in case of data for 66.7 mbar.

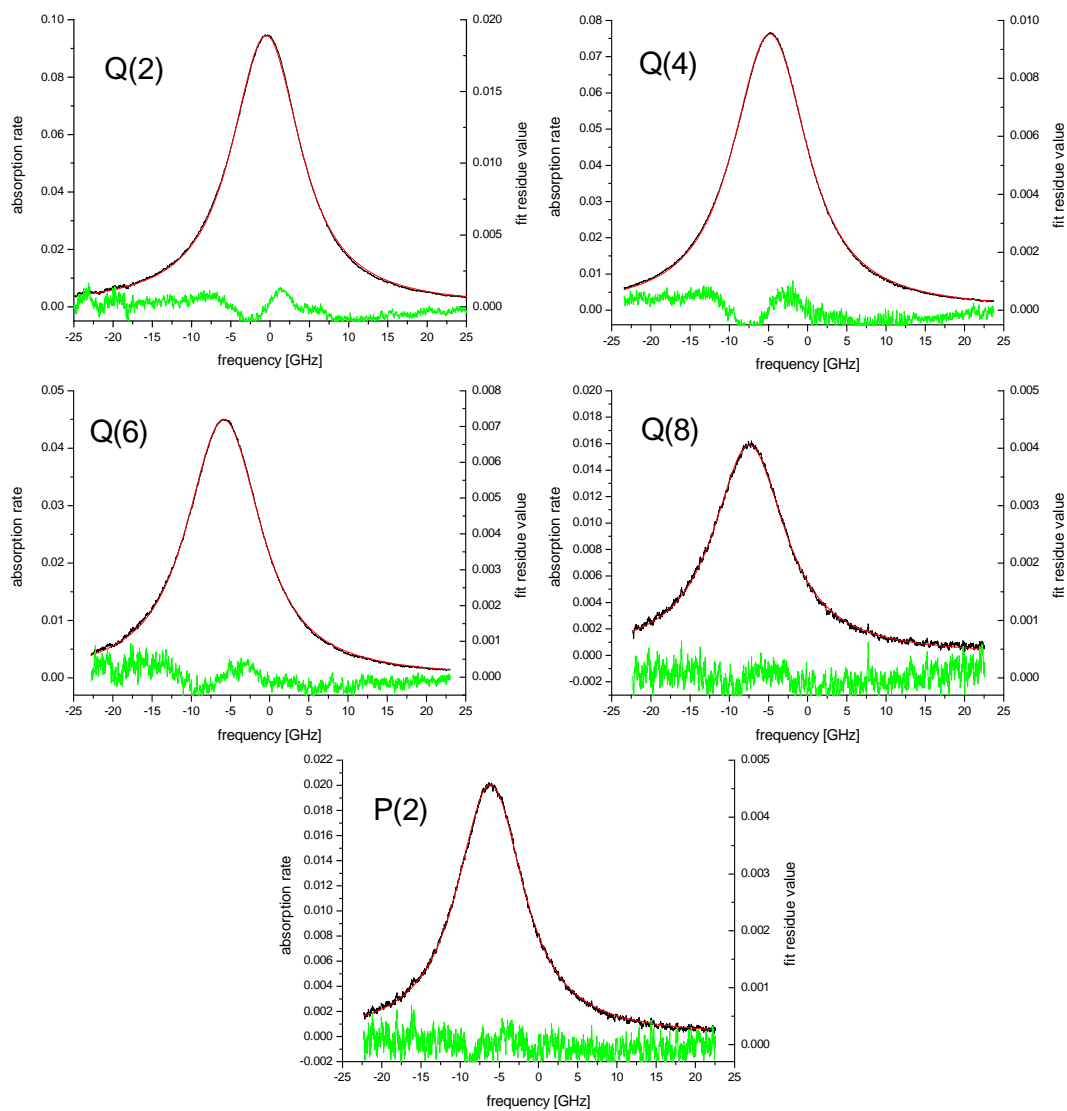


Figure 4.11: Graphs with even-N numbered Q branch line profiles for 266 mbar pure  $^3\text{He}$  cell. The curve described by the Voigt function was fit to each profile, however, in case of this pressure characteristic maxima of the fit residues seen at lower pressures are not observed.

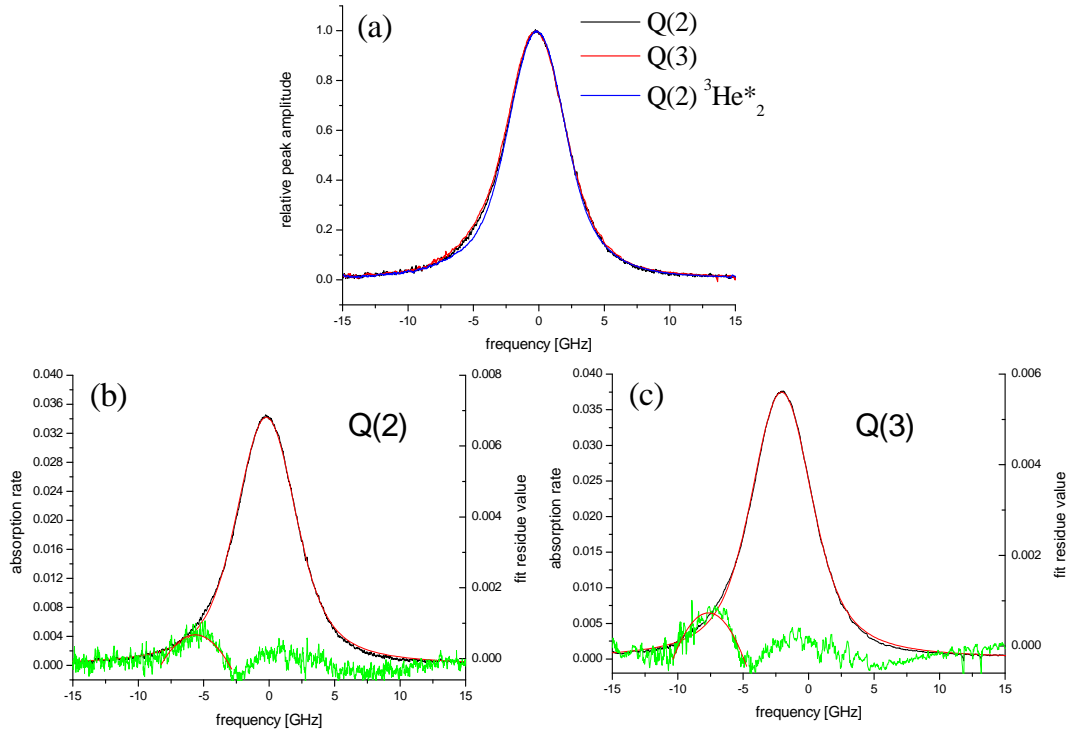


Figure 4.12: Comparison of the only well-resolved absorption lines of  $({}^3\text{He}-{}^4\text{He})^*$  with the profile of Q(2) line of  ${}^3\text{He}_2^*$ . Mixture lines, although one odd-N numbered and the second even-N numbered are of the same shape (compare with the difference of even-N and odd-N numbered lines for  ${}^3\text{He}_2^*$ ), similar to the "not-distorted" even-N numbered line (i.e. Q(2)) of  ${}^3\text{He}_2^*$  isotopologue. Small broadening, in comparison with Q(2) of  ${}^3\text{He}_2^*$ , is present on the negative frequency wings for Q(2) and Q(3) lines of the heteronuclear dimer, what is confirmed in the existence of fit residue maxima relatively (as compared to the line height) higher than for Q(2) lines

in their linewidth analysis. For the case of single line corresponding to a single transition the linewidth is a resultant of several process discussed in paragraph (a) of the appendix A - Doppler and pressure broadening. Here, several lines are present within the single profile, thus resolving the Gaussian and Lorentzian widths is impossible, as the profile given can't be described by single Voigt function.

The accurate values of the absorption rate measured for presented molecular transitions for both  ${}^3\text{He}_2^*$  and  ${}^4\text{He}_2^*$  are presented in the tables 4.4 and 4.5 respectively. For the 66.7 mbar two discharge regimes are considered weak and strong. Those two regimes differs in the rf discharge excitation amplitude. The best indication of the discharge conditions is the 1083 nm laser absorption on the atomic transitions and thus the metastable atom density  $n_m$ . It increases with the strength of excitation reflecting the change in plasma properties more reliably than any of the voltage generator amplitude or the sent/reflected power amplifier displayed values. Thus, the absorption values on the  $C_8$  and  $D_0$  transitions has been given in the tables for  ${}^3\text{He}$  and  ${}^4\text{He}$  respectively.

Line designation	Absorption[%]				
	66.7 mbar		8 mbar	128 mbar	266.7 mbar
	weak discharge	strong discharge			
$C_8$	77.5	87.5	83	28.5	7.8
$n_m[\text{cm}^{-3}]\times 10^{11}$	2.76	3.85	3.28	0.62	0.15
Q(1)	1.20	2.61	0.05	4.44	1.75
Q(2)	5.07	11.53	0.24	11.68	9.22
Q(3)	1.57	3.49	0.06	4.75	1.99
Q(4)	4.86	10.53	0.23	12.75	5.99
Q(5)	1.12	2.51	0.06	3.03	1.25
Q(6)	2.73	5.87	0.14	4.92	2.94
Q(7)	0.50	1.07	0.01	0.60	0.32
Q(8)	0.97	2.09	0.03	1.68	0.69
P(2)	1.29	2.67	0.04	1.81	0.72
R(0)	3.17	6.54	NR	NR	NR

Table 4.4: Absorption values for observed molecular transitions for  $^3\text{He}_2^*$  at different pressures between 8 to 266.7 mbar of isotopic pure cells. For 66.7 mbar two discharge regimes are considered of weak and strong rf excitation. The plasma condition inside the cells can be compared via 1083 nm absorption on  $C_8$  atomic transition given in the first row of the absorption values. NR - not recorded in the experiment.

Line designation	Absorption[%]	
	66.7 mbar, $^4\text{He}$	
	weak discharge	strong discharge
$D_0$	25.94	89.94
$n_m \times 10^{11} [\text{cm}^{-3}]$	0.44±0.02	1.70±0.02
Q(1)	3.00	9.90
Q(3)	4.34	14.23
Q(5)	3.58	11.23
Q(7)	1.88	6.43
Q(9)	0.79	2.51
P(3)	1.52	5.26

Table 4.5: Absorption values for observed molecular transitions for  $^4\text{He}_2^*$  at 66.7 mbar of isotopic pure cell. Two discharge regimes are considered of weak and strong rf excitation. The plasma condition inside the cell can be compared via 1083 nm absorption on  $D_0$  atomic transition given in the first row of the absorption values.

## 4.4 Position of absorption lines

Reference data of [6] and [28] provide the positions of the Q,P and R branches of rotational spectrum corresponding to the transitions occurring between rotational levels of  $a^3\Sigma_u^+$  and  $e^3\Pi_g$  states. Any structure of the observed lines was not mentioned by the authors of the references. In the previous section the shapes of the profiles were discussed, that are different for even- and

odd-N numbered lines. The fact of bigger or smaller line distortion due to its internal structure implies the contribution to the error value of position determination beside the error induced by hysteresis of voltage current sweep, reproducibility of line profile recording and statistical accuracy of the fit for position determination.

#### 4.4.1 Wavelength calibration of the laser setup

For the purpose of the blue laser 3 wavelength calibration the observed absorption line positions has to be determined in terms of the laser setup control settings that allows the emitted wavelength change. These are the laser diodes temperature and voltage of the 937 nm laser diode control. For consistency the temperature change equivalence of current change has to be known resulting in the same effect on the wavelength.

To obtain such relation following experiment was performed: the laser settings (temperature for set value of laser diode current) was tuned to the position of the top peak of one rotational transition (Q(2)). Later the 937 nm laser diode current was being lowered in several steps, each time correcting the temperature of the laser diodes to remain the maximum value of the signal - top peak value of the chosen line. As a result, correspondence between  $\Delta I_{937}$  and  $\Delta T_{LD}$  resulting in the same value of the wavelength change was determined to be:  $\Delta I_{937} = 19.5 \cdot \Delta T_{LD}$ . The negative slope of measured dependency shown on the fig. 4.13 can be confusing when it is compared with the positive value of the  $\frac{\Delta I_{937}}{\Delta T_{LD}}$ , however it has to be mentioned, that this is a conditional dependency of current and temperature change assuring the tuning to the maximum of the absorption line. The decrease of the current changes the wavelength, which has to be corrected (the same absolute value of wavelength change but with a different sign) by the increase of the temperature to maintain the maximum absorption signal on the top of the line. It means that the increase of the current is equivalent in terms of the effect on the wavelength (with coefficient of the positive sign) to the increase of the temperature, similarly with the decrease of the current and the decrease of temperature.

Obtained values of the line positions of  $^4\text{He}_2^*$  isotope (Q(1),Q(3),Q(5),Q(7),Q(9), R(0) and P(2)) and  $^3\text{He}_2^*$  (Q(1-8),R(0) and P(2)) from the profiles recorded in isotopic pure  $^3\text{He}$  and  $^4\text{He}$  cells of 67 mbar pressure expressed in terms of the laser diodes temperature were added to the temperature values of laser diodes measured with the thermistor, for which the voltage scans were performed. These temperature values together with the wavelength values of the observed absorption lines were put on the graph providing absolute wavelength calibration of the blue laser setup, shown on the fig.3.8a. The choice of 67 mbar pressure cells was conditioned by good SNR for the absorption lines of both isotopologues, less broaden than for higher (i.e. 128 mbar) pressure values - more accurate line position determination, as well as availability equal pressure isotopic pure cells.

#### 4.4.2 Isotopic mixture cell - recordings of multiple lines

Independent recordings performed in isotopic pure cells that provided the wavelength calibration of the blue laser, show that there are close lying absorption lines of both isotopologues within laser diodes temperature/wavelength acceptance bandwidth for certain crystal temperature (according to a matching curve 3.13b  $^3\text{He}_2^*$  -  $^4\text{He}_2^*$  : Q(2)-Q(5),Q(3)-Q(5),Q(5)-Q(7), Q(7)-Q(9), Q(8)-P(3), P(2)-P(3)).

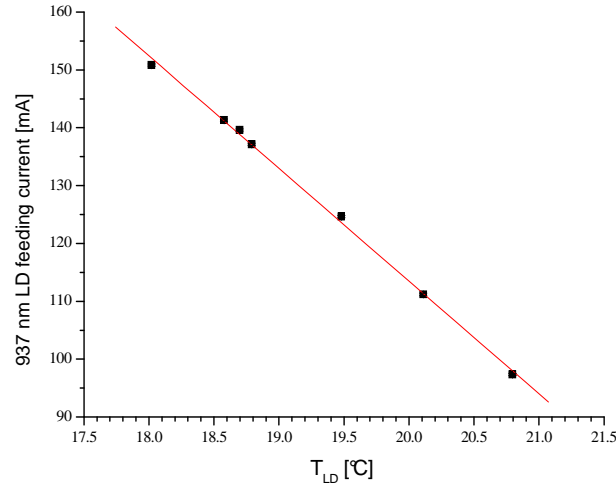


Figure 4.13: (a) Compensation of the wavelength change due to 937 nm laser diode current by the laser diodes temperature ( $T_{LD}$ ) change providing tuning of the blue laser setup to Q(2) transition of  $^3\text{He}_2^*$ ; (b) the proportionality curve of laser diode current  $I_{937}$  and control voltage  $V$ . Linear fits to both curves provide the slope values of  $dI/dV$  and  $dI/dT$  necessary for rescaling the voltage scale of the scans to the temperature.

Moreover, when the cell is filled with 1:1 proportion of both isotopes, there are expected also the absorption lines of the heteronuclear dimer ( $^3\text{He}-^4\text{He}$ )\* that, according to the mass scaling rules for the isotopes, are shifted in respect to their isotopologues' equivalents. For the heteronuclear dimer, due to lack of the symmetry of nuclei interchange, the overall symmetry properties results in presence of both even- and odd-N numbered lines (as for  $^3\text{He}_2^*$ ), however any of lines amplitude alternation is expected. Due to presence of the line of the heteronuclear dimers, there are only three pairs of 6 mentioned before  $^3\text{He}_2^*$  -  $^4\text{He}_2^*$  close lying doublets in which the homonuclear molecule lines are well resolved - see Fig. 4.14. In other cases one of the line in the pair is overlapped with the line of ( $^3\text{He}-^4\text{He}$ )\* - Fig.4.15. On both figures peaks are designated with proper letter for the rotational branch and the isotopic composition in the subscript (e.g.  $^{44}$  for  $^4\text{He}_2^*$ ,  $^{34}$  for ( $^3\text{He}-^4\text{He}$ )\* )

Using the mentioned mass scaling rules for molecular constants equations:(2.27), (2.28) and reference values of the constants for isotopic pure isotopologues from [6, 28] (see Appendix C), the constants are determined for the ( $^3\text{He}-^4\text{He}$ )\* (presented in table 4.6) and so the wavelengths of the rotational transitions Q(1-9), R(0), P(2) are calculated using eq.(2.19) together with the dependencies given in subsections 2.2.1 (b) and (c). The results of the calculations are presented in the table 4.7, together with the experimental results.

The positions of Q(3) and Q(4) lines of ( $^3\text{He}-^4\text{He}$ )\*, the only well resolved from two close lying (close enough to be able to scan together) isotopologues' neighboring lines, were determined from the frequency scans where three absorption lines were present - one line of heteronuclear dimer and two lines of pure  $^3\text{He}$  and  $^4\text{He}$  isotopologues. Q(3) of the heteronuclear dimer in the vicinity of the isotopologues lines is shown on the Fig.4.16, while Q(4) was presented on the Fig.4.14 (b). This gave the local value of  $\frac{d\lambda}{dV}$  and the position of heteronuclear dimer line was determined with better accuracy (0.002 nm).

Other local values of wavelength-voltage coefficient were determined using the frequency scans of line pairs (i.e. Fig.4.17) on which the Q(1)-Q(5) lines of isotopic pure isotopologues

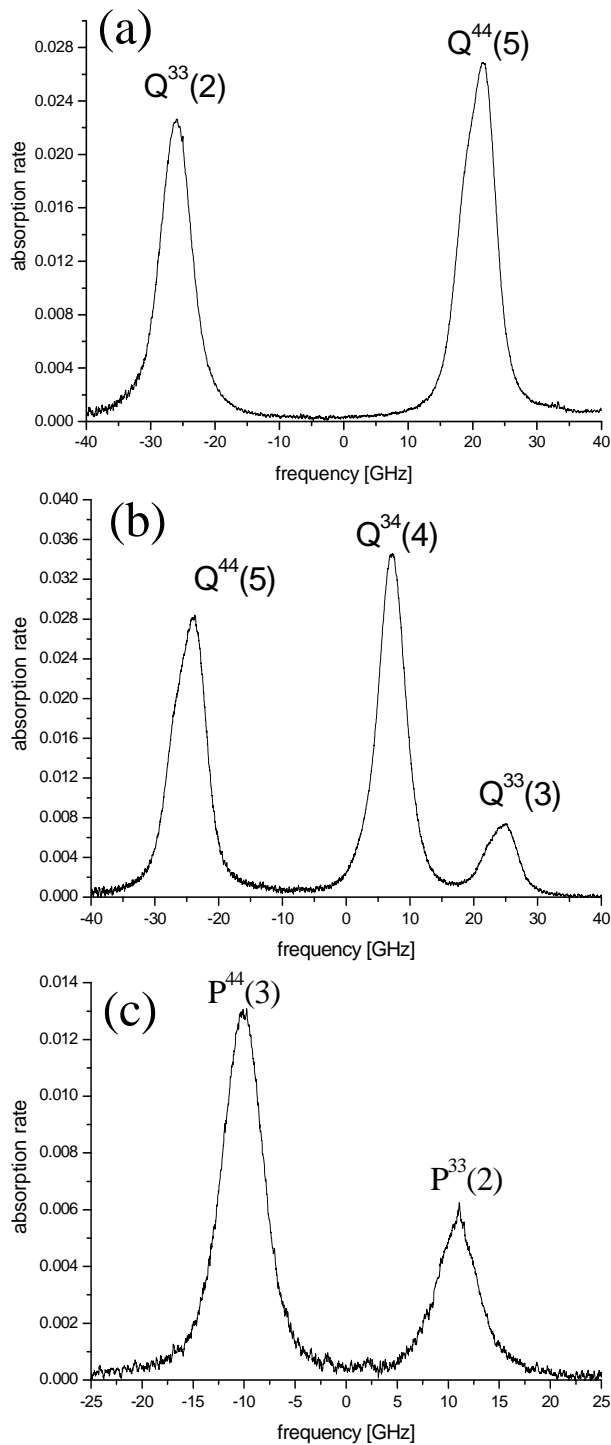


Figure 4.14: Three frequency scans of close lying molecular lines (a) doublet of  ${}^3\text{He}_2^*$  and  ${}^4\text{He}_2^*$  lines Q(2) and Q(5) respectively; (b) triplet consisting of  ${}^3\text{He}_2^*$ ,  ${}^4\text{He}_2^*$  and  $({}^3\text{He}-{}^4\text{He})^*$ ; doublet of P(3) and P(2)  ${}^4\text{He}_2^*$  and  ${}^3\text{He}_2^*$  isotopologues.

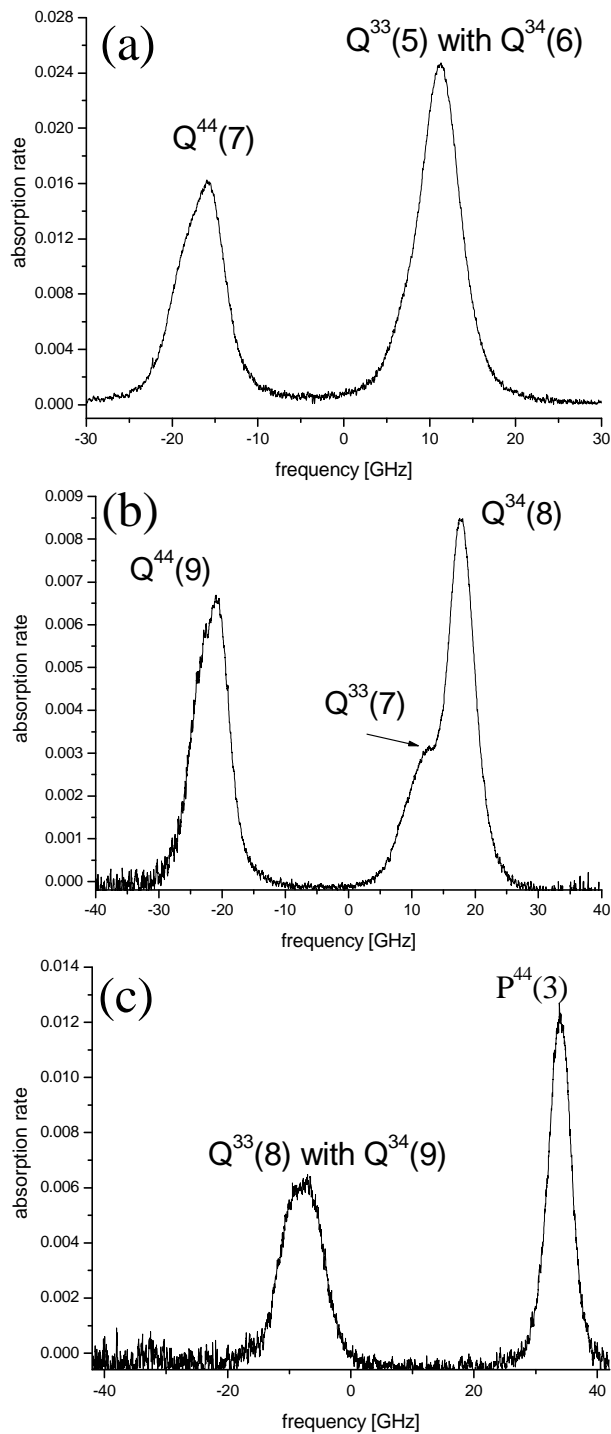


Figure 4.15: Frequency scans of close lying  ${}^3\text{He}_2^*$  and  ${}^4\text{He}_2^*$  molecular lines of which one is overlapped with the absorption line of  $({}^3\text{He}-{}^4\text{He})^*$ .

	$a^3\Sigma_u^+$	$e^3\Pi_g$
$B_0$	8.82	8.34
$D_0 \cdot 10^4$	7.49	7.02
$\omega_e$	1951.85	1856.69
$\omega_e x_e$	44.95	40.55
$T_e + G(v = 0)$	21503.37	

Table 4.6: Molecular constants for ( $^3\text{He}-^4\text{He}$ )\* calculated with use of the mass scaling relations applied to known rotational constants for  $^3\text{He}_2^*$  and  $^4\text{He}_2^*$  isotopologues.  $T_e + G(v = 0)$  is energy of so-called *band origin*. All the values are given in  $\text{cm}^{-1}$  unit.

Line designation	$\lambda_{calc}$ [nm]	$\lambda_{exp}$ [nm]	$\delta\lambda_{exp}$ [nm]	$\lambda_{ref}$ [46]
Q(1)	465.064	-	-	465.064
Q(2)	465.106	465.106	0.001	465.106
Q(3)	465.169	465.169	0.001	465.169
Q(4)	465.252	465.253	0.002	465.253
Q(5)	465.357	465.365	0.003	465.357
Q(6)	465.482	-	-	465.482
Q(7)	465.629	465.627	0.002	465.628
Q(8)	465.795	465.794	0.002	465.794
Q(9)	465.982	-	-	465.980
P(2)	465.828	465.838	0.003	465.832
R(0)	464.682	-	-	464.683

Table 4.7: Position in wavelength scale of 11 absorption lines of within expected tuning range of the blue laser.  $\lambda_{calc}$  values are calculated using the molecular constants (Table 4.6),  $\lambda_{exp}$  are experimentally determined positions of the lines,  $\delta\lambda_{exp}$  are the uncertainties of line positions determination in voltage scale and its scaling to the wavelengths. Calculated values of the positions are in very good agreement (within 3rd decimal place) with given in [46].

were present (due to different combinations multiple values within this range are given - see fig.3.8b). These values are equal within their uncertainties, thus weighted average was determined  $((3.52 \pm 0.01) \cdot 10^{-3} \text{ nmV}^{-1})$ , which can be used for voltage-wavelength scaling in the positions range between Q(1) and Q(5) of  $^3\text{He}_2^*$ .

The coefficient  $\frac{d\lambda}{dV}$  was also determined from the common scan of P(3) and P(2) lines of  $^4\text{He}_2^*$  and  $^3\text{He}_2^*$  Fig.4.14 (c) respectively.

Lines of ( $^3\text{He}-^4\text{He}$ )\* such as Q(1) (Fig.4.18), Q(6),Q(9) (Fig. 4.15 (a) and (c)) are completely overlapped with the lines of isotopologues, thus their precise position could not be determined.

The line Q(2) was recorded on the single scan together with Q(1) of  $^3\text{He}_2^*$  (Fig.4.17), thus, with the same value of  $\frac{d\lambda}{dV}$  as for Q(3) and Q(4) lines of ( $^3\text{He}-^4\text{He}$ )\*, the exact position could be determined from the experiment. The heteronuclear dimer lines Q(5), Q(7) (Fig.4.19(a) and (b)) and Q(8) (Fig.4.15(b)) are partially overlapped with isotopologue's neighbors on the frequency scans where two lines are present.

For those lines one should be aware of increased error in position (shift) due to the influence

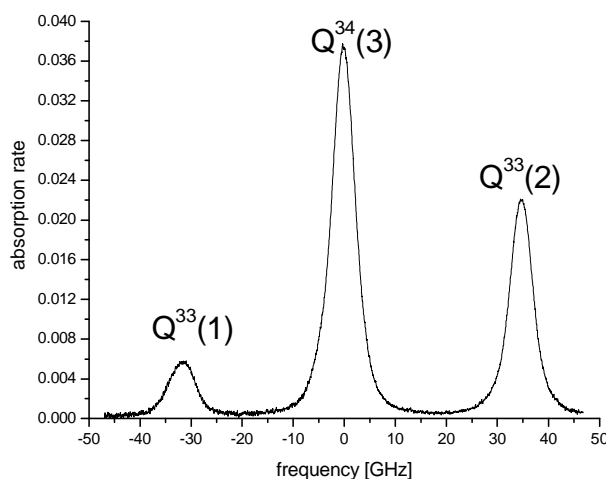


Figure 4.16: Frequency scans of close lying  ${}^3\text{He}_2^*$  and  ${}^4\text{He}_2^*$  molecular lines of which one is overlapped with the absorption line of  $({}^3\text{He}-{}^4\text{He})^*$ .

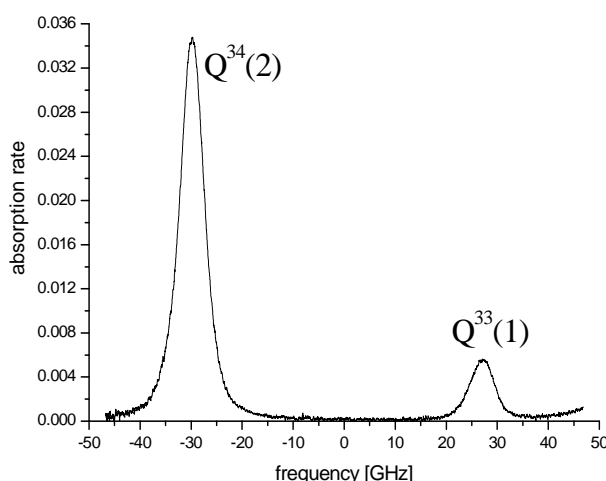


Figure 4.17: Example of the frequency scan containing only two absorption lines of  ${}^3\text{He}_2^*$  and  $({}^3\text{He}-{}^4\text{He})^*$  used to determination of mixture line position assuming the value of  $\frac{d\lambda}{dV}$  to be known from the frequency scan of 3 lines - including  $Q(1)$  of  ${}^3\text{He}_2^*$  - see Fig.4.16.

of the signal of the partner.  $Q(8)$  line is partially overlapped with  $Q(7)$  of  ${}^3\text{He}_2^*$ , however there is  $Q(9)$  of  ${}^4\text{He}_2^*$  on the scan that allows  $Q(8)$  scaling of position in the wavelength. In case of determination of  $({}^3\text{He}-{}^4\text{He})^*$   $Q(5)$  line partially overlapped with  ${}^3\text{He}_2^*$   $Q(4)$  also the value of  $\frac{d\lambda}{dV} = 0.00352$  was used.

For  $Q(7)$  and  $Q(8)$  lines the wavelength-voltage coefficient is in between the values obtained for  $Q(3), Q(4)$  and for  $P(3)$  ( ${}^4\text{He}_2^*$ ),  $P(2)$  ( ${}^3\text{He}_2^*$ ) (value placed on the fig.3.8b). Thus, the positions of  $Q(7)$  and  $Q(8)$  were determined using both values of  $\frac{d\lambda}{dV}$ . As the results the average of positions values was taken together with the averaged errors.  $P(2)$  line was recorded on a single frequency scan with  $Q(8)$  (Fig.4.19(c)) for which the wavelength position is also determined here. The error of  $Q(8)$  wavelength position determination adds up to the value uncertainty for  $P(2)$  line. No information about  $\frac{d\lambda}{dV}$  in the vicinity of  $R(0)$  line results in the lack of wavelength position scaling for this line, despite of the fact, that it is present with  $R(0)$  line

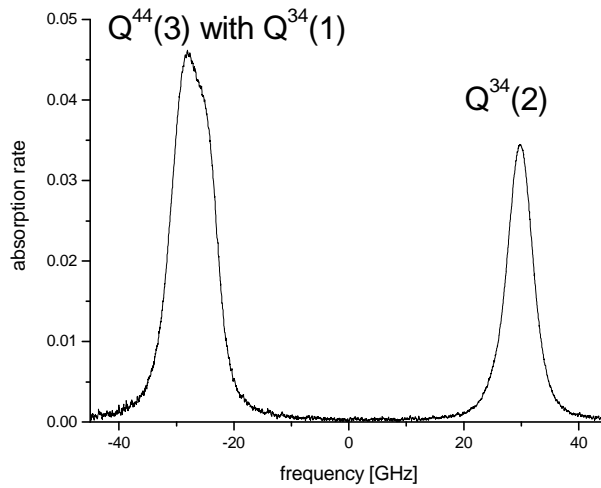


Figure 4.18: Frequency scans of three absorption lines: two of the  $(^3\text{He}-^4\text{He})^*$  molecule and one of  $^4\text{He}_2^*$  overlapped with one of the former ones.

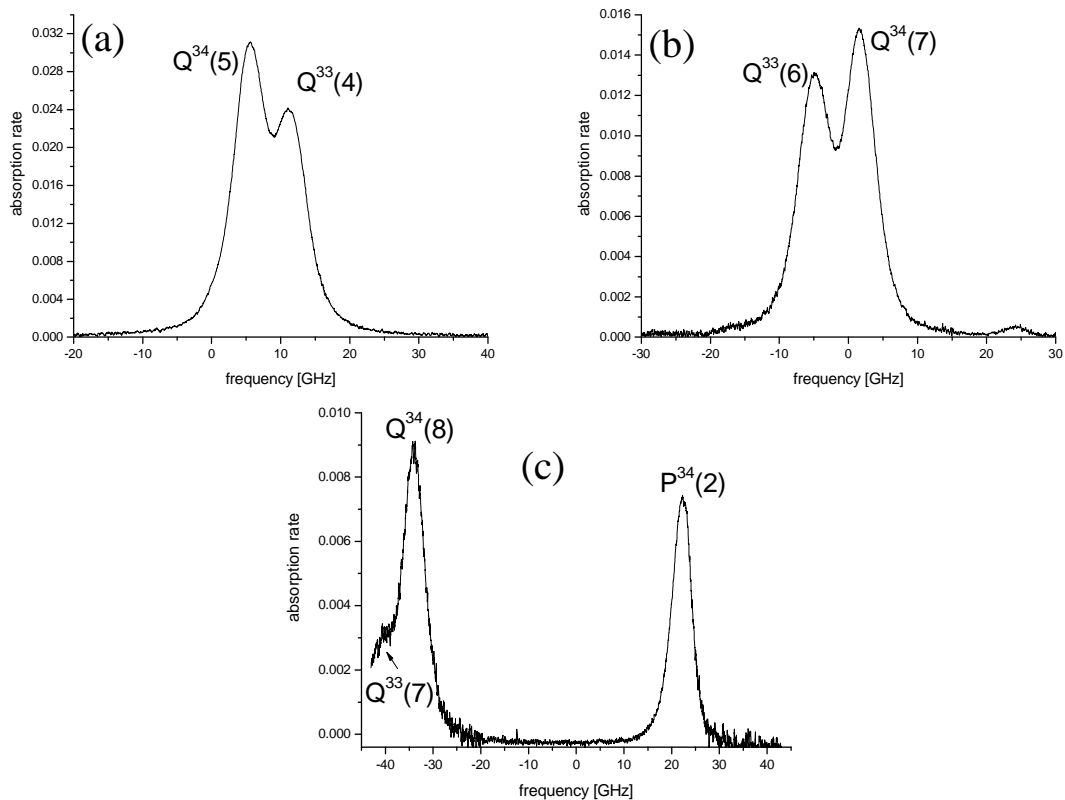


Figure 4.19: Frequency scans of partially overlapped absorption lines of  $^3\text{He}_2^*$  and  $(^3\text{He}-^4\text{He})^*$ . Graph (c) can be compared with Fig.4.15(b) where the same complex of  $Q^{34}(8)$  and  $Q^{33}(7)$  is shown, however, here the range of higher frequency is presented containing the  $P^{34}(2)$  absorption line.

of  ${}^3\text{He}_2^*$  on single frequency scan - Fig.4.20. However, using  $({}^3\text{He}-{}^4\text{He})^*$  wavelength data [46], the value of  $\frac{d\lambda}{dV}$  shown on the fig. 3.8b was determined.

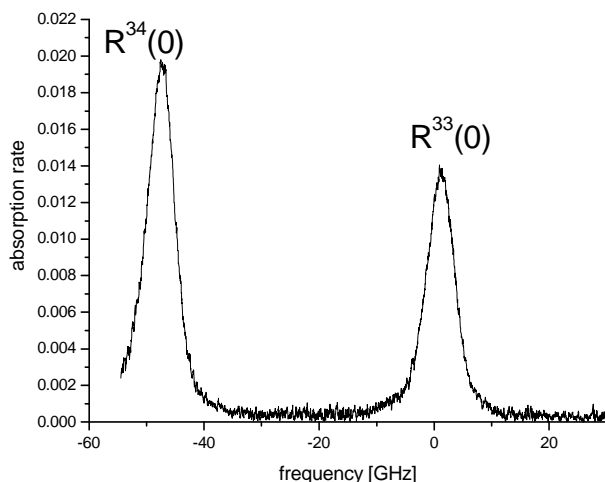


Figure 4.20: Frequency scans of partially overlapped absorption lines of  ${}^3\text{He}_2^*$  and  $({}^3\text{He}-{}^4\text{He})^*$

After the time when the calculation had been made and experimental confirmation of obtained results was performed, the reference [46] was found staying in well agreement with Author's calculations (within 3rd decimal place - the order of accuracy of the data presented in [46] and in the sources of the rotational constants for  ${}^3\text{He}_2^*$  and  ${}^4\text{He}_2^*$ , as well as given molecular constants error). The mentioned reference was found much later the calculations and the measurements were made and serves as a check of calculations correctness, especially with the peak positions that are not available experimentally due to the lines overlapping.

The accurate values of the absorption rate measured for presented molecular transitions of three helium molecule isotopologues are presented in the table 4.8. Here as well the two discharge regimes - weak and strong are considered. In the table the overlapping of respective lines has been explicitly given mentioning which line is partially or totally overlapped with the isotopologue's neighbor.

Line designation	Absorption [%]					
	66.7 mbar 1:1 $^3\text{He}:$ $^4\text{He}$ mixture					
	weak discharges			strong discharges		
$D_0$	NR			86.51		
	$^3\text{He}_2^*$	$^4\text{He}_2^*$	$(^3\text{He}-^4\text{He})^*$	$^3\text{He}_2^*$	$^4\text{He}_2^*$	$(^3\text{He}-^4\text{He})^*$
Q(1)	0.10	0.38	o Q <sup>44</sup> (3)	0.55	2.25	o Q <sup>44</sup> (3)
Q(2)	0.38	–	0.75	2.20	–	3.43
Q(3)	0.12	o Q <sup>34</sup> (1)	0.69	0.74	o Q <sup>34</sup> (1)	3.65
Q(4)	po Q <sup>34</sup> (5)	–	0.58	po Q <sup>34</sup> (5)	–	3.46
Q(5)	o Q <sup>34</sup> (6)	0.39	po Q <sup>33</sup> (4)	o Q <sup>34</sup> (6)	3.10	po Q <sup>33</sup> (4)
Q(6)	po Q <sup>34</sup> (7)	–	o Q <sup>33</sup> (5)	po Q <sup>34</sup> (7)	–	o Q <sup>33</sup> (5)
Q(7)	o Q <sup>34</sup> (8)	0.23	po Q <sup>33</sup> (6)	o Q <sup>34</sup> (8)	1.60	po Q <sup>33</sup> (6)
Q(8)	o Q <sup>34</sup> (9)	–	o Q <sup>33</sup> (7)	o Q <sup>34</sup> (9)	–	o Q <sup>33</sup> (7)
Q(9)	NA	0.10	o Q <sup>33</sup> (8)	NA	0.66	o Q <sup>33</sup> (8)
P(2)	NR	–	0.15	0.58	–	0.73
P(3)	NA	NR	NA	NA	1.28	NA
R(0)	NR	–	NR	1.36	NA	1.94

Table 4.8: Absorption values for observed molecular transitions for  $^3\text{He}_2^*$ ,  $^4\text{He}_2^*$  and  $(^3\text{He}-^4\text{He})^*$  at 66.7 mbar of isotopic 1:1 mixture cell. Two discharge regimes are considered of weak and strong rf excitation. Some molecular absorption lines are totally (o) or partially (po) overlapped with close lying lines of other isotopologue. Some lines are not available for detection (NA) due to limited blue laser tuning range, there are lines absorptions that has not been measures (NR)

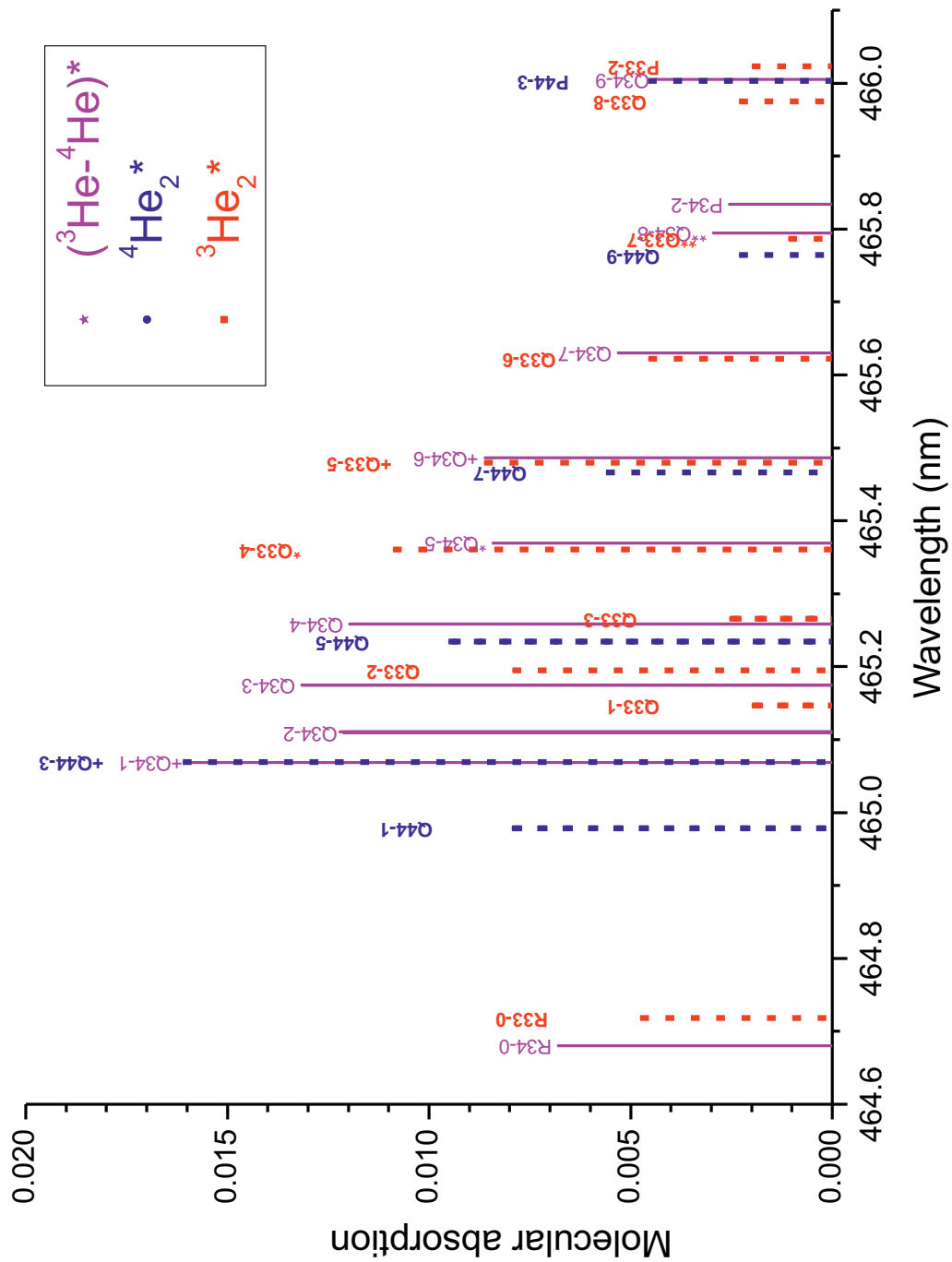


Figure 4.21: Positions of all the helium molecule isotopologues  $^3\text{He}^*_2$ ,  $^4\text{He}^*_2$  and  $(^3\text{He}-^4\text{He})^*$  absorption lines of  $a^3\Sigma^+_u(0) - e^3\Pi_g(0)$  transition around 465 nm. Overlapping of the lines are present according to the information in the Table 4.8

## 4.5 Intensities of absorption lines

### 4.5.1 Rotational temperature determination from relative absorption rates

Apart from the numerical factors of the line oscillator strength (discussed in subsection 2.2.4), the Doppler and pressure broadening values  $\omega_G$  and  $\omega_L$  required in the spectral term of the cross-section (see (A.6),(A.16)) and besides the light transmission value when the frequency is tuned to the chosen transition ( $\omega_{if}$ ), the gas rotational temperature  $T$  (that appears in eq.(2.51)) is needed for absolute molecular density  $N_M$  determination. This temperature is commonly standing as  $T_{rot}$ .

For the determination of  $T_{rot}$  value the knowledge of relative line intensities within one pressure cell and discharge condition is sufficient. In case of such ratios, several factors present in the cross-sections  $\sigma_{fi}$  and line strengths  $s^i$  definitions simplify, as the electronic and vibrational terms are common here, as well as total electronic spin value and  $\Lambda$  quantum number are the same for each of transitions between rotational sublevels of  $a^3\Sigma_u^+$  and  $e^3\Pi_g$  states. If  $T_1$  and  $T_2$  stand for the transmission values for the laser beam tuned to transitions occurring from  $N_1''$  and  $N_2''$  rotational sublevels, their ratio can be expressed as:

$$\frac{T_1}{T_2} = \frac{\phi_1 S_{HL}(N_1', N_1'')}{\phi_2 S_{HL}(N_1', N_2'')} \exp\left(-\frac{hc}{kT_{rot}}(F(N_1'') - F(N_2''))\right) \quad (4.6)$$

As before (subsection 2.2.4)  $S_{HL}(N', N'')$  is the Hönl-London coefficient adequate to considered branch (P,Q or R);  $\phi$  is a parameter depending on the parity of the sublevel ( $a, s$  for like nuclei). All these parameters are known and were discussed in mentioned subsection. Their values are given explicitly in the Tables 4.9 and 4.10 for observed transitions together with their relative peak amplitudes in respect to Q(2) and Q(3) transitions for  $^3\text{He}_2^*$  and  $^4\text{He}_2^*$  molecules respectively for investigated pressures of 8, 66.7, 128 and 266.7 mbar. The values of rotational energies of the  $N''$  sublevels has been calculated using the eq. (2.21b) applying the rotational constants met in [6] and [28] for  $^3\text{He}_2^*$  and  $^4\text{He}_2^*$  respectively. These constants has been determined assuming that the observed lines correspond to single transition within the rotational sublevels structure of  $a^3\Sigma_u^+$  and  $e^3\Pi_g$  states. However, as discussed in the section 4.3 this is not the case, as clear evidence of the line structure is presented in the absorption line frequency scans. This leads to the lower accuracy in determined molecular constant values in [6, 28] that has been applied here. This uncertainty on rotational constants and later on the rotational energies and then fit of linear function to extract the  $T_{rot}$  value is hard to estimate and won't be performed here, however one has to take it into account when the results will be compared and unexplained discrepancies met.

Line designation	$N''$	$F(N'')$ [ $\text{cm}^{-1}$ ]	$S_{HL}(N', N'')$	$\phi$	Relative (to Q(2)) $OUT_nLIA$				
					8	66.7 w	66.7 s [mbar]	128	266.7
Q1	1	20.09	4.5	0.25	0.22	0.24	0.24	0.25	0.23
Q2	2	60.24	7.5	0.75	1.00	1.00	1.00	1.00	1.00
Q3	3	120.41	10.5	0.25	0.32	0.31	0.31	0.34	0.30
Q4	4	200.53	13.5	0.75	0.97	0.94	0.91	0.77	0.81
Q5	5	300.5	16.5	0.25	0.19	0.22	0.22	0.22	0.23
Q6	6	420.21	19.5	0.75	0.54	0.53	0.51	0.50	0.48
Q7	7	559.52	22.5	0.25	0.09	0.10	0.10	0.10	0.10
Q8	8	718.25	25.5	0.75	0.23	0.19	0.18	0.18	0.17
P2	2	60.24	$\frac{3}{2}(N'' - 1)$	1.5	NR	0.25	0.23	0.23	0.21
R0	0	0	$\frac{3}{2}(N'' + 1)$	3	NR	0.61	0.56	NR	NR
$T_{rot}$ [K]					<b>331±9</b>	<b>313±8</b>	<b>320±6</b>	<b>314±13</b>	<b>318±8</b>
Discharge amplitude modulation function type					SIN	SQ	SIN	SIN	SIN
Absorption on Q(2) transition [%]					0.24	5.07	11.53	11.68	9.22
X factor					1.56	NC	10.41	12.28	7.08

Table 4.9: Pressure compilation of the relative (in respect to the value for Q(2) transition) absorption lines amplitudes of numerical lock-in output data for  $^3\text{He}_2^*$ . These data has been used for the  $T_{rot}$  determination (see fig.4.22) using the relation (4.6). The results of obtained rotational temperatures are presented as well. Error values  $\delta T_{rot}$  results from the error on line intensities determination of which the ratios were used for temperature determination through the linear fit. In the lowest rows of the table the absolute absorption values measured on the Q(2) transition has been given as a reminder (see Table 4.4) of the considered order of magnitude as well as, for the sine modulation, the X factor values that were applied in  $OUT_nLIA$ -to-absorption scaling (see subsection 4.2.3.2). Abbreviations:  $n$  - density of atoms in  $2^3S_1$  state,  $w$  - weak discharges excitation,  $s$  - strong discharge excitation SIN, SQ - partial sinusoidal and 100% square amplitude modulation, NR- not recorded, NC- not considered for 100% square modulation

If the  $T_2$  is fixed to be the transmission for one chosen line (i.e. Q(2) for  $^3\text{He}_2^*$ ) and  $T_1$  is going through all the transmission values obtained for all the other lines within the pressure cell, isotope and discharge conditions, the dependency of the transmission ratios on the rotational energy differences  $\Delta F = F(N'_1) - F(N'_2)$  can be set - it is linear when the natural logarithm of the transmission ratio is taken and the ratios of  $\phi$  and Hönl-London factors are calculated. Fitting the linear function, the slope is obtained, that, through the velocity of the light  $c$ , Planck's  $h$  and Boltzmann  $k$  constants leads to the value of  $T_{rot}$ . On the figure 4.22, the performed fits for  $T_{rot}$  determination for different pressures of  $^3\text{He}$  are shown, and the obtained values of the temperature are given in the Table 4.9. The intensity of P(2) line of  $^3\text{He}_2^*$  was not taken into account in the linear fit, as is overlapped with the R(2) line of (1-1) vibrational band.

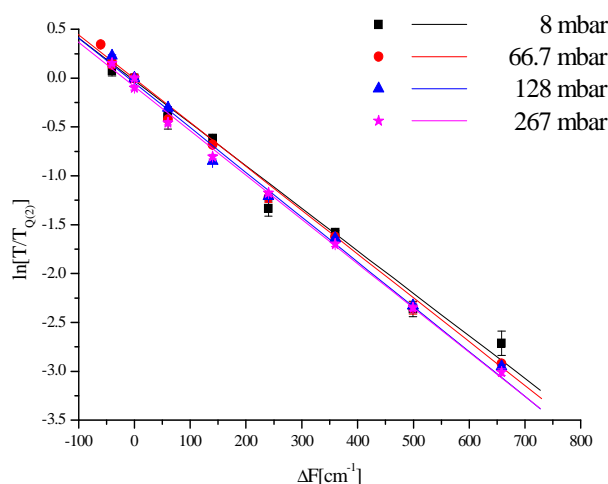


Figure 4.22: Comparison of the linear fits to the  $\ln(T/T_{Q(2)})$  (under the natural logarithm - the relative blue light transmission ratio for chosen transition from N rotational sublevel);  $T_{Q(2)}$  is a blue laser beam transmission tuned to Q(2) transition) dependency on rotational sublevels energy difference  $\Delta_F = F(N) - F(2)$  in 8, 66.7, 128 and 266 mbar pure  $^3\text{He}$  cell. From the slope value the rotational temperature  $T_{rot}$  has been determined (see the text and the Table 4.9)

Across the considered pressure range no significant (beyond the error values) change of rotational temperature value is observed. The only exception is the data for 8 mbar pressure, where increased value is noticed. However, it is not clear if this is the effect of the pressure change on  $T_{rot}$  (not observed for example between 67 and 266 mbar) or the low SNR for the frequency scans at this lowest pressure, affecting the line intensities values and thus their ratios. Besides the value for 8 mbar, the average  $T_{rot} = 318 \pm 4\text{K}$  was determined. This value is reasonable as it is close to the expected gas temperature inside the cell with applied rf discharges - increase of the temperature could be felt with hand (no dedicated measurement was performed) and could be roughly estimated to be slightly above human body temperature - it agrees with the value of  $45^\circ\text{C}$ .

It is difficult to state about the difference in  $T_{rot}$  temperature between the two discharge regimes within the same pressure cell. For both isotopologues  $^3\text{He}_2^*$  and  $^4\text{He}_2^*$  the differences in rotational temperature for weak and strong discharge excitation are within the error bars of both  $T_{rot}$  values (see Table 4.9 and 4.10), however the tendency of a slight increase by 7 and 2 K respectively in the temperature with increase of the excitation amplitude would be in agreement with the expectations - it could be felt that the cell heats up more for the stronger discharges.

Line designation	$N''$	$F(N'')$ [cm <sup>-1</sup> ]	$S_{HL}(N', N'')$		$\phi$	Relative (to Q(3)) <i>OUT<sub>n</sub>LIA</i>	
						66.7 [mbar]	
						weak	strong
Q1	1	15.17	$\frac{3}{2}(2 \cdot N'' + 1)$	4.5	1	0.69	0.66
Q3	3	90.97		10.5		1.00	1.00
Q5	5	227.12		16.5		0.82	0.82
Q7	7	423.16		22.5		0.43	0.46
Q9	9	678.40		28.5		0.18	0.18
P3	3	90.97	$\frac{3}{2}(N'' - 1)$	3		0.35	0.37
<b><math>T_{rot}</math> [K]</b>						<b>306±5</b>	<b>308±6</b>
Discharge amplitude modulation function type						SQ	SIN
Absorption on Q(3) transition [%]						4.34	14.23
X factor						NC	8.84

Table 4.10: Pressure compilation of the relative (in respect to the value for Q(3) transition) absorption lines amplitudes of numerical lock-in output data for <sup>4</sup>He<sub>2</sub><sup>\*</sup>. These data has been used for the  $T_{rot}$  determination (see fig.4.23) using the relation (4.6). The results of obtained rotational temperatures are presented as well. Error values  $\delta T_{rot}$  results from the error on line intensities determination of which the ratios were used for temperature determination through the linear fit. In the lowest rows of the table the absolute absorption values measured on the Q(2) transition has been given as a reminder (see Table 4.5) of the considered order of magnitude as well as, for the sine modulation, the X factor value that were applied in *OUT<sub>n</sub>LIA*-to-absorption scaling (see subsection 4.2.3.2). Abbreviations: SIN, SQ partial sinusoidal and 100% square amplitude modulation, NC not considered for 100% square modulation

The change of  $T_{rot}$  with different isotope was investigated for two 66.7 mbar cells filled with <sup>3</sup>He and <sup>4</sup>He as well as in 67 mbar mixture cell only for <sup>4</sup>He (see comment further in the text) - Fig.4.23.

Presented values shows the decrease of  $T_{rot}$  between two isotopologues, going from <sup>3</sup>He to <sup>4</sup>He, what is expected behavior even from the model of simple rigid rotor, for which the rotational temperature is inversely proportional to the moment of inertia, that increases with molecule mass. The consistency of this dependency could not be checked using the value of  $T_{rot}$  for (<sup>3</sup>He-<sup>4</sup>He)\* for the reason discussed below.

In case of the cell filled with 67 mbar 1:1 helium isotopic mixture the reliable determination of the  $T_{rot}$  for the (<sup>3</sup>He-<sup>4</sup>He)\* as well as <sup>3</sup>He<sub>2</sub><sup>\*</sup> was not possible due to insufficient number of well resolved lines. Partially overlapped lines could not be used, as their measured intensity would not correspond to the population of the  $N''$  sublevel and thus would give the transmission ratio not reflecting the rotational temperature distribution. For (<sup>3</sup>He-<sup>4</sup>He)\* 4 lines were available, however, corresponding to the transition occurring from the neighboring rotational sublevels. Thus, the small range of  $\Delta F$  values (-60 to 120 cm<sup>-1</sup>) allow obtaining  $T_{rot} = 284 \pm 7K$  that could not be trusted, especially when in similar case of <sup>3</sup>He<sub>2</sub><sup>\*</sup>, the fit to only three available points within  $\Delta F$  (-40 to 60 cm<sup>-1</sup>) gave unreasonable value of  $T_{rot} = 236 \pm 8K$ , much below the room temperature and the results obtained earlier for the same pressure and similar

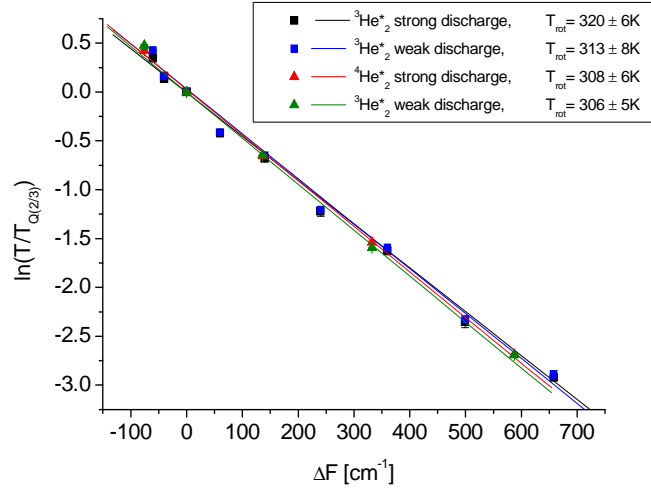


Figure 4.23: Comparison of the rotational temperatures between two isotopologues  ${}^3\text{He}_2^*$  and  ${}^4\text{He}_2^*$  at the pressure of 66.7 mbar. Investigations were performed in two separate isotopic pure cells for two discharge regimes - weak and strong in each case. Change in the slope value indicates the change in  $T_{rot}$ . Higher the absolute value of the negative slope, lower the temperature - for the weak discharges  $T_{rot}$  is lower than for strong discharge regime in case of both isotopologues. Temperatures are higher for  ${}^3\text{He}_2^*$  than for  ${}^4\text{He}_2^*$ .

discharge conditions. However, the spectral lines for  ${}^4\text{He}_2^*$ , except Q(3) do not coincide with any of other isotopologue's, and determination of rotational temperature confirmed previously obtained values ( $T_{rot} = 299 \pm 13\text{K}$ ).

Obtained results of the rotational temperature  $T_{rot}$  are close to the room temperature of the experiment and estimated temperature of the cell with rf discharge applied. Similar experimental conditions has been met in [64] where  ${}^4\text{He}_2^*$  has been investigated in the pressure range of 2 to 160 mbar. Authors report about two coexisting thermal ensembles up to  $N'' = 9$  and for  $N'' > 9$  for which two different temperatures has been determined: about 300K and 2000 K respectively. According to their division, in this work only low temperature ensemble is available for the investigations and fair agreement has been obtained in comparison with reported value that is given as approximated one without the error value. Higher rotational sublevels are out of the laser source range can't be investigated nor compared with this reference. Also [6] reference mention about change in the slope of the linear fit for rotational temperature determination, however much stronger discharge excitation has been used and therefore temperatures ranging between 580 to 820 K are reported.

## 4.5.2 Dynamics of helium molecule

Measurements of the transmission using continuous wave laser source as it is the case of 465 nm laser setup allows following of the molecular dynamics, that is the decay process of their density when the discharge plasma fades after the applied alternate voltage is stopped. At the beginning, before the discharge is being switched off the processes of formation and destruction of molecular species are in balance, so the steady state is set, the density of metastable molecule is constant. When the discharges are turned off, the decay of metastable atoms species results in simultaneous decrease of the three body collisions being the source of the molecules in  $a^3\Sigma_u^+$

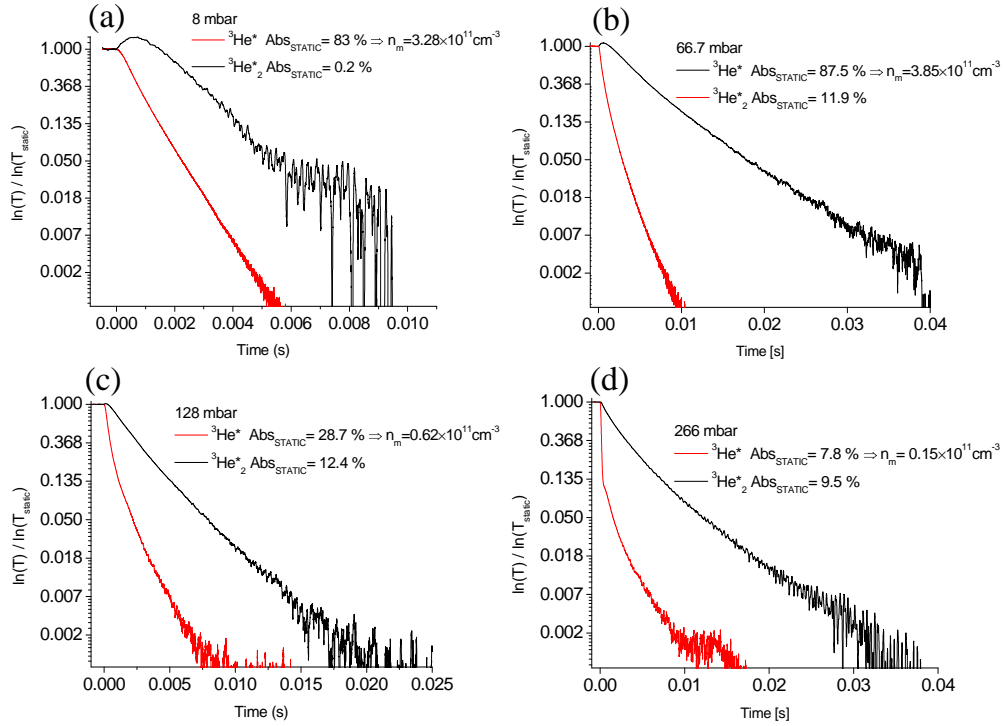


Figure 4.24: Time decay curves of atomic (red lines) and molecular (black lines) relative to the static situation (before switching off the plasma discharges -for Time <0 s on the graphs) densities expressed as the ratio of transmission logarithms  $\ln(T)/\ln(T_{static})$  in pure  $^3\text{He}$  cells at: (a) 8 mbar, (b) 66.7 mbar, (c) 128 mbar, (d) 267 mbar. Ordinate axis on graphs (a)-(d) are in ln scale showing non-exponential character of both atomic and molecular decays.

state. Predominance of the destruction processes results in progressive decrease of their density. This behavior can be observed by the laser transmission changes observation that reflects the metastable molecules density variations. By the comparison between the decay processes of metastable atoms and molecules, the proper terms in differential equations describing the dynamics of both related species can be identified and characterized quantitatively. As it will be shown those decays are not simply exponential what is a consequence of variety of occurring processes of the destruction and domination of one over the others. Also the gas pressure change has its consequences in the shape of the decay curve giving the information about the increase importance of the destruction terms related to this intensive parameter.

#### 4.5.2.1 Molecular and atomic density decay curves

The recordings of the transmission decays were performed in four different gas pressure between 8 and 266 mbar of  $^3\text{He}$  gas as well as for isotopic pure  $^3\text{He}$ ,  $^4\text{He}$  and mixture at 66.7 mbar when no optical pumping is performed (neglecting formation from  $\text{He}(2^3\text{P})$ ). As a result of measurements described in subsection 4.1.3, proportional to the absorber density  $-\ln(T)$  value change in time is obtained as presented on figures 4.24. The dynamics for both atomic and molecular species are shown. The non-exponential character of the decays of both atomic and molecular densities is clearly visible on the plots in the ln scale, where simple exponential dependency should result in the linear change in time.

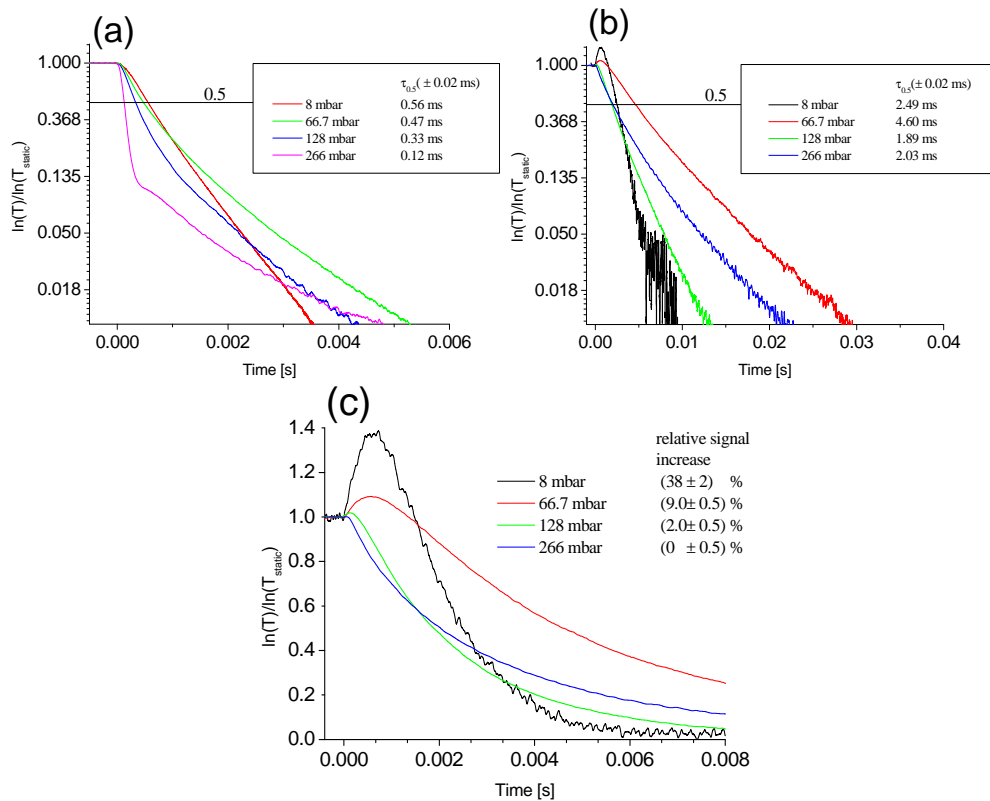


Figure 4.25: Pressure change of the atomic (a) and molecular (b) decay times. The values of half-decay  $\tau_{0.5}$  are given on the graphs for every pressure,  $y=0.5$  curve is plotted as a guide for the eye. The early time decay part is blown-up on the graph (c) to present the increase of molecular density in respect to the static value before Time=0 s. The percentage values of signal increase are given for each pressure.

Comparing the decay curves for the atoms and molecules for pressure range between 8 - 266 mbar on Fig.4.24(a)-(d) , one can see the difference not only in the decay rate between both species, but also the character of this process is different.

For the atoms, the half-decay rate  $\tau_{0.5}$  (time after which the absorber density reaches the half of the initial value - before the plasma discharge is being switched off) decreases with pressure - Fig.4.25(a) - what is expected due to pressure dependent auto-ionizing Penning collisions and association into the molecular species. There is no such tendency in the decay half-times for the molecules - Fig.4.25(b). In case of the molecules, just after the discharge is being turned off, there is an increase of  $-\ln(T)$  value at early times ( 0.1-0.7 ms) for 128 - 8 mbar respectively. The effect decreases with pressure - Fig.4.25(c), starting at the increase of 38% in respect to the static value for 8 mbar ending at almost no increase ( 0.1%) after discharge turning off at 266 mbar. Such effect does not occur for the atoms, however for the latter the decay at the highest considered pressure is worth noting. Up to about 0.3 ms the decay is much rapid then for the later times - the effect is increased when going from lower to higher pressure indicating that there are different leading processes of metastable atoms density decay at considered time periods. The fact, that both - the increase of the molecular density and the change of the atomic decay slope occurs at common time scale of gives the indication of relation between the decrease of metastable atoms number and increase of molecular density.

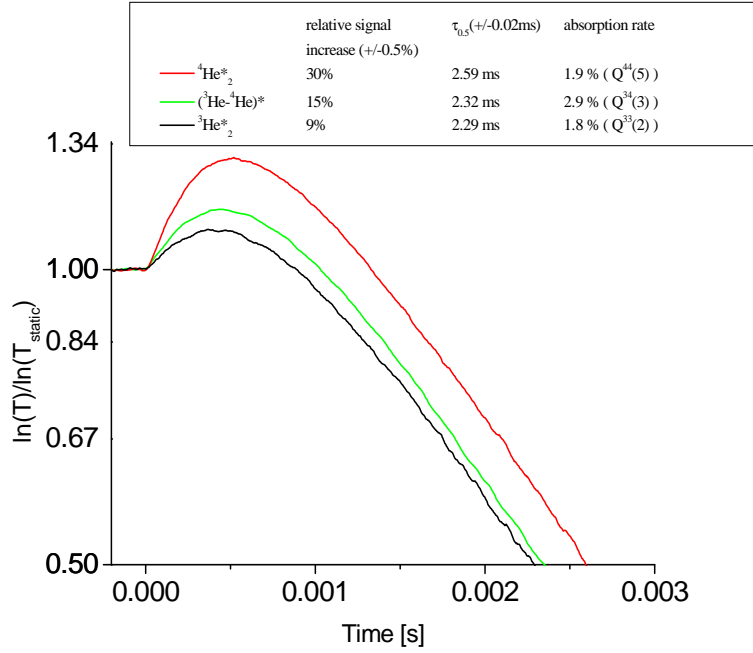


Figure 4.26: Difference between the decay curves for three isotopologues of  $\text{He}_2^*$ . Relative increase of the molecular density is given on the graph as well as half-decay times and static molecular absorption are compared - both increase with the mass of molecule.

The difference is also visible when comparing the molecular decays between three isotopologues. The increase of the  $-\ln(T)$  signal at early times ( 0.4 ms) is the lowest for the  $^3\text{He}_2^*$  and rises with the mass of the molecule, so as the half-decay time.

In contrast to the molecular species, the comparison of the atomic  $^4\text{He}$  and  $^3\text{He}$  decay curves does not exhibit any qualitative or quantitative difference - Fig.4.27.

#### 4.5.2.2 Atomic and molecular coupled rate equations

As the molecular species formation relies on the three-body collision between the excited state atom and two ground state atoms, one expect the rate equation of formation and destruction of molecular and atomic species to be coupled. As the processes driving the both atomic and molecular species population changes  $\frac{\partial n_m}{\partial t}$  and  $\frac{\partial N_M}{\partial t}$  are common it is useful to mention them together allowing straightforward comparison as well as emphasizing the coupling terms in which both populations occur simultaneously.

Making use of the terms presented in the Table 4.11 global evolution equations can be written for both metastable species as follows:

$$\frac{\partial n_m}{\partial t} = D_{at} \nabla^2 n_m - \delta_m P^2 n_s - \beta_{at} n_m^2 - \frac{1}{2} \alpha n_m N_M + \text{creation}_{n_m} \quad (4.7)$$

$$\frac{\partial N_M}{\partial t} = D_{mol} \nabla^2 N_M + \delta_m P^2 n_s - \beta_{mol} N_M^2 - \frac{1}{2} \alpha n_m N_M + \text{creation}_{N_M} \quad (4.8)$$

Presented equations refers to the situation when no laser enhanced molecular formation takes place - no OP pump beam present. In this conditions the term  $\pm \delta_p^2 n_P P^2$  related to the formation from  $\text{He}(2^3P)$  has been neglected in both equations.

Term description	Equation rate term	
	$\frac{\partial n_m}{\partial t}$ for He( $2^3S$ )	$\frac{\partial N_M}{\partial t}$ for He <sub>2</sub> ( $a\Sigma_u^+$ )
Diffusion term - atoms and molecules freely diffuse due to their densities gradients. It is assumed that the densities are null at the cell wall surface due to collisional de-excitation.	$D_{at}\nabla^2 n_m$ $D_{at}$ - diffusion coefficient for helium atom	$D_{mol}\nabla^2 N_M$ $D_{mol}$ - diffusion coefficient for helium atom
Conversion of metastable atoms into the molecule in 3 body collision - see eq.(2.1) (presence of ground state atoms impose the pressure dependency of $P^2$ )	$-\delta_m P^2 n_s$ $\delta_m$ - creation rate from the $2^3S_1$ state (see section 2.1)	$+\delta_m P^2 n_s$
Ionization collisions within one species - Penning collisions with the destruction rates $\beta_{at}$ and $\beta_{mol}$ for atoms and molecules respectively.	$-\beta_{at} n_m^2$	$-\beta_{mol} N_M^2$
Ionization collisions between the two considered species with common destruction rate $\alpha$	$-\frac{1}{2}\alpha n_m N_M$	
Creation rates through the electron-ion recombination	$+creation_{n_m}$ i.e. electron capture and ionization	$+creation_{N_M}$ i.e. electron capture and ionization, autoionization, vibrational relaxation, dissociative recombination

Table 4.11: Atomic and molecular rates terms for creation and destruction processes in condition of no OP performance.

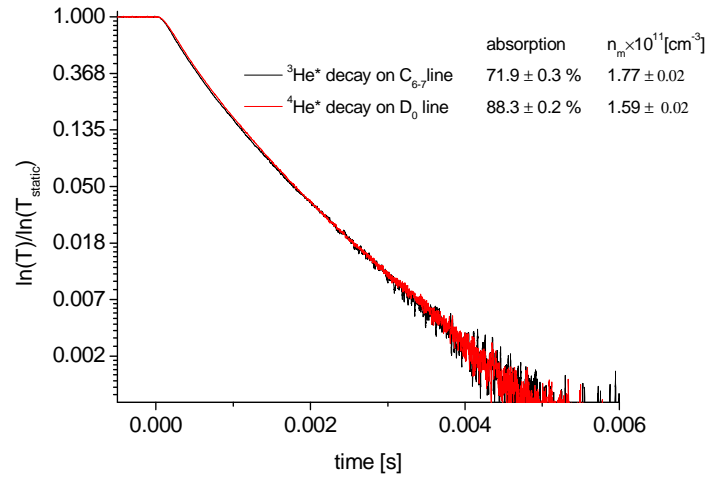


Figure 4.27: Comparison of the atomic  $^3\text{He}$  and  $^4\text{He}$  density decay curves in the 1:1 isotopic mixture cell at 66.7 mbar. Absorption values and corresponding  $n_m$  densities are given on the figure measured on  $\text{C}_{6-7}$  and  $\text{D}_0$  transitions.  $\text{C}_8$  nor  $\text{C}_9$  has been used to determinate metastable atoms density for  $^3\text{He}$  as they overlap with  $\text{D}_1$  and  $\text{D}_2$  transition lines of the second isotope in the gas mixture - see Fig.5.1.

Preliminary numerical analysis of the atomic and molecular coupled equation rates that relies on molecular creation through 3-body collisions and destruction processes in Penning collisions and quenching between two metastable species, provides qualitative reconstruction of the time evolution behavior of both densities including:

- the increase of  $N_M$  above the equilibrium value (when the discharges are still *on* before the decay recording) in early decay ( $\approx 0.5$  ms), the difference of the increase magnitude between three isotopologues and disappearance of the effect with the pressure increase
- differences in the decay speed between isotopologues
- identity of the time evolution for metastable  $^3\text{He}$  and  $^3\text{He}$  in the mixture cell recordings
- correct orders of magnitude of observed changes when the rate values for formation and Penning collisions from [54] (shown in the 4.12) with experimental  $n_m$  values as input.

Required parameters standing next to the rate terms of the Table 4.11 has been found in the literature and are compiled in the Table 4.12.

Parameter name	Rate equation parameters values	
	${}^3\text{He}^*$	${}^3\text{He}^*_2$
Diffusion coefficient [ $\text{cm}^2\text{Torr s}^{-1}$ ]	$D_{at} = (554 \pm 30)^{[65]}$	$D_{mol} = (416 \pm 39)^{(*)}$
$\delta_m$ [ $\text{Torr}^{-2}\text{s}^{-1}$ ]	$(0.16 \pm 0.04)^{[15]}$	
$\beta \times 10^{-9}$ [ $\text{cm}^3\text{s}^{-1}$ ]	$\beta_{at} = (1.5 \pm 0.3)$	$\beta_{mol} = (1.5 \pm 0.5)$
$\alpha \times 10^{-9}$ [ $\text{cm}^3\text{s}^{-1}$ ]	$(2.5 \pm 1.5)^{[67]}$	
$creation_{n_m}$ [ $\text{at}\cdot\text{cm}^{-3}\text{s}^{-1}$ ]	$10^{13}$	

Table 4.12: Compilation of parameters in the rate equations (4.8) and (4.8).

(\*) - Obtained using the  $D_{mol}$  value for  ${}^4\text{He}^*_2$  [66] through the isotopic mass scaling:  $D_i = D * \sqrt{(M/M_i)}$



# Chapter 5

## Investigations on Metastability Exchange Optical Pumping dynamics with blue laser

The Metastability Exchange Optical Pumping (MEOP) process is known for almost 50 years way of obtaining polarized  $^3\text{He}$  gas for the variety of applications such as polarized targets in nuclear physics experiments, cold neutron spin filters and magnetic resonance imaging (MRI) of human respiratory system air spaces. The MEOP is an alternative method of obtaining the polarized helium-3 to Spin Exchange Optical Pumping (SEOP). For the details about the second method the Reader is sent to [51]. In this work the former method of polarization has undergone investigations with use of the laser setup working at 465 nm for helium molecule detection serving complementary information to the model of MEOP developed by both cooperating scientific groups since 1985 [53, 54, 52]. Presented in this work details of the MEOP model are limited to the minimum providing the background of the main target of these investigations which is the expected influence of molecular helium species on the polarization loss induced by optical pumping light at 1083 nm. For more detailed description of the model the Reader is sent to the references mentioned.

### 5.1 Basics of MEOP

Metastability Exchange Optical Pumping is a two stage process that results in non-equilibrium distribution of nuclear spin orientation of  $^3\text{He}$  atoms for which the  $I = \frac{1}{2}$ . During the process three populations are involved that are: ground state atoms  $1^1\text{S}_0$  of which the nuclear polarization is of the main interest, the metastable state  $\text{He}(2^3\text{S})$  atoms and helium atoms in the second excited state  $2^3\text{P}$ . The 6 hyperfine structure sublevels ( $a_i, i = 1, \dots, 6$ ) of the long-lived ( $10^3$  s compared to  $10^{-7}$  s of natural lifetime)  $2^3\text{S}_1$  state are populated through the decay cascade (radiative and collisional) of atoms highly excited in collisions with electrons present in the discharge plasma sustained in the gas. This metastable states serves as a bottom state in the optical pumping process (OP) that is the first stage of the MEOP. The excited state in this OP scheme is the  $2^3\text{P}$ , which 18 hyperfine structure sublevels ( $b_j, j = 1, \dots, 18$ ), is coupled to the  $2^3\text{S}_1$  with optical transition at infra-red wavelength of 1083 nm. Orientation of the electronic angular momentum enforced by OP induces the orientation of spin of the nucleus due to strong entanglement existence between both electronic and nuclear spin state in the  $2^3\text{S}_1$ . In the second stage of MEOP the orientation of the nuclei is transferred to the ground  $1^1\text{S}_0$  state through the metastability exchange (ME) collisions. In this binary process the electronic excitation of

the  $2^3S_1$  is overtaken by the colliding partner - the ground state atom, as well as the electron spins are exchanged (this is the only non-zero electronic angular momentum in both states). Contrary to the metastable excitation that is fully (without change any of describing quantum number) transferred from one atom to another, the nuclear orientation of both partners is conserved. It can be simply considered as the exchange of the nuclei spins, so that the output of the collision are the ground state atom with the nuclear spin with desired orientation and the metastable state atom with the nuclear orientation of the incident  $1^1S_0$  atom.

The MEOP was originally performed in so-called "standard" conditions of low helium gas pressure of several mbar and magnetic fields of several mT and in this pressure and field regime has been mainly developed. However, the application requirements of the polarized gas at higher pressures at about 1 bar, enforced the development of gas compression methods characterized by low polarization losses during this mechanical procedure. Alternatively the MEOP at high (several tens or hundredths mbar, reducing or even avoiding the compression) helium-3 pressures was proposed and successively and efficiently performed at much higher ( $10^2 - 10^3$  times) magnetic field exclusively. The details about the electronic states involved in the MEOP process as well as the possible optical transitions used in optical pumping stage are well described in [53, 54] and their notation has been applied in this work.

Both populations coupled by the ME collisions follow the Boltzmann-like distribution of angular momentum ( $\exp(\beta)$ ), providing that no OP is performed and relaxation has negligible influence on the populations. This distribution is driven completely by the spin temperature ( $1/\beta$ ) of the ground state  $1^1S_0$ , which number density  $N_g$  is about 6 orders of magnitude higher than  $n_m$  of the  $2^3S_1$  state. The spin temperature depends on the nuclear polarization  $M$  of the ground state, defined as the difference between amount of atoms for which nuclei  $m_I = 1/2$  and  $m_I = -1/2$  normalized by the total number of the atoms in the gas ( $M = \frac{N_{1/2} - N_{-1/2}}{N_{1/2} + N_{-1/2}}$ ), by the relation

$$\exp(\beta) = (1 + M)/(1 - M) \quad (5.1)$$

Independently of the magnetic field the knowledge of the polarization  $M$  and therefore spin temperature allows obtaining the relative  $a_i$  ( $\sum_{i=1}^6 a_i = 1$ ) populations of chosen metastable state sublevel characterised by the projection of total atomic angular momentum  $m_F$ :

$$a_i = \frac{e^{\beta m_F}}{e^{-3\beta/2} + e^{-\beta/2} + e^{\beta/2} + e^{3\beta/2}} \quad (5.2)$$

Affected, by the OP, performed with use of the circularly polarized light at 1083 nm, distribution of metastable state within its 6 sublevels by the collisional ME coupling with the ground state changes the  $M$  value. Of course during only the OP process the spin distribution is not valid, as the sublevels addressed by the laser, depending on chosen transition  $C_8$  or  $C_9$  (see Fig.5.1), are efficiently depleted, however, if only the pumping light is off, the system returns to the Boltzmann distribution with spin temperature determined by the increased value of  $M$ . At each of the MEOP stages as well as for already polarized gas there are relaxation processes that tends to restore the equilibrium conditions where  $M$  is close to 0 (low thermal polarization of order  $10^{-9}$  at 1 atm and field 1 mT to  $10^{-6}$  at 1.5 T still remains). When the discharge plasma is exposed to the pumping laser beam, relaxation is competing with the OP, that depopulates certain sublevels of  $2^3S_1$  creating unbalanced nuclear orientation in one direction that is transferred to the ground state atoms in ME collisions occurring at the pressure dependent rate  $\gamma_e/p 3.75 \times 10^7 \text{ s}^{-1}/\text{mbar}$

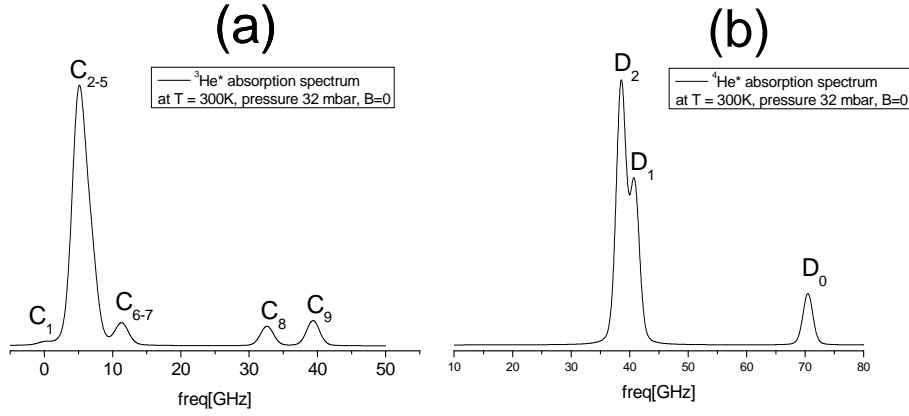


Figure 5.1: Calculated absorption spectra of  $^3\text{He}^*$  (a) and  $^4\text{He}^*$  (b) at 300 K, pressure 32 mbar and null magnetic field  $B$ . Doppler and pressure broadening effects has been taken into account. The lines designation is given according to well established nomenclature [53]. Notice the frequency scale and overlapping of  $C_8$  and  $C_9$  lines with  $D_2$  and  $D_1$  if absorption spectroscopy in isotopic mixture gas is performed.

The  $2^3\text{S}_1, 2^3\text{P}$  and  $1^1\text{S}_0$  states populations development is driven by the two stages of the MEOP and so called relaxation in the metastable and  $2^3\text{P}$  state that is the aim of these states to equalize their sublevels population as it is the case for equilibrium case of  $M=0$ . The relaxation in the metastable state is rather slow compared to the  $2^3\text{P}$  state. The collisions in which the  $2^3\text{S}_1$  atoms are involved in can couple the populations only through the spin exchange and the relaxation is associated for instance with de-excitation of the atom and re-excitation in the plasma, providing the relaxation rate  $\gamma_r^S$  value of order  $10^3 \text{ s}^{-1}$ . The loss of metastable excitation takes place usually during its collision with the cell wall what is a result of the atoms diffusion and provides a lower bound for the rate. The relaxation in the  $2^3\text{P}$  state is much faster due to possible  $J$  changing collisions occurring at the pressure dependent rate  $\gamma_r^P = 0.32 \times 10^7 \text{ s}^{-1}/\text{mbar}$ . This means the significant transfers between populations of the state sublevels during its radiative lifetime  $\tau (\equiv 1/\gamma \cdot 10^{-7} \text{ s})$ . Detailed equations of the  $2^3\text{S}_1$  and  $2^3\text{P}$  states evolution when relaxation, OP and ME processes are taken into account are given in the [52] for certain velocity class with  $v_z$  projection along OP beam. This velocity dependence is introduced by the OP process due to presence of the Doppler shifts and a given laser beam spectral profile. Characterization of OP influence on the electronic and nuclear orientations and on the light absorption by the gas can be performed by numerical calculations of the populations in  $2^3\text{S}_1$  and  $2^3\text{P}$  states from the rates equation, under following assumptions. Due to complexity induced by presence of various velocity classes and coupling of their populations by velocity-changing and ME collisions, the model of two broad classes has been proposed: strongly pumped atoms in the center of Maxwell velocity distribution and weakly pumped atoms in the wings of the distribution. This attempt has been confirmed to give a reliable quantitative results. Comparing the rates values  $\gamma_e$  and  $\gamma$  that drives the evolution of the two states involved in the OP with about 6 orders of magnitude lower rate of ground state nuclear polarization time evolution justifies the method of solving the  $2^3\text{S}_1$  and  $2^3\text{P}$  rate equations adiabatically, what means fixing all these values together with  $M$  as the constants. The solutions providing also an information about changes of OP laser beam absorption due to different than spin-temperature populations distribution, that is decreasing of absorption with the increase of  $M$  as well as increase of the incident laser power.

## 5.2 Achievements in MEOP in standard and non-standard conditions

The MEOP method, originally developed in the low field and low pressure condition has been extensively and in detail investigated on the purpose of working out the theoretical model as well as finding optimal parameters determination such as pressure, magnetic field, radio frequency discharge intensity, pumping laser power as well as its spectral and spatial profile in the plane perpendicular to the propagation direction. The most of work was done in the sealed cells containing pure helium-3 gas or helium-3 and helium-4 at desired pressure, prepared, cleaned and filled according to developed procedure. Analogous investigations were performed at high magnetic fields of order 1 T (up to 4.7 T) and pressures up to 266 mbar. Satisfactory results obtained were then transferred to the case of open cell with the gas flow during the MEOP process in constructed polarizer setup, that produces the polarized gas ready to use in various applications. In the time of performing this work the first high field MEOP polarizer is under construction and testing [55].

The result of performed systematic investigations on MEOP brought several conclusions about the process efficiency in various conditions. Here, only the main will be discussed and for detailed results altogether with the relevant figures the Reader is sent to the cited references:

- Equilibrium polarization  $M_{eq}$  decays with the increased gas pressure. At low magnetic field the values of  $M_{eq}$  0.8 is obtained at about 1 mbar gas pressure and changes to less than 0.1 at 32 mbar [57]. This effect is attributed to the increased with pressure auto-ionizing Penning collisions[56] that shortens the metastable state atom lifetime and limits its density in the plasma. Another reason of  $M_{eq}$  with pressure is the intensified formation of helium metastable molecules  $\text{He}_2^*$  as it takes place in three-body collisions. The polarized metastable and ground state atoms associated in the molecule can lose the orientation of its nuclear angular momentum, due to strong coupling of the nucleus spin and orbital angular momentum, in one of the rotational molecular states. The results presented in [60] clearly shows the inhibition of the influence of relaxation processes on achieved  $M_{eq}$  values for high (>10 mbar) pressure cells at high magnetic field of 1.5-4.7 T, where high values of  $M_{eq}$  achieved, i.e. 0.75 for 32 mbar at 2T and 0.25 for 266 mbar at 4.7 T. The difference with the low magnetic field results comes from the nuclear spin and electronic angular momentum decoupling at high fields [54] so that the changes in electronic states of polarized metastable atoms have less influence on the nucleus angular momentum orientation. In other words, for the same pressure cell the reached equilibrium polarization value increases with the magnetic field.
- The time required to reach the steady state polarization (so-called built-up time  $\equiv t_b$ ) increases with pressure and with the magnetic field. The former dependence is the result of increasing with pressure the relaxation rate in the  $2^3\text{P}$  state that decreases the photon efficiency  $\eta$  (see further subsection 5.3). The field influence on the  $t_b$  value relies, as in case of inhibition of the relaxation rate in the metastable state discussed earlier, on the hyperfine structure decoupling. Thus, the transfer of electronic angular momentum to the nucleus orientation is less efficient and thus slower. Improvement in the  $t_b$  value can be obtained increasing an incident power of the pump laser. Simultaneously the increase of achievable steady-state polarization occurs, however,  $M_{eq}$  in function of the laser power shortly reaches a plateau value [59]. In spite of the increase of  $M_{eq}$  with laser

power it is still lower than predicted by the model, what suggests additional relaxation channel enhanced by the presence of the pumping light. The discrepancies increase with the gas pressure (see previous point), so the effect is supposed to be of the collisional nature. More details about the manifestation of such relaxation channel is are discussed in following subsection 5.3 where angular momentum budget during the MEOP is presented and compared with the results of previous investigations.

### 5.3 MEOP angular momentum budget and laser induced relaxation

The effect of OP and ME on the built up of ground state nuclear polarization can be investigated also considering the angular momentum budget in the system, where angular momentum deposited by the photon in the atomic variables of metastable state flows through the ME collisions to the ground state and the mechanism is affected by the relaxation of the angular momentum in both states. The stored in the  $1^1S_0$  and  $2^3S_1$  states angular momentum (the two terms on the left side of eq.(5.3)) can be expressed as a difference between deposited angular momentum in the OP process (first term on the right) and amount that has been lost due to relaxation process occurring in these states (the second and the third term on the right):

$$\frac{dM}{dt} = 2\eta \left( \frac{(1 - T_{pump})W_{las}}{N_g V_c \hbar \omega_{ij}} \right) - M\Gamma_R \quad (5.3)$$

$T_{pump}$  is transmission of the pump beam through the gas sample;  $W_{las}$  is incident pump laser power;  $\omega_{ij}$  is the angular frequency of OP transition;  $\Gamma_R$  is total polarization loss rate (see also eq.(5.4));  $V_c$  is the optical pumping cell volume filled with the gas. In the absence of relaxation the number of ground state flipped nuclei is given by  $(N_g V_c / 2) dM/dt|_{ME}$  that can be expressed as the product of the quantity  $\eta$  called photon efficiency (PE) defined as the number of polarized nuclei per absorbed photon, and number of absorbed photons per unit time  $(1 - T_{pump})W_{las} / \hbar \omega_{ij}$ .

Within the total relaxation rate  $\Gamma_R$  two components can be distinguished:  $\Gamma_g$  - decay rate corresponding to relaxation processes directly acting on atoms in the ground state and the term related to the relaxation of the ground state polarization from the ME collisions. The latter results from the fact that when OP is interrupted the relaxation occurring in the  $2^3S_1$  state, that tends to equalize the  $a_i$  populations, induces a flow of angular momentum from earlier polarized ground state atoms so that the spin temperature distribution coupling the M and  $a_i$  values remains valid. Writing  $f_\Gamma$  as M dependent coefficient that scales the ME relaxation term  $n_m \gamma_r^S$  at M=0 for the values of M  $\gg$  0 we obtain:

$$\Gamma_R = \Gamma_g + f_\Gamma \frac{11}{3} \frac{n_m}{N_g} \gamma_r^S \quad (5.4)$$

Introduced photon efficiency depends on several parameters of actually performed MEOP experiment. In all situations it depends on the magnetic field. If the OP transition addresses a single sublevel in Zeeman structure of  $2^3S_1$  state  $\eta$  is independent of the pumping light intensity and nuclear polarization, what is the case for  $C_8$  transition, contrary to the  $C_9$ , where two metastable state sublevels are depopulated by OP. The PE for  $C_8$  line  $\eta_{C8}$ , due to its dependency

on relaxation rates  $\gamma$  - radiative and  $\gamma_r^P$  can take different values depending on the gas pressure:

$$\eta_{c8} = \frac{\gamma\eta_{c8}^K + \gamma_r^P\eta_{c8}^D}{\gamma + \gamma_r^P}, \quad (5.5)$$

where  $\eta_{c8}^K = 0.896$  is evaluated for the low-pressure OP where negligible redistribution in  $2^3P$  state occurs, i.e.  $\gamma_r^P \ll \gamma$  (so called Kastler regime), and  $\eta_{c8}^D = 0.5$  is evaluated in opposite limit of full redistribution at high pressures so that  $\gamma_r^P \gg \gamma$  (Dehmelt regime of OP). In the experimental conditions of the experiment performed here the pressure of 32 mbar inside the optical pumping cell brings us to the Dehmelt regime and  $\eta = 0.5$  that has been used in further calculations.

Thus, from the measurement of pumping light transmission at  $M_{eq}$ , when the deposited by OP angular momentum is totally balanced by the losses terms, value of total relaxation rate  $\Gamma_R$  is available through the relation:

$$\Gamma_R M^{eq} = 2\eta \frac{\left(1 - T_{pump}^{M=M^{eq}}\right) W_{las}}{N_g \hbar \omega_{ij}} \quad (5.6)$$

The studies of the MEOP performance, apart from looking only at the time evolution of polarization during the OP until  $M$  reaches the steady-state value  $M_{eq}$ , also relies on observations of polarization change (decay rate  $\Gamma_{decay}$ ) after the pumping light is turned off. In this situation the relaxation processes are not balanced by the delivery of angular momentum from photons and obtained decay rate  $\Gamma_{decay}$ , on the basis of model presented above, is expected to be equal to  $\Gamma_R$ . However, as reported in [52, 57, 58, 59], there is pump laser power dependent difference between these two values:  $\Gamma_R$  is higher than  $\Gamma_{decay}$ . As it is presented, for three different pressure cells in the low field MEOP, the  $\Gamma_R$  value changes linearly in function of the increasing absorbed laser power (the same slope independently of pressure) and asymptotically reaches the  $\Gamma_{decay}$  when the absorbed power is being lowered. At high enough absorbed power, independently of the transition,  $\Gamma_R$  can reach the value more than 2 orders of magnitude higher than the relaxation rate in the absence of OP. The effect is present also in the non-standard conditions of elevated pressure and magnetic field. The difference between two relaxation rates is an indication of existence of, additional to presented in the angular momentum budget, relaxation process during the OP stage:

$$\Gamma_{laser} = \Gamma_R - \Gamma_{decay}. \quad (5.7)$$

Therefore, obtained for a given OP laser power value of  $M_{eq}$  is lower than expected and the pressure dependence of this difference, indicating the collisional character of the process, leads to the hypothesis of the influence of metastable helium molecules. As discussed in 2.1 their formation rate increases about 100 times when considering association from the  $2^3P$  state than from  $2^3S_1$ , coupled with the transition at 1083 nm - presence of OP light. Creation of the molecule can affect the MEOP process in two ways: involving two atoms in formation process, one of the metastable state and the second ground state, reduces the amount of the species that participate in the optical pumping; by collisions occurring between the molecule and polarized ground state atoms that may exchange its electronic excitation with the ground state atom within the helium dimer, so that the ground state atom outgoing from the collision is unpolarized, while spin polarization of the bounded atom is being dissipated in numerous rotational states of the molecule due to spin-orbit coupling.

## 5.4 Description of MEOP experiment with blue light transmission measurement

Studies on the possible contribution of increased molecular species formation in the helium plasma in presence of OP radiation to the laser enhanced relaxation  $\Gamma_{laser}$  were performed including the 465 nm laser beam transmission through the OP cell recording to the standard MEOP dynamics measurements. So that, direct comparison between the atomic nuclear angular momentum development, restricted by the relaxation processes, and the molecular species density increase in function of the absorbed OP light power can be made. This requires the modification in standard MEOP setup (basically consisting of the OP pumping cell, pump laser beam and probe laser beam transmitted through the cell - together with necessary optical elements, homogeneous magnetic field in the cell volume and the source of the rf discharge excitation, see i.e. [52]) enriching with the blue laser beam transmitted through the OP cell. The final shape of such system depends of course on the conditions in which the MEOP is performed. In this work, the low magnetic field and moderate pressure (24 torr) conditions impose the optical polarization measurement technique described in [61] and the main issues are discussed in the subsection 5.4.1.2. The section is devoted to the experimental setup description involving optical arrangement and data acquisition technique. Experimental time charts are described allowing extraction of the parameters included in the equations describing the angular momentum budget (i.e. pump laser transmission at  $M=0$  and  $M_{eq}$ ) as well as calculation of the atomic and molecular densities at different stages of the process. Later, the raw measurement data reduction and processing are discussed providing quantitative information about parameters describing the MEOP process such as  $M_{eq}$ ,  $\Gamma_{decay}$ ,  $\Gamma_R$  and  $\Gamma_{laser}$ . On the basis of obtained values, the relations of the parameters characterizing the MEOP and atomic species with the molecular density change are shown and discussed.

Before the description of the experimental setup used in the investigations on influence of helium molecular species on Metastability Exchange Optical Pumping dynamics the details about the method conditions and measurement technique are discussed putting certain constraints on the geometry of the arrangement

### 5.4.1 MEOP experimental setup - design

#### 5.4.1.1 General constraints

Basically realization of the MEOP requires a few conditions to be fulfilled, namely:

- presence of the magnetic field in the volume of optical pumping cell filled with  $^3\text{He}$  gas (the cell with optical quality windows minimizing the transmitted laser beam distortion; cell rather of cylindrical shape increasing the optical path). The homogeneity of the field in this volume is important as any existing field gradients results in shortening of the nuclear polarization relaxation time to reach the equilibrium value of  $M \approx 0$  in the absence of MEOP. Efficient optical pumping occurs at low pressure (a few mbar) and low magnetic field induction (a few mT). Efficient polarization of the gas at the pressure of tens or hundreds of mbar is possible but requires magnetic field much stronger - of order 1 T - not considered in this work.

- discharge plasma that allows populating the  $2^3S_1$  state, usually coming from the alternate voltage (frequency of order MHz) applied to the electrodes wired on the OP cell forming around the cylinder the series of loops pairs with opposite polarity.
- presence of the 1083 nm circularly polarized light that induces the transition between hyperfine sublevels of  $2^3S_1$  and  $He(2^3P)$  states so that non-equilibrium distribution of the metastable atoms is created and transferred to the  $1^1S_0$  state in the metastability exchange collisions.

The investigations on the MEOP process dynamics as well as the relaxation processes of obtained polarization when the pumping beam is off requires the knowledge of the instantaneous polarization value (that provides also the  $M_{eq}$  value after the balance of MEOP and relaxation is obtained). In general there are 3 methods of nuclear polarization measurement in the  $1^1S_0$  state from which one has to choose the most suitable in terms of experimental conditions:

- direct method - nuclear magnetic resonance (NMR) technique - requires calibration to filling factor determination and has low sensitivity at low pressure. The main difficulties of using the method for continuous monitoring of OP dynamics are presence of rf discharges being the source of the noise as well as short transverse relaxation times.
- indirect - optical polarimetry of the light emitted by the atoms that are spontaneously decaying radiatively (preserving the nuclear orientation) from the various excited states induced by the rf discharge. Due to the hyperfine coupling the nuclear orientation is reflected in the electronic orientation and therefore in the circular polarization of the emitted light - this excludes the method in high magnetic fields above  $\approx 10$  mT [54] due to increasing decoupling between nuclear and electronic momenta. Nuclear polarization is inferred from the degree of circular polarized light. The method requires calibration and is not suitable for pressure higher than 5 mbar [54] when the rate of depolarizing collisions becomes important.
- indirect - optical absorption of 1083 nm light, that relies on the determination of the relative populations of  $2^3S_1$  state, what, according to (5.2) leads to M value of  $1^1S_0$  through the common spin temperature distribution of these states driven by ME collisions. This method does not require any calibration and can be used in arbitrary pressure and magnetic field, however, it demands additional laser beam presence transmitted through the discharge plasma. The beam has to be weak enough providing proportionality (linear regime) between absorber light intensity and the beam intensity value along all its path through the absorber - discharge plasma, as well as not to disturb the spin temperature distribution through optical pumping effect.

#### 5.4.1.2 Nuclear polarization measurement method choice - pros and cons

Analyzing the requirements and optimal performance conditions of mentioned before ground state atoms nuclear polarization measurement the choice of the most suitable one is determined by the MEOP conditions to be investigated. Due to expected pressure dependency of correlations between atomic and molecular dynamics (three body collisions responsible for their formation) the wide range of pressure is investigated - from a few to a few hundreds of mbar - what excludes the polarimetry method valid up to 5 mbar. From the other hand, the NMR

method is difficult to perform during the polarization build-up when discharge excitation is present due to the rf noise generation in the pick-up coils. Looking at this main issues it points out that the most suitable method of polarization measurements is the absorption technique that does not require any calibration and provides good sensitivity in the all range of pressures and magnetic fields.

Among the absorption technique two schemes taking advantage of linearly polarized probe beam at 1083 nm are considered:

- probe laser propagating at the right angle in respect to the magnetic field B direction and, in case of used OP cells, transversally to the cylindrical part. The information about the M value is inferred from the ratio of two different sublevels populations what in fact can be expressed as the ratio ( $r_{\perp} = A_{\pi}/A_{\sigma}$ ) of the absorption signals of two linear polarizations  $\pi$  - parallel to B and  $\sigma$  - perpendicular to B that are probing these two sublevels. This constraints the choice of the probing line transition for MEOP in pure  $^3\text{He}$  to  $C_9$  as for  $C_8$  the  $\pi$  and  $\sigma$  polarizations probes the same sublevels. This implies intrinsic difficulties of probing on  $C_9$  line that are described in [61].
- probe laser propagating parallel to B and along the cell length. The M value is inferred using the ratio  $r_{\parallel} = A_{\sigma+}/A_{\sigma-}$  of absorption signals of two circular polarizations of opposite helicity  $\sigma+$  and  $\sigma-$  for which the linear polarization of the probe beam can be decomposed. In this case, for  $^3\text{He}$  MEOP use of both  $C_8$  and  $C_9$  transitions as a probes is possible, however, mentioned in the transverse method difficulties with  $C_9$  are still valid here, not present when the  $C_8$  is chosen.

Important issue of the both methods is that the absorption of the different polarization beam component are measured simultaneously at exactly the same position in the plasma volume. In the MEOP however, the magnetic field B is present in the cell volume causing the frequency splitting of the transition components for different polarization that in null field conditions overlapping in terms of the frequency transition. In this work, the low field MEOP is performed, where, according to [63], the splittings at  $B < 30\text{mT}$  are negligible in comparison with the Doppler width of absorption profiles at room ( $T=300\text{ K}$ ) temperature of the experiments. Thus, the idea of the probe beam frequency fixing to the line position at  $B=0$  and measurement of both polarization components absorption at higher magnetic fields within the condition  $<30\text{ mT}$  remains valid.

Comparing of both schemes and desired experimental conditions the choice of Author is toward the longitudinal configuration. In this case, the longer optical path of the probe beam along the cell length instead of the path along the radius (transverse) increases the SNR of absorption measurements. Moreover, the longitudinal configuration (beam passes through the optical quality windows) does not require any optical geometry corrections of the probe beam contrary to the case of the transverse path where beam's wavefront is being distorted passing the curved surfaces of the cylinder walls[61]. As the experiment of MEOP in low field are performed for the elevated pressure of a few tens of mbar, the expected polarization value in that pressure range is  $<20\%$  [59]. According to [61], where details about absorption method of polarization are given, the sensitivity of the transverse method is low below that M value. At this point the longitudinal probe scheme is advantageous and  $C_9$  is better choice than  $C_8$  as it comes to the sensitivity at low M range. The details about the measurement principle is given for example in [54]. The main issue is to simultaneously measure the absorption signals of both

light polarization components in the same probed plasma volumes at arbitrary period of MEOP process or during the decay (with the rf discharge still applied) preceded with the measurement of these quantities at  $M=0$  ( $A^{M=0}$ ) before the OP is performed. In such case, according to (5.2) one obtains:

$$e^\beta = \frac{A_{\sigma^-}^{M=0} A_{\sigma^+}}{A_{\sigma^+}^{M=0} A_{\sigma^-}}, \quad (5.8)$$

from what the  $M$  value is obtained.

### 5.4.1.3 Blue laser in MEOP setup

For the realization of the purpose of this work the observation of molecular density change when MEOP experiment is performed is needed. The laser setup generating 465 nm was developed allowing the metastable molecular species  $\text{He}_2(a\Sigma_u^+)$  excitation to the  $e^3\Pi_g$  state. In comparison with the previously used methods based on laser induced fluorescence [62] the single-photon absorption technique allows direct detection of  $\text{He}_2^*$  as well as absolute and time resolved density measurements. The beam has to probe the same plasma distribution profile (characterized by the radial symmetry due to cylindrical cell shape together with collinearity of magnetic field and cell axes) in the cell as the infra red probe to assure the proportionality between observed changes for both atomic and molecular species. Thus, the path of the blue beam is also chosen to be in longitudinal configuration.

## 5.4.2 MEOP experimental setup - realization

The arrangement of the optical elements of the Metastability Exchange Optical Pumping setup with simultaneous molecular absorption measurements is shown on the Fig.5.2. The setup was placed on the aluminum threaded board 120 cm long and 30 cm wide so that the geometrical realization of the scheme of simultaneous transmission of 3 laser beams (infra-red pump and probe beam as well as blue laser light) is possible. The main constraint here is the optical pumping cell shape and size: cylindrical of 11.6 cm long and 1.6 cm diameter, imposing the low incident angles (in respect to the cell axis) of the IR and blue beams entering the cell. This required using long beam paths to fit into the cell geometry and not to shade the co-existing beams with the optical elements such as mirrors, cubes and the analyzer setup. Also these elements, that interacts with magnetic field - contains magnetic elements - especially photodiodes has to be far away from the OP cell position not to introduce magnetic field inhomogeneities that speeds up nuclear relaxation processes. The whole optical setup stands on the XX cm high supports matching the cell axis height to the axis position of the magnetic field generated by the system of the square coils. The setup is placed inside the coils volume so that the cell is collinear with magnetic field axis and the cell volume stays in the center of the coil system - the volume of the lowest field inhomogeneity. The current value delivered by the power supply system of the coils was set to be 1.0 A providing the magnetic field induction  $B=8.2$  G.

The infra-red (IR) 1083 nm pump and probe laser beams are delivered to the setup with the fibers and collimated with the  $f_{pump}=50$  mm and  $f_{IRprobe} = 8mm$  focal length 1" and 0.5" anti-reflection coated lenses respectively. As the pump laser, the Manlight 10 W fiber laser has been used. The collimation lens focal length was chosen so that the outgoing Gaussian beam FWHM  $\approx 5$  mm providing the intensity value at the radial distance of the cell radius between

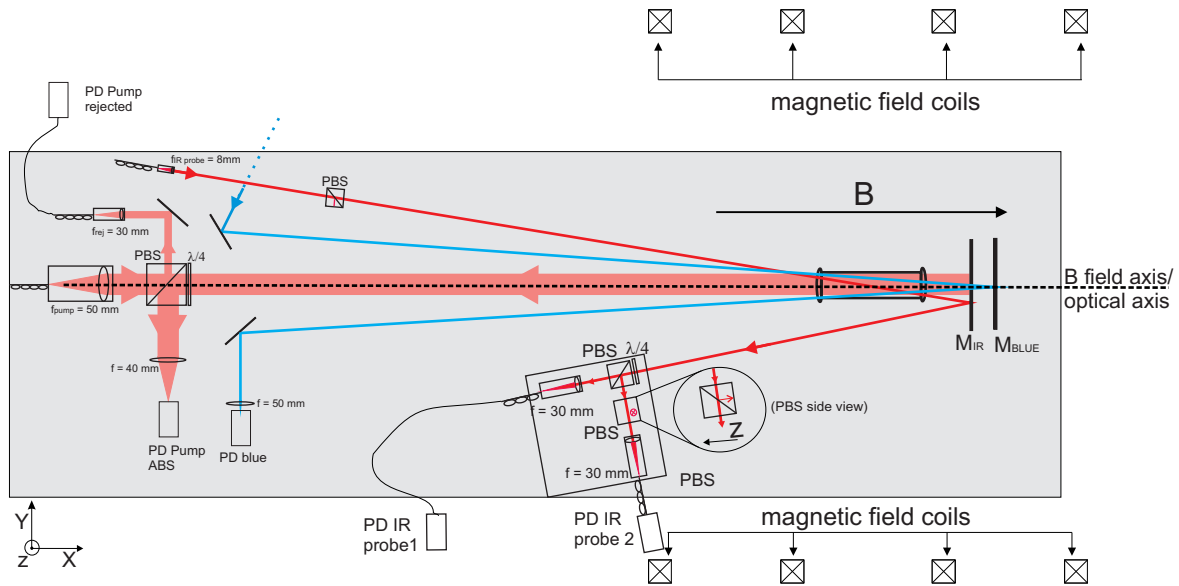


Figure 5.2: Arrangement of the optical elements for MEOP setup realisation with simultaneous 465 nm laser transmission measurement mounted on a single breadboard 120x30 cm. Pump, infra-red (IR) probe and 465 nm probe beams paths are shown. PBS - polarizing beam splitter,  $\lambda/4$  - quarterwave plate, PD - photodiode, M - mirror for the IR or 465 nm wavelength, f - the value of lenses focal lengths. In the small square part of the setup - polarization analyzer - the cutting plane of the PBS before the PD of the second IR probe beam is  $45^\circ$  to the drawing plane (breadboard plane).

1% and 1‰. As for the probe beam,  $15 \mu \text{W}/\text{cm}^2$  has been provided by a single frequency 1083 nm DBR diode.

The pump beam linear polarization in the drawing plane is purified by the polarizing beam splitter (PBS) and orthogonal polarization is reflected at monitored for any pump laser polarization changes by the photodiode (after rejected beam part it is focused by  $f_{reject}=30$  mm collimator to the fiber of which the second end is placed close to the photodiode surface). After the PBS, actually glued on its outer surface, the pump beam passes the quarter-wave-plate that the axis is at  $45^\circ$  to the polarization plane of the beam. In such way the circular  $\sigma_-$  (determined in the first MEOP experiment after probe laser components - see below - signals comparison according to[52]) pump beam polarization is achieved. Pump propagates along the magnetic field axis passing through the optical pumping cells windows and reflecting from the  $M_{IR}$  broadband dielectric mirror with reflectivity  $R=99.6\%$  at 1083 nm placed after the cell. After passing the OP cell for the second time the transmitted beam polarization is changed by the quarter-wave-plate back to the linear, however perpendicular to the previous linear polarization. In this way the beam is reflected by the PBS at the right angle - in opposite side than the rejected beam mentioned before.  $f=50$  mm lens is focusing the transmitted beam onto the photodiode allowing the transmission observation of the pump beam during the OP process. Infra-red probe beam is also first passing through the PBS, however in that case no quarter-wave-plate is used after the cube - the polarization remains linear in the plane of the scheme. Probe beam passes the cell once - diagonally and is reflected by the same mirror  $M_{IR}$  as the pump beam. The probe beam enters the analyzer part of the setup. If one considers the linear polarization as the product of two opposite circularly polarized waves, entering the analyzer through the  $\lambda/4$  plate (also glued

to PBS) results in their change into two orthogonal linear polarizations that are being separated in following PBS by the  $90^\circ$  angle. Each of resolved linearly polarized probe beams is focused by  $f = 30\text{mm}$  lens of the collimator to the fiber, that, as in case of the rejected fraction of the pump beam, leads close to the surface of the photodiode. This solution was used due to limited space on the optical board as well as the fact that photodiodes contain elements that could introduce additional field inhomogeneity. In this way, the simultaneous observation of transmission of both circular polarizations through the cell can be performed allowing further nuclear polarization determination with the optical method described in [61]. In the simple experiment relying on the observation of the shift of the C8 and C9 due to Zeeman effect in magnetic field, determination of the probe polarizations in two detection channels was performed. Described on the Fig.5.2 PD IR probe 1 (noted also as S1 in the text) photodiode detects the linear polarization in the drawing plane coming from  $\sigma_+$  component, while the PD IR probe 2 (S2) detects the linear polarization perpendicular to the drawing plane coming from  $\sigma_-$  component. To remove about 4% of beam with horizontal linear polarization that is reflected by the cutting plane of PBS to the probe 2 photodiode of which signal should come only from the vertical one, the second PBS was put before the IR probe 2 collimator lens. The orientation (zoomed part on the analyzer part on Fig.5.2) of the PBS allows removing the light with unwanted polarization by reflecting it to the analyzer support, while the vertical polarization passes the cube unaltered to the photodiode 2. The 465 nm laser beam is delivered to the optical board with the set of mirrors - no fiber is used. The blue beam passes the optical pumping cell twice in the V-shape path configuration. The enters the cell near its edge and propagates towards to the setup axis, leaving the cell and passing the  $M_{IR}$  mirror (transmission  $T=43\%$  at 465 nm). The beam is then reflected by the  $M_{blue}$  mirror placed behind the  $M_{IR}$  and comes back to the OP cell leaving it near the opposite edge of the input window. 465 nm light is reflected by the mirror and focused by  $f=50$  mm lens to the photodiode (PD blue). The OP cell is mounted on the non-magnetic  $\theta - \phi$  holder allowing precise regulation of the its position in respect to the incoming pump beam.

### 5.4.3 Acquisition scheme and measurements protocols

#### 5.4.3.1 Acquisition scheme and recorded signals

The experimental setup presented on the Fig.5.2 has been coupled with the data acquisition system. The block scheme is presented on the Fig.5.3.

Intensities of both IR probes polarizations are measured by 2 of 3 photodiodes placed in common box with inlets for the fiber. The remaining infra-red dedicated photodiode detects the fraction of the pump beam of polarization component in vertical plane that is rejected by the PBS after the pump beam collimator - this allows OP incident pump beam intensity changes monitoring, related to the light polarization and power changes. The blue light probe transmission signal and the transmitted pump intensity are measured by the separate photodiodes dedicated to the visible and IR wavelengths respectively. Photodiodes signals are collected by multichannel acquisition card connected to the PC. Used in the experiments sampling frequency was set to 1kHz.

Single modulation technique has been used in the experiment - amplitude of the rf discharge was modulated with the frequency of 180 Hz allowing the increase of SNR resulting from distinction between atomic response to the resonant light excitation and the power fluctuations of the source. The modulation has the sine course with small modulation amplitude (about 20%

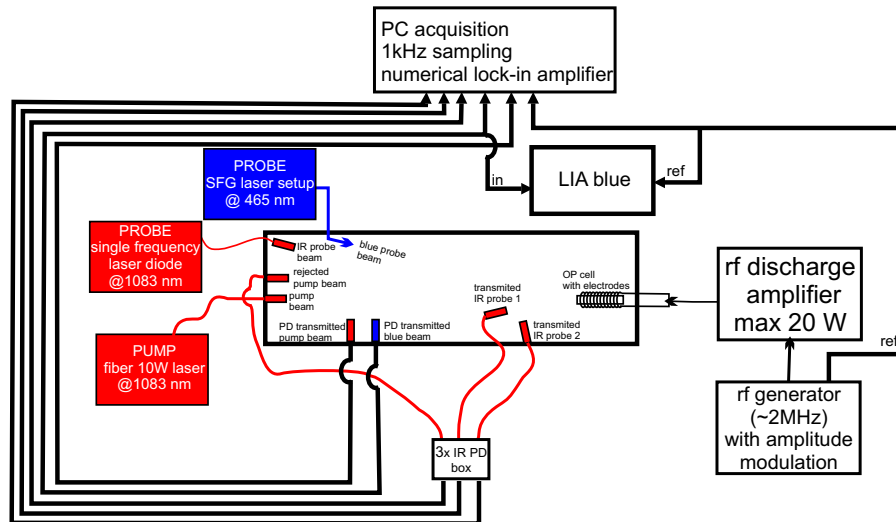


Figure 5.3: Block scheme of the measurement and acquisition setup. Detailed description of the optical part inside the magnetic field coils is given in 5.4.2 with Fig.5.2.

- see below) to keep discharges at stable and constant excitation level, hence constant plasma conditions.

Modulated IR and blue probes transmission signals as well as of the pump beam can be demodulated using the numerical lock-in computer program written in Fortran by P.-J. Nacher. The detailed description of the software properties is given in [63]. As the program requires the reference signal of modulation, the discharge generator TTL signal is recorded. For the blue laser tuning control, set permanently during the MEOP experiment on the top of Q(2) molecular absorption line, the photodiode signal as well as TTL reference were sent to the DSP lock-in amplifier on which the absorption signal could be observed and laser tuning performed to maximize the value if needed.

Post-processing of the measurement data has its advantage in the possibility of repeatedly demodulation setting change and optimal values finding for each of considered signals. The regulated in this experiment user-defined parameters are: time constant, sampling (data acquisition) period, time of the offset for  $M=0$  (pump off) of the probes signal determination and phases of the recorded transmission signals. From the input data file the program generates two out put files. The first contains:

- time scale of the experiment
- averaged transmitted signals of both IR probe components, blue probe and the pump beam
- magnitudes (commonly named as R in lock-in detection terminology) of demodulated signals divided by the averaged transmitted signals separately for each of above mentioned beams
- averaged rejected signal of the pump beam

For adjusted phase values (set separately for each of the demodulated signals) the second file contains:

- time scale of the experiment
- in-phase probes and pump components divided by their averaged transmitted signals
- quadrature probes and pump components divided by their averaged transmitted signals

Having calculated the in-phase and quadrature components together with the magnitude of the signal becomes important when processed photodiode voltage contains contributions other than just the targeted transmitted power. As only the phase amplitude is pure additive quantity it allows to properly remove them.

Making the ratios of magnitude, in-phase and quadrature of the transmission signals to the averaged transmitted signals for each of the beams allows reducing effects of laser intensity fluctuations and of optical thickness of the gas on measured absorptions [54, 63]. These ratio for magnitude (and in-phase component if the phase is properly set) is proportional to the absorbing species density providing the rf discharge modulation depth do not exceed about 20% of peak-to-peak discharge voltage variation amplitude [62].

It is important from the practical point of view, that the mentioned signals delivered in the output files of used numerical lock-in software are pure peak amplitudes of sinusoidal oscillation due to the discharge modulation, contrary to the hardware lock-ins that provide RMS (root mean square) values ( $R^{RMS}$ ) at their output ( $1/\sqrt{2}$  of the peak value in case of sinusoidal change). Furthermore, all the signals included in the output files are corrected for any DC offset in the input data acquired directly from the photodiodes, so that the values of magnitudes ( $\sqrt{2}R^{RMS}$ ) divided by the averaged transmission signal ( $\langle PD \rangle$ ) corrected for the DC offset ( $\emptyset$ ) can be written as:

$$OUT_nLIA = \frac{\sqrt{2}R^{RMS}}{\langle PD \rangle - \emptyset} \quad (5.9)$$

### 5.4.3.2 Measurements protocol

During the MEOP with blue laser transmission systematic measurements three experimental protocols were applied allowing further extraction of interesting quantities in terms of the laser-induced relaxation rates and its correlations with the molecular species density in helium plasma. The protocols are shown on the standard chronograms on which the time courses of 1083 and 465 nm probe beams has been shown. For the clarity of the presentation, the averaged blue laser probe has been divided by the factor 2.5 as well as the ordinate axis was broken between 0.2 and 1.7 V

**(a) Probe beams absorption measurements** The protocol was developed to allow obtain absolute absorptions of infra-red probe beams and blue beams in absence of pump beam ( $M=0$ ), so that the absolute densities of the atoms in conditions (mainly discharge intensity is relevant) of further MEOP tests in the for the same rf discharge settings. The recordings with use of such protocol were performed at before and after the systematic MEOP tests for one discharge conditions so that the change in the plasma conditions could be monitored over the experimental time scale.

**(b) MEOP with blue experiment protocols** Two protocols of polarization build-up and decay recordings during the MEOP process in which the molecular detection has been applied

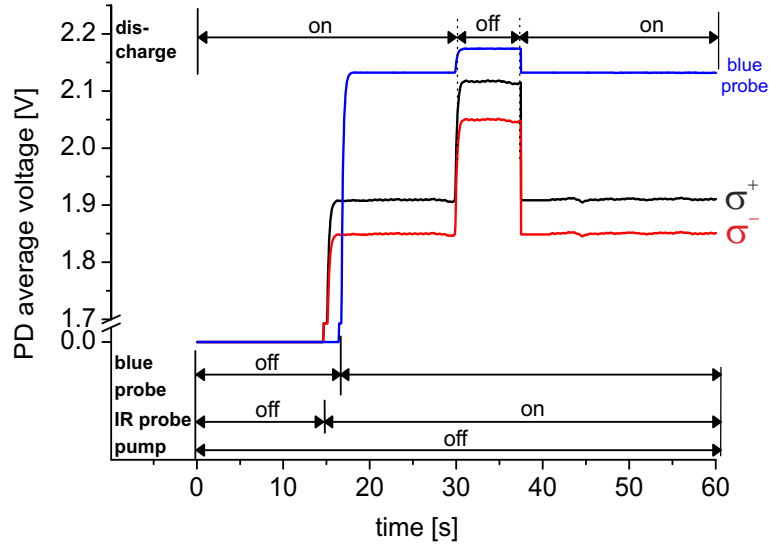


Figure 5.4: Time chart of the IR and blue probe beams course in the absence of OP light. Absolute values of absorptions can be deduced from the signals value in proper time periods.

are shown on the Fig.5.5 and will be described together allowing their comparison in respect to the purposes of each change.

At the beginning, for about 10 s, only the rf discharges remains ON allowing probes and pump electrical offset measurement. After that time, the probe laser is being unblocked and both component transmissions are recorded at  $M=0$  for 10 s as well - essential in further signals ratio for nuclear polarization determination at  $M \neq 0$ . Pump beam becomes unblocked - for the period depending - decreasing with the incident pump laser power - from 480 s for the lowest power of 0.1 W to 120 s at 6 W. . At this part the similarity of both protocols ends.

For the protocol B, after the steady state  $M$  value is reached the discharges are being switched off for 10 s providing the signal required to pump and probes absorption at  $M_{eq}$ . After switching the discharges back, the nuclear polarization builds-up again reaching the steady state value - the time of this period also depends on the incident pump power and is about  $2/3$  of the precedent time dedicated to polarization build-up. The pump beam is being blocked allowing decay of the polarization in presence of the discharge, so that the  $T_{disch}$  can be determined with good accuracy from the exponential fit. In the 90th second of the decay the small magnet is put for a few seconds inducing strong inhomogeneity of the field causing rapid relaxation down to  $M = 0$  - then the discharges are switched off for 10 s during which signal recorded is used for metastable atoms density calculation (the results serves as a control of discharge stability in each of MEOP recording performed with this protocol).

For the protocol C, after reaching the  $M_{eq}$  during the build-up period, the pump beam is being switched off (contrary to the switching off the discharge in protocol B). The polarization decay lasts here 30s serving as a check of the discharge conditions rather than the way of  $T_{disch}$  determination - lower accuracy on the fit to due to lower amount of points than for protocol B. After the short decay period, there is second build-up period to recover  $M_{eq}$  value at the end of which the discharges are being switched off, what is essential for pump and probes absorption calculation at the steady state nuclear polarization. 10 s after switching off the discharges the pump laser is blocked.

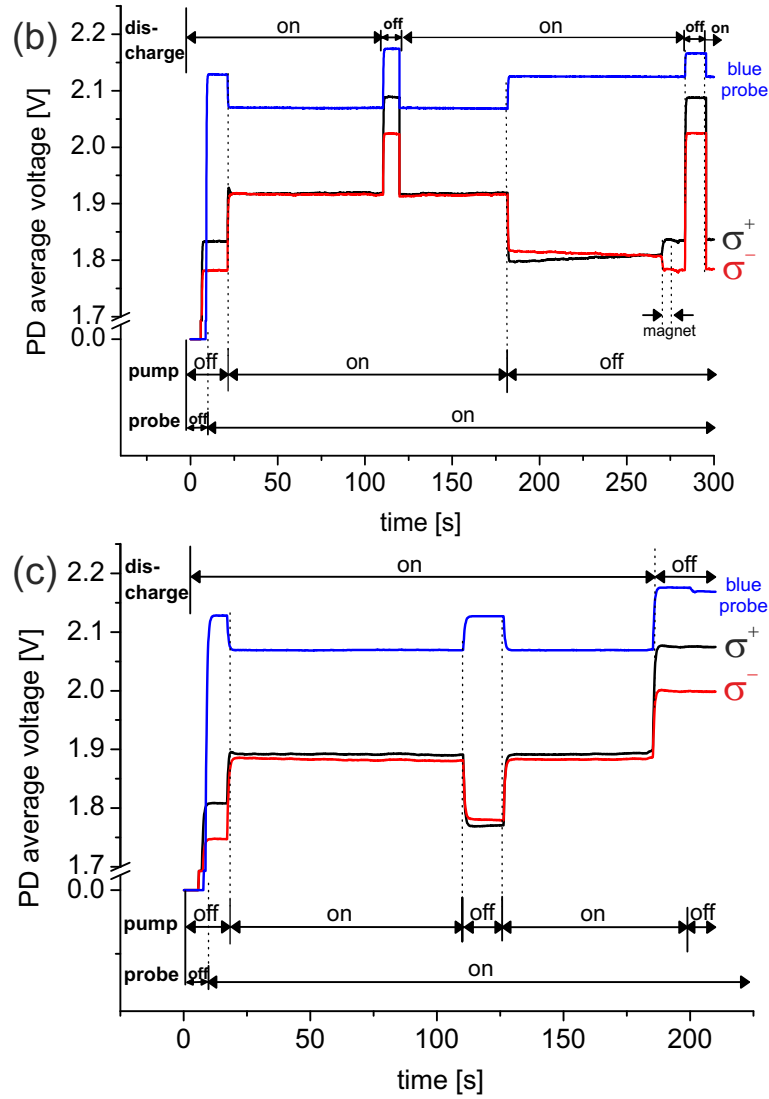


Figure 5.5: Time chart of the IR and blue probe beams course in the absence of OP light. Absolute values of absorptions can be deduced from the signals value in proper time periods.

## 5.5 Experimental data reduction and processing

There are a few quantities that has to be extracted from the measurement data recorded using described before A,B and C protocols. They are necessary to perform any investigations on the influence of molecular helium on OP induces polarization losses. Namely they are:  $M_{eq}$  and  $T_{disch}$  - polarization value and relaxation time in absence of the OP light; absorption rates for the pump beam and the blue light at  $M = 0$  and  $M_{eq}$ , IR probe beam absorption at  $M = 0$ . In this section the method of these quantities extraction is described - first the parameters describing the MEOP and later the absorption values relying on the measurement protocol A and dedicated sequences in protocol B and C.

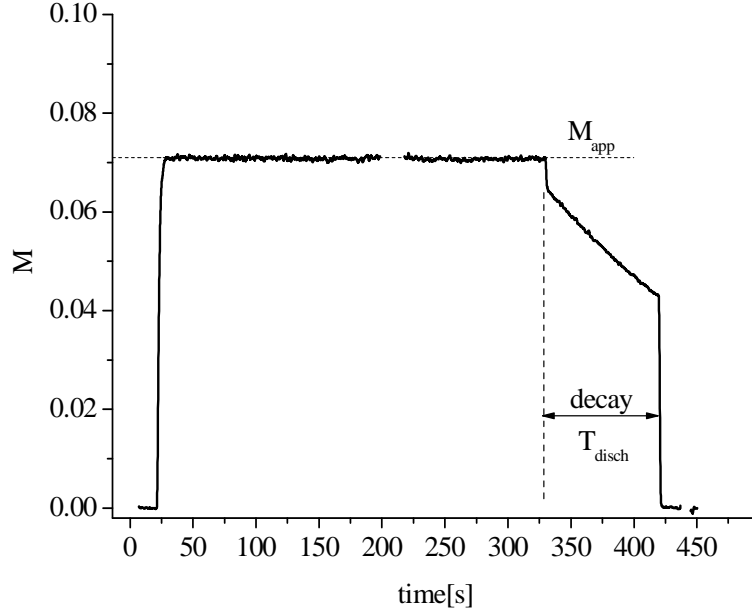


Figure 5.6: Build up and the decay of polarization as a function of time for the MEOP experiment performed with protocol B. The discontinuities of the presented curve corresponds to the periods when the discharges were off. Apparent value of the polarization  $M = M_{app}$  has been marked with the dashed line as well as the decay period (330-420 s) after the OP beam was blocked. Recording performed for the "weak" discharges and 0.17 W of absorbed pump power at  $M_{eq}$ ; time constant applied in the numerical lock-in  $\tau_{LIA}=0.2$  s.

### 5.5.1 Polarization build-up and decay curve for $M_{eq}$ and $T_{disch}$ determination

According to the longitudinal optical method of the polarization measurement at arbitrary stage of the MEOP process (section 5.4.1.2) the absorption signals related to the transitions occurring from different sublevels  $a_i$  of atomic metastable state are required. Thus, relevant signals recorded during the B and C measurement protocols realization, are magnitudes of demodulated signals divided by the averaged transmitted signals for both probe beam polarization components  $\sigma^+$  and  $\sigma^-$ , named  $A_{\sigma^+}$  and  $A_{\sigma^-}$  [61] and eq.(5.8). For the spin temperature determination and thus the polarization value, performing the normalization of the  $\frac{A_{\sigma^+}}{A_{\sigma^-}}$  is needed in respect to the ratio value at  $M = 0$  ( $\frac{A_{\sigma^+}^{M=0}}{A_{\sigma^-}^{M=0}}$ ), which value was obtained by taking the average of divided signals of both components recorded within 10 s before turning on the pump beam (see the protocols B and C time charts 5.5). Example of the polarization build-up and relaxation obtained with protocol B measurement is shown on the graph 5.6.

The polarization value called "apparent"  $M_{app}$  is not the true value of the  $1^1S_0$  atomic state polarization as it is measured from the  $a_i$  population ratio in presence of the OP light - thus strongly disturbed in comparison to the spin temperature distribution on which the polarization measurement method relies. The spin distribution holds true immediately after the OP light is off thus it can be inferred from the extrapolation of the decay part to the moment of removing the influence of the pumping light on plasma as shown on the fig.5.7(a) and (b), where the way of  $M_{eq}$  and  $T_{disch}$  determination has been shown.

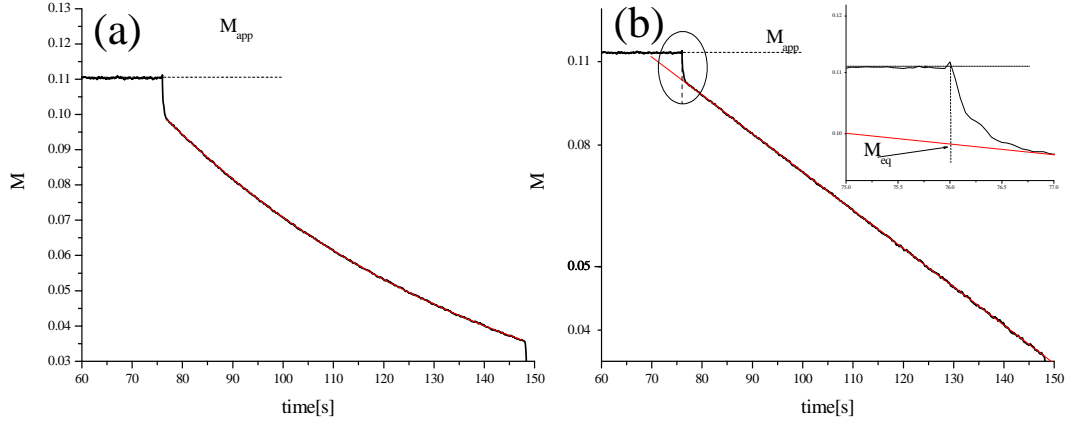


Figure 5.7: Decay part of the MEOP experiment recording curve shown in the linear scale (a) and logarithmic scale of ordinate (b). The red solid lines represent exponential fit - graph (a) and the linear fit - graph (b) to the experimental data. This MEOP recording has been performed at "strong" discharge level where the difference between exponential character of the decay in linear scale of ordinate is clear when compared to the linear character in ln scale. This difference for "weak" discharges (fig.5.6) is not as emphatic due to longer decay time.

On the graph (a) of the fig.5.7 the exponential decay fit ( $M(t) = M_{eq} \exp(-t/T_{disch})$ ) to the decay part of the curve is presented. This functional character of the decay is confirmed on the graph (b) where ordinate is given in the ln scale and the decay part stays linear all the time - the linear fit is given with the red solid line. Both exponential and linear fits provide  $T_{disch}$  value. The sudden drop of the polarization value at the end of exponential decay is caused by placing the small magnet in the vicinity of the cell inducing fast relaxation to the  $M=0$  value. Extrapolation of the linear function to the time when the pump beam is being blocked (76 s) allows obtaining the  $M_{eq}$  value as a true nuclear polarization of the ground state helium atoms.

**(c) Absorption rates determination from MEOP recordings** Apart from the demodulated signals of probes and the pump beam absorptions the output files of the numerical lock-in program provides also the averaged signals from the photodiodes from which the offset was subtracted. These are used to determine the absorption values of the IR and blue probe lasers and the pump laser. Absorption values of IR probe at  $M = 0$  delivers information about absolute  $n_m$  density for certain discharge intensity. Absorptions of the 465 nm light at  $M = 0$  and  $M_{eq}$  allows investigation of molecular density increase due to the presence of OP light. The pump beam absorption at  $M_{eq}$  provides information about fraction of the incident pump power that has been deposited in the discharge plasma ( $W_{abs}^{Meq}$ ).

The way that the IR probe and pump absorption was determined in MEOP recordings is similar to that in case of blue and therefore only the latter is presented here. For the blue probe beam the two sequences of turning off/on the rf discharge at  $M_{eq}$  and  $M = 0$  are used to absorption determination at these polarization values. In each of them two, lasting about 10 s, periods for the signal level determination at discharges ON were averaged. Between these periods 5-10 s lasting discharge OFF signal was recorded and its average was taken for absorption calculations according to expression (4.1). The periods in which the averages were taken provided the statistical accuracy on the 4th decimal place, while when the single value of

the  $S_{ON}$  was taken as an average of two values - before and after switching OFF the discharges, the discrepancy were on the 3rd decimal place leading in overall relative error in the absorption value less than 1%. There was no need to subtract any offset, as it has been done by the numerical lock-in program basing on the first seconds recording when all the lasers were off.

### 5.5.2 Metastable atoms number density determination

The details about the method of number density  $n_m$  of atoms in the metastable state determination has been well described in [63, 60] thus only the relevant in terms of this work informations about this quantity determination will be given.

In general the formula for  $n_m$  calculation from the transmission value  $T$  ( $\equiv 1 - Abs$ ) measured for the probe laser exactly tuned to the considered transition frequency (center of the absorption line profile), depends on the chosen transition, the gas pressure, its temperature, the magnitude of the applied magnetic field if present in the cell volume, chosen optical path of the probe beam and the value of nuclear polarization  $M$  due to inhibited Penning collisions influence that tends to decrease metastable atoms number density[63]. The choice of the transition determines the used transition matrix element value (frequently noted as  $T_{ij}$ [53]) as well as the value of relative population of the transition initial state sublevels. While for null nuclear polarization value the metastable state atoms are equally populate 6 sublevels, what is independent of the magnetic field value, the matrix elements  $T_{ij}$  are not[54]. As it is reported in [57, 58, 59, 60, 54] the sublevels energies of both metastable and  $2^3P$  state changes linearly with field what influences the absolute and relative positions of the absorption lines - completely changing the spectrum appearance for high enough magnetic fields so that redefinition of the transition nomenclature is required. The temperature and the pressure dependencies comes in with the broadening effects of the absorption lines, namely Doppler and collisional broadening effects respectively. In the room temperature, in which the experiments of this work has been performed, of about  $T = 300K$  the Doppler broadening expressed in Gaussian profile's FWHM is  $w_G = 1.9773$  GHz for  $^3He$ . This states the lower limit of measured linewidths that is further increased depending on the pressure of the gas inside the OP cell within the range from 0.4 GHz for 8 mbar to 3.3 GHz at 267 mbar of Lorentzian profile FWHM [60]. Thus the total linewidth (of the Voigt profile being a convolution of Gaussian and Lorentzian functions) of observed line profiles was expected to be of several GHz what allows to treat the probe laser beam as a single frequency radiation due to 3 orders of magnitude lower spectral width (several MHz, monomode laser sources). The effect of the line broadening (temperature and pressure influence),  $T_{ij}$  element value (field dependency) and probed frequency can be enclosed in one single parameter called the line strength  $S(\omega/2\pi)$ . The detailed equations expressing the absorption profile function can be written as:

$$n_m(M) = \tilde{\sigma}^{-1} \frac{-\ln T}{L_{path}} \frac{1}{S(\omega/2\pi, M)}, \quad (5.10)$$

where  $T$  is the transmission of the light of frequency tuned to the  $\omega$  frequency of probed transition,  $L_{path}$  is the beam optical path, whereas  $\tilde{\sigma}$  - generic cross section of the surface dimension  $m^2$ , is given by:

$$\tilde{\sigma} = \frac{\hbar \sqrt{\pi} \alpha f}{m_e D} \quad (5.11)$$

$$\tilde{\sigma}^{-1} = 1.47105 \cdot \sqrt{T/300} \cdot 10^{15} \text{m}^{-2} \quad (5.12)$$

$$(5.13)$$

$\alpha$  is the fine structure constant,  $f = 0.5392$  - the oscillator strength of the  $2^3S_1$ - $2^3P$  atomic transition,  $m_e$  - mass electron,  $D = \frac{\omega_G}{2\sqrt{\ln 2}}$  is the Doppler width dependent on the gas temperature  $T$  as well as the mass of considered particle  $M_p$ :

$$D = \frac{\omega}{2\pi} \sqrt{\frac{2k_B T}{M_p c^2}}, \quad (5.14)$$

with Boltzmann constant  $k_B$  and speed of light in the vacuum  $c$ .

The value of  $S(\omega/2\pi, M)$  used in this work for probed transitions has been calculated in *Voigt* program written by P.-J.Nacher. It computes the spectrum - the line strength values in function of the frequency of the helium  $2^3S_1$ - $2^3P$  transition taking into consideration the magnetic field effects on the line position, splitting, the line broadening effects (thus the baseline increase due to influence of neighboring lines is also included) and changes of the line strengths with the nuclear polarization. While for the  $n_m$  determination, the measurement of the transmission has been performed for the laser tuned to the top of the line profile, the value of  $S(\omega/2\pi, M)$  has been also taken for the maximum of absorption line of calculated spectrum.

## 5.6 Experimental results of MEOP with molecular density measurements

Described in the previous section experimental and acquisition setup allowed both dynamic and static measurements performance. By the dynamic Author means the Metastability Exchange Optical Pumping investigations of laser induced relaxation as continuation of the experiments performed in [59, 63] with simultaneous measurements of molecular density variations in helium plasma due to presence of optical pumping light at 1083 nm. The static measurements are the investigations of molecular density change with the pump beam presence, however at null nuclear polarization value, what is obtained by continuously exposing the cell to the strong magnetic field gradient of small magnet placed in its vicinity, so that the induced total relaxation rate  $\Gamma_R$  is equal or higher than the pumping rate and metastability exchange rate responsible for ground state polarization build-up. The  $\Gamma_{laser}$  increase due to the absorbed 1083 nm light power can be thus compared with the size of molecules number change. These two approaches allow to compare and check if any dependency exists between the growth of molecular density and presence (and value) or absence of nuclear polarization.

For the first tests the 32 mbar pure  $^3\text{He}$  cell was chosen. The choice of this pressure from accessible OP cells filled with the gas for the earlier purposes of MEOP investigations in low and high magnetic field, was a compromise between the SNR of the blue absorption signal (in between poor at 8 mbar and good at 66.7) and achievable nuclear polarization value in low magnetic field conditions ( $< 10\%$ )[57, 59].

The investigations, however performed for a single pressure cell, were made for two different voltage amplitudes of rf discharge excitations and for various incident pump laser power values at each of discharge intensities. The pump laser was tuned to the  $C_8$  transition frequency due to, as mentioned in section 5.3 the quantum efficiency for this transition ( $\eta_{C_8}$ ) does not depend on the OP light intensity nor on the nuclear polarization of the atoms. For the majority of MEOP experiments with certain pump laser power, the IR probe beam frequency was set on  $C_8$  line, however recordings with  $C_9$  were made additionally for comparison.

The result will be presented in the way that first allows the straightforward comparison with previously achieved [59, 63] and after the new informations brought by transmission measurements with the additional frequency laser. As the performed series of measurement were made to deliver additional information about laser induced relaxation and its potential source in the presence of helium molecules in the plasma, the main variable in the experiment was the OP laser power. To relate this variable with the plasma conditions the other quantity becomes relevant, namely absorbed pump power - deposited power. It gives the information what fraction of the light interacts with the metastable atoms, creates the polarization but also is partially responsible for its relaxation. Apart from that it is a relevant parameter related to the pump light power that comes into the angular momentum budget equation (5.3)  $(1 - T_{pump})W_{las}$ , the first term is the absorption (1-transmission) and  $W_{las}$  is incident pump power.

### 5.6.1 Discharge intensity

. As written in the introduction to this section, two different discharge conditions were studied in 32 mbar cell, namely weak and strong. The amplitude of the rf excitation in the first case was chosen so that the infra-red probe absorption in absence of the pump beam, at  $M=0$  was about 10% on  $C_8$  line what, given the geometry of the probe beam path, the cell dimensions and transition probabilities results in the  $n_m$  value of  $(3.22 \pm 0.05) \cdot 10^{10} \text{cm}^{-3}$ . The second discharge regime settings of rf excitation amplitude was chosen so that the absorption on  $C_8$  line was 40% - this gives the  $n_m = (1.61 \pm 0.01) \cdot 10^{11} \text{cm}^{-3}$ .

The absorption values were checked performing the recordings with protocol A before and after the series of MEOP measurements for chosen discharge intensity.

Apart from the absorption values and thus calculated metastable atoms densities, the plasma condition indications was deduced from the value of the  $T_{disch}$  time ( $\equiv 1/\Gamma_{decay}$ ) determined from the polarization decay after the OP process was stopped. From both measurements protocols B and C  $T_{deccay}$  determination is possible, however better accuracy, due to longer recording of the decay part, was obtained for B. The values of  $T_{disch}$  coming from C-protocol measurements serves as rough check of plasma condition stability from one recording to another, rather than for accurate value determination. For the weak discharge conditions  $T_{disch} = 216 \pm 0.7\text{s}$ , while for the strong discharge regime  $T_{disch} = 70 \pm 0.7\text{s}$ . Up to 4 h for weak and strong discharge conditions stability within the  $T_{disch}$  error bar is estimated from the data acquired with protocol C, what can be shown on the example of the strong discharge, where the average  $T_{disch}$  determined from recording with this protocol gave  $69 \pm 3\text{s}$  in good agreement with precise value from protocol B, Fig.5.8. The error bars of the values obtained from the data recorded with protocol C are mainly due to systematic error of about 10 s determined from the differences between  $T_{disch}$  obtained in B-protocol measurement for the full decay part fit of exponential function and restricted fit to the first 15 s of the decay (as this period of the decay time is for C protocol)

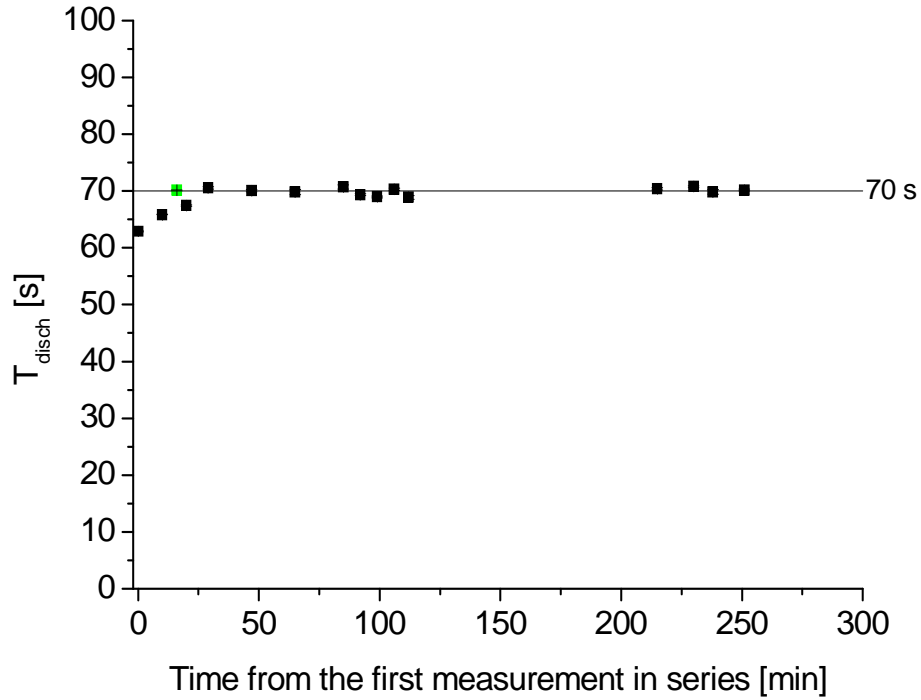


Figure 5.8: Discharge stability during 4 h series of the MEOP measurements in 32 mbar cell expressed as a stability of  $T_{disch}$  value . Regime of strong discharge (40% of IR probe,  $C_8$  absorption). Presented data results from the exponential fits to the 15 s decay recordings in the absence of pump beam within protocol C. With the line, the  $T_{disch}$  value is presented obtained from B-protocol recording where recording of the decay lasts 90 s. All the values from protocol C recordings agree within the error bars with the B-protocol value.

This is confirmed by the fair agreement of IR probe absorptions values coming from the A-protocol recordings before and after the measurement series (absolute difference up to 0.3% between absorption values before and at the end of measurement series, while absolute error of the absorption values was estimated to be 0.1%).

The discharges conditions stability allows further direct comparison of results obtained for the same rf discharge excitation voltage amplitude and its modulation while changing other experimental parameters as pump laser beam power.

The results of measured  $n_m$  value with related  $T_{disch}$  both characterizing the discharge conditions in *weak* and *strong* regime of rf excitation voltage amplitude values as well as atomic and molecular absorption values at  $M = 0$  condition are given in the table 5.1.

MEOP at 66.7 mbar, $^3\text{He}$ , B=0.82 mT		
Experimental parameters	Discharge excitation regime	
	<i>weak</i>	<i>strong</i>
atomic absorption on $C_8$ transition[%]	10.9±0.4	39.8±0.2
molecular absorption on Q(2) transition	1.92 ±0.03	4.73±0.04
$n_m$ [ $\text{cm}^{-3}$ ]	$(3.22\pm0.05)\times10^{-10}$	$(1.61\pm0.01)\times10^{-11}$
$T_{disch}$ [s]	216±0.7	70±0.7

Table 5.1: Parameters characterizing the discharge plasma in MEOP experiment at 66.7 mbar of  $^3\text{He}$ , 0.82 mT magnetic field in *weak* and *strong* regimes of excitation.

## 5.6.2 Results of MEOP - nuclear polarization values

Optical absorption method of polarization measurements delivers the information about level of nuclear polarization  $M$  at each time of the MEOP process. Just after unblocking the pump beam the polarization buildup occurs until the photon angular momentum deposition and metastability exchange transfer to the ground state are balanced by the relaxation processes, the polarization reaches "equilibrium"  $M_{eq}$ . According to [52] the polarization value inferred during the OP stage (when the pump beam interacts with the metastable atoms) is significantly different than for the case when the pump beam is being temporarily switched off. The presence of the pump beam perturbs the metastable atom distribution that is no more driven by the spin temperature  $1/\beta$ . So that determined polarization is called "apparent" ( $M_{app}$ ) and is out of interest, as it does not reflect the polarization of the ground state (related to the spin temperature). The "true" value of achieved polarization is inferred when the pump beam is blocked, that is after the second build up period in the protocol B and after the first in protocol C. Apart from the information about the achieved nuclear polarization - the target of the MEOP method, the  $M_{eq}$  value is necessary to determine the  $\Gamma_{laser}$  from the angular momentum budget equations (Sec.5.3).

Performed tests revealed discrepancies (of order 1% in absolute value) between obtained values of  $M_{eq}$  in two different probe tuning measurements confirm previous expectations about difficulties of using  $C_9$  as a probe transition. The values of  $M_{eq}$  are systematically lower for  $C_9$  probe than for  $C_8$  at the same value of absorbed pump power. Thus, only the results, where  $C_8$  component was probed will be shown in the results presentation of the  $M_{eq}$  dependency on absorbed OP light power 5.9.

In both cases of the discharges regime achieved nuclear polarization values are in agreement with the expectations (<10%) based on the previous measurements [59] performed with 32 mbar cell in low field. Up to about 0.6 W of absorbed pump laser power the  $M_{eq}$  value is increasing about 9% and 7% in respect to the lowest value at 0.04 and 0.07 W for "weak" and "strong" discharges respectively. There are no data above about 0.6 W of absorbed power for "weak" discharges. For the "strong" above 0.6 W the  $M_{eq}$  value stays at the level of 6.7% - similar behavior is expected for the first discharge regime ( $M_{eq}$  is expected to stay at the level of about 7.5%).

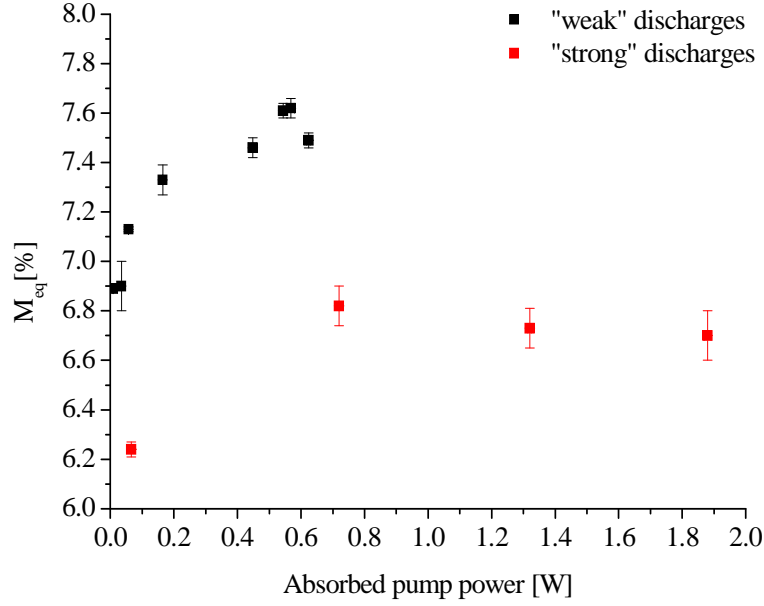


Figure 5.9: Values of  $^3\text{He}$  nuclear polarization in condition of the balance between build-up and relaxation - "equilibrium" state, obtained in the MEOP for various absorbed OP light powers for two discharge regimes: "weak" (black squares) and "strong" (red squares).  $M_{eq}$  values is presented in terms of the absorbed pump laser power at this  $M = M_{eq}$ .

### 5.6.3 Light induced relaxation and molecular absorption rates at $M_{eq}$

Relying on the equations (5.4) and (5.7) laser induced relaxation rate can be determined as the parameters required in both equation, namely:  $T_{disch}$ ,  $M_{eq}$  and absorbed pump power at  $M = M_{eq} \left(1 - T_{pump}^{M=M_{eq}}\right) W_{las} \equiv W_{abs}^{M_{eq}}$ , has been obtained as shown in preceding subsections. The value of quantum efficiency in this case for 32 mbar, according to what has been written in the section 5.3, was taken as  $\eta_{C8} = 0.5$ .

The results of  $\Gamma_{laser}$  determination at two discharge regimes and for investigated pump beam powers when both IR probe and pump beams were tuned to  $C_8$  are shown together on the fig 5.10. As before, the pump beam absorbed power scale is on abscissa.

The values of  $\Gamma_{laser}$  presented on the Fig 5.10 are in line with the other measurement data for lower gas pressure at low field conditions and are already taken into account in comparison performed by [63]. The increase of the total relaxation rate, due to  $\Gamma_{laser}$ , is up to 310 (for "weak" discharges) and 350 ("strong" discharges) times the value of the  $\Gamma_{decay}$  rate when no OP light is present. The slopes of the linear fits to the experimental data show the relative increase of  $\frac{d\Gamma_{laser}}{dW_{abs}^{M_{eq}}}$  with the discharge strength by 15% - the difference in slopes of the linear fits is clearly visible on the graph with linear scale on abscissa and ordinate axes (inset) of the Fig. 5.10.

From the other hand, there are absorption measurements of the molecular species with the blue laser. Following graphs 5.11 show the change of the absorption with the absorbed IR pump power.

According to the Fig. 5.11 (a), the change in the discharge intensity from "weak" to "strong" regime, causing 5 fold increase of the helium metastable  $2^3S_1$  atoms, results in the 2.5 times

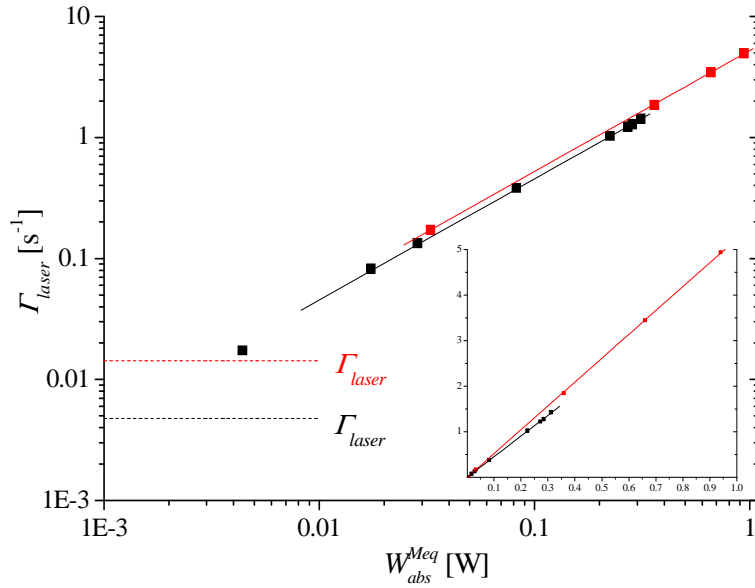


Figure 5.10: Laser induced relaxation rates  $\Gamma_{laser}$  in function of absorbed OP beam power at  $M_{eq}$  - when build-up kinetics are balanced by relaxation processes. Both abscissa and ordinate of the main graph are given in the log scale to exaggerate the dependency in the range of low absorbed power that in the linear scale of both axes (inset) is not clear. Two discharge regimes at 32 mbar, 0.82 mT are presented showing both the same functional dependency character (linear, within one slope) of  $\Gamma_{laser}$  in terms of absorbed pump power. Black/red squares - data for "weak"/"strong" discharge regime, black/red dashed line -  $\Gamma_{decay}$  values at this rf excitations. Solid black/red lines are the linear function fits independently to the data of both discharge regimes.

increase in the absolute molecular absorption signal at null absorbed 1083 nm laser power (the situation when the pump beam is off). Applying the OP light, the increase of the molecular density is noticed - linear in function of the absorbed power. The slopes for both discharges regime are similar, however it is hard to compare them quantitatively, as for the "weak" discharges data reach only 0.3 W, while for the "strong" they end up at 1 W of absorbed pump power. The comparison of the linear fits' slopes performed for the full data range for "weak" discharges (up to 0.3 W of absorbed power - black line on the 5.11; slope  $0.11 \text{ W}^{-1}$ ) and fits to the restricted data of "strong" discharges (up to 0.4 W - red - slope  $0.105 \text{ W}^{-1}$ , up to 0.2 W - blue - slope  $0.116 \text{ W}^{-1}$ ). does not allow to conclude about existence or absence of any difference in the molecular density increase in function of the absorbed power for the two regimes. Thus, the comparison with the small increase in previously discussed slope value of  $\Gamma_{laser}$  versus  $W_{abs}^{Meq}$  between the two discharge intensities cannot be made.

Considering the relative increase of the molecular density (Fig.5.11(b)) it is faster (about 2.5 times) for the "weak" discharge regime than for the "strong". It is a natural consequence of the  $\frac{d(-\ln T)}{dW_{abs}}$  rate equality for both regimes (fig.5.11 (a)) and factor of  $2.5 \times$  difference in absolute value of  $-\ln T_{M=0}$  - at  $M = 0$ .

Performed investigations does not allow to state that the origin of the laser induced relaxation processes can be explained only by the presence of the molecular species in helium plasma and its collisional interaction with polarized ground state atoms. The magnitude of the  $\Gamma_R = \Gamma_{decay} + \Gamma_{laser}$  increment due to presence of the OP light reaches 350 times the decay

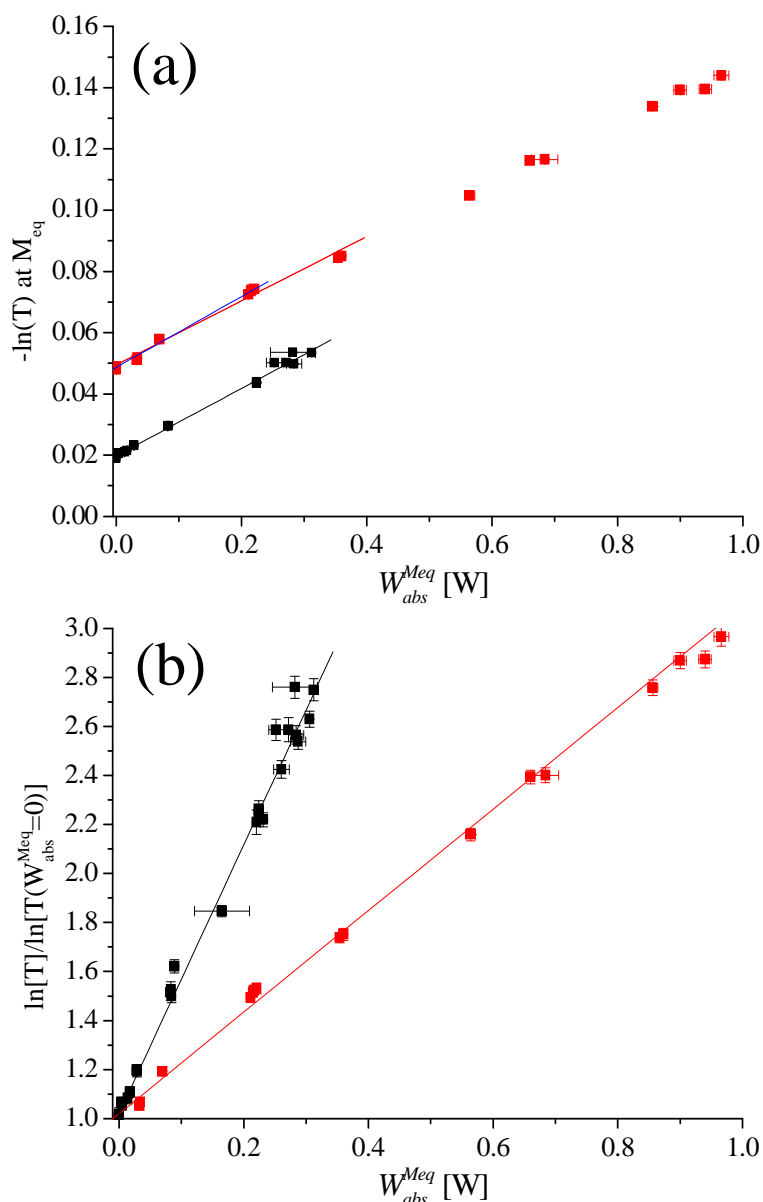


Figure 5.11: Values of  $-\ln(T)$  for 465 nm laser light tuned to Q(2) molecular transition for 32 mbar cell in which MEOP experiment is performed in parallel. Transmittances are measured at  $M_{eq}$  and shown as a function of the absorbed IR pump laser power nuclear polarization. Red/black squares - data for "strong"/"weak" discharges. On the graph (a) the  $-\ln(T) \propto N_M$  has been shown while on (b)  $-\ln(T)/\ln(T(W_{abs}=0)) \propto N_M/N_M(W_{abs}=0)$  - relative  $-\ln(T)$  in respect to the value in absence of the OP beam are presented. On the graph (b) the linear fits to the two "discharge" regimes are shown. On the graph (a) black/red/blue solid lines are the linear fits for comparable absorption power ranges in case of both discharge regimes: ("weak" full range up to 0.3 W)/("strong" up to 0.4 W)/("strong" up to 0.2 W) of absorbed pump laser power.

without the pump beam while the increase in the molecular density is 3 times at the highest absorbed pump beam power value of 1W. This discrepancy in two orders of magnitude between  $\Gamma_{laser}$  and molecular density change with absorbed pump power can indicate that the molecular species has minor influence on the laser induced relaxation.

In work [59] it has been shown, that in the same pressure cell but at much higher magnetic field (1.5 T) the laser induced relaxation rate is about 2-3 orders of magnitude lower than observed here. This gives the possibility of performing another experiments in which the behavior of molecular density with changed absorbed pump power will be investigated finally answering to the yet unknown size of impact of helium dimmers on  $\Gamma_{laser}$ .

#### 5.6.4 Atomic and molecular metastable species density change with polarization

In the work of [63] it has been shown (Fig. 6.18 of the referred work), that the metastable atomic species number density  $n_m$  is increasing with the square of the polarization  $M$ . For the high polarization values  $\approx 75\%$  the increase reaches even 20% of the  $n_m$  value at  $M = 0$ . As the effect decreases quadratically with  $M$ , at  $M \approx 7.5\%$ , reached in this work,  $n_m/n_m(M = 0) \leq 1$  As shown on the Fig.5.12, the data scatter of obtained  $n_m/n_m(M = 0)$  values during the polarization evolution in its decay part when the pump laser is switched off and no OP occurs, is about  $\pm 2.5\%$  in respect to the  $n_m/n_m(M = 0) = 1$ . This does not allow to conclude about variation of  $n_m$  with nuclear polarization value. From the other hand, considering the

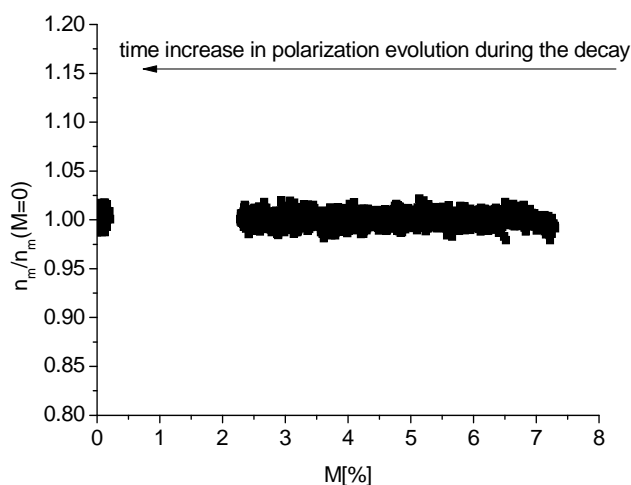


Figure 5.12: Relative change in respect to the value at  $M = 0$  of metastable  $^3\text{He}$  atoms density with nuclear polarization  $M$  during its decay when no OP is present. The polarization decrease is toward the origin of the horizontal axis what is reflection of the  $M$  evolution in the time domain.

coupling between equation rates of both atomic and molecular metastable species, the variation of relative molecular metastable species number density  $N_M/N_M(M = 0)$  has been investigated during the polarization decay (Fig.5.13.) In case of the molecular species also within the data scatter there is no indication of variation of  $N_M$  with nuclear atomic polarization.

Obtained in high magnetic field of order 1.5 to 2 T polarization values up to 75% at considered pressure 32 mbar of  $^3\text{He}$  gas open a possibility of performing analogous investigations in

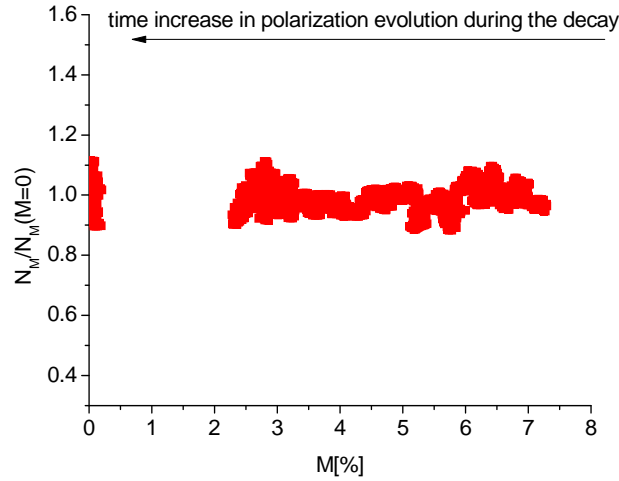


Figure 5.13: Relative change in respect to the value at  $M = 0$  of  ${}^3\text{He}_2^*$  density with nuclear polarization  $M$  during its decay

elevated magnetic field conditions so that the changes in both atomic and molecular densities is expected to exceed the level of data scatter observed in this work.

## 5.7 Absorption measurements in presence of OP pump beam at $M = 0$

Using the experimental setup presented on the graph 5.2 the complementary absorption measurements has been performed. The absorption of blue, IR probe and IR pump beam has been measured for increasing power of the last one in presence of the small magnet put on the top of the OP cell. That provides high inhomogeneity of the magnetic field in the cell volume, resulting in significant relaxation rate increase to the value comparable with OP and ME rates, so that the polarization build-up process is inhibited and  $M \approx 0$ . The comparison of the blue light absorptions with earlier presented results at  $M = M_{eq}$  (Fig.5.14) allows to check if the presence of non-zero ground state polarization affects somehow their association into the molecule.

The error bars of the 465 nm absorption measurements performed at  $M = 0$  (relative errors up to 10% for "weak" and 8% for "strong" discharges) and are about 1 order of magnitude higher than those measured at  $M = M_{eq}$  (up to 1% and 0.4% respectively). This difference results from the fact that for the  $M = 0$  case the absorption was determined on the base of single values of photodiode measurement transmitted light power in presence and absence of the discharge plasma (absorber). For the  $M_{eq}$  signal levels for these two cases were determined from average on multiple points acquired during the MEOP recording when the discharges remained on and off for the time of a few tens of a second, thus in the average the total error is reduced in comparison to the error of a single value. Such discrepancy in the error values does not occur when the absorbed pump power values are compared: for "weak discharges the relative error of  $W_{abs}$  reaches 5% for  $M = M_{eq}$  measurements and 7% at  $M = 0$ , while for the "strong" 2% and 4% respectively. In case of the measurements at  $M = 0$  the reason for such relative error magnitude is the same as it has been given for the molecular absorption error. At  $M = M_{eq}$ , in spite of the fact of averaging the data points of pump beam transmitted power

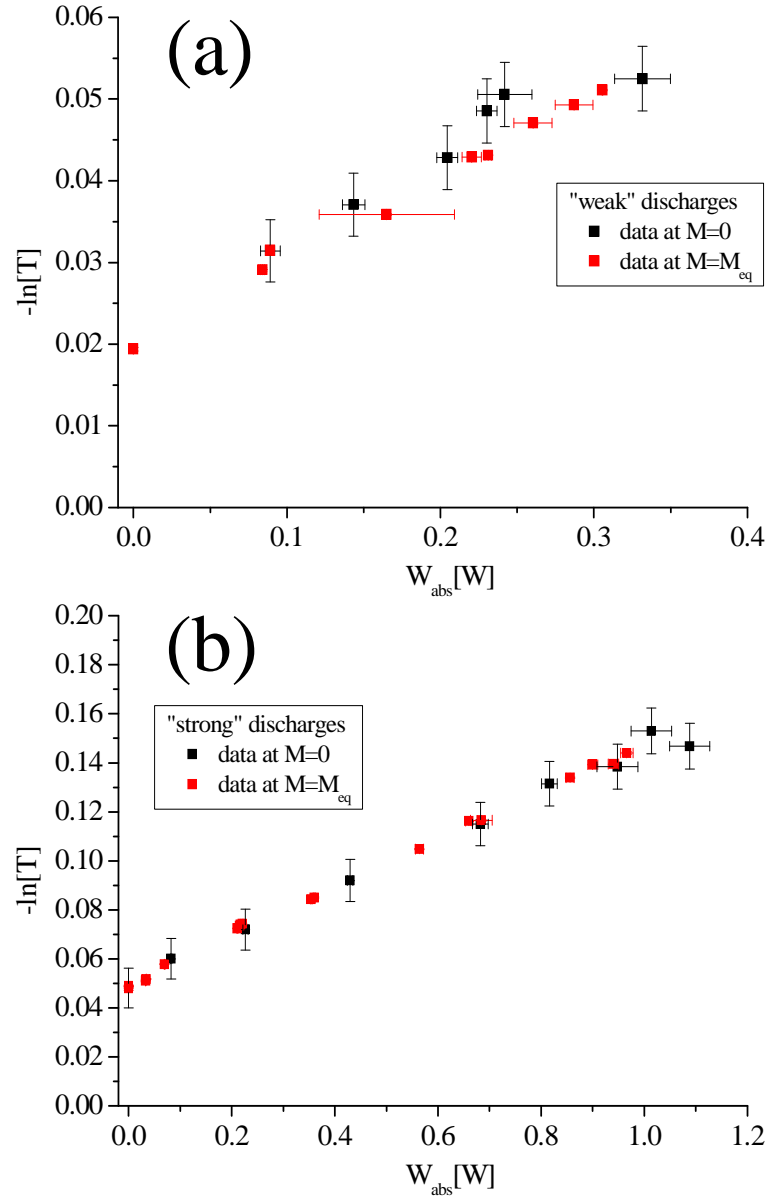


Figure 5.14: Comparison of  $-\ln(T) \propto N_M$  values measured at  $M = M_{eq}$  (red squares) and  $M = 0$  (black squares) in "weak" (a) and "strong" (b) discharge regimes in function of the absorbed pump beam power  $W_{abs}$

recordings for the levels related to plasma presence and absence, the relative error is comparable with the value obtained for single-values measurements. This is due to higher uncertainty on the mentioned levels average value due to laser light polarization instability in that time scale of a few tens of a second and necessity of linear or quadratic functions fit for "plasma on" laser transmission signal determination. Within the uncertainty of presented data on the Fig.5.14 the molecular density does not depend on the value of nuclear polarization. At much higher values of  $M$  (tens of %) the significant (up to  $\sim 20\%$ ) increase in helium metastable atoms number density is reported [63] due to inhibited, by spin conservation rules, Penning ionizing collisions in that state. Thus, the increase of the metastable molecule density is possible. This, however, can be investigated in the high magnetic field conditions where high  $M$  values at elevated pressures are achieved [60].

# Chapter 6

## Conclusion and outlook

The main objective of the present PhD work was the development of tools allowing detection of metastable helium molecules and quantitative investigation of  $^3\text{He}_2^*$  densities in typical MEOP conditions.

To this aim a dedicated laser setup providing continuous wave emission at 465 nm and 1.4 nm tuning range has been built, based on an original design allowing nonlinear Sum Frequency Generation from two closely lying input wavelengths. The laser features and performances have been shown to be in line with expectations and to provide a probe beam suitable for accurate absorption measurements on the  $a^3\Sigma_u^+$  state(0)-  $e^3\Pi_g$  state(0) transition. In particular, measurements of relative changes in absorption rates with high SNR could be performed on the main lines of the rotational Q branch. The laser has been mostly used to investigate room temperature pure helium-3 gas in radiofrequency plasma discharge conditions at pressures ranging from 8 to 267 mbar, but a few complementary experiments have been performed to observe the two stable isotopologues of the  $^3\text{He}_2^*$  molecule:  $^4\text{He}_2^*$  and  $(^3\text{He}-^4\text{He})^*$ . This blue laser source can serve as a tool for investigations of a variety of room temperature He plasmas but also in denser phases at low temperature, in particular in the liquid phase where  $a^3\Sigma_u^+$  is especially long-lived [1]. The current laser setup, based on basic post assemblies, can be readily made more robust using stable optomechanics components. Temperature control could be automated for improved convenience in experiments where operating wavelength must be frequently changed. A few ways to improve output power for more demanding applications, have been discussed in [1].

A number of spectroscopic observations on the  $^3\text{He}_2^*$  molecular isotopologues have been performed. The measured absorption line shapes systematically depart from the Voigt profiles expected for single lines, providing evidence of underlying structure. Knowledge of the  $e$ -state fine structure and/or the hyperfine structure of both  $a$  and  $e$  states for the dimers involving  $^3\text{He}$  are needed to quantitatively account for the observed shapes for the various isotopologues and to obtain reliable measurements of pressure broadenings. Doppler-free spectroscopy experiments might be carried out for precise measurements of underlying line splittings. Comparisons of relative peak amplitudes at fixed rf excitation level have been performed for the accessible components of the Q branch. They indicate that in our plasma conditions thermal equilibrium is observed over the probed low-N part of the spectrum, with rotational temperatures close to gas temperatures, and allow assessment of relative abundances for the various coexisting metastable species. More systematic investigations can be performed using the described modulation techniques. Moreover the SNR of absorption measurements has been

shown good enough to allow quantitative monitoring of  $\text{He}_2^*$  dynamics with moderate time averaging down to a few-millibar gas pressures. Simultaneous monitoring of  $\text{He}_2^*$  and  $\text{He}^*$  absorption rates have been performed at 465 nm and 1083 nm, respectively, and, as expected, a strong correlation between steady-state values and decay rates has been observed. Dependence on gas pressure and discharge intensity can be investigated in detail and quantitative comparison with time evolutions computed from the relevant coupled rate equations would provide strong tests of the description of the system, in terms of both leading processes and values of coefficients for the various formation, ionization, and quenching rates involved.

Quantitative monitoring of  $\text{He}_2^*$  and  $\text{He}^*$  has also been successfully combined and performed during metastability exchange optical pumping  $^3\text{He}$ . The first simultaneous measurements of the rate of additional relaxation of nuclear polarization induced by the strong 1083 nm pump laser ( $\Gamma_{laser}$ ) and of the change in  $\text{He}_2^*$  density ( $N_M$ ) have been performed at 32 mbar and 8 G. First, our results complement those of a series of systematic investigations recently carried out in the same magnetic field range at lower gas pressures (0.65-2.65 mbar) [63]. They confirm that the light-induced polarization loss exclusively depends on the absorbed pump power and they show that the linear increase of  $\Gamma_{laser}$  with absorbed power reported in [63] holds over a gas pressure range and absorbed power range that are both increased here by more than an order of magnitude. So far, the preliminary measurements of the correlated increases in  $\Gamma_{laser}$  and in  $N_M$  with absorbed 1083 nm light power show that the change in relaxation rate is about two orders of magnitude larger than that of the molecular density. This suggests that interactions of polarized atoms with molecular species may not play a dominant role in  $^3\text{He}$  relaxation. However, more systematic measurements remain to be carried out, over the whole range of operating gas pressures and plasma conditions. Of particular interest would be investigations at higher magnetic field strengths, where much higher nuclear polarizations can be achieved in this pressure range (in contrast with the 6-7 % achieved at 0.8 mT, polarizations up to 60% can be obtained at 32 mbar and about 25% at 267 mbar [60, 55]). If operation at high field can significantly influence the various processes occurring in the complex plasma system, it definitely modifies deeply the level structure of all metastable species and introduces hyperfine decoupling. Preliminary studies of the Zeeman effect and hyperfine decoupling, similar to those performed for the metastable atom [54], would thus need to be performed for the molecule using the blue laser. Then experiments with combined 465 nm and 1083 nm absorption measurements analogous to ours could be carried out.

# Appendix A

## Absorption measurements

Straightforward information about absolute density of atoms or molecules in a certain electronic state is available only through application of absorption methods. They rely on the measurement of change in the light power  $P$  passing through the volume of absorber - atomic or molecular species, providing that light frequency  $\omega_{las}$  is in the vicinity of the resonance value  $\omega_{if}$  for transition occurring between particle (atomic or molecular) initial state sublevel  $i$  and final state sublevel  $f$ . As the absorption process is considered, the initial  $i$  sublevel is the lower state, and  $f$  is the excited one. If  $P_0$  stands for light power before interaction with absorber, then value of transmission rate  $T$  is given by

$$T = \frac{P}{P_0} \quad (\text{A.1})$$

and connected with absorption rate  $A$  in relation:

$$A = 1 - T. \quad (\text{A.2})$$

In further considerations the power change per unit surface  $dS$  perpendicular to the direction of beam propagation  $l(x, y, z)$ :

$$\frac{dP(x, y, z)}{dS} \equiv I(x, y, z), \quad (\text{A.3})$$

which is defining the local light intensity (spatial dependency is emphasized), will show up. The coordinates  $x, y, z$  corresponds to the frame of the absorber, thus, in general, surface element  $dS$  as well as the direction of propagation can be expressed by the function of all coordinates. Of course, in the volume devoid of the absorbing species or when the radiation frequency  $\omega$  is beyond the values within the absorption line profile (see further: (a)) the value  $P_0$  implicates  $I_0$ . The local value of intensity change in function of the infinitesimal path length  $dl(x, y, z)$  (along the direction of propagation  $l$ ) of light through the absorber can be written:

$$\frac{dI(x, y, z)}{dl} = -I(x, y, z) \left( N_i(x, y, z) - \frac{g_i}{g_f} N_f(x, y, z) \right) \sigma_{if}(\omega_{las}) \quad (\text{A.4})$$

Except obvious dependency of equation (A.4) on the initial local intensity and number of atoms in initial state sublevel per unit volume ( $N_i$   $\hat{U}$  number density), the number density of atoms in the final state sublevel appears ( $N_f$ ) together with degeneracy factors  $g_i$  and  $g_f$  of both sublevels connected by transition. The reason for  $N_f$  presence in (A.4) is the process of

stimulated emission that is taken into account. However, if the laser beam power is small, so that population of the  $f$  sublevel is negligible comparing to population of  $i$  state, as it is in case of our probe lasers, stimulated emission process can be neglected and (A.4) goes into:

$$\frac{dI(x, y, z)}{dl} = -I(x, y, z)N_i(x, y, z)\sigma_{if}(\omega_{las}) \quad (\text{A.5})$$

Apart from the assumption about the low laser power, the approximation of its monochromaticity was applied, what allows avoiding the integration about the laser frequency in eq. (A.4) and (A.5). Both laser systems - used for MEOP and blue light generation, emit laser light with spectral width of a few MHz, about two orders of magnitude less than natural absorption line broadening or collisional and Doppler broadening of a few GHz. In other words, it is assumed that all the radiation with power  $P_0$  is emitted at single chosen value of frequency  $\omega_{las}$  that can be tuned and matched to the transition frequency  $\omega_{if}$ .

Using (A.1) requires the knowledge about the value of power  $P$  and  $P_0$  which are, due to (A.3), surface integrals of  $I$  and  $I_0$  respectively. Absorption is then determined by geometrical properties and mutual relations of the laser beam power spatial profile, its path through the absorber with the geometry of absorber itself - spatial distribution of  $N_i$ . Therefore, explicit equation relating absorption requires the knowledge of the experimental setup conditions what is the matter of the chapters 4 and 5.

The factor  $\sigma_{if}(\omega_{las})$  that appears in (A.4) and (A.5) is called cross-section for absorption. After [30, 31]:

$$\sigma_{if}(\omega) = \frac{1}{g_i} \frac{\pi\omega_{if}}{3\epsilon_0\hbar c} S_{fi} w(\omega - \omega_{fi}), \quad (\text{A.6})$$

where  $g_i$  is the degeneracy of the initial sublevel of the transition.  $S_{fi}$  is the strength of the line of the transition and  $w(\omega - \omega_{fi})$  is the line profile with the central frequency  $\omega_{fi}$ . For absorption the  $\omega \equiv \omega_{las}$ . The designation of the states:  $i$  (initial) and  $f$  (final) is matched to the absorption case  $i \rightarrow f$ . For emission, where the process occurs in the opposite direction  $i \leftarrow f$  it is denoted by reverse order of  $i$  and  $f$  in the subscript of  $S_{fi}$  than in case of the absorption:  $if$ .

The line strength  $S_{fi}$  is related to the matrix element of the electric moment  $d_{fi} = \int \Psi^{f*} \hat{d} \Psi^i d\tau$  by expression:

$$S_{fi} = g_2 \left| \int \Psi^{f*} \hat{d} \Psi^i d\tau \right|^2. \quad (\text{A.7})$$

$d$ , the electric dipole moment is the sum of all (electrons' and nuclei)  $e_i \vec{r}_i$  multiplicities.  $\Psi^i$  and  $\Psi^f$  are the wavefunctions of the initial and final states of the transition respectively. The integral in (A.7) is to be taken over the whole configuration space of the  $3(N\text{-particles})$  coordinates

This identity (A.7) is useful as the starting point of detailed expression for the cross-section derivation for the atoms or molecules.

### (a) Spectral line profile and line broadening

The last term in eq. (A.6):  $w(\omega - \omega_{fi})$  is the normalized line profile function centered on the transition  $i - f$  frequency  $\omega_{fi}$ . The shape of the  $w(\omega - \omega_{fi})$  reflects spectral distribution of emitted or absorbed light intensity around  $\omega_{if}$ . Non-monochromatic response of the atomic or molecular system in emission or absorption is the result of several so-called broadening processes.

The principal one is the natural broadening, that results from the decrease of oscillation amplitude of damped oscillator to which classical model the atom or molecule can be approximated. Natural linewidth can be related to the uncertainties of energy of upper and lower states of the transition being a consequence of the uncertainty principle and their finite lifetime. According to [30] the resulting line profile is given by:

$$L(\omega - \omega_{fi}) = \frac{1}{2\pi} \frac{\gamma}{(\gamma/2)^2 + (\omega - \omega_{fi})^2} \quad (\text{A.8})$$

The second broadening effect is the resultant of the Doppler effect which the absorbing particle in motion experiences. The frequency of radiation emitted (absorbed) by a particle moving with the velocity  $v$  toward the observer (in the beam direction of propagation) changes with  $v$ :

$$\omega_{fi} \rightarrow \omega_{fi} \left(1 + \frac{v}{c}\right). \quad (\text{A.9})$$

The Maxwellian velocity distribution is given by:

$$G(v) = \frac{1}{\sqrt{\pi}\bar{v}} \exp\left(-\left(\frac{v}{\bar{v}}\right)^2\right), \quad (\text{A.10})$$

where the most probable velocity  $\bar{v} = \sqrt{\frac{2kT}{m}}$  ( $k$ -Boltzmann constant,  $T$ -temperature,  $m$ -particle mass).

When both equations: (A.9) and (A.10) are combined, the Doppler broadened line profile takes form:

$$G(\omega - \omega_{fi}) = \frac{c}{\sqrt{\pi}\bar{v}\omega_{fi}} \exp\left(-\left(\frac{c(\omega - \omega_{fi})}{\bar{v}\omega_{fi}}\right)^2\right) \quad (\text{A.11})$$

The third important line broadening process is the collisions between particles when the mutual interaction, interatomic distance dependent, causes the energy shifts in the  $i$  and  $f$  levels (generally shifts are different for  $i$  than for  $f$ ). If, during the collision, no energy transfers between colliding partners occur, the collision is called *elastic*. It can additionally cause the transition frequency shift. For the inelastic collision the complete or partial internal energy transfer of between particles takes place or the energy is transferred into their translational energy. Both elastic and inelastic collisions influence on the line profile are described by the Lorentzian function [30] as in the eq. (A.8). When the contributions from elastic and inelastic collisions to the line broadening are noted as:  $\gamma^{el}$  and  $\gamma^{inel}$ , writing  $\Gamma = \gamma + \gamma^{el} + \gamma^{inel}$  the eq. (A.8) can be rewritten:

$$L(\omega - \omega_{fi}) = \frac{1}{2\pi} \frac{\Gamma}{(\Gamma/2)^2 + (\omega - \omega_{fi})^2}. \quad (\text{A.12})$$

In general, if no special Doppler-free techniques are applied, both collisional and Doppler effects has to be considered simultaneously what results in the total lineshape to be the convolution of Lorentzian and Gaussian functions, the Voigt profile. The convolution of the two functions is defined as:

$$w(x) \equiv (f * g)(x) = \int_{-\infty}^{\infty} f(t)g(x - t)dt \quad (\text{A.13})$$

Applying this definition to the  $G(\omega - \omega_{fi})$  and  $L(\omega - \omega_{fi})$  functions one obtains:

$$w(\omega - \omega_{fi}) \equiv (G * L)(\omega - \omega_{fi}) = \frac{c\Gamma}{2\omega_{fi}\bar{v}\pi^{3/2}} \int_{-\infty}^{\infty} \frac{\exp\left(-\left(\frac{ct}{\omega_{fi}\bar{v}}\right)^2\right)}{(\Gamma/2)^2 + (\omega - \omega_{fi} - t)^2} dt. \quad (\text{A.14})$$

After the substitutions:

$$y = \frac{ct}{\omega_{fi}\bar{v}}, \quad (\text{A.15a})$$

$$w_G = 2\sqrt{\ln(2)}\frac{\omega_{fi}\bar{v}}{c}, \quad (\text{A.15b})$$

$$w_L = \Gamma, \quad (\text{A.15c})$$

the line profile being a consequence of broadening processes discussed here is given by:

$$w(\omega - \omega_{fi}) = 2\ln(2)\frac{1}{\pi^{3/2}}\frac{w_L}{w_G^2} \int_{-\infty}^{\infty} \frac{\exp(-y^2)dy}{\left(\frac{2\sqrt{\ln(2)}(\omega - \omega_{fi})}{w_G} - y\right)^2 + \left(\sqrt{\ln(2)}\frac{w_L}{w_G}\right)^2} \quad (\text{A.16})$$

$w_G$  and  $w_L$  are the angular frequency full width at half maximum (FWHM) of the Gaussian and Lorentzian profiles contributing to overall Voigt profile half-width of the transition line.

Considering the angular frequency dependency of (A.16) it is clear that the profile has the maximum  $w(0)$  at  $\omega = \omega_{fi}$  and is symmetric at around this value. This translates into the fact that the highest absorption of radiation occurs when the light frequency is tuned to the transition frequency  $\omega_{las} = \omega_{fi}$  and decreases as the difference  $\omega_{las} - \omega_{fi}$  increases.

# Appendix B

## Sellmeier equation and coefficients

There are several approaches to the refractive indexes determination in function of the wavelength for KTP material within reported literature sources [73] - [71]. [69, 70, 72] are using standard Sellmeier equation relating the refractive index with  $\lambda$  as follows:

$$n = \sqrt{A + \sum_i \frac{B_i}{1 - C_i \lambda^{-2}} - D \lambda^2} \quad (\text{B.1})$$

The parameters  $A$ ,  $B_i$ ,  $C_i$  and  $D$  are given in the following table B.1 for the  $n_z$  component relevant in this work. It has to be mentioned that references using up to  $i=1$ ,  $i=2$  or  $i=3$  expansions respectively thus different number of coefficients are needed in calculations.

Following references includes also the temperature dependency of the nonlinear crystal on the refractive index. They based on the Sellmeier equation with additional terms responsible for the crystal temperature variation.

Introduced by [71] equation for  $n_z(\lambda, T)$  is given by:

$$n_z(\lambda, T) = \sqrt{A + \beta(T^2 - 400) + \frac{B_1 + \delta(T^2 - 400)}{\lambda - C_1 \phi(T^2 - 400)} - [D + \rho(T^2 - 400)] \lambda^2} \quad (\text{B.2})$$

Coefficient for $n_z$	[69]	[70]	[72]
$A$	2.25411	2.12725	1
$B_1$	1.06543	1.18431	1.71645
$B_2$	-	0.6603	0.5924
$B_3$	-	-	0.3226
$C_1$	0.05486	$5.14852 \times 10^{-2}$	0.013346
$C_2$	-	100.00507	0.06503
$C_3$	-	-	67.1208
$D$	0.02140	$9.68956 \times 10^{-3}$	0.01133

Table B.1: Coefficients of the Sellmeier equation for the  $n_z$  refractive index component reported in [69, 70, 72]

Coefficient for $n_z$	[71]	[73]	[74]	
$A$	3.3134	4.59423	$n_1(\lambda)$	$n_2(\lambda)$
$B_1$	0.05694	0.06206		
$B_2$	-	110.80672		
$C_1$	0.05657	0.04763		
$C_2$	-	86.12171		
$D$	0.01682	-		
$\beta \times 10^{-7}$	-1.1327	-18.97	99.587	-0.11882
$\delta \times 10^{-7}$	1.6730	366.77	99.228	1.0459
$\phi \times 10^{-7}$	-0.1601	-292.2	-89.603	-0.98136
$\rho \times 10^{-7}$	0.52833	92.21	41.01	0.31481

Table B.2: Coefficients of the Sellmeier equation for the  $n_z$  refractive index component reported in [71, 73, 74]

In [73] the refractive index dependency on the wavelength at  $T=20^\circ\text{C}$  has been taken as:

$$n_z = \sqrt{A + \sum_{i=1}^2 \frac{B_i}{\lambda^2 - C_i}}, \quad (\text{B.3})$$

with the temperature derivative useful for  $T \neq 20^\circ\text{C}$ :

$$\frac{dn_z}{dT} = \beta + \frac{\delta}{\lambda} + \frac{\phi}{\lambda^2} + \frac{\rho}{\lambda^3} \quad (\text{B.4})$$

with coefficients of both equations (B.3) and (B.4) given in the table B.2.

[74] reference delivers the parabolic dependency of the refractive index on the temperature in the following form:

$$\Delta n(\lambda, T) = n_1(\lambda)(T - 25) + n_2(\lambda)(T - 25)^2 \quad (\text{B.5a})$$

$$n_i(\lambda) = \beta + \frac{\delta}{\lambda} + \frac{\phi}{\lambda^2} + \frac{\rho}{\lambda^3} \quad (\text{B.5b})$$

with coefficients given explicitly in the B.2 for different for  $n_1$  and  $n_2$  in separate columns. The result of the equation (B.5a) for  $n_z$  index calculation for KTP has to be added to the result of calculations performed using (B.1) with coefficients from the B.1 - column of [70] reference.

# Appendix C

## Constants

The constants used in this work together with the reference sources are given below. There are both fundamental constants as well as molecular constants for  ${}^4\text{He}_2^*$  and  ${}^3\text{He}_2^*$ .

$c = 2.99792458 \times 10^8$ m/s	speed of light in vacuum [85]
$\epsilon_0 = 8.854187817 \times 10^{-12}$ F m <sup>-1</sup>	permittivity of free space [85]
$\alpha = 7.2973525376(50) \times 10^{-3}$	fine structure constant [85]
$h = 6.62606896(33) \times 10^{-34}$ J s	Planck constant [85]
$\hbar = 1.054571628(53) \times 10^{-34}$ J s	Planck constant $h/2\pi$ [85]
$k_B = 1.3806504(24) \times 10^{-23}$ J/K	Boltzmann constant [85]
$m_e = 9.10938215(45) \times 10^{-31}$ kg	electron mass [85]
$u = 1.660538782 \times 10^{-27}$ kg	atomic mass unit [85]
$a_0 = 0.52917721092(17) \times 10^{-10}$ m	Bohr radius [85]
$f = 0.5391$	oscillator strength of the $2^3\text{S}_1$ - $2^3\text{P}$ transition[83, 84]

(b) Molecular constants

Molecular constant designation	${}^4\text{He}_2^*$		${}^3\text{He}_2^*$
	[28]	[6]	[6]
	[cm <sup>-1</sup> ]		
	$a^3\Sigma_u^+$ state		
$B_e$	7.703	7.698	10.222
$B_0$	7.589	7.587	10.046
$D_0 \times 10^{-4}$	5.60	5.47	9.76
$\alpha_e$	0.228	0.217	0.3465
$\gamma_e \times 10^{-2}$	-0.46	-0.95	-1.06
$\omega_e$	1808.5	1811.2	2085.65
$\omega_e x_e$	38.2	39.2	51.83
$T_e$	21549.95	21549.54	21549.79
$e^3\Pi_g$ state			
$B_e$	7.283	-	9.664
$B_0$	7.1728	7.17	9.495
$D_0 \times 10^{-4}$	5.22	5.05	9.08
$\alpha_e$	0.2215	-	0.3346
$\gamma_e \times 10^{-2}$	-0.13	-	-0.47
$\omega_e$	1721.1	1724.6	1982.95
$\omega_e x_e$	34.7	36	46.44

Table C.1: Molecular constants for  ${}^4\text{He}_2^*$  and  ${}^3\text{He}_2^*$  reported in [28] and [6] respectively.

# Bibliography

- [1] G. Tastevin, B.Glowacz and P.-J. Nacher, *J.Low Temp.Phys.*, **158** (2010) 339
- [2] W. Guo et al., *Phys.Rev.Lett.*, **102** (2009) 235301
- [3] F.D. Colegrove, L.D. Scheerer, G.K. Walters, *Phys. Rev.* **132** (1963) 2561
- [4] A.V.Phelps, *Phys.Rev.*, **99** (1955) 1307
- [5] W.E.Curtis, *Roy.Soc.Proc.*, **89** (1913) 146
- [6] G.H.Dieke, *Phys.Rev.*, **80** (1950) 1
- [7] P.Rosen, *J.Chem.Phys.*, **18** (1950) 1182
- [8] Y.Tanaka and K.Yoshino, *J.Chem.Phys.*, **50** (1969) 3087
- [9] X.Wu et al. *J.Chem.Phys.*, **132** (2010) 204304
- [10] Y.-H. Uang, W.C.Stwalley, *J.Chem.Phys.*, **76** (1982) 5069
- [11] D.R.Yarkony, *J.Chem.Phys.* **90** (1989) 7164
- [12] A.Köymen et al., *Chem.Phys.Lett.*, **168** (1990) 405
- [13] X.Zhao et al., *Phy Rev. A*, **48** (1993) 4350
- [14] A.B.Callear and R.E.M.Hedges, *Trans.Farraday Soc.*, **66**, 2921 (1970) 66
- [15] F.Emmert et al., *J.Phys.D*, **21** (1988) 667
- [16] H.Herzberg, "*Molecular Spectra and Molecular Structure: I. Spectra of Diatomic Molecules*", Van Nostrand Reinhold Company, 2nd edition, (1950)
- [17] M. Born and J.R. Oppenheimer, *Ann.Phys.*, **84** (1927) 457
- [18] H. Haken, H. C. Wolf, "*Fizyka molekularna z elementami chemii kwantowej*", PWN, Warszawa (1998)
- [19] P.M.Morse, *Phys.Rev.*, **34** (1929) 57
- [20] C. L. Pekeris, *Phys.Rev.*, **45** (1934) 98.
- [21] J. L. Dunham, *Phys.Rev.*, **41** (1932) 721.

- [22] J. Chevalerey, *J.Phys.B:At.Mol.Phys.*, **11** (1977) 1227.
- [23] G.Myers and A.J.Cunningham, *J.Chem.Phys.*, **67** (1977) 1942.
- [24] J. Brown,A. Carrington, "*Rotational Spectroscopy of Diatomic Molecules*" Cambridge University Press (2003).
- [25] C.Focsa, P.F. Bernath, R. Colin, *J.Mol.Spect.*, **11** (1998) 209.
- [26] W. Lichten, M.V. McCusker, and T.L. Vierima, *J.Chem.Phys.*, **61** (1998) 22000.
- [27] S.A. Rogers, C.R. Brazier, P.F. Bernath, *Mol.Phys.*, **63** (1988) 901.
- [28] C.M. Brown, M.L. Ginter, *J.Mol.Spect.*, **5** (1971) 302.
- [29] J.B. Tatum, *ApJS*, **124** (1967) 21.
- [30] W. Demtröder, "*Laser Spectroscopy Basic Concepts and Instrumentation*" Springer-Verlag Berlin Heidelberg New York (1981)
- [31] J.Stevelfelt, J.M. Pouvesle and A. Bouchoule, *J.Chem.Phys*, **76** (1982) 4006.
- [32] J.-C.Gauthier et al., *Phys.Rev.A*, **13** (1976) 1781.
- [33] A.Schadee., *B.A.N.*, **17** (1964) 311.
- [34] D.C.Morton, L.Noreau, *ApJS*, **95** (1994) 301.
- [35] S.Neeser et.al, *Z.Phys.D*, **31** (1994) 61.
- [36] F.Luo et.al, *J.Chem.Phys.*, **98** (1993) 3564.
- [37] M.L. Ginter and R.Battino, *J.Chem.Phys.*, **52** (1970) 4469.
- [38] W. P. Risk, T. R. Gosnell, A. V. Nurmikko *COMPACT BLUE-GREEN LASERS* Cambridge University Press (2003)
- [39] G. Boyd, D. Kleinman, *J.Appl.Phys.*, **39** (1968) 3597
- [40] R. Le Targat, J.-J. Zondy, P. Lemonde, *Opt.Commun.*, **247** (2005) 471
- [41] S. Johansson et al., *Opt.Express*, **12** (2004) 4935
- [42] E. Mimoun, *Opt.Express*, **16** (2008) 18684
- [43] H. GhafouriŪShiraz, *Distributed Feedback Laser Diodes and Optical Tunable Filters* John Wiley & Sons Ltd (2003)
- [44] P.Zeppini, *Opt. Laser Eng.*, **37** 553
- [45] V.A.Dyakov et al., *Sov.J.Quantum Electron.*, **18** 1059 (1988)
- [46] J.-F. Delpech, J.-C. Gauthier, and F. Devos, *J.Chem.Phys.*, **67** (1977) 5934
- [47] S.Takao et al., *J.Chem.Phys.*, **73** (1980) 148

- [48] I.Hazell et al., *J.Mol.Spec.*, **172** (1995) 135
- [49] W.Lichten,T.Wik, *J.Chem.Phys.*, **69** (1978) 98
- [50] M.Kristensen and Nis Bjerre, *J.Chem.Phys.*, **93** (1990) 983
- [51] T.G.Walker and W.Happer, *Rev.Mod.Phys.*, **69** (1997) 629
- [52] M.Batz, G.Tastevin and P.-J.Nacher, *J.Phys: Conf.Series*, **294** (2011) 012002
- [53] P.J.Nacher and M.Leduc, *Journal de Physique*, **46** (1985) 2057-2073
- [54] E. Courtade et al., *The European Physical Journal D - Atomic, Molecular, Optical and Plasma Physics*, **21** (2002) 25-55
- [55] G.Collier, "*Metastability Exchange Optical Pumping (MEOP) of  $^3\text{He}$  in situ*" Phd thesis at Jagiellonian University, Krakow 2011
- [56] L. D. Schearer and L. A. Riseberg, *Phys. Lett. A*, **33** (1970) 326
- [57] M.Abboud et al., *Europhys.Lett.*, **68** (2004) 480-486
- [58] M.Abboud et al., *Laser Physics*, **15** (2005) 475-479
- [59] M. Abboud, *Pompage optique de l'Helium-3 'a forte pression dans un champ magnetique de 1.5 Tesla* These de doctorat Universit'e Pierre et Marie Curie (2005) URL <http://tel.archives-ouvertes.fr/tel-00011099/>
- [60] A.Nikiel, "*POLARYZACJA  $^3\text{He}$  W WARUNKACH ROZERWANIA SPRZĘŻENIA STRUKTURY NADSUBTELNEJ*" Phd thesis at Jagiellonian University, Krakow 2010
- [61] C.Talbot et al., *J.Phys.:Conf.Ser.*, **294** (2011) (1929)
- [62] E. Courtade, *Pompage optique de l'Helium dans des conditions non-standard*(in French); Ph.D. thesis Universit'e Paris XI (2001), available online at <http://tel.archives-ouvertes.fr/tel-00001447>
- [63] M.Batz, *Metastability exchange optical pumping of  $^3\text{He}$  gas up to 30 mT: Efficiency measurements and evidence of laser-induced nuclear relaxation* Phd dissertation at These Universit'e Pierre et Marie Curie, Paris and Johannes Gutenberg-Universiät, Mainz (2011)
- [64] B.Stahlberg et al., *J.Chem.Soc.,Faraday Trans. 2*, **81** (1985) 207
- [65] W.A. Fitzsimmons, N.F. Lane and G.K. Walters, *Phys. Rev.*, **174** (1968) 193
- [66] M.A. Gusinow, R.A. Gerber, *Phys.Rev A*, **2** (1970) 1973
- [67] R. Deloche et al., *Phys.Rev.A*, **13** (1976) 1140
- [68] J.J.Olivero, R.L.Longbothum, *J.Quant.Spectrosc.Radiat.Transfer*, **17** (1977-02) 233
- [69] T.Y.Fan et al., *Appl.Opt.*, **26** (1987) 2390
- [70] K.Fradkin et al., *Appl.Phys.Lett.*, **74** (1999) 914

- [71] B.Boullanger et al., *J.Opt.Soc.Am.B, Optical physics*, **17** (2000) 775
- [72] M.Katz et al., *J.Appl.Phys.*, **90** (2001) 53
- [73] K.Kato and E.Takaoka, *App.Opt.*, **41** (2002), 5040
- [74] S.Emanueli and A.Arie, *Appl.Opt.*, **42** (2003) 6661
- [75] F.M.Librecht and J.A.Simons, *IEEE J.Quant.Electron.QE*, **11** (1975) 850
- [76] A.Steinbach et al., *Opt.Comm.*, **123** (1996) 207.
- [77] T.Freearde et al., *J.Opt.Soc.Am.B*, **14** (1997) 2010
- [78] M.Peltz et al., *Appl.Phys.B: Lasers and Optics*, **73** (2001) 663
- [79] A.Aire et al., *Opt.Communications*, **142** (1997) 265
- [80] J.D.Bierlein and H.Vanherzeele, *JOSA B*, **6** (1989) 622
- [81] W.P.Risk W. P. Risk, *Proc. SPIE*, **2700** (1996)
- [82] M.M.Fejer et al., *IEEE J.Quantum Electron.*, **28**(1992) 2631.
- [83] W.L.Wiese, M.W.Smith, B.M.Glennon, *Atomic transition probabilities; Nat.Stand.Ref.Data Ser.NBS 4*, US Government Printing Office, Washington DC (1966)
- [84] G.W.F.Drake, *Atomic, molecular, and optical physics handbook*, AIP press (1996).
- [85] CODATA Internationally recommended values of the Fundamental Physical Constants (2006). Available online at <http://physics.nist.gov/constants>